APPLIED COMPUTATIONAL ELECTROMAGNETICS SOCIETY JOURNAL

JULY 2024 REVIEWERS

Rajini A. R.
Priya Anumuthu
Ravi Kumar Arya
Alireza Baghai-Wadji
Bhattacharya
Grzegorz Bogdan
Vinh Dang
Atef Elsherbeni
Nunzia Fontana
Piotr Gas
Alfredo Gomes Neto
Lihua Li
Xiaoyong Liu
Matteo Bruno Lodi

Vinoth M.
Li Ma
Behih Mohamed
Andrew Peterson
Yusnita Rahayu
C. J. Reddy
Francesco Scappaviva
Michele Schirru
Somchat Sonasang
Marcin Szczech
Shu Wang
Yunshan Wang
Zhengyong Yu

THE APPLIED COMPUTATIONAL ELECTROMAGNETICS SOCIETY JOURNAL

Vol. 39 No. 7   July 2024

TABLE OF CONTENTS

Parameter Optimization of Electromagnetic Sensing and Driving Scheme of a Compact Falling-body Viscometer

Kun Zhang[1], Hongbin Zhang[2], Yuan Xue[3], Jinyu Ma[2], Jiqing Han[1], and Xinjing Huang[2]

[1]Shandong Non-Metallic Materials Institute
Jinan 250031, China
zhangkun8185@163.com, qddxhjq@163.com

[2]State Key Laboratory of Precision Measurement Technology and Instruments
Tianjin University, Tianjin 300072, China
1360387520@qq.com, jinyu.ma@tju.edu.cn, huangxinjing@tju.edu.cn

[3]National Institute of Measurement and Testing Technology
Chengdu 610021, China
383622356@qq.com

Abstract – In order to achieve automatic fast reset of the falling-body (FB) viscometer, and reduce the volume of the device and the amount of sample used, this paper proposes to use a single coil to reset the FB and use another single coil to measure the FB position. In this paper, the characterization ability of the sensing coil impedance to the FB position and its influencing factors, and the reset ability of the driving coil to the FB and its enhancement factors, are studied via electromagnetic finite element simulations and experiments. There is a linear zone between the FB position and the sensing coil impedance, with the slope being largest. The lower limit of the FB motion should be designed in this linear zone to accurately determine the moment when the FB reaches the lower limit point. Increase in the FB height, and in the number of turns of the sensing coil, and decrease in the wire diameter are beneficial to the FB positioning. There is a maximum force point when the FB approaches the driving coil, and the FB's motion range needs to cover this point for reliable reset. Using iron plugs allows the FB to obtain greater electromagnetic attraction and ensure its successful reset. Experimental results show that the device requires only 1 mL of sample to measure liquid viscosity. For 9.5-1265 mPa·s dimethyl silicone oil, the average absolute value of the relative measurement error is 0.22% and the maximum value is 4.3%.

Index Terms – Electromagnetic coil, electromagnetic force, falling-body method, impedance measurement.

I. INTRODUCTION

Viscosity is an inherent physical property of fluid that reflects the friction between molecules when the fluid is subjected to external force [1]. Measuring the viscosity of a high-temperature and high-pressure liquid can assess the flow characteristics of the liquid, which is of great importance in the fields of oil and gas exploitation [2], coal liquefaction [3][4], the chemical industry and the operation of power equipment. At present, commonly used methods for measuring high-temperature and high-pressure liquids are the capillary method [5][6], the resonance string method [7][8], the rotation method [9][10] and the falling-body (FB) method.

Due to the small diameter of the capillary tube, the capillary viscometer has a high risk of clogging when measuring high-viscosity liquids. The resonant string viscometer necessitates the utilization of a long container in order to facilitate the vibration of the metal wire, thereby increasing the demand for liquid samples. The structure of the rotary viscometer is relatively complex and there is rotary transmission friction. The rotary viscometer requires a great number of components and has a large volume. It necessitates a considerable quantity of samples for measurement of liquids, which render it unsuitable for the viscosity measurement of expensive liquids.

Compared with the capillary method, the resonance string method and the rotation method, the FB method exhibits distinctive advantages. Its structure is simple, and it is easy to form a closed cavity to carry out viscosity measurements under high temperature and high pressure.

Development of the FB viscometer can be traced back to Bridgman [11][12] who used a falling cylinder to test the viscosity of 43 different fluids under high pressure. Bridgeman pointed out that the viscosity of the fluid

is positively related to the falling time of the falling cylinder. The theory of measuring liquid viscosity using the FB method has been continuously improved. As the FB descends, the liquid is displaced, forcing it through the annular area between the tube wall and the FB. This displacement of the liquid creates considerable resistance to the FB movement. Lohrenz et al. [13] conducted a theoretical analysis of laminar flow in the ring of a FB viscometer and determined the calibration constant of the viscometer based on the analysis results. Ashare et al. [14] compared the difference in viscosity measurement using the FB method between non-Newtonian fluids and Newtonian fluids and gave an approximate expression for the viscosity of non-Newtonian fluids. Cristescu et al. [15] obtained the velocity profiles of liquid flow in open tubes and closed tubes, simplified the influence of various parameters of the FB on the fluid flow, obtained the formula for measuring the viscosity coefficient, and designed a FB viscometer with an ultrasonic transducer that measures the falling time of the FB. Gui et al. [16] obtained the numerical solution of the flow field around the cylindrical FB, determined the end correction factor, and gave the relevant equations for the end correction factor. Irving and Barlow [17] pointed out that when the diameter of the falling cylinder is less than 93% of the pipe diameter, the FB will fall eccentrically, resulting in unstable fall-time measurement. They therefore developed a high-pressure automatic falling cylinder viscometer using a solid cylinder and a FB with a central hole adapted to liquids of different viscosities. The falling time of the FB is measured by a series of detection coils on the viscometer tube.

In the measurement of viscosity of high-temperature and high-pressure liquids, the FB method has been applied often. Průša et al. [18] studied the measurement of viscosity of liquids of variable viscosity values with a FB viscometer and derived a modification of the classical formula for fluids with pressure-dependent viscosity. The systematic error introduced by the classical formula in measuring fluids with pressure-dependent viscosity is analyzed. Bair et al. [19][20] developed a compact and easy-to-operate viscometer using the FB method. Two concentric cylinders are used to form a pressure vessel. High temperature conditions are achieved by heating the air in the gap between the two cylinders. The inner cylinder and the plug are connected through threads to form a sealing device. The inner cylinder is connected to an external pressure-generating device to achieve high-pressure conditions. This device can be used to measure the viscosity of lubricants under high-temperature and high-pressure conditions of 1 GPa and 100°C. Bair measured the viscosity of two compressor oils at 1.2 GPa using the same device and provided correlations between compressor oil viscosity and temperature as

well as between compressor oil viscosity and pressure [20]. This correlation has broad applicability and can be generalized to other liquids. Harris [21] designed a FB viscometer to operate in the pressure range 0.1-400 MPa. A hollow cylinder with a hemispherical surface was used as the FB, and it was verified through experimental data that the relationship between the calibration constant (A) of this shape of FB and the gap (c) between the FB and the cylinder conforms to the dependence of $A \propto c^{-3}$.

When applying the FB method to measure the viscosity of high-temperature and high-pressure liquids, two problems need to be solved: the non-contact detection of the FB position and control of the FB reset for the next measurement.

The commonly used method for detecting the FB position is to construct a Wheatstone bridge using two sensing coils. When the FB passes through the two sensing coils, it will cause an imbalance of the bridge signal. The imbalance signal is then amplified and shaped in order to control the opening and closing of the timer. By measuring the time of the FB passing through the two sensing coils, the stable speed of the FB and the viscosity of the liquid can be calculated. Harris [21] developed a high-pressure FB viscometer using this method. Due to the need to distinguish the unbalanced signals of the two sensing coils, the inductance change of the two coils cannot be affected simultaneously during the falling process of the FB. Consequently, the distance between the two sensing coils exceeds 100 mm, which results in a significant range of motion for the FB, a long detection period and the necessity for a large amount of liquid sample. Seung-Ho Yang et al. [22][23] developed a non-contact position sensor based on the change of magnetic core position using a single detection coil, but not for the FB viscometer. When the movable magnetic core is inserted into the detection coil, the change of the coil impedance is measured to indicate the change of magnetic core position, and the factors affecting the linearity and sensitivity of the sensor are studied. Compared with the method of using two sensing coils to construct a Wheatstone bridge to detect the FB position, this method can make the device more compact by delicately designing the coil size and position. Wang [24] developed a high-pressure liquid viscosity test system based on the FB method. However, they do not provide a FB reset scheme and the system can only measure once. The high-pressure FB viscometer developed by Bair [19][20] and Schaschke et al. [25][26] uses the reset method of rotating the entire pressure vessel by 180°, which requires a large space and a considerable length of time for detection. Due to the large range of movement of the FB, it cannot be reset by the electromagnetic force of a single driving coil.

In order to utilize the electromagnetic force of a single energized coil to achieve the FB reset, this paper proposes to use the impedance of a single sensing coil to detect the position of the FB to reduce the distance of travel of the FB, that is, to reduce the maximum distance between the driving coil and the FB. This can also reduce the length and volume of the sealing cavity. However, it is necessary to study the ability of a single sensing coil's impedance to characterize the position of the FB and its influencing factors. It is necessary to study the ability of a single driving coil to attract and reset the FB as well as the factors that can enhance this ability.

In this paper, the electromagnetic drive and sensing device of the FB viscometer with a single sensing coil are studied and optimized. The device to be optimized comprises a closed stainless steel tube sealed by a plug within which an iron FB moves. Two coils are wound externally. One is the driving coil, which is used to control the reset motion of the FB after energization, and the other is the sensing coil, which is used to measure the positional change of the FB. Via finite element simulation, the number of turns, wire diameter and size of the sensing coil are optimized in order to improve the positioning ability of the FB. In order to enhance the reset force obtained by the FB, the distance between the two coils and the material of the plug are optimized. The feasibility of using the designed device to measure liquid viscosity is experimentally verified with dimethyl silicone oil of different viscosities.

II. MEASUREMENT PRINCIPLE

The developed FB viscometer device based on electromagnetic drive and sensing is shown in Fig. 1. It is expected that the designed device size will not exceed $\Phi 40$ mm*H80 mm. A stainless steel tube and a plug create a closed chamber filled with the liquid to be tested. The iron FB moves inside the closed cavity, and the movement range is the upper and lower limits of the closed cavity. The upper limit is the base of the plug, while the lower limit is the base of the chamber. The exterior of the steel tube is wrapped with two identical-sized coils serving distinct purposes: one for driving the FB to reset and the other for sensing the FB position.

The driving coil generates a magnetic field after being passed through current, which is used to attract the FB to move vertically upward until the FB reaches the upper limit to complete the reset of the FB. After the driving coil is powered off, the magnetic field disappears, and the FB falls coaxially in the tube under the action of gravity. When the FB reaches force balance under the combined action of gravity, buoyancy and viscous force that increases with speed, the FB's speed reaches a stable value v_s. The formula for calculating the liquid viscosity
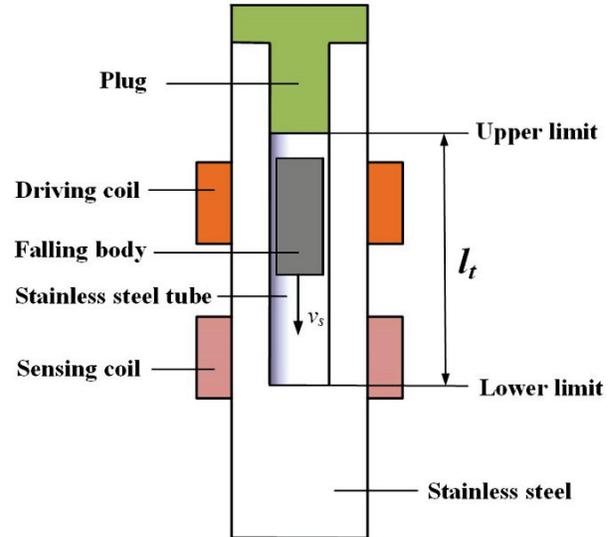
Fig. 1. Schematic diagram of liquid viscosity measuring device.

η is presented in equation (1) [25]:

$$\eta = \frac{mg}{2\pi v_s h_1} \left(1 - \frac{\rho_{liq}}{\rho_s}\right) \left[\ln\frac{r_2}{r_1} - \frac{r_2^2 - r_1^2}{r_2^2 + r_1^2}\right]. \tag{1}$$

In this equation, r_1 is the radius of the FB, h_1 is its length, r_2 is the radius of the tube within which the FB is falling, m is the mass of the FB, ρ_{liq} is the density of the liquid to be measured, and ρ_s is the density of the FB. Replacing the stable speed v_s of the FB with the moving distance l_t of the FB divided by the falling time t, equation (1) can be rewritten as:

$$\eta = At\left(1 - \frac{\rho_{liq}}{\rho_s}\right). \tag{2}$$

A is the instrument coefficient, and its expression is:

$$A = \frac{mg\left[\ln\frac{r_2}{r_1} - \frac{r_2^2 - r_1^2}{r_2^2 + r_1^2}\right]}{2\pi l_t l_s}. \tag{3}$$

It can be seen from equation (2) that the liquid viscosity η is proportional to the time t for the FB to fall over a fixed distance l_t with a stable speed.

It was found through experimental observation that when the radius r_1 of the FB is close to the radius r_2 of the tube, the FB will quickly reach the stable speed v_s in the falling initial stage. Reasonable design of r_1 and r_2 can make the acceleration process very short. The FB can be regarded as falling at a stable speed v_s. By measuring the change in the impedance value of the sensing coil, the falling process of the FB is monitored and the time difference between the upper and lower limits of the FB movement is obtained. After calibrating the instrument coefficient A using a standard liquid with known viscosity, the liquid viscosity to be tested can be calculated according to equation (2) by measuring the ratio of the falling time t of the FB.

In order to achieve more accurate FB position detection, in section III an electromagnetic finite element simulation study is conducted to reveal the relationship between the FB position and the coil impedance with different coil parameters and FB parameters, and appropriate combination of parameters is provided. In order to increase the reset force and achieve more reliable FB reset, in section IV the law of electromagnetic force generated by the driving coil is simulated and studied, the upper and lower limit positions are designed, and the material of the plug is optimized.

III. SENSING SCHEME DESIGN

The finite element simulation software COMSOL was used to conduct a simulation study on the relationship between the position of the FB and the coil impedance. A 2D rotational axial symmetry model was constructed as shown in Fig. 2 (a). The stainless steel tube's inner wall $r_2 = 4$ mm, thickness is 5 mm, length is 100 mm; the FB's radius $r_1 = 3.5$ mm, height $h_1 = 20$ mm. The coil width $WH = 16$ mm, the coil thickness is calculated by the coil width WH, the number of the coil turns N and the wire diameter d. The distance between section A-A and the center of the sensing coil is $D_1 = 30$ mm, the distance between the centers of the sensing coil and the driving coil is $D_2 = 18$ mm, the material of the FB is pure iron, the relative magnetic permeability is set to 300, and the electrical conductivity is set to 1.12×10^7 S/m. The relative magnetic permeability of stainless steel is set to 1.2, and the electrical conductivity is set to 4.03×10^6 S/m. The coil material is copper, the relative magnetic permeability is set to 1, and the electrical conductivity is set to 5.99×10^7 S/m. The physical field is a magnetic field. The coil model is set to "uniform multi-turn". The number of turns $N = 400$, and it is the parameter to be swept. The wire diameter $d = 0.25$ mm, and it is the parameter to be swept. The excitation voltage is set to 5 V. The mesh is set to "Physics Control Mesh" and the unit size is selected to "Ultra-Fine". A frequency domain study is set and the frequency is set to 500 Hz. The position of the FB is described by the distance S from the center of the FB to the section A-A. In order to study the electromagnetic law between the FB position and the sensing coil regardless of travel distance limit, in the simulation in section III, the driving coil is set to "disabled", the position of the FB is not restricted by upper and lower limits, and parameterized sweeping can be performed. A parametric sweeping on the FB position S is carried out, with a sweeping range of 0~60 mm and a sweeping interval of 1 mm. Among them, the magnetic flux density distributions when $S = 0$ mm, $S = 15$ mm, and $S = 30$ mm are shown in Figs. 2 (b-d).

The sensing coil is energized and excited due to the need to measure its impedance. It can be observed

from Figs. 2 (b-d) that the magnetic field generated is mainly concentrated on the surface of the FB. The FB at different locations will have a significant impact on the magnetic flux density distribution. When $S = 0$ mm, the distance between the falling object and the sensing coil is far, and the magnetic field generated by the coil's energization excitation has very little impact. When $S = 15$ mm, as the distance between the FB and the sensing coil decreases, the magnetic field intensity on the FB increases and the magnetic induction lines become denser. When $S = 30$ mm, the FB is located at the center of the sensing coil, and the magnetic field intensity on the

(a)

(b)

Fig. 2. *Continued.*

(c)
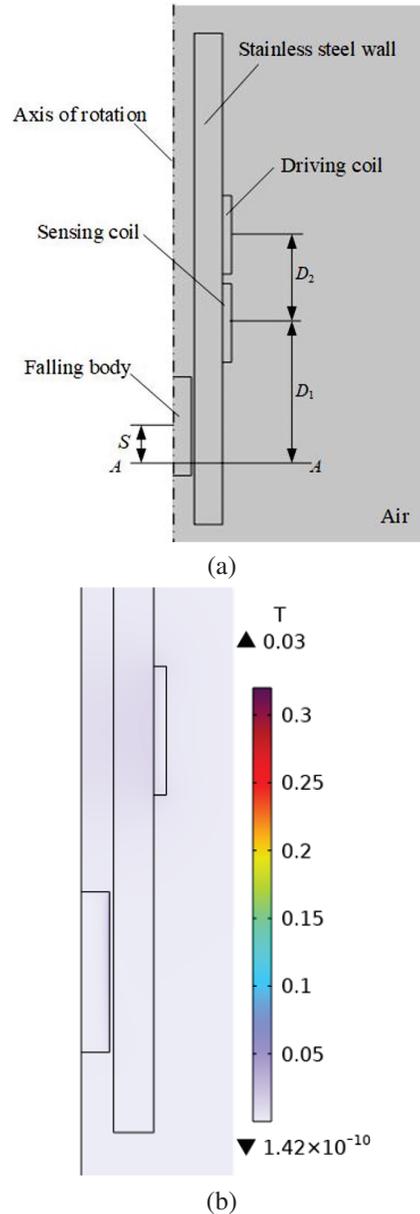
(d)
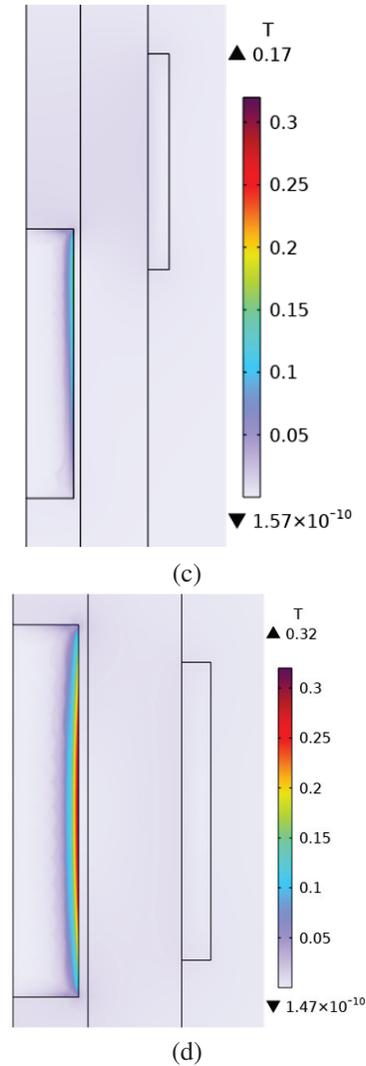
Fig. 2. Magnetic flux density distributions generated by energizing the sensing coil when measuring the impedance of the sensing coil: (a) simulation model, (b) magnetic flux density distribution when $S = 0$ mm, (c) magnetic flux density distribution when $S = 15$ mm, and (d) magnetic flux density distribution when $S = 30$ mm.

falling object is the largest among the above three scenarios. As the FB moves toward the coil, it gathers magnetic flux, causing the inductance and impedance values of the coil to increase.

When measuring liquid viscosity by monitoring the impedance change of the sensing coil, the falling process of the FB can be monitored and the time difference of the FB falling from the upper limit to the lower limit can be obtained. The moment when the FB starts to fall at the upper limit is the moment when the driving coil is powered off, and the moment when the FB reaches the lower limit is the moment when the coil impedance value sud-

denly stops changing. Subsequently, parametric sweeping simulation will be used to optimize the number of the coil turns N, the wire diameter d, the length of the FB h_1, the upper and lower limits of the FB, and the plug material of the closed tube, to ensure the accuracy of the falling time measurement and the reliability of reset.

A. Number of turns of sensing coil N

Based on the above simulation model and parameters, the number of turns of the sensing coil N is parametrically swept, the sweeping range is $200 \sim 1200$, the sweeping interval is 200, and the law of coil impedance value Z changing with the change of S is obtained. The simulation results are shown in Figs. 3 (a) and (b).

(a)

(b)
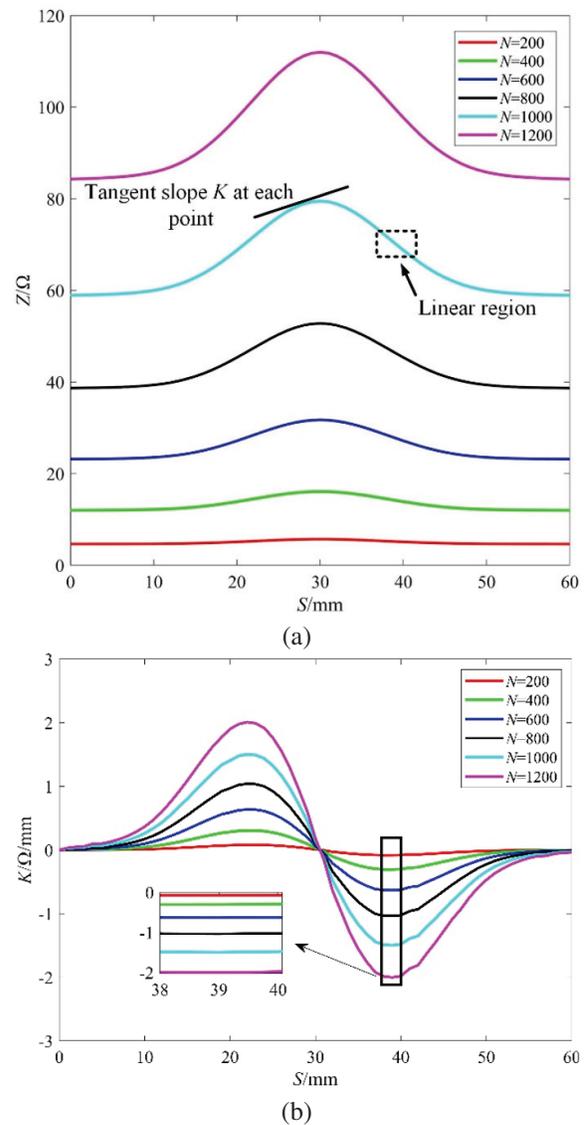
Fig. 3. Impedance simulation results of different sensing coil turns N: (a) Z-S diagram for different turns N and (b) K-S diagram for different turns N.

In Figs. 3 (a) and (b), the horizontal coordinate is the position S of the FB. The vertical coordinate of Fig. 3 (a) is the impedance value Z. The vertical coordinate of Fig. 3 (b) is the slope K of the tangent line at each point of the Z-S curve, that is, the change rate of Z with S. It can be observed from Figs. 3 (a) and (b) that there is a stable and regular correspondence between the position of the FB and the impedance of the sensing coil. There is a part of the Z-S curve where the changes in coil impedance and position represent an approximately linear change pattern, which is called the linear zone. Moreover, the slope of Z-S diagram in the linear region is the largest, that is, the change rate of the impedance value of the sensing coil is the largest. It can be observed from Fig. 3 (b) that in the process of decreasing the relative distance between the FB and the sensing coil, the change rate of the impedance value increases first. In the linear region, the change rate of the impedance value is basically unchanged, and then the change rate of the impedance value begins to decrease.

As the number of turns of coil N increases from 200 to 1200, the impedance value Z of the coil increases, the change of impedance value Z increases, and the slope of the linear region increases. Because the subsequent liquid viscosity measurement process needs to use a circuit to detect the coil impedance, in order to facilitate the circuit design, it is appropriate to use the impedance value of 50~100 Ω, and too many turns of the coil will lead to an increase in the volume of the coil, so the number of turns $N = 1000$ is preferred.

B. Wire diameter d

Based on the simulation model and parameters mentioned above, the sensing coil's turns $N = 1000$ is set, and the wire diameter d is parametrically swept. The sweeping parameters are 0.1, 0.25, 0.5 and 1 mm, and the simulation results are obtained as shown in Fig. 4.

It can be observed from Fig. 4 (a) that the impedance value of the sensing coil is the largest when $d = 1$ mm, followed by the impedance value of $d = 0.1$ mm. This is because the coil resistance value of $d = 0.1$ mm is much larger than the resistance value of other wire diameter coils, and the coil reactance value of $d = 1$ mm is much larger than the reactance value of other wire diameter coils, resulting in the coil impedance value of these two wire diameters being larger. It can be observed from Fig. 4 (b) that the impedance value of the sensor coil with $d = 0.1$ mm and $d = 0.25$ mm has a larger change rate. The smaller the wire diameter, the easier the wire is to break, increasing the difficulty of assembly. Moreover, the smaller the wire diameter, the higher the heat generated in the driving part, the greater the temperature change, and the greater the influence on the viscos-
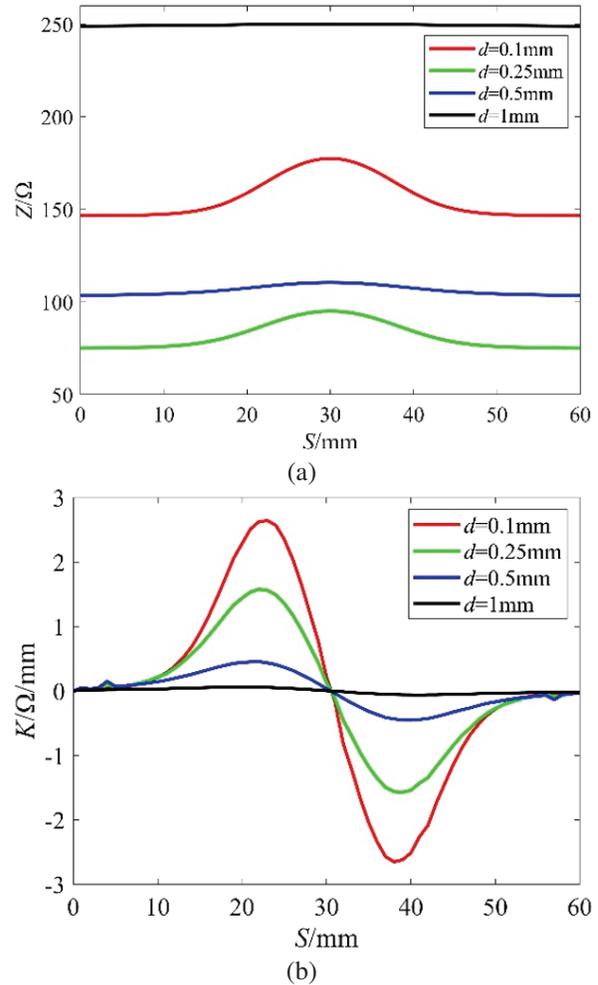
Fig. 4. Simulation results of sensing coil impedance with different wire diameters d: (a) Z-S diagram of different wire diameters d and (b) K-S diagram of different wire diameters d.

ity measurement results. Therefore, the wire diameter is optimized to $d = 0.25$ mm.

C. Dimensions of the FB

The FB height h_1 should not be too large, because the higher the FB, the greater the electromagnetic force required to reset the FB and the longer the closed chamber. The height of the FB should not exceed 1/4 of the overall size of the device. The sensing coil's wire diameter is set to 0.25 mm, and the FB height h_1 is parametrically swept. The sweeping range of h_1 is 12-20 mm, and the sweeping interval is 2 mm. The simulation results are shown in Fig. 5.

It can be observed from Figs. 5 (a) and (b) that as the height of the FB increases, the change of the impedance value of the sensing coil increases, and the length of the linear region also increases, which is conducive to the
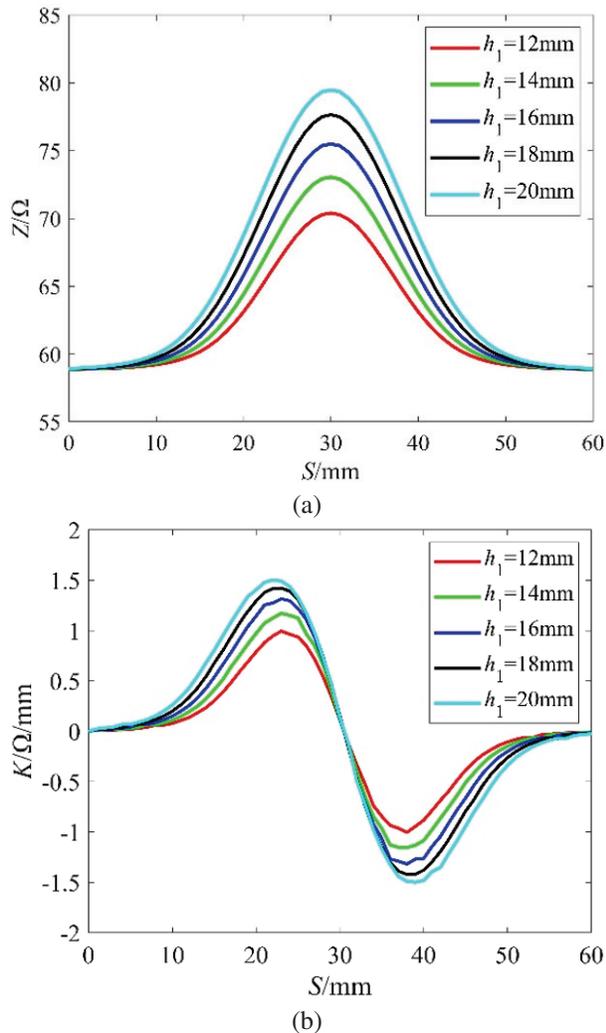
Fig. 5. (a) *Z-S* diagrams of different FB heights h_1 and (b) *K-S* diagrams of different FB heights h_1.

measurement of the FB velocity. The height of the FB is preferably set to $h_1 = 20$ mm.

According to experience, the closer the FB's radius r_1 is to the radius r_2 of the stainless steel tube, the smaller the stable velocity of the FB, and the longer the measurement time. Therefore, it is necessary to design falling bodies with different radii according to liquids with different viscosity ranges to ensure that the measurement time is adequate. The design is as follows: for liquid of 1-20 mPa·s, the FB radius r_1 is 3.9 mm; for liquid of 20-50 mPa·s, the FB radius r_1 is 3.85 mm; for liquid of 50-100 mPa·s, the FB radius r_1 is 3.8 mm.

IV. DRIVING SCHEME DESIGN
A. Upper and lower limit design

Through the simulation mentioned above, the dimensions of the FB and sensing coil are determined.

Considering the ease of manufacturing and the aesthetics of the device, the drive coil and the sensing coil are of the same size. A 2D rotational axisymmetric model is constructed, as shown in Fig. 2 (a), to carry out a simulation study on the electromagnetic force of a FB generated by the driving coil. Set falling radius $r_1 = 3.8$ mm and height $h_1 = 20$ mm. Set coil width $WH = 16$ mm, number of turns $N = 1000$, wire diameter $d = 0.25$ mm, and coil spacing $D_2 = 18$ mm. Other simulation parameters are the same as those set in section III. Steady state study is carried out, current source is used to excite the driving coil, and the current value is set at 1 A. The parametric sweeping of position S of the FB is carried out, and the law of change of the electromagnetic force F with change of S is obtained. Voltage source is used to excite the sensing coil and the excitation voltage is set at 5 V. Frequency domain study is added and the frequency is set at 500 Hz. The parametric sweeping of the position S of the FB is carried out, and the law of coil impedance changing with change of S is obtained. The simulation results are shown in Fig. 6.
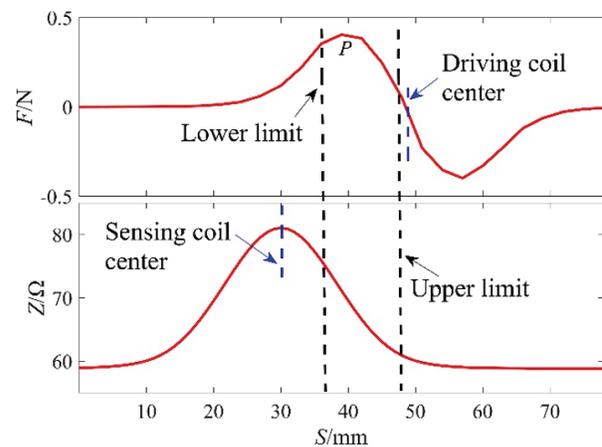
Fig. 6. Upper and lower limits.

It can be observed from Fig. 6 that the electromagnetic force received by the FB in the process of approaching the driving coil increases first and then decreases, and there is a maximum force position P. When the FB is far away from the driving coil or close to the center of the driving coil, the electromagnetic force FB received is 0. Therefore, it is most appropriate to set the moving range of the FB to cover point P. When the FB approaches the center of the sensor coil, the impedance value increases. The impedance change rate increases first and then decreases, and reaches maximum value in the linear region. When liquid viscosity is measured, the process of falling is monitored by measuring the change of the impedance value of the sensing coil, and the time difference of the FB passing through the upper and lower

limits is obtained. The moment when the FB begins to fall at the upper limit is the moment when the driving coil is powered off, and the moment when the FB reaches the lower limit is the moment when the coil impedance value no longer changes. Therefore, it is most appropriate to set the lower limit in the linear region with the largest impedance change rate. The movement range of the FB is set as $l_t = 9$ mm, and the position of the upper and lower limits is shown in Fig. 6.

B. Plug material

A 2D rotation axis symmetric model is constructed as shown in Fig. 7 (a). Set the FB radius $r_1 = 3.8$ mm and height $h_1 = 20$ mm. The width of the driving coil and the sensing coil is set $WH = 16$ mm, the number of turns $N = 1000$, and the wire diameter $d = 0.25$ mm. Other simulation parameters are the same as the simulation parameter settings in section III. Current source is used to excite the driving coil, and the excitation current is 1 A. The mesh is set to "Physical Field Controlled Grid" and the unit size is selected as "Super Fine". The plug material is set to iron and stainless steel, respectively, and a steady-state study is added. For iron, the relative magnetic permeability is set to 300. For stainless steel, the relative magnetic permeability is set to 1.2. The FB position S_1 is parametrically swept with a sweeping range of 0-9 mm. The law of the change of the electromagnetic force F with the change of S_1 is obtained. The simulation results are shown in Figs. 7 (b-d).

Figures 7 (b) and (c) show the distribution of magnetic field generated by the driving coil when plugs of different materials are at different positions. It can be seen from Figs. 7 (b) and (c) that, whether it is an iron plug or a stainless steel plug, the closer the distance between the FB and the driving coil, the stronger the magnetic field intensity around the FB. When the FB is far away from the driving coil, and the bottom surface of the FB is at the lower limit, whether it is an iron plug or a stainless steel plug, the maximum magnetic field intensity near the FB is about 0.3 T and, near the plug, the magnetic field intensity of the iron plug is much higher than that of the stainless steel plug. When the FB is close to the driving coil, and the top surface of the FB is at the upper limit, the magnetic field intensity near the FB and the plug is significantly higher for the iron plug than for the stainless steel plug.

Figure 7 (d) shows the electromagnetic force exerted on plugs of different materials at different positions. It can be observed from Fig. 7 (d) that when the FB is far away from the driving coil, and the bottom surface of the FB is close to the lower limit, whether an iron plug or a stainless steel plug is used, the electromagnetic force generated by the driving coil on the FB is similar, and the iron plug is slightly higher. When the FB is close to

the driving coil, and the top surface of the FB is close to the upper limit, the electromagnetic force generated by the driving coil on the FB using an iron plug is signifi-

(a)

(b)

(c)
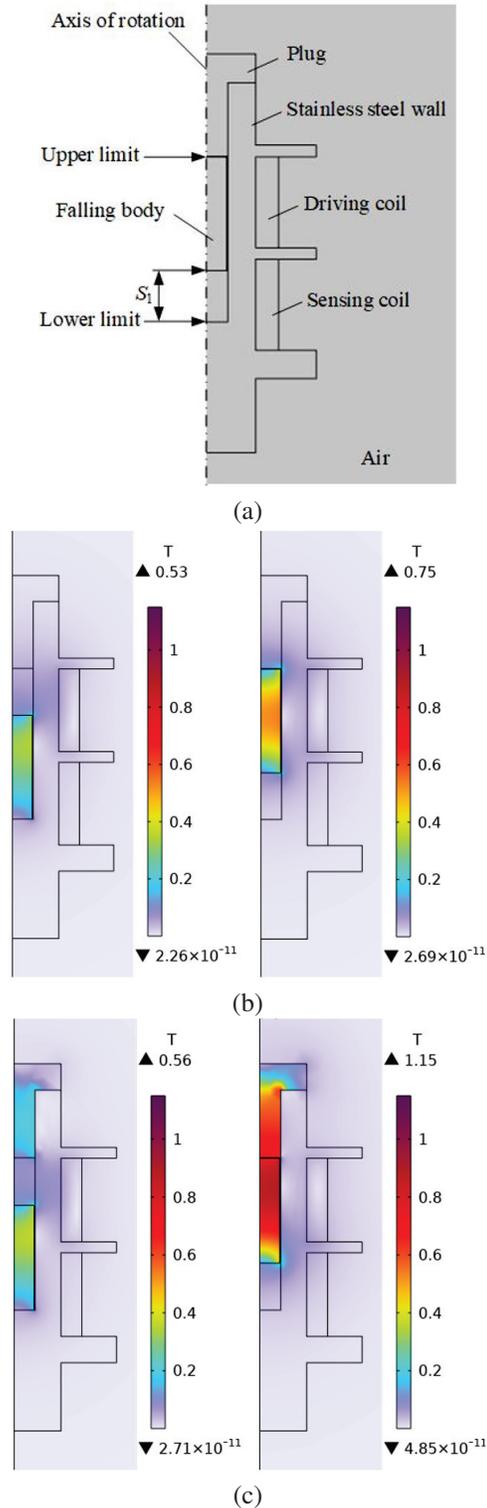
Fig. 7. *Continued.*

(d)
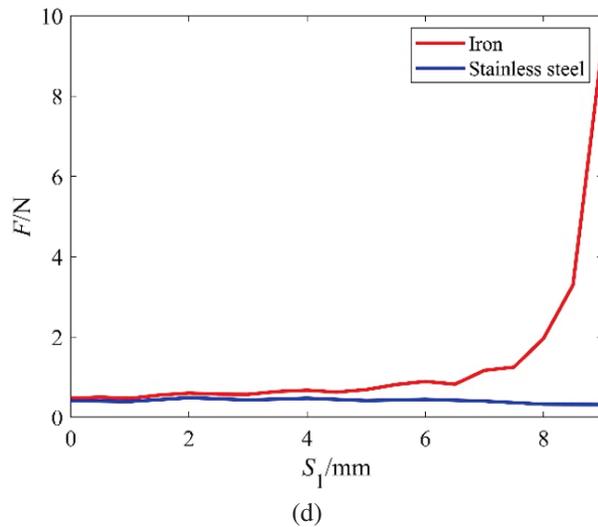
Fig. 7. Electromagnetic simulation results of plug material: (a) diagrammatic figure, (b) magnetic flux density distributions of stainless steel plug, (c) magnetic flux density distributions of iron plug, and (d) comparison diagram of electromagnetic forces of different plug materials.

Fig. 8. Cross-sectional view of the device.

cantly higher than that using a stainless steel plug, which is consistent with the conclusion obtained about the magnetic field strength in Figs. 7 (b) and (c). Therefore, iron is selected as the material of the plug.

V. EXPERIMENTS

A. Electromagnetic sensing and driving function verification

The liquid viscosity measuring device is designed and manufactured according to the parameters determined by the above simulations. The inner diameter r_2 of the stainless steel tube is 4.05 mm and the wall thickness is 5 mm. The number of turns of the driving coil and the sensing coil is $N = 1000$, the width $WH = 16$ mm, and the wire diameter $d = 0.25$ mm. The center distance between the sensing coil and the driving coil is $D_2 = 18$ mm. The thermocouple model used is GG-K-30-SLE, with an accuracy of $1.1°C$. In order to obtain a more accurate temperature, a higher precision thermocouple, such as the PT100, can be used. The distance between the thermocouple and the liquid is 10.45 mm. This distance can be changed by changing the depth distance of the thermocouple. The cross-sectional view of the device is shown in Fig. 8. An image of the device is shown in Fig. 9.

The top of the FB is designed as an arc surface to prevent the possibility that the top of the FB cannot freely fall due to a large viscous force after resetting. The bottom of the FB is designed as a conical surface, which is matched with the bottom of the stainless steel chamber
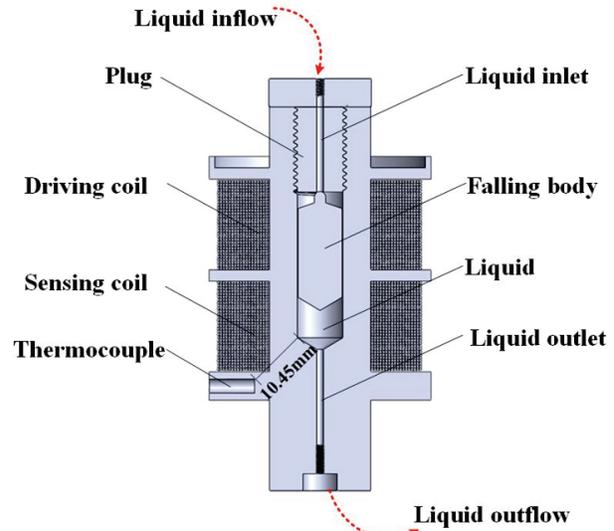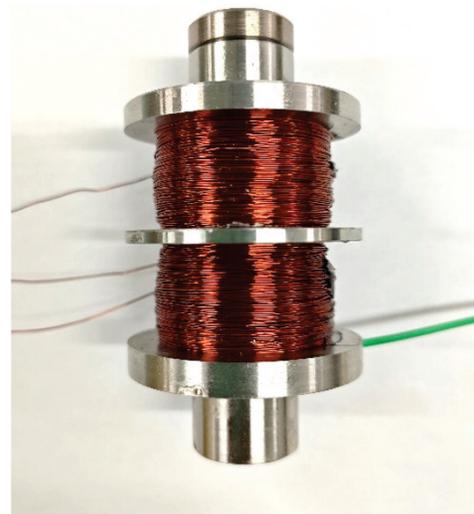
Fig. 9. Image of the device.

to ensure that the movement of the FB in the chamber is coaxial during each measurement. The height of the FB h_1 is 20 mm. The size of the FB is as follows: for liquids with viscosities 1-20 mPa·s, the radius of the FB r_1 is 3.93 mm; for liquids with viscosities 20-50 mPa·s, the radius of the FB r_1 is 3.88 mm; for liquids with viscosities 50-100 mPa·s, the radius of the FB r_1 is 3.79 mm; for liquids with viscosities 100-1265 mPa·s, the radius of the FB r_1 is 3.72 mm. The FB model diagram is shown in Fig. 10.

The measuring system is shown in Fig. 11, which includes the measuring device, the thermocouple, the measurement circuits, and the computer software.

Fig. 10. FB model diagram.
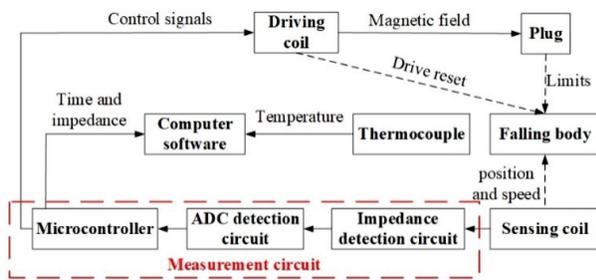
Fig. 11. System block diagram.

The microcomputer in the measurement circuits outputs a DC signal via internal DAC. This DC signal is amplified by a power amplifier and reaches the drive coil to generate a magnetic field. The iron plug and the coil form an electromagnet which generates electromagnetic force to reset the FB. The impedance detection circuit outputs the impedance value Z of the sensing coil in real time, which is collected by the microcontroller through the ADC to detect the position of the FB. The microcontroller sends the collected impedance data to the computer software for further analysis and calculation. A thermocouple is used to measure the liquid temperature and display it.

In this experiment, dimethyl silicone oils with different viscosities are mixed in different proportions to provide 10 kinds of dimethyl silicone oils with different viscosities as test liquids covering the viscosity range of 9.5-1265 mPa·s. The viscosity of each test liquid is measured by the standard viscometer SV-10. Liquid #1 and liquid #2 are taken as experimental samples for showing falling impedance curves and are respectively loaded

into the device for viscosity measurement. The radius of the FB used is $r_1 = 3.93$ mm. In the experiment, the timing is started when the driving coil is powered off, and the impedance value of the sensing coil is recorded at each moment. The impedance value data and time data are plotted, and the results are shown in Fig. 12.
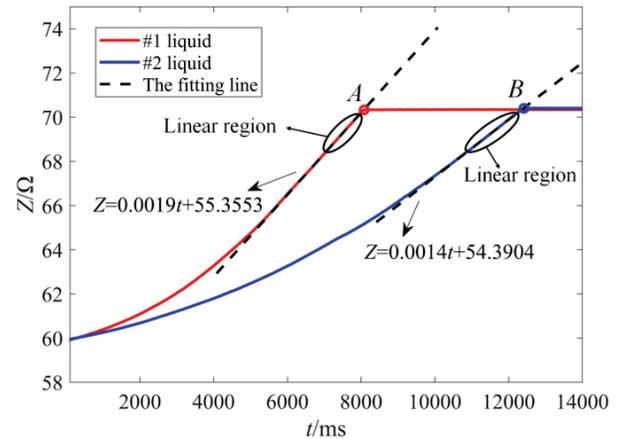
Fig. 12. Tested impedance change curves of the sensing coil during the falling process of the FB when two liquids are respectively loaded for viscosity measurement.

It can be observed from Fig. 13 that when the FB falls in two different liquids, the impedance value Z no longer changes at points A and B, indicating that the FB has reached the lower limit at these two moments. In the Z-t curve, when verifying whether the linear region exists, starting from point A and point B, the program extracts data of 1/10 of the total falling time of the FB for verification of the linear zone. The program performs a linear fit on the data in the linear region. The linear region fitting results in Fig. 12 are as follows: $Z = 0.0019t+55.3553$, $R^2 = 1$ and $Z = 0.0013t+54.3903$, $R^2 = 0.9998$. The linearity is very good. The correctness of the detecting scheme of the FB position through the sensing coil is verified.

Figure 13 shows the curves of the impedance of the sensing coil changing with time after the driving coil is energized when the FB is in two different liquids. It can be observed from Fig. 13 that when the FB is in two different liquids, the driving coil generates electromagnetic force after the current is passed through the driving coil. The FB moves upward under the action of electromagnetic force, liquid viscous force, gravity and buoyancy, and the impedance value Z decreases. The impedance value Z of the sensing coil no longer changes at points C and D, indicating that the FB has been reset to the upper limit at these two moments. The feasibility of the scheme of resetting the FB through the electromagnetic force of an energized coil is experimentally verified.
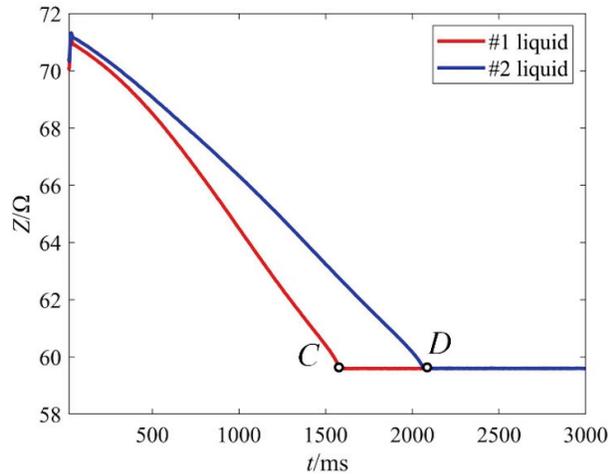
Fig. 13. Experimental verification results of the FB reset scheme.

B. Viscosity measurement results

To obtain the reference viscosity of different liquids, the SV-10 viscometer was used as a reference. The SV-10 viscometer has a measurement accuracy of ±3% and a repeatability of 1% in the viscosity range 1-1000 mPa·s. First, the SV-10 sine wave vibration viscometer was used to measure the viscosity of 10 test liquids at different temperatures, and a linear function was used to fit the temperature and viscosity data. The viscosity-temperature curves of these 10 test liquids in the temperature range 20-35°C were obtained. Then, the 10 blends of dimethyl silicone oils were divided into four groups according to their viscosity, corresponding to the FBs in the four measuring ranges. Four types of FBs needed to be calibrated separately. Taking the first group as an example, the #2 liquid was put into the experimental device, and the falling time t of the FB was recorded. At the same time, the temperature of the liquid at this time was recorded, and the viscosity η of the liquid at this time through the viscosity-temperature curve of #2 liquid is obtained. Since the temperature does not change much, it is believed that the density of dimethyl silicone oil only changes slightly, and $1-\rho_{liq}/\rho_s$ is a determined calculated value of 0.8718. The calibration coefficient A is calculated according to equation (2). An image of the SV-10 viscometer is shown in Fig. 14, and the fitting results are shown in Fig. 15. The grouping and resulting instrument coefficients A are shown in Table 1.

Using the manufactured FB viscosity measuring device, the viscosity of 10 liquids was measured. The liquid temperature during measurement was obtained through the thermocouple, and the viscosity value of the liquid to be measured at the temperature was obtained according to the viscosity-temperature fitting curve as the reference viscosity value η_r. The time t of the FB
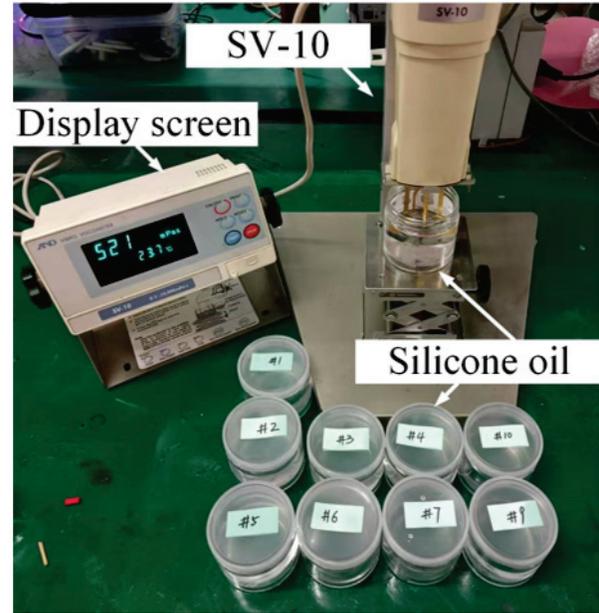
Fig. 14. SV-10 sine wave vibration viscometer.
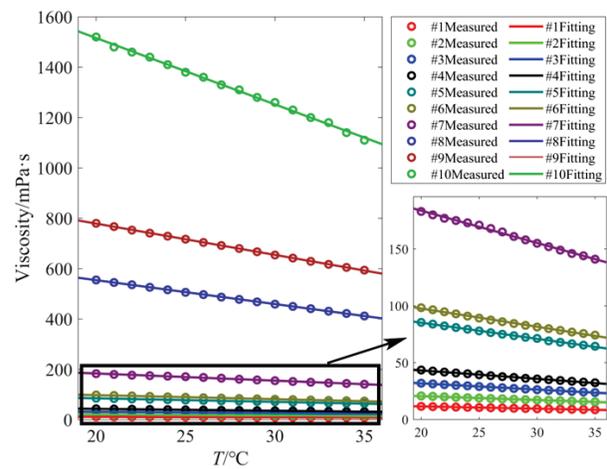
Fig. 15. Viscosity measurements and results of different initial viscosities at different temperatures.

falling in liquids of different viscosities is measured through the sensing coil, and the measured value η_m of the liquid viscosity is calculated according to equation (2). The movement range of the FB is only 9 mm, which can make the closed cavity in the stainless steel tube very small. Only 1 mL of liquid is needed to completely fill the closed cavity containing the FB. The falling time of the FB is between 4 and 37 seconds. The falling time of the FB in each liquid was measured three times and the average value was calculated. The viscosity was calculated using the FB method formula and recorded in Table 2. According to Table 2, it can be calculated that

Table 1: Instrument coefficients

Number	1-ρ_{liq}/ρ_s	r_1/mm	A/mPa
#1		3.93	1.5293195
#2			
#3		3.88	4.1635895
#4			
#5	0.8718	3.79	16.399665
#6			
#7		3.72	40.345561
#8			
#9			
#10			

Table 2: Viscosity measurement results

Liquid Number	T/℃	η_r/mPa·s	t/s	η_m/mPa·s	Relative Error
#1	30.3	9.52	7.11	9.483	-0.4%
#2	29.5	17.29	12.56	16.74	-3.2%
#3	30.3	26.14	7.44	27.00	-3.3%
#4	30.2	35.58	9.64	34.99	1.6%
#5	30.1	70.81	4.76	68.07	-3.8%
#6	30.1	81.42	5.54	79.16	2.7%
#7	32.1	149.3	4.44	156.17	4.3%
#8	31.8	442.2	12.81	450.57	1.9%
#9	30.1	653.4	18.72	658.44	0.8%
#10	29.5	1265	36.56	1285.93	1.6%

the average absolute value of the relative error is 0.22%, and the maximum value is 4.3%. In order to visually display the error results, the error bar plots for the 10 test liquids are shown in Fig. 16. It can be observed in Fig. 16 that the error bar length is short, which verifies the accuracy of the device.
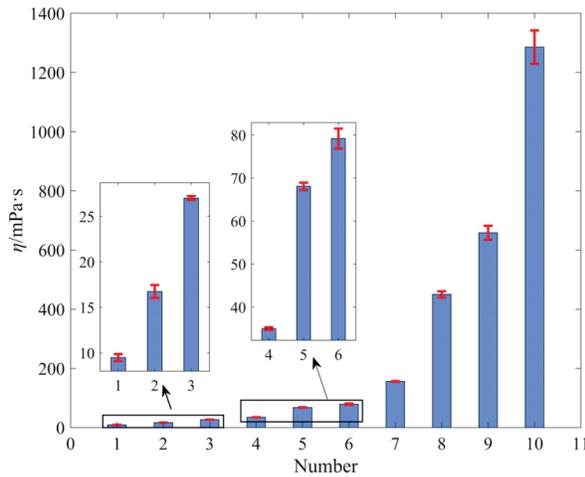
Fig. 16. Error bar plot of the test results.

VI. HIGH-TEMPERATURE AND HIGH-PRESSURE TOLERABILITY ANALYSIS

A. Theoretical analysis of high-temperature tolerability

Our measuring system consists of 304 stainless steel cylinders, two enameled wire electromagnetic coils, an iron plug, an iron FB and measuring circuit. The stainless steel cylinder, iron plug and iron FB are in direct contact with the high-temperature and high-pressure liquid to be measured. Two electromagnetic coils are placed near the high-temperature and high-pressure liquid. The measuring circuit is at a distance from the high-temperature and high-pressure liquid. For general industrial applications, 304 stainless steel is generally safe to use in the temperature range up to 800°C. The Curie temperature of iron is 770°C. Within this temperature range, iron can maintain strong magnetism. The temperature resistance of enameled wire electromagnetic coils mainly depends on the type of insulating paint used. The temperature resistance grade of ordinary polyester enameled wire is 130°C. The temperature resistance grade of modified polyester enameled wire is 155°C. The temperature resistance grade of polyimide enameled wire is 240°C. The enameled wire we use can tolerate high temperatures of 130°C. Therefore, the working temperature range of this device can reach 130°C.

B. Simulation analysis of high-pressure environment tolerability

Simulation verification of pressure resistance capability of the developed closed chamber device for measuring liquid viscosity was carried out with COMSOL software. A 2D rotational axial symmetry model is constructed, as shown in Fig. 17 (a). Model dimensions are the same as those in section IV, part B. The closed cavity material is stainless steel whose density is 7850 kg/m^3, Young's modulus is 200 GPa, and Poisson's ratio is 0.3. Solid mechanics was chosen as the physics field. The model is set to linear elastic material. Wherein, the density, Young's modulus and Poisson's ratio are all determined by "from material" option. The outer boundary of the model is set to "free", and boundary loads are added to the inner boundary of the model. The load diagram is shown in Fig. 17 (b). The pressure is the parameter to be swept, the bottom boundary of the model is set as a fixed constraint, and the "rigid body motion suppression" condition is added to the entire model. The mesh is set to "Physics Control Mesh" and the unit size is selected to "Ultra-Fine". A steady state study is added, the pressure sweeping range is 10~100 MPa, and the sweeping interval is 10 MPa. The sweeping simulation results of the deformation and stress distribution of the device under different loads are obtained, as shown in Figs. 17 (c) and (d). The

inner boundary stress distribution results are shown in Fig. 17 (e).

It can be observed from Figs. 17 (c) and (d) that as the boundary load increases, the stress of the sealed cav-

(a)

(b)

(c)

Fig. 17. *Continued.*

(d)

(e)
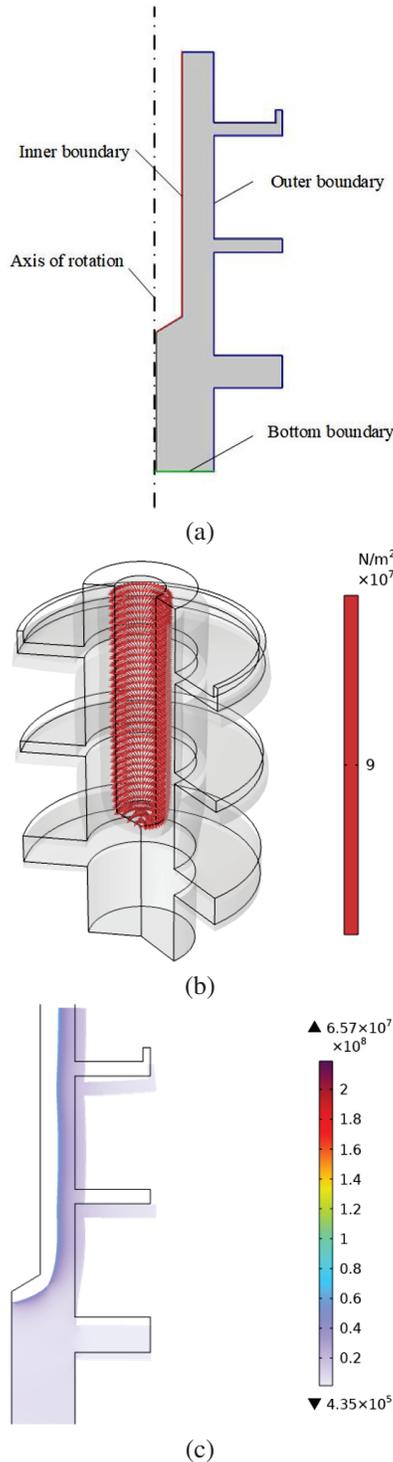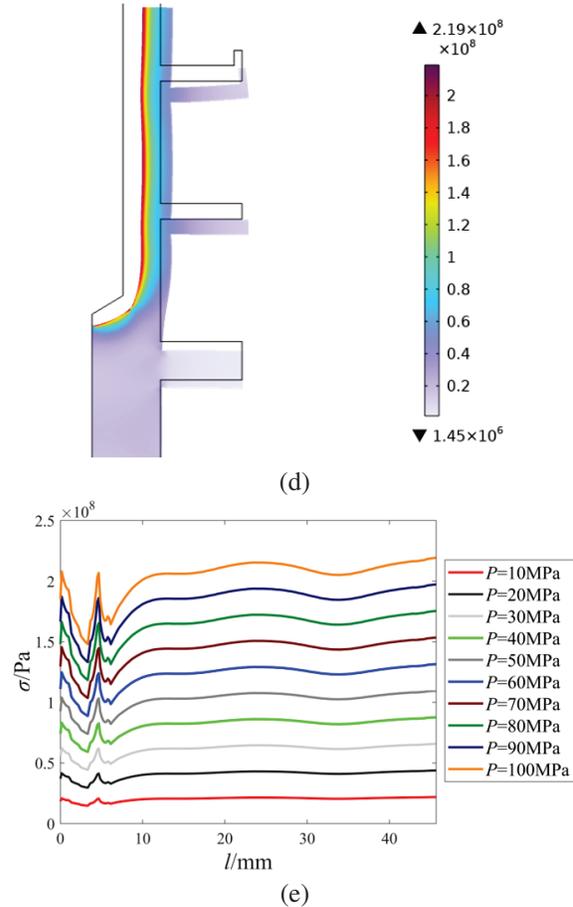
Fig. 17. Closed cavity pressure simulation: (a) simulation model, (b) boundary load diagram, (c) device deformation and stress distribution under 30 MPa load, (d) device deformation and stress distribution under 100 MPa load, and (e) internal surface stress distribution.

ity device increases. Under a load of 30 MPa, the maximum stress of the device is 65.7 MPa. Under a load of 100 MPa, the maximum stress of the device is 219 MPa. It can be observed from Fig. 17 (e) that there is a large stress concentration at the intersection of the inner boundary cylindrical surface and the conical surface (at $l = 5$ mm). On the cylindrical surface, the stress distribution is relatively uniform, and the stress on the cylinder surface is roughly the same as the stress at the intersection. When the boundary load increases to 100 MPa, the stress on the device may be greater than the allowable stress of the adopted 304 stainless steel, whose yield strength is 205~215 MPa. Therefore, the device can tolerate liquid pressure of 100 MPa.

VII. CONCLUSION

This paper proposes a FB-based device for measuring liquid viscosity in a closed cavity with simple

structure, small size, small amount of sample required, and fast FB reset speed. It includes a stainless steel closed tube with an iron FB, an iron plug, one driving coil, and one sensing coil. Through electromagnetic finite element simulation, the characterization ability of a single sensing coil impedance on the position of a FB and its influencing factors are studied, and the ability of a single driving coil to attract and reset a FB and its enhancement factors are studied. Dimethyl silicone oil viscosity measurement experiments are carried out to prove the feasibility of the designed device. The following conclusions can be obtained.

(1) There is a stable correspondence between the position of the FB and the impedance of the sensing coil; there is a region where the coil impedance and position show an approximately linear change pattern. Via elaborative size design, the lower limit of the FB's motion is set in this linear zone, so that the moment when the FB reaches the lower limit point can be accurately determined, and then the time difference method can be used to conveniently and accurately measure the steady speed of the FB.

(2) As the number of turns of the sensing coil increases and the wire diameter decreases, the coil impedance value and its variation increase, which is beneficial to determining the moment when the FB reaches the upper and lower limit positions. As the height of the FB increases, the change in the impedance of the sensing coil increases, and the length of the linear zone also increases, which is beneficial to the detection of the moment when the FB moves to the lower limit point.

(3) The electromagnetic force received by the FB when approaching the driving coil first increases and then decreases, and there is a maximum force position. Designing the movement range of the FB to make this range cover this point and setting the plug material to iron can make the FB gain greater electromagnetic attraction force and ensure its successful reset.

(4) Based on the simulation results, a FB viscosity measuring device is produced. Experiments have verified that a single driving coil can reliably reset the FB, and a single sensing coil can measure the position of the FB and characterize the liquid viscosity. The size of the closed cavity is very small, and the moving distance of the FB is only 9 mm. For dimethyl silicone oil with a viscosity range of 9.5-1265 mPa·s, only 1 mL of liquid sample is needed to measure the viscosity. The average absolute value of the relative measurement error is 0.22%, and the maximum value is 4.3%.

ACKNOWLEDGEMENT

REFERENCES

[1] H. L. Wang, Z. Li, and J. W. Zhao, "Discussion of viscosity measurement of liquids," *Physical Experiment of College*, vol. 7, no. 2, pp. 33-35, June 1994.

[2] B.-H. Shi, S. Chai, L.-Y. Wang, X. Lv, H.-S. Liu, H.-H. Wu, W. Wan, D. Yu, and J. Gong, "Viscosity investigation of natural gas hydrate slurries with anti-agglomerants additives," *Fuel*, vol. 185, pp. 323-338, Dec. 2016.

[3] S. Gautam, C. Guria, and L. Gope, "Prediction of high-pressure/high-temperature rheological properties of drilling fluids from the viscosity data measured on a coaxial cylinder viscometer," *SPE Journal*, vol. 26, no. 05, pp. 2527-2548, Oct. 2021.

[4] Y. F. Guo, "Research on the current situation and high-quality development path of coal-to-liquid: research on the high-quality development of coal direct liquefaction technology," *Inner Mongolia Petrochemical Industry*, vol. 47, no. 9, pp. 4-8, Sep. 2021.

[5] R. Wiśniewski, R. M. Siegoczyński, and A. J. Rostocki, "Viscosity measurements of some castor oil based mixtures under high-pressure conditions," *High Pressure Research*, vol. 25, no. 1, pp. 63-68, Mar. 2005.

[6] A. Miyara, Md. J. Alam, K. Yamaguchi, and K. Kariya, "Development and validation of tandem capillary tubes method to measure viscosity of fluids," *Transactions of the Japan Society of Refrigerating and Air Conditioning Engineers*, vol. 36, no. 1, pp. 18-47, Mar. 2019.

[7] M. E. Kandil, K. N. Marsh, and A. R. H. Goodwin, "Vibrating wire viscometer with wire diameters of (0.05 and 0.15) mm: Results for methylbenzene and two fluids with nominal viscosities at T = 298 K and p = 0.01 MPa of (14 and 232) mPa·s at Temperatures between (298 and 373) K and Pressures below 40 MPa," *Journal of Chemical Engineering Data*, vol. 50, no. 2, pp. 647-655, Mar. 2005.

[8] J. B. Zhang, X. Y. Meng, G. S. Qiu, and J. Wu, "Development of vibrating-wire viscometer for liquid at high pressure," *Journal of Xi'an Jiaotong University*, vol. 46, no. 11, pp. 30-34, Nov. 2012.

[9] M. Hosoda, Y. Yamakawa, and K. Sakai. "Electromagnetically spinning viscometer designed for measurement of low viscosity in low shear rate region," *Japanese Journal of Applied Physics*, vol. 63, no. 4, Mar. 2024.

[10] X. W. Zhang and P. He, "A high-temperature and high-pressure oil-coal slurry viscosity determination device," CN. Patent 200952994, 26 Sep. 2007.

[11] P. W. Bridgman, "The viscosity of liquids under pressure," *Proceedings of the National Academy*

of Sciences, vol. 11, no. 10, pp. 603-606, 1925.

[12] P. W. Bridgman, "The effect of pressure on the viscosity of forty-three pure liquids," *Proceedings of the American Academy of Arts and Sciences*, vol. 61, no. 3, p. 57, 1926.

[13] J. Lohrenz, G. W. Swift, and F. Kurata, "An experimentally verified theoretical study of the falling cylinder viscometer," *AIChE Journal*, vol. 6, no. 4, pp. 547-550, 1960.

[14] E. Ashare, R. B. Bird, and J. A. Lescarboura, "Falling cylinder viscometer for non-Newtonian fluids," *AIChE Journal*, vol. 11, no. 5, pp. 910-916, 1965.

[15] N. D. Cristescu, B. P. Conrad, and R. Tran-Son-Tay, "A closed form solution for falling cylinder viscometers," *International Journal of Engineering Science*, vol. 40, no. 6, pp. 605-620, Mar. 2002.

[16] F. Gui and T. F. Irvine, "Theoretical and experimental study of the falling cylinder viscometer," *International Journal of Heat and Mass Transfer*, vol. 37, pp. 41-50, Mar. 1994.

[17] J. B. Irving and A. J. Barlow, "An automatic high pressure viscometer," *Journal of Physics E: Scientific Instruments*, vol. 4, no. 3, pp. 232-236, Mar. 1971.

[18] V. Průša, S. Srinivasan, and K. R. Rajagopal, "Role of pressure dependent viscosity in measurements with falling cylinder viscometer," *International Journal of Non-Linear Mechanics*, vol. 47, no. 7, pp. 743-750, Sep. 2012.

[19] S. Bair, "A routine high-pressure viscometer for accurate measurements to 1 GPa," *Tribology Transactions*, vol. 47, no. 3, pp. 356-360, July 2004.

[20] S. Bair, "A new high-pressure viscometer for oil/refrigerant solutions and preliminary results," *Tribology Transactions*, vol. 60, no. 3, pp. 392-398, May 2017.

[21] K. R. Harris, "A falling body high-pressure viscometer," *International Journal of Thermophysics*, vol. 44, no. 12, p. 184, Dec. 2023.

[22] S. Yang, K. Hirata, T. Ota, Y. Mitsutake, and Y. Kawase, "Impedance characteristics analysis of the non-contact magnetic type position sensor," *Electronics and Communications in Japan*, vol. 94, no. 3, pp. 33-40, Mar. 2011.

[23] S.-H. Yang, K. Hirata, T. Ota, and Y. Kawase, "Impedance linearity of contactless magnetic-type position sensor," *IEEE Transactions on Magnetics*, vol. 53, no. 6, pp. 1-4, June 2017.

[24] X. Wang, S. Zhu, and X. Wang, "Experimental system for high-pressure viscosity measurement based on the falling-body method," *Journal of Engineering Thermophysics*, 2020.

[25] C. J. Schaschke, S. Allio, and E. Holmberg, "Viscosity measurement of vegetable oil at high pressure," *Food and Bioproducts Processing*, vol. 84, no. 3, pp. 173-178, Sep. 2006.

[26] C. J. Schaschke, S. Abid, I. Fletcher, and M. J. Heslop, "Evaluation of a falling sinker-type viscometer at high pressure using edible oil," *Journal of Food Engineering*, vol. 87, no. 1, pp. 51-58, July 2008.

Kun Zhang received her master's degree in analytical chemistry from Jilin University (Changchun) in 2008. She is currently working at Shandong Non-Metal Materials Research Institute. Her research interests mainly involve chemical measurement and viscosity and density detection technology.

Hongbin Zhang (corresponding author) received the B.Sc. degree in measurement and control technology and instrument from Hebei University of Technology, Tianjin, China, in 2022. He is currently pursuing the M.Sc. degree in Tianjin University, under the guidance of Associate Professor Xinjing Huang. His research interests include pipeline stress measurement, signal feature extraction, and the application of magnetic sensors.

Yuan Xue has his bachelor's degree, and works as an engineer, first-class registered metrology, national laboratory qualification accreditation assessor, metrology standard evaluator. He entered the China Institute of Testing Technology in 2004, and since then he has been mainly engaged in metrology and testing technology research and reference material research.

Jinyu Ma received her B.E. and M.E. degrees in Instrument Science and Technology from Shandong University of Science and Technology, Qingdao, China, in 2010 and 2012, respectively. She received her Ph.D. degree in Instrument Science and Technology from Tianjin University, Tianjin, China, in 2016. In 2016, she joined the Sensor and Electronic Testing Laboratory of Tianjin University as a lecturer and engineer. She also works at State Key Laboratory of Precision Measurement Technology

and Instrument, Tianjin University. Her research topics mainly cover electric sensing and measurement, precision measuring circuit, measurement and control based on embedded system.

Jiqing Han received his master's degree in chemical engineering from Qingdao University in 2015. Currently, he works at Shandong Nonmetallic Materials Research Institute as an associate researcher. His research interests are mainly in oil property measurement.

Xinjing Huang (corresponding author) received the B.E. and Ph.D. degrees in instrument science and technology from Tianjin University, Tianjin, China, in 2010 and 2016, respectively. He is currently an Associate Professor with the School of Precision Instrument and Opto-Electronics Engineering, Tianjin University, where he also works with the State Key Laboratory of Precision Measurement Technology and Instruments. His research topics mainly cover acoustic and/or electromagnetic sensing and measurement technologies.

Equivalent Circuit Model for Convoluted Meander Line Frequency Selective Surface for Multi-frequency Applications

Deepa Jeyaraman and Suganthi Santhanam

Department of Electronics and Communication Engineering
K. Ramakrishnan College of Technology, Trichy, Tamil Nadu, India
shanjeya0308@gmail.com, suganthis.ece@krct.ac.in

Abstract – This research investigates a multi-resonant frequency selective surface (FSS) structure with convoluted meander line. An equivalent circuit analysis was conducted in three different 10×10 array structures having 200 mm $\times$ 200 mm size with 10 mm $\times$ 10 mm unit cell. The simple plus structure achieved a single resonant frequency of 10 GHz at -27 dB, dual frequencies of 4.6 GHz at -22 dB and 11.6 GHz at -28 dB while increasing the length of meander lines to three turns. By adding an extra six turns for a total of nine turns, the structure achieved three resonant frequencies of 3.4G Hz at -28 dB, 10.6 GHz at -22 dB and 16 GHz at -20 dB. The polarization insensitivity and transmission coefficient in transverse electric (TE) and transverse magnetic (TM) modes has been validated with the equivalent circuit model (ECM) and tested with measurement also. The result demonstrates that the proposed FSS can be applied for WiMax, X and Ka-band wireless communication and radar systems applications.

Index Terms – Convoluted meander line, frequency selective surface, polarization insensitivity, transmission coefficient, wireless communications.

I. INTRODUCTION

Frequency selective surfaces (FSS) have emerged as a key technology in various fields of electromagnetic wave engineering due to their ability to selectively control the transmission and reflection of electromagnetic waves at specific frequencies [1–3]. However, they might not fully address real-world problems such as difficulty in fabrication, scaling concerns and performance constraints in particular scenarios. Meander line structures have been widely used in FSS design to achieve multi-resonant behavior [4–6], further improved by using convoluted meander lines. These works might not include in-depth analyses of constrained bandwidth, sensitivity to environmental changes and challenges in attaining desired resonant behavior over a broad frequency range. Convoluted meander line structures differ from traditional meander lines by incorporating folds or curves. Polarization insensitivity as a result of the uneven composition has been reported in [7] and shows angular stability under transverse electric (TE) and transverse magnetic (TM) modes from $0°$ to $80°$ with a minimum frequency deviation of less than 1% but at lower frequency band from 1 to 2 GHz only. FSS structures having conductive path extension and higher inductance value has been proposed for 5.5 GHz WLAN applications [8]. References [9–11] demonstrate the approach to enhance the resonant behavior of FSS to operate at multiple frequencies.

Many researchers have proposed the different types of convoluted meander line structures, such as zigzag [12–14], serpent [15–17] and square convoluted meander lines [18, 19]. These studies examined the resonant characteristics of FSS structures based on convoluted meander lines, and designed and analyzed three different convoluted meander line structures, each with increasing numbers of turns, to explore their resonant behavior. The equivalent circuit model (ECM) was used to obtain inductance and capacitance values for each structure, providing insights into the underlying physics [20–22]. These results demonstrated the potential of convoluted meander lines for achieving multi-resonant frequency behavior in FSS, with potential applications in numerous fields [23–25]. Recent advancements in FSS technology have led to the development of new structures with improved performance. For instance, the use of fractal geometries has been shown to enhance the bandwidth and polarization selectivity of FSS structures [26–28]. Similarly, the incorporation of metamaterials has enabled the design of FSS structures with unique characteristics like inverse refraction index and complete absorption [29–31]. However, the use of convoluted meander lines remains an attractive option due to its simplicity and versatility. The structures can be easily fabricated using standard photolithography techniques, and their performance can be easily optimized by adjusting the quantity of rotations and the distance between meander lines [32–34]. Moreover, the resonant behavior of convoluted meander line FSS structures can be further enhanced

by incorporating additional elements such as slots and patches [35–37].

These elements can introduce flexibility in the design process, resonant frequencies and bandwidths variation. In summary, convoluted meander line structures have emerged as a promising approach for achieving multi-resonant behavior in FSS structures. Miniaturization is one of the reasons to overcome these constraints, especially with regard to unit cell size [7]. Smaller unit cells in FSS and meander line architectures are frequently preferred for a variety of uses, including integrated microwave components or compact antenna designs. It is difficult to achieve miniaturization without sacrificing performance. At smaller scales, fabrication techniques might find it difficult to produce exact features, which would raise complexity and cost. Reducing the size of unit cells can also bring additional electromagnetic phenomena that influence the behavior of the device, for impacts of surface roughness or heightened sensitivity [8] to surrounding objects or substrate qualities. Proposing new fabrication methods that are optimized for miniaturization and creative design strategies that lessen the effects of environmental influences are crucial. Overcoming these obstacles advances our knowledge of FSS and meander line topologies while also paving the way for more reliable and useful applications across a range of industries.

A compact single-layer bandstop FSS with good angular and resonant stability is presented in [38]. In contrast, [39] introduces a single-layer band pass FSS that resonantly covers the entire X-band (8-12 GHz) with good polarization and angular stability, thanks to tunable filter elements. The smaller size of the unit cell [39] may prevent it from providing a solution as compact, and it does not emphasize the miniaturization. Reference [40] suggested downsized double stop-band FSS for WLAN was built on the cross-zigzag loaded line and internal branches of a ring patch.

Hexagonal split-ring 2.5-dimensional unit cell is suggested in [41] for applications involving FSS. A metallic structure that has a dual-bandstop feature and a convoluted meander line incorporated cross dipole is presented in [42]. The fabrication of microwave components has made use of various additive manufacturing (AM) techniques and those are discussed in [43]. A compact single-layer bandstop FSS with good angular and resonant stability is presented in [44]. A novel tri-band complementary frequency selective surface (CFSS) with a conventional geometry made up of double concentric rings was proposed by the authors in [45]. FSS with gain improvement is included in an efficient ultrawideband (UWB) cyclic monopole antenna, as reported in [46]. In [47] the grating lobes are used for miniaturization and create a reduced single-layer FSS operating

at 2.6 GHz. Using square loop, ring loop and cross dipole structures on a single layer, two small dual-band FSS structures [48] and a tri-band FSS [49] and low-profile tri-band bandpass FSS using two-dimensional repetition of a unit cell with four apertures [50] are detailed for the investigation of angle variation.

In this research article, we presented a novel miniaturized tri-band FSS featuring meander lines. We proposed the design and analysis of three different FSS structures, each exhibiting a resonant frequency that varies as the convoluted meander line's length and turns are adjusted. To illustrate our approach, we introduce the suggested FSS arrangement along with unit cell schematic and an equivalent circuit. Miniaturization has been achieved with a unit cell having dimensions 10 mm × 10 mm. The characteristics of structure have been evaluated with different polarizations and angles of incidence of the planar wave. After many trials, three structures have been chosen and the optimized FSS 3 structure is proposed to a wide range of WiMax, X-band and Ka-band wireless communications and radar system applications that use FSS to reflect, absorb or transmit electromagnetic waves, which improve radar effectiveness in applications such as surveillance, navigation and target detection. The FSS's polarization insensitivity and high transmission coefficient highlight its potential for a wide range of communication and radar applications, displaying versatility and performance across multiple frequency bands. This analysis aims to evaluate the effectiveness and performance of the proposed FSS 3.

The uniqueness of our proposed work has been listed here.

- Multi-resonant FSS with convoluted meander lines
- Design evolution for miniaturization
- Equivalent circuit model analysis
- Tri-band resonant behavior: At 3.4 GHz, 10.6 GHz and 16 GHz. This tri-band behavior is a significant advancement, offering versatility for applications requiring operation across multiple frequency bands.
- Stability and polarization insensitivity
- Compact and cost-effective design.

II. DESIGN EVOLUTION

The meander line length from FSS 1 to FSS 3 has been decided based on the change in resonant frequency which in turn depends on the inductance and capacitance values. The turns in the meander lines have been increased to alter the electrical characteristics at multiple frequencies simultaneously, as demonstrated by the tri-band behavior in FSS 3. The other parameters like meander line length and slot are obtained by equations (1) and (2).

The design process from FSS 1 to FSS 3 with change in turns number has been depicted in Figs. 1 (a-c). The design has been fabricated on a FR4 substrate having thickness of 1 mm, permittivity of 4.3 and loss tangent of 0.02 to be cost-effective compared to Roger material which was used by most of the researchers in the literature. The permittivity of 4.3 gives precise electrical resistance to successfully manipulate electromagnetic waves inside the structure, and low loss tangent of 0.02 guarantees the signals pass with minimal loss. A magnetic susceptibility of 1 signifies the substrate's non-responsiveness to magnetic fields, which simplifies the process of designing and analyzing the FSS structure.

For conducting simulations, the CST Microwave Studio simulation tool is used for employing periodic boundary conditions based on Flouquet's method. First, FSS 1 is designed in a plus-shaped structure as shown in Fig. 1 (a) that results in single resonant frequency. To improve the performance of the structure to multi-band, FSS 1 has been extended with an L-shaped slot connected at each end of the plus structure and thereby increasing the meander line with three turns as depicted in Fig. 1 (b). To examine the connection between meander line length and resonant frequency, we incorporated two more L-shapes as meander lines with six turns, as presented in Fig. 1 (c).

The transmission characteristic of FSS 1 resonates at 10 GHz and dual resonant frequency was observed from the FSS 2 structure at 4.7 GHz and 11.6 GHz as shown in Figs. 2 (a) and (b). With a meander line length increase, due to inductive reactance variation, the FSS 3 structure exhibits tri-band resonant transmission characteristics at 3.4 GHz, 10.6 GHz and 16 GH as shown in Fig. 2 (c). The shift in resonant frequency for the additional slot introduced has been compared in Fig. 2 (d). The optimum dimensions of unit cell were chosen after many trials and based on defined formulas. They are p=10 mm, l=4.6 mm, W=0.3 mm and W_s=0.7 mm, with a unit cell free space wavelength of 0.038λ. The dimensions of a single-layer FSS having convoluted meander line FSS design has been calculated using equations (1) and (2). Each unit cell is composed of 10 metallic strips featuring nine turns with length decided by:

$$M_L = 2L1 + 2L2 + 2L3 + 2L4 + 2L5. \qquad (1)$$

The slots dimension is given by:

$$M_s = 2\,slot1 + 2\,slot2 + 2\,slot3. \qquad (2)$$

The stability of the proposed FSS 3 is investigated in terms of its polarization as shown in Fig. 3. For the FSS 3 structure, the signal transmission efficiency has been analyzed for 0° to 45° θ and φ values at both TE mode and TM mode. It proves good stability with 0% shift in frequency at triple band having 3.4 GHz, 10.6 GHz and 16 GHz resonant frequencies at both TE mode and TM mode for different polarizations. The resonance is main-
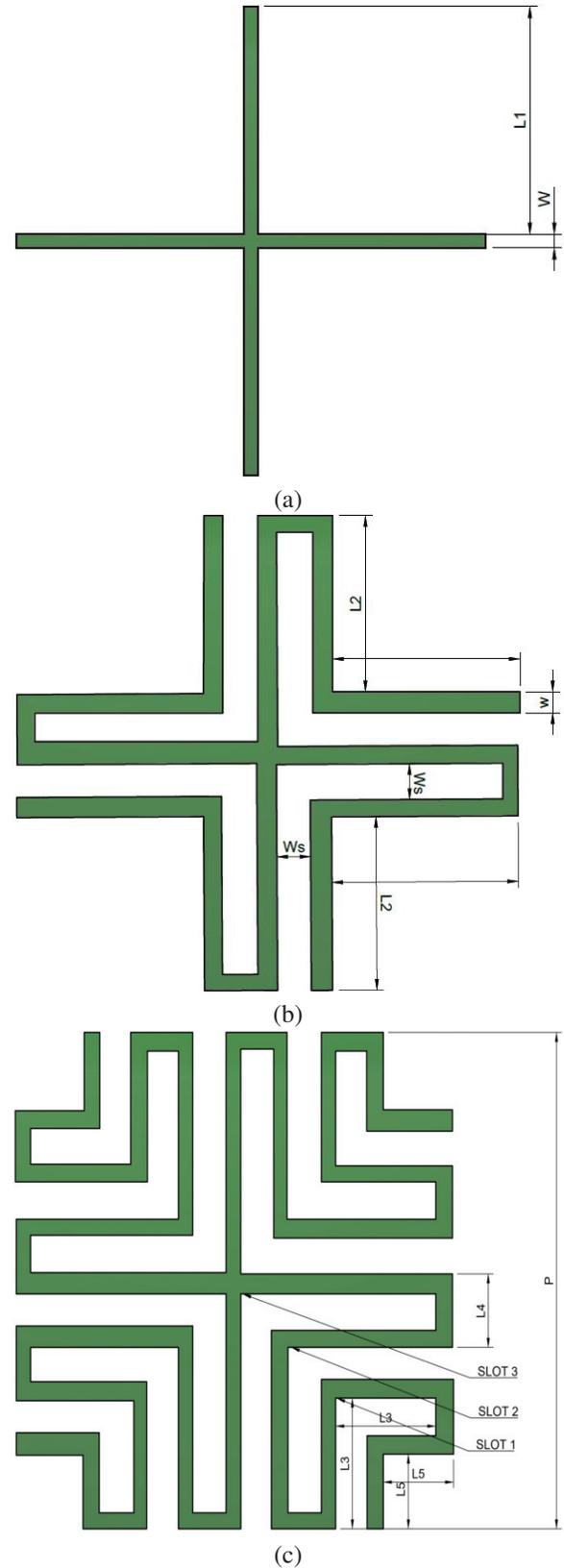
Fig. 1. FSS structure design: (a) FSS 1, (b) FSS 2, and (c) FSS 3.

(a)

(b)

(c)

(d)
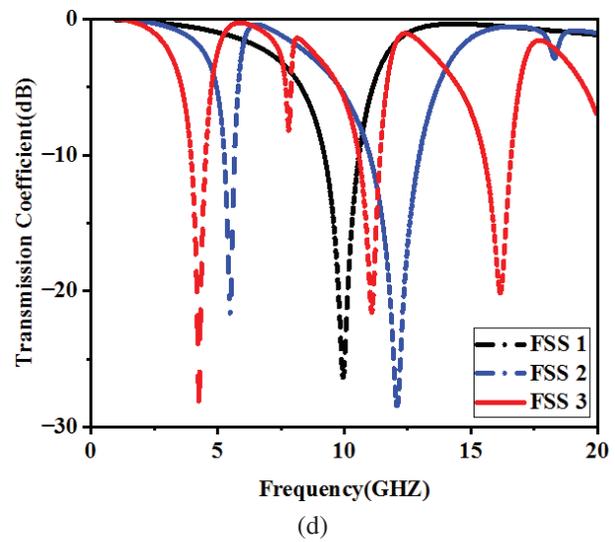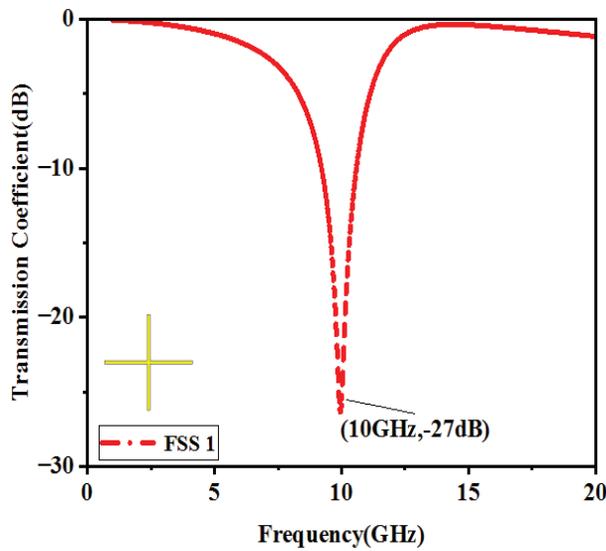
Fig. 2. Transmission properties: (a) FSS 1, (b) FSS 2, (c) FSS 3, and (d) comparison of all structures.
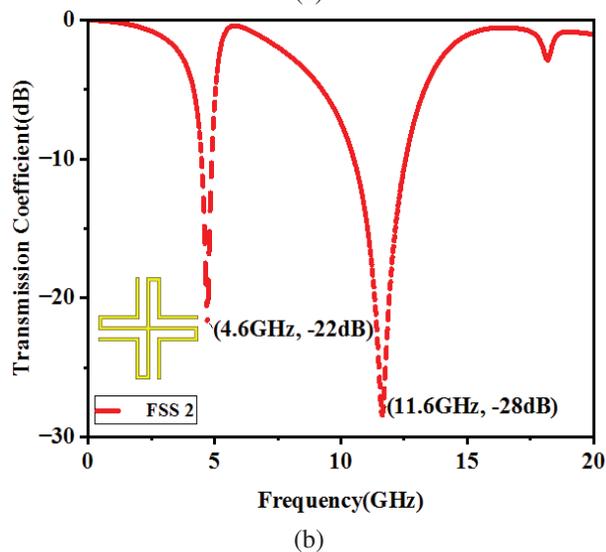
tained across all four values of ϕ, with the transmission coefficients being -28 dB, -21.5 dB and -20 dB for the three bands, respectively. In Figs. 3 (c) and (d), the proposed FSS 3 is examined for vertical and horizontal polarizations, respectively.

When the angle of incidence θ is $0°$ for vertical polarization, FSS 3 displays a tri-band with 0% shift. At $\theta=15°$, there is a 0.2% shift in the resonant frequency at 16 GHz, which changes to 15.8 GHz at -19 dB. Similarly, at $\theta=30°$, the resonant frequency shows a 0.2%

(a)
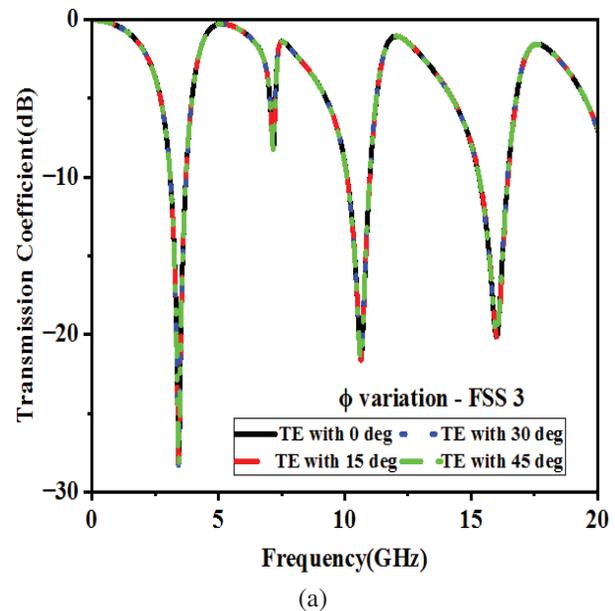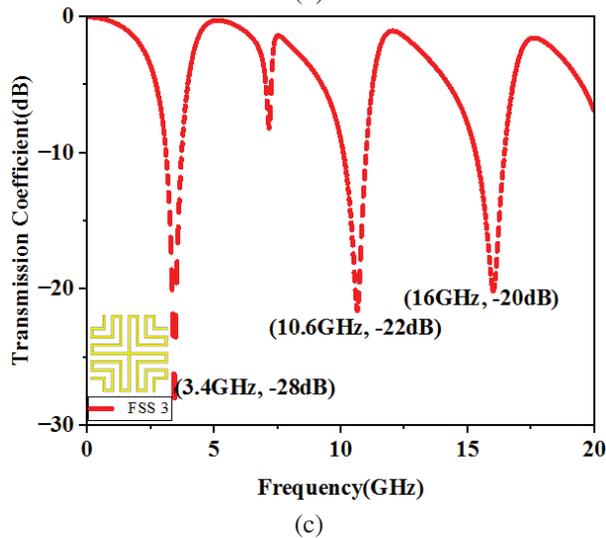
Fig. 2. *Continued.*

Fig. 3. *Continued.*

(b)

(c)

(d)
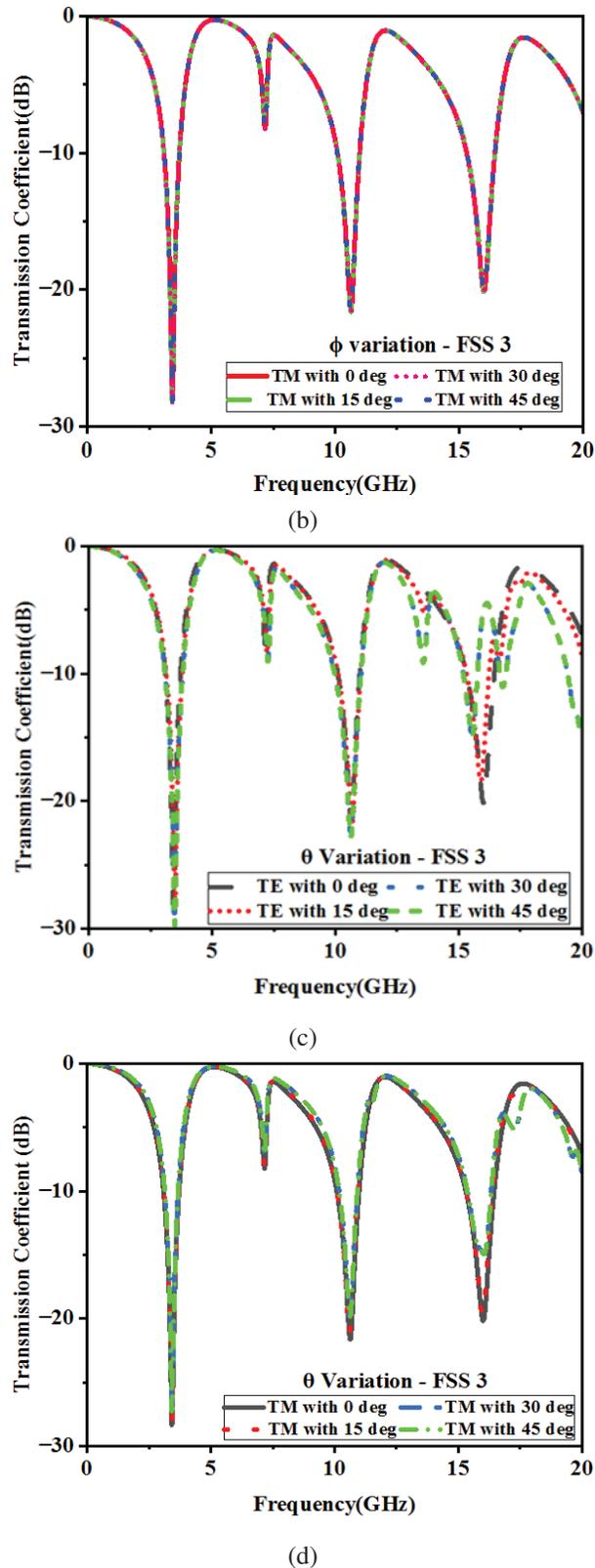
Fig. 3. Transmission co-efficient of single-layer FSS 3 with various ϕ and θ: (a) and (c) TE mode and (b) and (d) TM mode.

shift, resulting in a value of 15.6 GHz at -15 dB. However, at $\theta=45°$ there is no shift, and the resonant frequency remains the same as that at $30°$.

For horizontal polarization at $\theta=0°$, there is a 0% shift in all three resonant frequencies. At $\theta=15°$, there is no change in the first and second resonant frequencies, but there is a 0.2% shift in the return loss at 16 GHz from -20 dB to -19.8 dB. At $\theta=30°$ and $\theta=45°$, there is a 0% shift in the 3.4 GHz resonant frequency, while there is a 0.1% shift in the return loss of the 10.6 GHz resonant frequency from -21.7 dB to -20.1 dB. The return loss for 16 GHz resonant frequency shifts from -20 dB to -15 dB, but the resonant frequency remains stable at 16 GHz.

III. EQUIVALENT CIRCUIT MODEL

Monitoring the electric and magnetic field distributions is an important task throughout the development process of FSS structures. Particularly, the electric field distribution holds significant value as it reflects the conservation of energy within the unit cell. Analyzing this electric field distribution enables the identification of the resonant frequencies of the FSS configuration. To design these resonances effectively, an equivalent LC resonant circuit can be employed, which can be applied in addition to transmission line section, especially when dealing with convoluted meander line structures. This method is highly effective in determining resonant frequencies of FSS structures, which is vital for optimizing their performance. Furthermore, studying the distribution of electric and magnetic fields can lead to a better comprehension of the behavior of FSS structures, which in turn can enhance their design and performance.

Figure 4 (a) shows the simulated electric field distribution of 2×2 unit cell array. From the figure it is understood that the field distribution is of higher strength at the vertical end of the plus slot rather than at the center. The electric field distribution of FSS 1 displays a strong concentration of charges at both the top and bottom edges, resulting in a dominant capacitive effect.

Figure 4 (b) displays the ECM of an individual layer FSS unit cell as the series LC resonator having free space wave impedance, $Z_0 = 377\ \Omega$. The inductance L represents the metallic strip and the coupling between strips represents the capacitance C. Figure 4 (c) shows the comparison of transmission coefficient at 10 GHz for full wave analysis and equivalent circuit model analysis having lumped parameters $L_1 = 0.679$ nH and $C_1 = 0.37$ pF. The ability of signal propagation is slightly higher in simulation than the ECM model but no shift in resonant frequencies was observed.

This analogous circuit model-series LC resonator is used to represent the basic behavior of the FSS. The resonant behavior of the FSS at particular frequencies and the

(a)

(b)

(c)
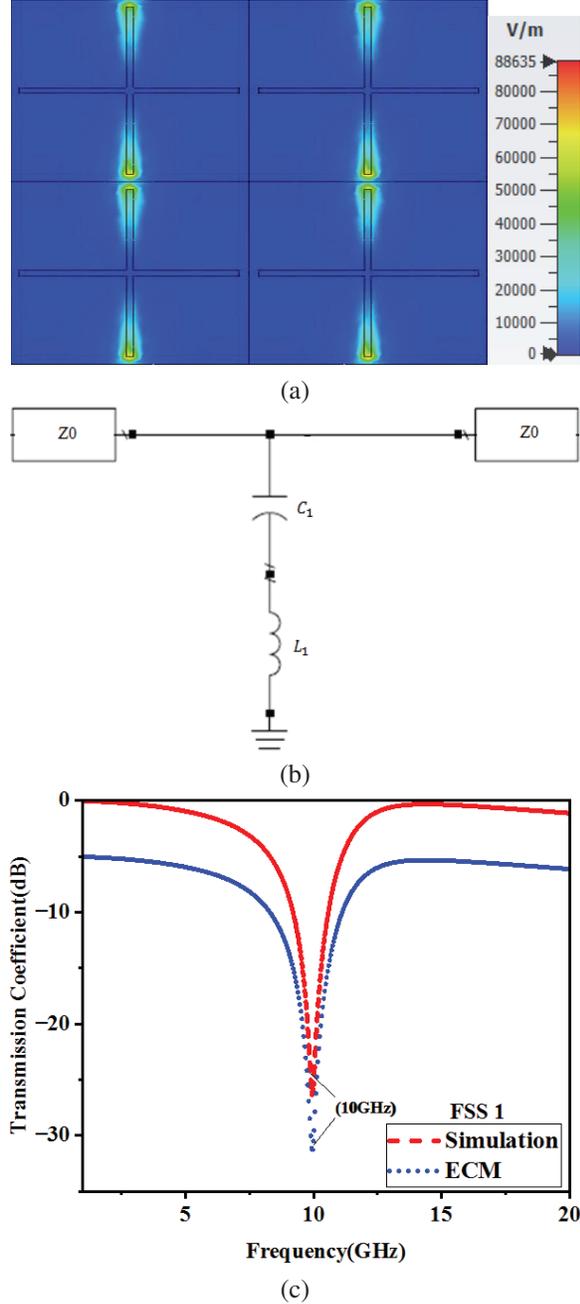
Fig. 4. (a) Electric field distribution at 10 GHz, (b) ECM circuit, and (c) Comparison between full wave and the ECM analysis of FSS 1.

relationship that exists between the external electromagnetic fields and the FSS structure has been derived from this circuit. The relationship between the circuit parameters and the proposed FSS parameters is outlined based on [51]:

$$C \alpha \varepsilon_0 \left(1 + \varepsilon_r\right) \frac{L_{slot}}{\pi} L_n \left(\frac{1}{\sin\left(\pi g /_{zL_{slot}}\right)}\right), \quad (3)$$

$$L \alpha \mu_0 \frac{L_{line}}{2\pi} L_n \left(\frac{1}{\sin\left(\pi w /_{zL_{line}}\right)}\right). \quad (4)$$

The impedance Z_{FSS} of the ECM can be obtained by calculating the sum of the dimensions of the meander lines (L_{line}) and the dimensions of the meander slots (L_{slot}).

$$Z_{FSS} = \frac{\left(j\omega L_1 + \frac{1}{j\omega C_1}\right)\left(j\omega L_2 + \frac{1}{j\omega C_2}\right) + \left(j\omega L_3 + \frac{1}{j\omega C_3}\right)}{j\omega \left(L_1 + L_2 + L_3\right) + \frac{1}{j\omega C_1} + \frac{1}{j\omega C_2} + \frac{1}{j\omega C_3}}, \quad (5)$$

where Z_{FSS} is ECM's impedance equivalent. Utilizing the tenets of wave propagation, the transmission factor of the novel ECM can be determined through the subsequent calculation:

$$T(\omega) = \frac{2Z_{FSS}}{2Z_{FSS} + Z_0}. \quad (6)$$

By examining the equivalent circuit, we can deduce that when $Z_{FSS} = 0$ Ω, three transmission zeros are present, and when $Z_{FSS} = \infty$, one transmission pole exists. Equation (7) can be utilized to calculate the frequencies of these zeros and poles:

$$\omega_{1zero} = \frac{1}{\sqrt{L_1 C_1}}; \omega_{2zero} = \frac{1}{\sqrt{L_1 C_1} + \sqrt{L_2 C_2}}, \quad (7a)$$

$$\omega_{3zero} = \frac{1}{\sqrt{L_1 C_1} + \sqrt{L_2 C_2} + +\sqrt{L_3 C_3}}, \quad (7b)$$

$$\omega_{pole} = \sqrt{\frac{(C_1 + C_2 + C_3)}{(L_1 + L_2 + L_3)(C_1 + C_2 + C_3)}}. \quad (7c)$$

The electric field distribution of two parallel LC sections as a result of convoluted meander lines addition has been analyzed in Fig. 5. The electric field distribution of the resultant FSS 2 structure exhibits a greater concentration of charges at the edges of the convoluted meander lines in comparison to FSS 1, as displayed in Fig. 5 (a).

Unlike in FSS 1, all four ends of the plus slot have been charged equally with electric fields due to additional L slots in the form of convoluted meander lines. The ECM and comparison of transmission behavior between the ECM and full wave simulation are displayed in Figs. 5 (b) and (c), respectively. The calculated and simulated optimum LC values are: L_1=4 nH and C_1=0.29 pF, L_2=0.2 nH and C_2=0.94 pF. The transmission behavior is similar to FSS 1 at 4.6 GHz and 11.6 GHz dual resonant frequency.

FSS 3 has been analyzed at 3.4 GHz, 10.6 GHz and 16 GHz resonant frequencies as shown in Fig. 6. The derived LC values for the meander lines having higher number of turns are: L_1=4 nH and C_1=0.55 pF, L_2=0.55 nH and C_2=0.41 pF, and L_3=0.5 nH and C_3=0.196 pF. The combination of three different inductances and capacitances were connected in parallel, as

(a)

(b)

(c)
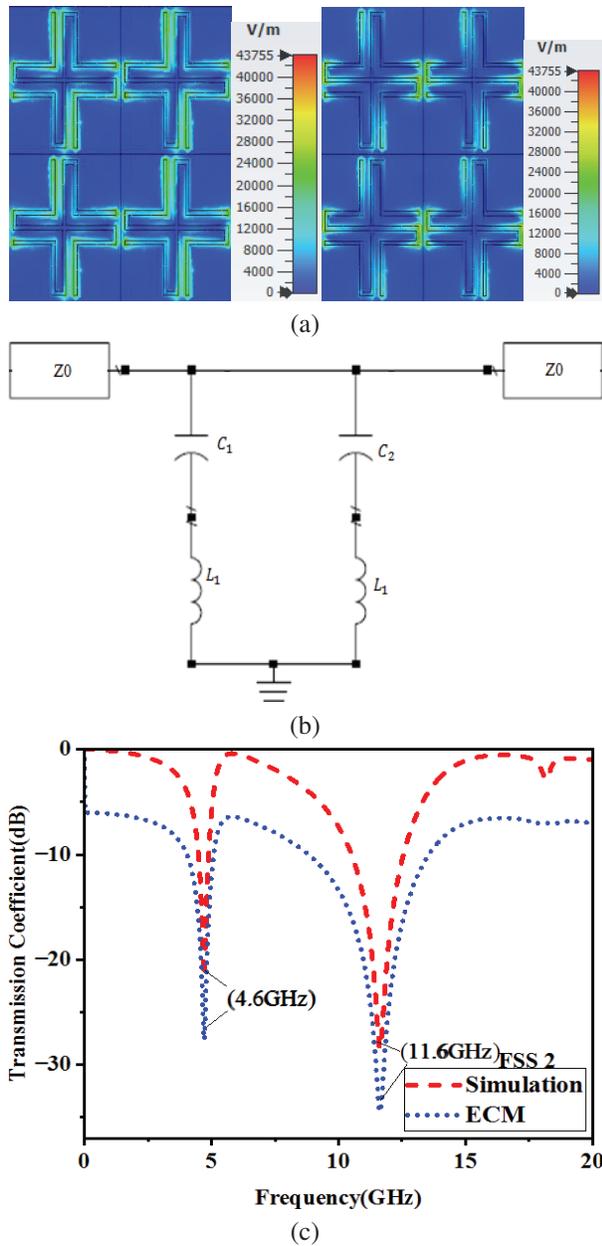
Fig. 5. (a) Electric field distribution at 4.6 GHz and 11.6 GHz, (b) ECM circuit, and (c) Comparison between full wave and the ECM analysis of FSS 2.

illustrated in Fig. 6 (b), was simulated and compared with the full-wave simulation of FSS 3 behavior presented in Fig. 6 (c).The comparison shows strong agreement between simulation and ECM analysis with no shift in frequency at three resonant frequencies.

It is important to note that these parameters are specific to the circuits proposed in the respective figures mentioned above. Figures 4, 5 and 6 indicate that a single resonant frequency of 10 GHz can be demonstrated by a

(a)

(b)

(c)
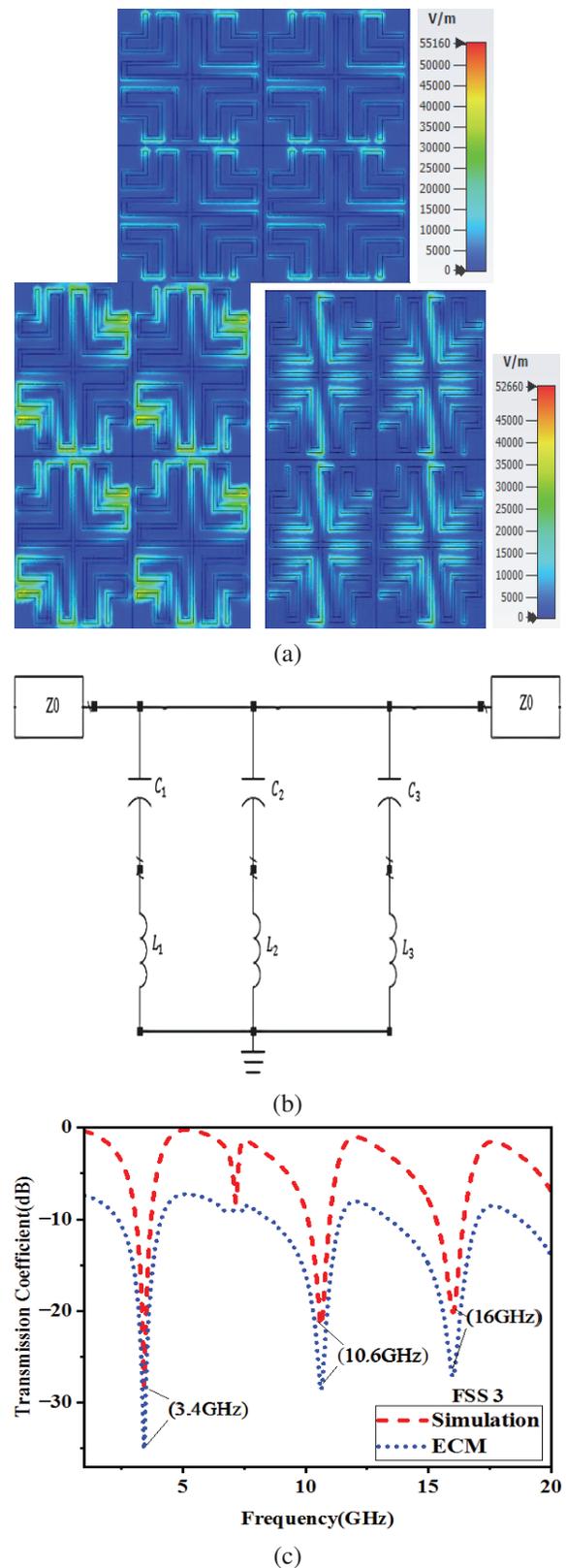
Fig. 6. (a) Electric field distribution at 3.4 GHz, 10.6 GHz and 16 GHz, (b) ECM model, and (c) Comparison of full wave and ECM model transmission of FSS 3.

single plus structure (FSS 1) and with increase in meander line length by three turns, a dual resonant frequency is achieved at 4.6 GHz and 11.6 GHz. Subsequently, the FSS 3 structure, which includes an additional six turns in the meander lines, achieves tri-band resonant frequencies at 3.4 GHz, 10.6 GHz and 16 GHz.

IV. MEASUREMENT ANALYSIS OF RESULTS

Measurements entail the usage of two wide-range horn antennas along with a vector network analyzer with the proposed FSS prototype at the center point between two horn surfaces as shown in Fig. 7 (a). The single-layer FSS created to demonstrate the simulated performance has been fabricated with 200 mm × 200 mm size as shown in Fig. 7 (b), accompanying an assembly of 20×20 individual unit cell. The unit cell of fabricated single-layer FSS for 10 mm × 10 mm is shown in Fig. 7 (c).

The measured TE and TM mode transmission coefficient for θ value from 0 to 45 degree in a 15-degree increased step size has been plotted in Figs. 8 (a) and (b), respectively. A multi-frequency reaction is observed with an augmentation in meander lines, and the points of zero transmission remain unwavering across different angles of incidence for both TE and TM mode polarizations, aligning through exhaustive wave simulations. Polarization insensitivity has been achieved for angle variation at multi frequency and proved through measurement. The discrepancy of 5 dB between the calculated and simulation results for the proposed three types of FSS is due to:

i) The ECM as a set of lumped circuit elements may not fully capture the intricacies of the actual electromagnetic interactions.

ii) Assumptions made in developing the ECM, such as neglecting mutual coupling between adjacent unit cells or ignoring edge effects, can lead to inaccuracies in the calculated results.

iii) Variations in fabrication tolerances, material properties or environmental conditions.

For easy understanding, the simulated and measured TE mode results of frequency shift for polarization insensitivity have been compared for an angle range from 15° to 45° as shown in Table 1. We observed zero frequency in simulation for all three resonant frequencies and this shift changes up to 0.2% in measurements. Similarly, the transmission coefficient has gained shift at third resonant frequency for all angle values and no change for the remaining two resonant frequencies.

The other notable achievement of this proposal, miniaturization, has been evidently compared with other similar FSSs having a single-layer for three band application as in Table 2. It is noticed that the frequency

(a)
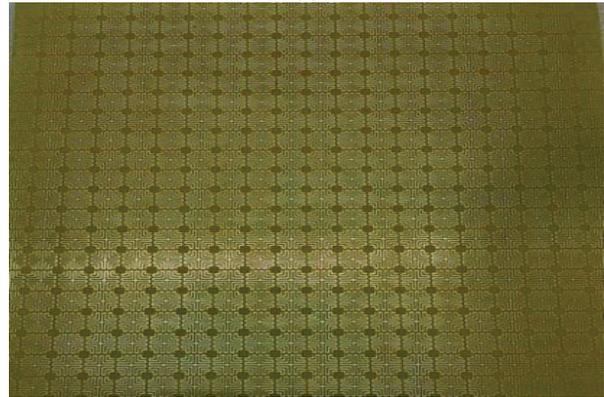
(b)
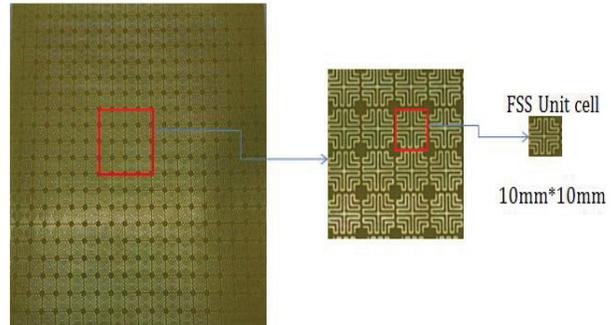
(c)

Fig. 7. FSS 3 structure: (a) measurement set up, (b) fabricated prototype, and (c) unit cell.

change with respect to θ angle is negligible at 0.2%, and happens at 45 degrees with size reduction of about half in both length and width of FSS as compared to [50] and [45] given in Table 3.

The proposals in [50], [49] and [45] achieved three bands with a single layer, but with higher size which is more than twice compared to our design. In contrast, [47] shows smaller unit cell diameters than the others but with a single band. These dimensions differ greatly amongst references, reflecting different designs and applications.

(a)

(b)
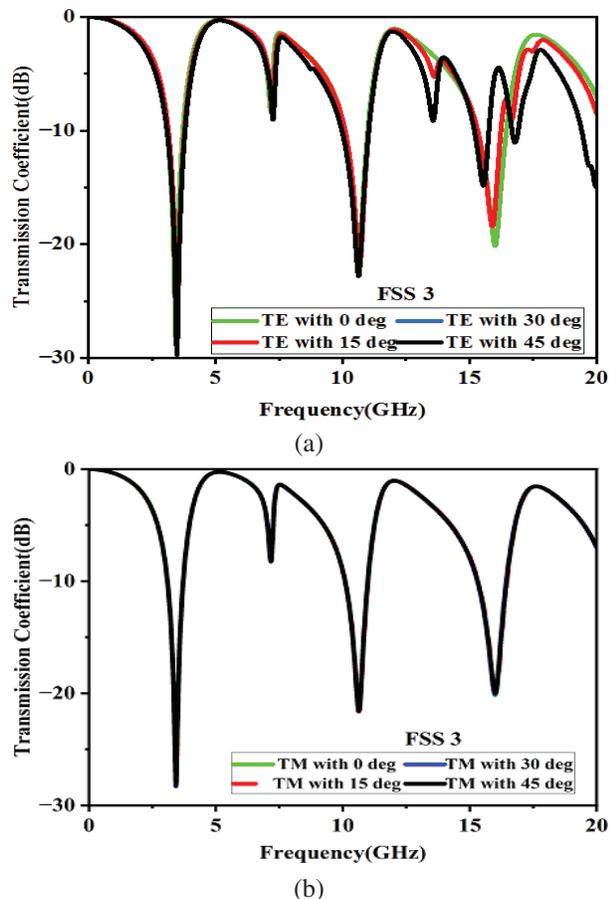
Fig. 8. Measurement of transmission coefficient of FSS 3 using network analyzer: (a) TE mode and (b) TM mode.

Table 1: Comparison of simulated and measured results for TE mode

Degree	Simulated	Measured
Transmission Coefficient (dB)		
15	−28 @ 3.4 GHz	−20 @ 15.9 GHz
30	−21 @ 10.6 GHz	−15 @ 15.8 GHz
45	−20 @ 16 GHz	−15 @ 15.8 GHz
Shift in Frequency (GHz)		
15	No shift	0.1% @ 15.9
30		0.2% @ 15.8
45		0.2% @ 15.8

This shows the newness of our work having tri-band application aimed at compactness.

V. CONCLUSION

In this study, a miniaturized approach of FSS structure having single layer and periodicity of 10 mm^2 for triple band wireless application has been presented. To achieve the desired performance, the convoluted structure based on meander lines was fabricated in FR4 sub-

Table 2: Parametric comparison with other works

Ref	Thickness (mm)	ε_r	Layer	Band	θ shift (%) & (°)
[38]	1	4.4	2	2	0.9 & 60
[39]	1	4.4	2	1	0.8 & 60
[40]	0.4	4.4	1	2	2.2 & 85
[41]	0.125	2.7	1	1	6.93 & 45
[42]	1	4.3	1	1	6 & 60
This Work	**1**	**4.4**	**1**	**3**	**0.2 & 45**

Table 3: Unit cell size and bands comparison with other works

References	Number of Bands	Number of Layers	Size (mm^2)
[50]	3	Single	20.6 × 20.6
[47]	1	Single	9.45 × 9.45
[48]	2	Single	11.2 × 11.2
[46]	1	Single	30 × 30
[49]	3	Single	24 × 22
[45]	3	Single	24 × 24
This Work	**3**	**Single**	**10 × 10**

strate having well-defined dielectric properties and magnetic permeability. The proposed FSS in three versions has been simulated for single, dual and triple band resonant frequency. FSS 3 for triple band has been fabricated at 200 × 200 mm as an assembly of 20×20 individual unit cells. The structure exhibited tri-band resonance at 3.4 GHz, 10.6 GHz and 16 GHz, with a shift of 0% in frequency for both TE and TM mode, proving its stability for different polarizations. The resonance was maintained across all values of ϕ, with transmission coefficients being −28 dB, −21.5 dB and −20 dB for the three bands, respectively. FSS 3 was also examined for vertical and horizontal polarizations, and it was found that it had good stability for different angles of incidence θ. This paper demonstrates that the proposed FSS structure can be utilized for various applications in the field of wireless communications.

REFERENCES

[1] Y. Zhang, W. Liu, R. Liu, and F. Yang, "Frequency selective surface with independently controllable transmission and reflection characteristics," *Appl. Phys. Lett.*, vol. 115, no. 14, p. 141902, 2019.

[2] M. A. Al-Joumayly and A. Y. Al-Qudsi, "Frequency-selective surfaces for antenna applications:

A review," *IET Microw. Antennas Propag.*, vol. 13, no. 6, pp. 742-750, 2019.

[3] E. Karaboga and Z. Bayraktar, "Dual-band frequency selective surface with multilayered and hexagonal unit cell," *IEEE Trans. Antennas Propag.*, vol. 69, no. 2, pp. 836-842, 2021.

[4] Y. Wang, X. Huang, Y. Yu, and J. Chen, "Design and analysis of a broadband frequency selective surface with simple meander line unit cells," *IET Microw. Antennas Propag.*, vol. 14, no. 11, pp. 1119-1125, 2020.

[5] L. Guo, Y. Tang, X. Zhang, and X. Han, "Multi-band frequency selective surface with fractal meander line for electromagnetic interference shielding," *Appl. Phys. A*, vol. 126, no. 8, pp. 1-9, 2020.

[6] Y. Sun and Z. Zhu, "Dual-band polarization-independent frequency selective surface based on modified square-loop meander line," *IET Microw. Antennas Propag.*, vol. 14, no. 5, pp. 458-465, 2020.

[7] J. Garg, M. M. Sharma, and S. Yadav, "Design of a compact band pass frequency selective surface for WLAN applications based on meander line topology," in *2021 IEEE Indian Conference on Antennas and Propagation (InCAP)*, pp. 893-896, 2021.

[8] K. S. Yeo, H. C. Park, D. Ahn, and N. H. Myung, "A miniature band-pass filter using a meandered line," *IEEE Microw. Wireless Compon. Lett.*, vol. 12, no. 11, pp. 443-445, Nov. 2002.

[9] R. F. Harrington and J. R. Mautz, "Theory and experiment for periodic resonant structures," *IEEE Trans. Microw. Theory Tech.*, vol. 16, no. 4, pp. 182-186, Apr. 1968.

[10] K. Kim, K. Lee, K. Lee, and B. Lee, "Miniaturized filters using fractal-shaped resonators with complementary split ring resonators and meander lines," *IEEE Trans. Microw. Theory Tech.*, vol. 56, no. 11, pp. 2578-2586, Nov. 2008.

[11] J. E. Schutt-Aine and M. J. Howes, "An accurate equivalent circuit for meander lines and its application to coupled-line filters," *IEEE Trans. Microw. Theory Tech.*, vol. 44, no. 11, pp. 1957-1963, Nov. 1996.

[12] C. W. See and R. A. York, "Meander line band-pass filter design for harmonic suppression," *IEEE Trans. Microw. Theory Tech.*, vol. 49, no. 12, pp. 2355-2360, Dec. 2001.

[13] C. F. Tsai and L. J. Chen, "Design and performance of meander line filters with short-circuited stubs," *IEEE Trans. Microw. Theory Tech.*, vol. 50, no. 4, pp. 1219-1225, Apr. 2002.

[14] A. H. Aghvami and R. N. Simons, "Meander-line filters for VHF/UHF applications," *IEEE Trans.*

Microw. Theory Tech., vol. 29, no. 7, pp. 733-736, July 1981.

[15] K. W. Chau and K. M. Luk, "High-performance compact filters using folded meander-line resonators," *IEEE Microw. Wireless Compon. Lett.*, vol. 13, no. 8, pp. 329-331, Aug. 2003.

[16] J. W. Lee and K. Chang, "Miniaturized low-pass filter using L-shaped meander line," *IEEE Microw. Wireless Compon. Lett.*, vol. 12, no. 6, pp. 230-232, June 2002.

[17] M. Agostini, F. Freschi, and G. Ghione, "Modeling of lossy meander lines in multilayered substrates by a frequency-dependent surface impedance approach," *IEEE Trans. Microw. Theory Tech.*, vol. 44, no. 4, pp. 573-579, Apr. 1996.

[18] H. J. Tang, Q. Xue, and B. Wei, "A novel UWB bandpass filter based on a coupled meander line and SIRs," *IEEE Microw. Wireless Compon. Lett.*, vol. 22, no. 2, pp. 58-60, Feb. 2012.

[19] J. Zhang and Q. Xue, "Novel microstrip bandpass filter with meander lines and resonant stubs," *IEEE Microw. Wireless Compon. Lett.*, vol. 30, no. 5, pp. 413-415, May 2020.

[20] S. Chen, C. Yu, Y. Chen, S. Zhang, and Y. Liu, "Compact wideband bandpass filter based on E-shaped resonator with dual band-notched function," *Microwave Opt. Technol. Lett.*, vol. 61, no. 1, Jan. 2019.

[21] Z. Chen, X. Chen, C. Liu, H. Wang, and Y. Fan, "Miniaturized wideband bandpass filter with a novel perturbation technique," *J. Electromagn. Waves Appl.*, vol. 33, no. 3, pp. 241-250, 2019.

[22] K. Fang, Y. Zhang, X. Yang, and M. Hu, "Design of compact dual-band bandpass filter with high isolation and low loss," *Micromachines*, vol. 11, no. 1, Jan. 2020.

[23] M. Han, X. Mao, and G. Zhang, "Design of a compact quad-band bandpass filter with multiple transmission zeros," *Microwave Opt. Technol. Lett.*, vol. 62, no. 5, May 2020.

[24] L. Deng, H. Chen, S. Wang, Y. Huang, and Y. Wang, "Novel miniaturized bandpass filters based on substrate integrated waveguide," *J. Electromagn. Waves Appl.*, vol. 34, no. 13, pp. 1682-1694, 2020.

[25] C. Zhang, X. Chen, Q. Wu, and Y. Yuan, "Fractal frequency selective surfaces with multi-band characteristics," *Microwave Opt. Technol. Lett.*, vol. 61, no. 6, pp. 1639-1642, 2019.

[26] Y. Zhang, W. Xu, and L. Wang, "Fractal-inspired multiband frequency selective surface with polarization selectivity," *IEEE Trans. Antennas Propag.*, vol. 67, no. 7, pp. 4506-4510, 2019.

[27] Y. Zhang, W. Xu, and L. Wang, "A novel multiband fractal frequency selective surface with polarization selectivity," *Prog. Electromagn. Res. C*, vol. 91, pp. 79-88, 2019.

[28] C. R. Simovski, P. A. Belov, A. V. Atrashchenko, and Y. S. Kivshar, "Metamaterial-based perfect absorbers: Ultrathin structures and localization of the absorbed energy," *Phys. Rev. B*, vol. 85, no. 19, p. 195111, 2012.

[29] N. Liu, H. Liu, S. Zhu, and H. Giessen, "Three-dimensional photonic metamaterials at optical frequencies," *Nat. Mater.*, vol. 7, no. 1, pp. 31-37, 2008.

[30] X. Chen, T. M. Grzegorczyk, B.-I. Wu, J. Pacheco, and J. A. Kong, "Robust method to retrieve the constitutive effective parameters of metamaterials," *Phys. Rev. E*, vol. 70, no. 1, p. 016608, 2004.

[31] F. Yang, J. Li, and Q. Li, "Wide-angle polarization-independent infrared frequency selective surface with a three-layer structure," *J. Appl. Phys.*, vol. 107, no. 1, p. 014510, 2010.

[32] K. Zhang, Y. Jiang, and X. Chen, "Design of frequency selective surfaces with controllable multiple passbands," *J. Appl. Phys.*, vol. 124, no. 15, p. 154303, 2018.

[33] J. Li, L. Li, and W. Li, "A miniaturized dual-bandstop frequency selective surface with meander line," *IEEE Antennas Wireless Propag. Lett.*, vol. 16, pp. 266-269, 2017.

[34] R. Garg and P. Bhartia, "Design of bandstop frequency selective surfaces using planar quasi-Yagi antenna," *Microwave Opt. Technol. Lett.*, vol. 49, no. 10, pp. 2546-2551, 2007.

[35] L. Guo, J. Liu, C. Du, L. Guo, and X. Wang, "A wide-angle, polarization-insensitive, and low-profile frequency selective surface for X-band radar application," *Prog. Electromagn. Res. C*, vol. 81, pp. 233-242, 2018.

[36] C. Lv, Y. Zuo, and Y. Xu, "Dual-band frequency selective surface with sharp rejection," *IEEE Antennas Wireless Propag. Lett.*, vol. 15, pp. 1237-1240, 2016.

[37] H. Paik and K. Premchand, "Performance analysis of a single layer X-band frequency selective surface based spatial filter implementing half Jerusalem cross slot," *Prog. Electromagn. Res. Lett.*, vol. 108, pp. 25-30, 2023.

[38] Z. U. Abidin, Q. Cao, and G. Shah, "Design of a compact single-layer frequency selective surface with high oblique stability," *IEEE Trans. Electromagn. Compat.*, vol. 64, no. 6, pp. 2060-2066, Dec. 2022.

[39] A. B. Varuna, S. Ghosh, H. Sheok, and K. V. Srivastava, "A polarization insensitive miniaturized element frequency selective surface using meander lines," in *2018 Twenty Fourth National Conference on Communications (NCC)*, Hyderabad, India, 2018.

[40] Q. Li, Q. Wang, H. Zhang, J.-Q. Hou, and J. Zhao, "A new miniaturized double stop-band frequency selective surface," *Applied Computational Electromagnetics Society (ACES) Journal*, vol. 39, no. 01, pp. 9-16, Jan. 2024.

[41] A. Khajevandi and H. Oraizi, "Miniaturization of frequency selective surface by 2.5-dimensional meandered split ring cells for application in L-band," *Sci. Rep.*, vol. 13, no. 1, p. 18737, Oct. 2023.

[42] A. Bagwari, P. Jindal, A. Yadav, R. Tiwari, S. K. Sharma, and J. Logeshwaran, "Convoluted meander line-inspired metallic surface filter for Bluetooth and WLAN bands," *Mobile Inf. Syst.*, 2023.

[43] S. S. Karthikeyan and R. A. Mellita, "Additive manufacturing of MTM-FSS," in *Handbook of Metamaterial-Derived Frequency Selective Surfaces*, S. Narayan and A. Kesavan, Eds. Singapore: Springer, 2022.

[44] H. Paik and K. Premchand, "Performance analysis of a single layer X-band frequency selective surface based spatial filter implementing half Jerusalem cross slot," *Prog. Electromagn. Res. Lett.*, vol. 108, pp. 25-30, 2023.

[45] M. Sousa, B. Silva, H. Andrade, and M. da Silva, "A complementary frequency selective surface with tri-band frequency response for applications in Wi-Fi and 5G," *J. Commun. Inf. Syst.*, vol. 38, pp. 189-197, 2023.

[46] I. U. Din, F. A. Tahir, K. J. B. Rashid, and M. I. Iqbal, "A novel compact ultra-wideband frequency-selective surface-based antenna for gain enhancement applications," *J. Electromagn. Eng. Sci.*, vol. 23, no. 2, pp. 188-201, Mar. 2023.

[47] M. Qu, Y. Feng, J. Su, and S. M. A. Shah, "Design of a single-layer frequency selective surface for 5G shielding," *IEEE Microw. Wireless Compon. Lett.*, vol. 31, no. 3, pp. 249-252, Mar. 2021.

[48] W. Zhang, M. Li, M. Le, B. Li, and J. Wei, "A dual-frequency miniaturized frequency selective surface structure suitable for antenna stealth," *Wireless Commun. Mobile Comput.*, vol. 21, no. 2, pp. 263-270, 2021.

[49] S. Vahida and K. Shambavi, "A single layer tri-band frequency selective surface for WiFi and amateur radio applications," in *2017 IEEE International Conference on Smart Technologies and Management for Computing, Communication, Controls, Energy and Materials (ICSTM)*, pp. 349-352, 2017.

[50] U. Mahaveer, A. K. Gautam, and B. K. Kanaujia, "A tri-band frequency-selective surface," *J. Electromagn. Waves Appl.*, vol. 35, no. 7, pp. 861-873, 2021.

[51] P.-C. Zhao, Z.-Y. Zong, W. Wu, and D.-G. Fang, "A convoluted structure for miniaturized frequency selective surface and its equivalent circuit for optimization design," *IEEE Trans. Antennas Propag.*, vol. 64, no. 7, pp. 2963-2970, July 2016.

Suganthi Santhanam received the B.E. degree in Electronics and Communication Engineering from Bharathidasan University, Tiruchirappalli, Tamil Nadu, India in 1998, the M.E. degree in computer and communication from the Anna University, Chennai, Tamil Nadu, India, in 2006, and Ph.D. (RF MEMS) from Anna University Chennai. She is currently working as Professor in the Department of Electronics and Communication Engineering, K. Ramakrishnan College of Technology, Tamil Nadu, India. Her research interests include ANN's, digital signal processing, MATLAB, CAD of VLSI circuits, and computer-aided design methodologies for microwave modeling techniques.

Deepa Jeyaraman received the B.E. degree in Electronics and Communication Engineering from Dhanalakshmi Srinivasan Engineering College, Anna University, Perambalur, Tamil Nadu, India, in 2009 and the M.Tech. degree in VLSI Design from the Kalasalingam University, Chennai, Tamil Nadu, India, in 2013. She is currently working as an Assistant Professor in the Department of Electronics and Communication Engineering, K. Ramakrishnan College of Technology, Tamil Nadu, India. Her research interests include microwave devices modeling & simulation, VLSI, MATLAB.

Contribution of Mobile Communication Technologies to EMF Exposure in the University of Novi Sad Campus Area

Dragan R. Kljajić[1], Nikola M. Djuric[1], Karolina K. Kasas-Lazetic[1], Miodrag M. Milutinov[1], and Snezana M. Djuric[2]

[1]Faculty of Technical Sciences
University of Novi Sad, Novi Sad 21000, Serbia
dkljajic@uns.ac.rs, ndjuric@uns.ac.rs, kkasas@uns.ac.rs, miodragm@uns.ac.rs

[2]Institute BioSens
University of Novi Sad, Novi Sad 21000, Serbia
snesko@uns.ac.rs

***Abstract* –** Densely populated areas are usually extensively exposed to the emission of electromagnetic fields (EMFs) that is primarily caused due to extensive use of wireless telecommunication technologies, particularly those providing mobile phone communication services. Consequently, observation and control of EMF levels in human surroundings have great importance in terms of human health and environmental protection. Particular efforts have to be devoted to EMF investigation in highly sensitive areas, where people can stay for quite long periods, such as university campuses. This paper brings the results of 2023 EMF monitoring campaign, performed over the University of Novi Sad campus for the third time, comparing them with EMF results obtained in previous 2012 and 2018 campaigns. Having in mind the emergence of new 4G Long Term Evolution (LTE) base stations in the campus, during 2022, a special focus of the 2023 campaign was on the inevitable increase of field levels, because of the contribution of 2G/3G/4G mobile communication technologies to human EMF exposure. Despite the expected increase of the field levels, obtained values were still significantly lower than the minimal reference levels, prescribed by the Serbian legislation.

***Index Terms* –** broadband measurement, continuous monitoring, EMF, exposure assessment.

I. INTRODUCTION

Exposure to electromagnetic field (EMF) radiation has become one of the major environmental concerns, considering continuous increase of a number of artificial EMF sources in surroundings. Among them, base stations (BSs) of new generations of mobile phone communication technologies are the most pronounced. Consequently, the investigation of EMF, thorough the long-term monitoring and control of its levels in the environment, is of a great importance.

In line with that, particular efforts have to be paid to EMF level measurements, as well as corresponding exposure assessment of population, in highly sensitive zones with long-term stay of people, as suggested by the World Health Organization [1]. University campuses are certainly highly sensitive areas, having in mind the high concentration of people in them, almost every day. Therefore, some scientific studies have been devoted to EMF investigation in those areas, performing short- and long-term stationary measurements in broadband or band selective frequency ranges [2–7].

Regarding the University of Novi Sad campus area, in the Republic of Serbia, the first broadband EMF monitoring campaign was conducted in 2012 [8], where 4-hour monitoring of the high-frequency electric field (E-field) was performed at 10 most crowded locations in the campus. Narda NBM-550 instrument with broadband E-field probe EF 0691 was used, covering a frequency range from 100 kHz to 6 GHz [9, 10]. The second monitoring campaign was carried out in 2018 [11], at the same locations and with usage of additional instruments (Wavecontrol SMP2) and its WPT broadband E-field probe designed to cover frequency ranges of 2G/3G/4G mobile communications services – from 700 to 2600 MHz [12, 13]. The 2023 campaign included also a third measuring instrument, the Narda SRM 3006 spectrum analyzer, to perform frequency selective scanning of EMF content, in the frequency range from 420 MHz to 6 GHz [14].

This paper brings comparative presentation of the three EMF campaigns and discusses the results acquired so far. Particular attention is devoted to the analysis of the contribution of mobile communication technologies

to EMF exposure in the campus, considering their dominant presence in this area.

II. MATERIALS AND METHODS

Detailed information about the measuring procedure applied in the first two EMF monitoring campaigns, as well as descriptions of the selected locations in the campus, are given in [8, 11]. The same measuring procedures were applied in the 2023 campaign, at the same locations, as listed in Table 1 and marked with yellow triangles in Fig. 1.

Table 1: Campus locations for EMF monitoring

Location	Description
Location 1	in front of the Rectorate building
Location 2	in front of the Faculty of Agriculture
Location 3	the square surrounded by three Faculty buildings
Location 4	entrance into the campus
Location 5	in front of Students' Cultural Center (former student cafeteria)
Location 6	in the vicinity of Novi Sad Business School and Student Sports Centre
Location 7	at the most frequented traffic crossroad
Location 8	between two students' dormitories
Location 9	in front of the entrance of a main student cafeteria
Location 10	the square in front of the Faculty of Technical Sciences

Regarding the measuring equipment used in monitoring campaigns, a list of instruments is provided in Table 2.

Table 2: Measuring equipment used in campaigns

Campaign	Measuring Equipment		
	NBM-550	SMP2	SRM 3006
2012	Yes	No	No
2018	Yes	Yes	No
2023	Yes	Yes	Yes

Broadband field meters NBM-550 and SMP2 were used for 4-hour continuous EMF monitoring of E-field strength. Technical parameters of the field probes are shown in Tables 3 and 4.

Table 3: Broadband electric field probe EF 0691 [10]

Parameter	Value
Frequency range	100 kHz to 6 GHz
Measurement range	0.35 V/m to 650 V/m
Linearity	$\pm$ 0.5 dB (2 to 400 V/m)
Frequency sensitivity	$\pm$ 1.5 dB (1 MHz to 4 GHz)

It should be highlighted that the WPT field probe performs broadband EMF monitoring, acquiring the EMF contribution from four frequency ranges dedicated for 2G/3G/4G mobile phone services, as given in Table 4.

Table 4: Mobile phone services' field probe WPT [13]

Parameter	Value
Frequency ranges	700 MHz to 900 MHz 1800 MHz to 1900 MHz 2100 MHz and 2600 MHz
Measurement range	0.04 V/m to 65 V/m
Linearity	$< \pm 0.4$ dB (0.2 to 50 V/m)
Frequency response	$\pm$ 3.3 dB

In the last campaign, a SRM 3006 spectrum analyzer was also applied, for short measurements, i.e. a few minutes long spectrum's content scanning. The basic settings of this instrument are listed in Table 5.

Table 5: SRM 3006 spectrum analyzer settings [14]

Parameter	Settings Value
Frequency ranges	420 MHz to 6 GHz
Resolution bandwidth (RBW)	500 kHz
Video bandwidth (VBW)	5 kHz
Averaging method	Time
Averaging time	60 s

Besides significant daily frequency of student population and university staff in the campus, this area is additionally interesting for EMF investigation due to periodic installation of new BSs, visually noticeable in this area. With the introduction of new generations of mobile communication, the number of BSs and their antennas in the campus has been increased in the last decade. Thus, they have become dominant EMF sources not only in this area, but also in its urban surrounding.

Currently, five BSs are present and operational in the campus, owned by three national operators (A1, Yettel and MTS). These BSs and their sector antennas are marked with red and pink circles in Fig. 1. Technical parameters of these antennas will be omitted here, but their radiation patterns are depicted in Fig. 1 by different colors per communication services.

It should be mentioned that only BS 1 and BS 3 were present in the campus in the 2012 campaign [8]. In that time, they were providing only GSM/2G service, while today they provide GSM/2G, UMTS/3G and LTE/4G services.

The next BS in the campus appeared during 2017 (a four-sector BS 4), whose antennas serve to cover the surrounding area with a signal of all existing services [11]. Finally, two additional BSs have been installed in
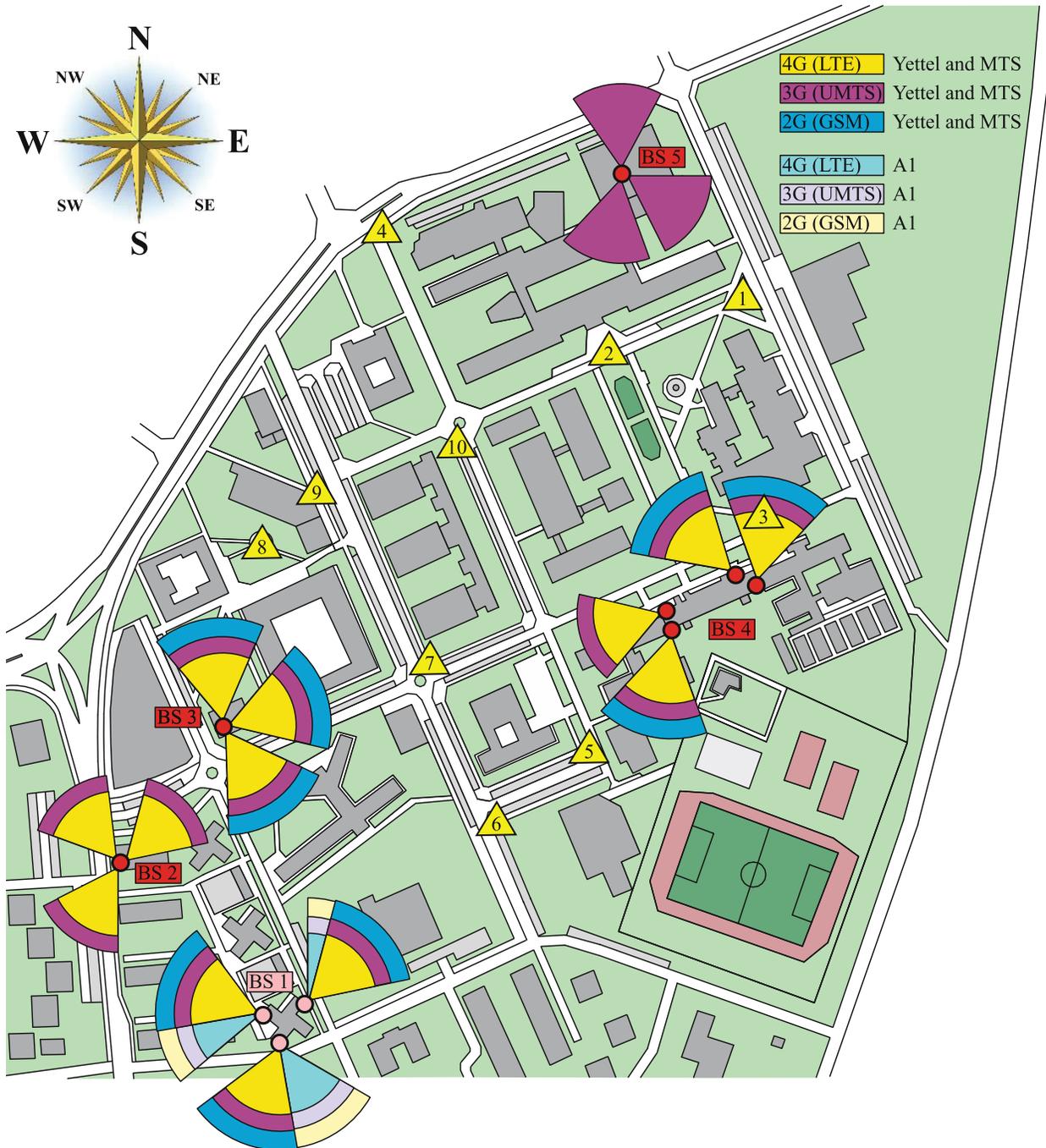
Fig. 1. Positions of BSs and monitoring locations in the University of Novi Sad campus.

the campus area, BS 2 (UMTS and LTE services) and BS 5 (only UMTS service), before the 2023 campaign.

III. RESULTS AND DISCUSSION

Measurement results acquired in the three EMF campaigns, by three types of measuring instruments, will be compared and discussed in the following subsections.

A. NBM-550 field meter

A graphical comparative presentation of the average, E_{avg}, and maximum, E_{max}, field strength values, obtained in all campaigns by the Narda NBM-550 field meter is given in Fig. 2.

Considering these graphs, a slight or significant increase of the E-field strength values, from campaign to
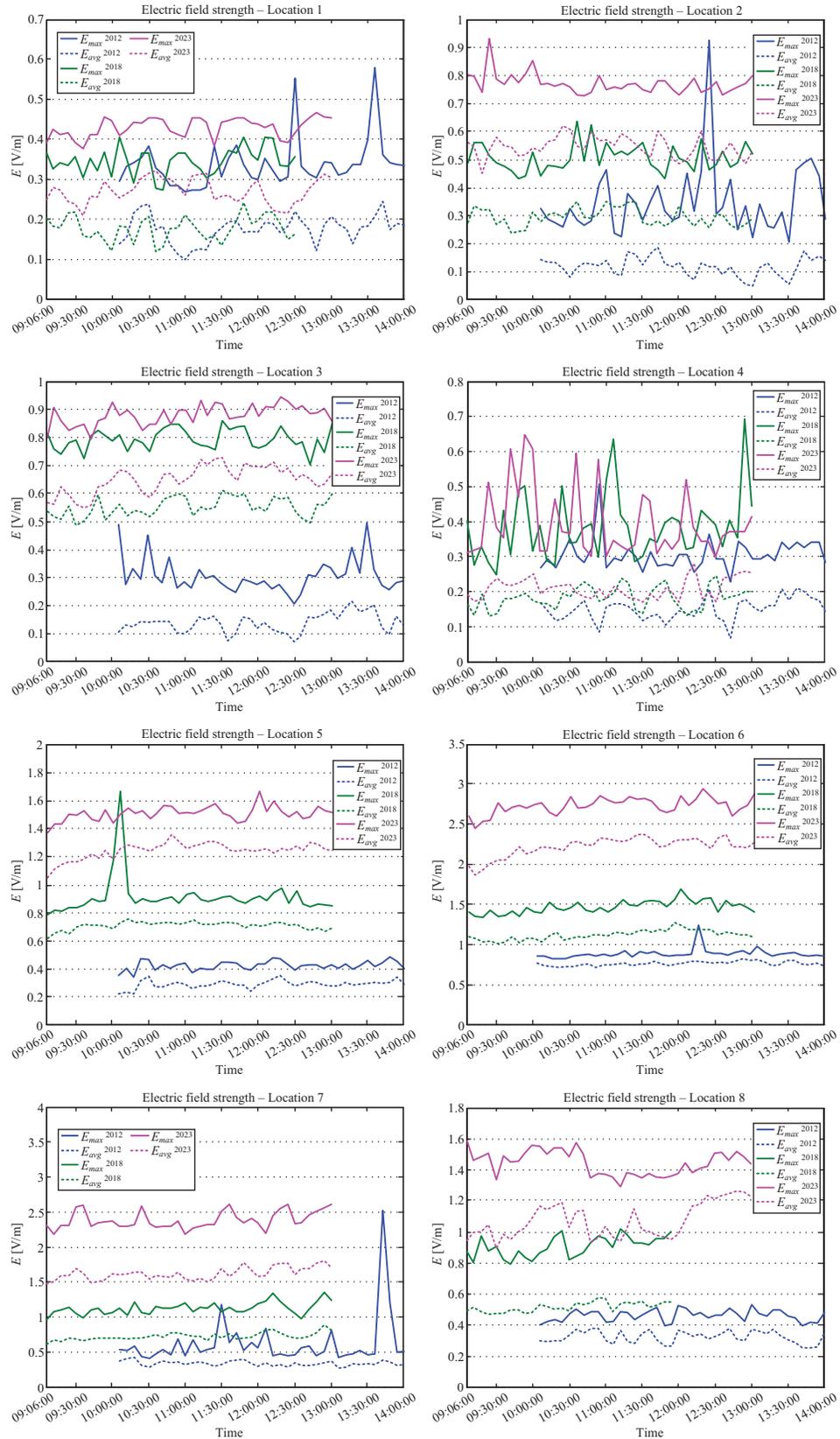
Fig. 2. *Continued.*
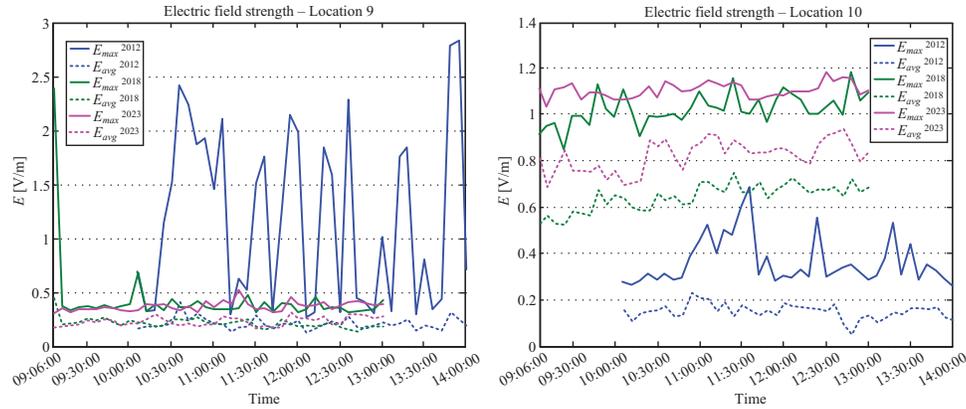
Fig. 2. E-field strength values – Narda NBM-550 [11].

campaign, is noticed at nine of the 10 locations (except Location 9). These conclusions are practically in line with those drawn in the previous paper [11].

The field strength values at Location 9 in 2023 remained very similar to those in 2018, while it was noticed their significant decrease in comparison with 2012 results. As stated in [11], those differences and observed short-term peaks of E_{max} values are primarily caused by the increased usage of mobile communication technologies (cell phones calls and internet connections) at that location.

Finally, the most pronounced increase and the highest E-field strength values (maximum of 2.946 V/m) were achieved at Location 6. A comparison of maximum values of E_{max}, obtained by the Narda NBM-550 field meter, is provided in Table 6.

Table 6: Maximum values of E_{max} (V/m) − NBM-550 [11]

Location	Campaign		
	2012	2018	2023
1	0.580	0.406	0.467
2	0.926	0.637	0.932
3	0.496	0.862	0.945
4	0.507	0.694	0.647
5	0.489	1.664	1.667
6	1.248	1.695	2.946
7	2.529	1.355	2.615
8	0.529	1.020	1.589
9	2.834	2.389	0.522
10	0.684	1.181	1.186

Considering data from Table 6, it is evident that all field strength values obtained in three campaigns were several times lower than the minimal reference level, prescribed by the Serbian legislation ($E_{ref\ min}$ = 11 V/m for frequency range 100 kHz to 6 GHz) [15].

In all campaigns, the exposure assessment was performed using the proposed boundary approach, where upper and lower boundaries of the Global Exposure Ratio (*GER*) [16] are evaluated. Those boundaries determine the range where actual exposure exists, while they are calculated by the following equations:

$$GER_{low} = \left(\frac{E_m}{E_{ref\ max}} \right)^2 \quad and \quad GER_{up} = \left(\frac{E_m}{E_{ref\ min}} \right)^2 \tag{1}$$

where E_m denotes measured value of the E-field, while $E_{ref\ min}$ and $E_{ref\ max}$ are the minimum and maximum reference levels, prescribed by the Serbian legislation [15], in monitored broadband frequency range.

GER boundaries were calculated taking the average field strength values, E_{avg}, as E_m in equation (1), acquired by the Narda NBM-550 meter. Their comparison by campaigns is shown in Fig. 3.

Results presented in Fig. 3 confirmed conclusions about the increase of exposure at nine of 10 locations, with a slight decrease at Location 9 only. Statistical analysis of maximum values of upper boundary, GER_{up}, a much more important exposure boundary, calculated with E_{avg} results from the Narda NBM-550 is given in Table 7, offering their comparison by campaign.

The highest value of GER_{up} boundary, achieved at Location 6 in the 2023 campaign, was about 21 times lower than the maximal allowable exposure level $GER_{allowed} = 1$.

All other values were several hundred or thousand times lower than the maximal allowable exposure level, suggesting that, from campaign to campaign, the campus area remained low EMF exposed.

B. SMP2 field meter

As regards measurements conducted by the Wavecontrol SMP2 field meter, this paper brings the first comparison of the results obtained by this instrument, since it was used for the first time in the 2018 campaign. The
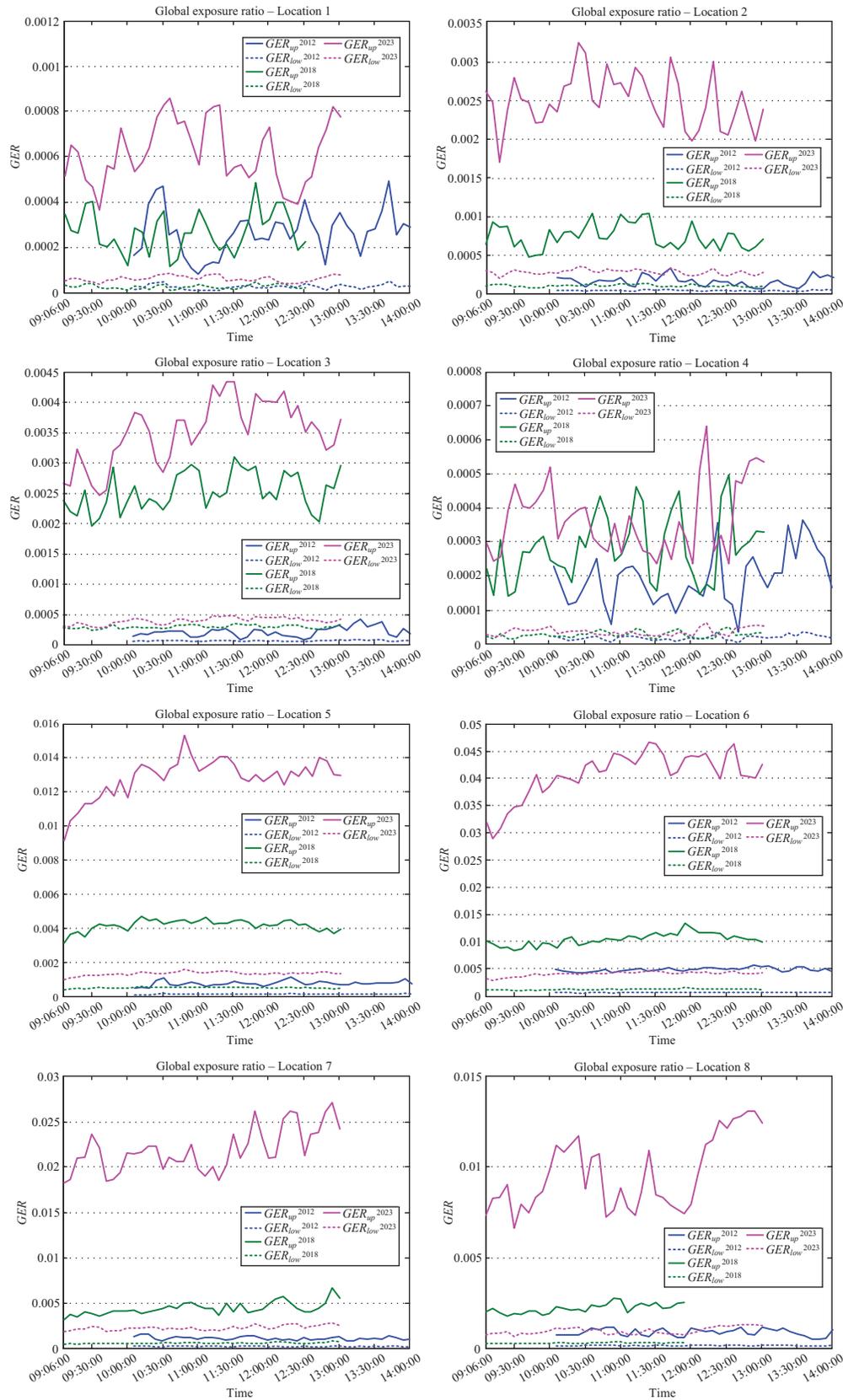
Fig. 3. *Continued.*
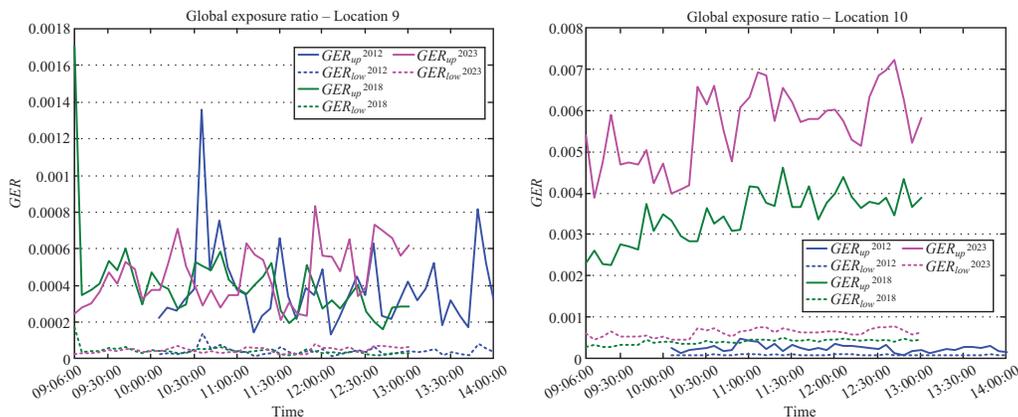
Fig. 3. The exposure boundaries – Narda NBM-550 [11].

Table 7: Maximum values of GER_{up} − NBM-550 [11]

Location	Campaign		
	2012	2018	2023
1	0.49×10^{-3}	0.49×10^{-3}	0.86×10^{-3}
2	0.29×10^{-3}	1.03×10^{-3}	3.21×10^{-3}
3	0.38×10^{-3}	3.10×10^{-3}	4.35×10^{-3}
4	0.36×10^{-3}	0.49×10^{-3}	0.64×10^{-3}
5	1.04×10^{-3}	4.72×10^{-3}	15.3×10^{-3}
6	5.56×10^{-3}	13.4×10^{-3}	46.5×10^{-3}
7	1.47×10^{-3}	6.61×10^{-3}	27.1×10^{-3}
8	1.18×10^{-3}	2.74×10^{-3}	13.1×10^{-3}
9	1.35×10^{-3}	1.70×10^{-3}	0.83×10^{-3}
10	0.43×10^{-3}	4.62×10^{-3}	7.23×10^{-3}

Table 8: Maximum values of E_{ins} (V/m) − SMP2 [11]

Location	Campaign	
	2018	2023
1	0.194	0.257
2	0.452	0.571
3	0.402	0.595
4	0.187	0.291
5	0.647	0.820
6	1.086	1.939
7	1.233	1.408
8	0.626	0.883
9	0.250	0.250
10	1.409	1.135

average, E_{avg}, and instant, E_{ins}, field strength values, obtained in the 2018 and 2023 campaigns, are graphically presented and compared in Fig. 4.

A graphical comparison revealed an increase of field strength values at nine of 10 locations. That increase was the highest at Location 6 and the lowest at Location 9, while Location 10 was the only one with a decrease of field strength values compared with the 2018 campaign. That location is at one of the central squares in the campus, surrounded by several high buildings and far distanced from all five BSs. These could be the reasons for the achieved slight decrease of field strength values from mobile phone services at that location.

A comparative overview of maximum values of E_{ins}, obtained in both campaigns by the Wavecontrol SMP2 field meter, is provided in Table 8.

The highest field strength value of 1.939 V/m was achieved at Location 6 in 2023. However, that value, as well all others obtained in both campaigns, were about 10 or more times lower than the minimal reference level, prescribed by Serbian legislation for the frequency range from 700 MHz to 2600 MHz ($E_{ref\ min}$ = 14.5 V/m) [15].

Graphical presentation of the exposure boundaries, calculated using the average field strength values, E_{avg}, of the Wavecontrol SMP2 field meter as E_m in equation (1), is given in Fig. 5.

Results presented in Fig. 5 additionally showed the tendency of an increase of exposure to mobile communication technologies in the campus in the past years. A comparison of maximum values of upper boundary, GER_{up}, calculated according to the Wavecontrol SMP2 measuring results is provided in Table 9.

The highest increase of upper exposure boundary can be noticed for Location 6, where the maximum value of GER_{up} was about 69 times lower than the maximal allowable level $GER_{allowed}$ = 1.

Despite an expected increase of exposure values in the 2023 campaign, most values were several hundred or thousand times lower than the maximal allowable level.

C. SRM 3006 spectrum analyzer

For the first time, in the 2023 campaign, a frequency selective analysis of the high-frequency part of
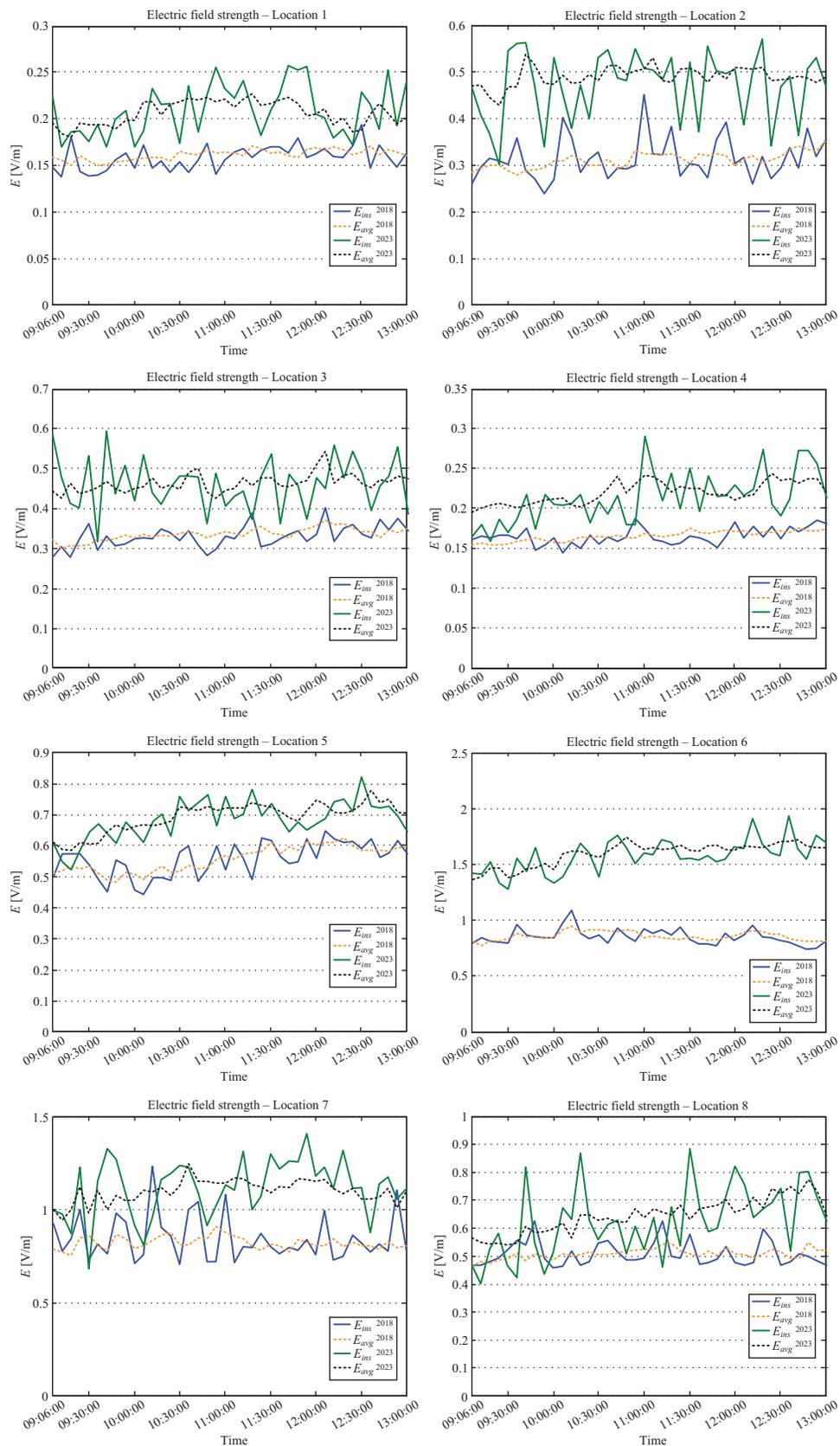
Fig. 4. *Continued.*
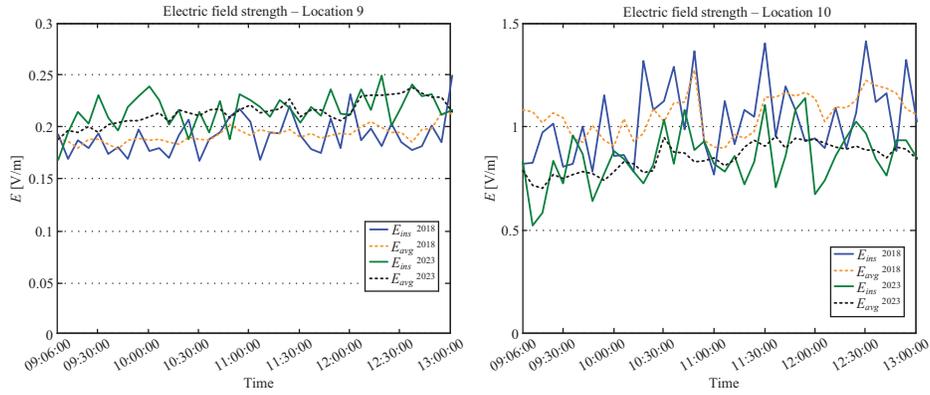
Fig. 4. E-field strength values – Wavecontrol SMP2 [11].

Fig. 5. *Continued.*
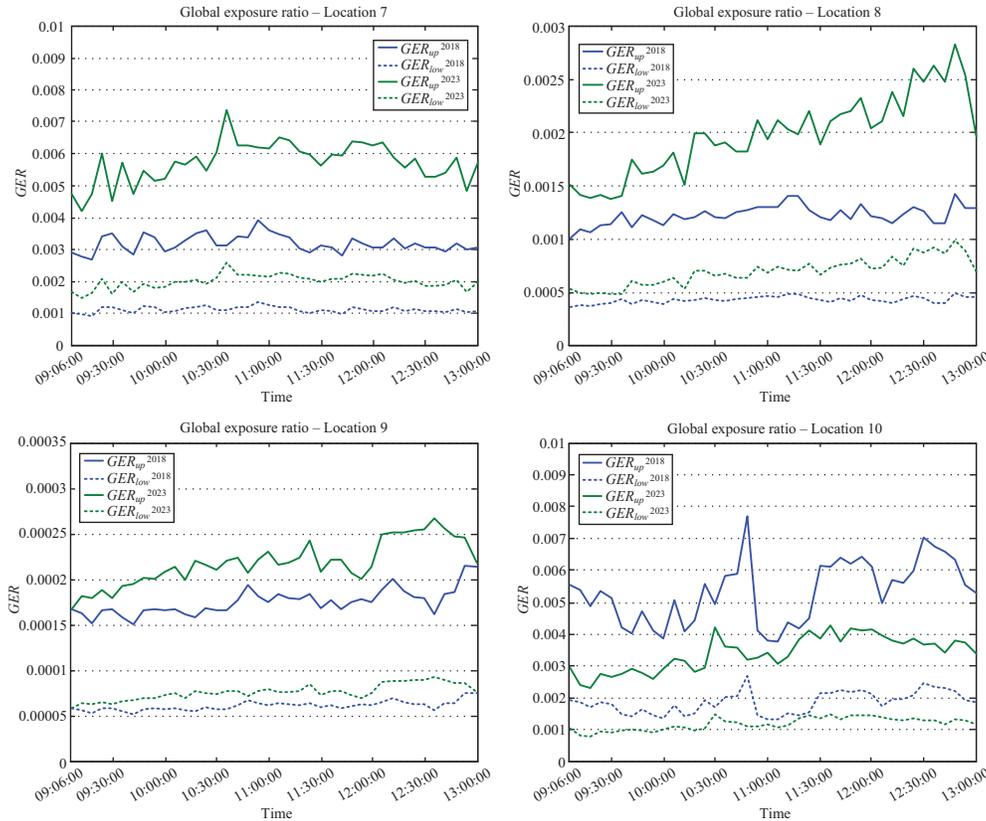
Fig. 5. The exposure boundaries – Wavecontrol SMP2 [11].

Table 9: Maximum values of GER_{up} − SMP2 [11]

Location	Campaign	
	2018	2023
1	0.14×10^{-3}	0.24×10^{-3}
2	0.59×10^{-3}	1.38×10^{-3}
3	0.65×10^{-3}	1.39×10^{-3}
4	0.14×10^{-3}	0.28×10^{-3}
5	1.85×10^{-3}	2.86×10^{-3}
6	4.20×10^{-3}	14.5×10^{-3}
7	3.91×10^{-3}	7.36×10^{-3}
8	1.43×10^{-3}	2.82×10^{-3}
9	0.22×10^{-3}	0.27×10^{-3}
10	7.69×10^{-3}	4.28×10^{-3}

the spectrum was performed by the Narda SRM 3006 spectrum analyzer. It recorded actual, maximal, and averaged values of E-field strength, in the frequency range from 420 MHz to 6 GHz, while the averaging time was set to 1 minute.

Since no spectral components were detected in the range between 3 GHz and 6 GHz, at each of 10 locations, analyses were repeated in the shrunken frequency range from 420 MHz up to 3 GHz. Figure 6 shows the results of spectral analyses of the E-field at the monitoring locations.

At all locations, a dominant presence of E-field components in several frequency subranges can be noticed. Most of them are downlink and uplink bands for GSM 900/1800 MHz, UMTS 2100 MHz and LTE 800/1800/2100 MHz mobile phone technologies. Practically, these data confirmed the dominant contribution of five BSs in the campus, as initially expected according to a visual inspection of this area.

Some spectral components were detected in the range between 2400 MHz and 2500 MHz, which could originate from a number of local Wi-Fi networks in the campus, technically and visually unknown to authors.

Finally, performed spectrum analyses showed that mobile communication technologies had dominant contribution to overall EMF exposure in the campus area. Therefore, these types of EMF sources could be regarded as those with the highest impact on exposure changes in this sensitive area.

Future campaigns should certainly include detailed analyses by the Narda SRM 3006 spectrum analyzer, bearing in mind the foreseen deployment of a new generation of mobile communication technology – 5G (New
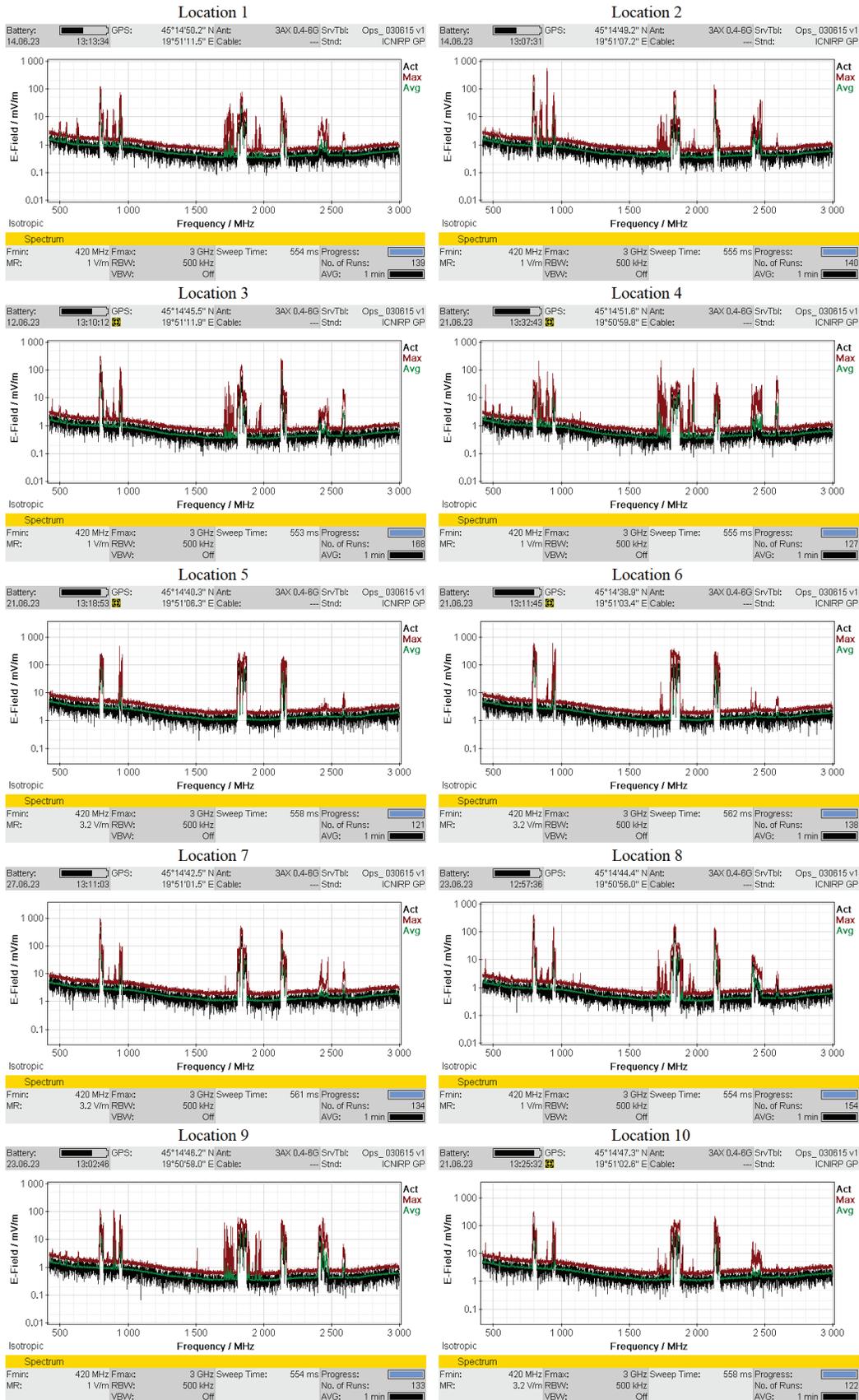
Fig. 6. Spectrum content of the high-frequency E-field in the campus.

Radio - NR), the appearance of which is expected in the near future in the Republic of Serbia.

IV. CONCLUSION

The results of the three EMF monitoring campaigns in the University campus area are presented in this paper. As regards broadband monitoring in the range from 100 kHz to 6 GHz, comparative analysis of the measurement results showed an increase of E-field values, as well public exposure, at nine of the 10 monitoring locations. Regardless of that increase, all values remained significantly lower than the minimal reference level prescribed by Serbian legislation.

Similar conclusions are drawn from the previous two monitoring campaigns and measurements in the range from 700 MHz to 2600 MHz, observing E-fields originating primarily from mobile communications services. An increase of E-field strength values at nine of the 10 locations was noticed, but all acquired values were a few dozen times less than the minimal reference level prescribed for that frequency range.

Considering the wide prevalence of existing mobile communication technologies in the campus, the 2023 campaign included frequency selective analysis of the high-frequency part of spectrum at monitoring locations. Results revealed a dominant contribution of 2G/3G/4G mobile communication technologies in the spectrum, as well as a slightly smaller contribution of Wi-Fi technology. Those sources for certain have had the highest impact on the increase of EMF exposure in the campus in last decade.

Although exposure is still far below the maximal allowable level, it is clear that the contribution of mobile communication technologies will remain the most dominant in the future. This assumption is additionally strengthened by the announced deployment of 5G technology in the near future. Therefore, beside the necessity for periodic monitoring campaigns, measurements and exposure assessment analyses should be extended to the frequency range beyond 6 GHz, considering the features of 5G communication standards.

ACKNOWLEDGMENT

REFERENCES

[1] World Health Organization, WHO research agenda for radiofrequency fields, [Online] Available: https://who.int/iris/bitstream/handle/10665/44396/9789241599948_eng.pdf.

[2] X. Zhao, Z. Ji, W. Chu, Y. Zhao, L. Yan, H. Zhou, Q. Liu, and K. Huang, "Measurement and analysis of electromagnetic environment characteristics on Wangjiang campus of Sichuan university," *Radio Science*, vol. 54, issue 7, pp. 633-645, July 2019.

[3] M. Fernández, D. Guerra, U. Gil, I. Trigo, I. Peña, and A. Arrinda, "Measurements and analysis of temporal and spatial variability of WiFi exposure levels in the 2.4 GHz frequency band," *Measurement*, vol. 149, no. 106970, pp. 1-9, Jan. 2020.

[4] S. Keshmiri, N. Gholampour, and V. Mohtashami, "Assessing the compliance of electromagnetic fields radiated by base stations and WiFi access points with international guidelines on university campus," *Radiation Protection Dosimetry*, vol. 192, issue 1, pp. 1-13, Oct. 2020.

[5] R. Ramirez-Vazquez, S. Arabasi, H. Al-Taani, S. Sbeih, J. Gonzalez-Rubio, I. Escobar, and E. Arribas, "Georeferencing of personal exposure to radiofrequency electromagnetic fields from Wi-Fi in a university area," *International Journal of Environmental Research and Public Health*, vol. 17, issue 6, 1898, pp. 1-19, Mar. 2020.

[6] R. Ramirez-Vazquez, I. Escobar, A. Martinez-Plaza, and E. Arribas, "Comparison of personal exposure to radiofrequency electromagnetic fields from Wi-Fi in a Spanish university over three years," *Science of the Total Environment*, vol. 858, Part 3, 160008, pp. 1-13, Feb. 2023.

[7] F. L. Suarez, S. M. Yepes, and A. Escobar, "Assessment of the electromagnetic field exposure due to wireless communication technologies in two university campuses of Medellin, Colombia," *Heliyon*, vol. 9, issue 9, e20323, pp. 1-14, Sep. 2023.

[8] N. Djuric, D. Kljajic, K. Kasas-Lazetic, and V. Bajovic, "The SEMONT continuous monitoring of daily EMF exposure in an open area environment," *Environmental Monitoring and Assessment*, pp. 187-191, Mar. 2015.

[9] Narda Safety Test Solutions GmbH, NBM-550 broadband field meter user's guide, Narda, 2006.

[10] Narda Safety Test Solutions GmbH, EF 0691 electric field user's guide, Narda, 2006.

[11] D. Kljajic and N. Djuric, "Comparative analysis of EMF monitoring campaigns in the campus area of the University of Novi Sad," *Environmental Science and Pollution Research*, vol. 27, issue 13, pp. 14735–14750, May 2020.

[12] Wavecontrol SMP2 Electromagnetic field meter and spectrum analyzer [Online] Available: https://www.wavecontrol.com/rfsafety/images/data-sheets/en/SMP2_Datasheet_EN.pdf.

[13] Wavecontrol WPT Field probe for mobile frequency bands [Online] Available: https://www.wa

vecontrol.com/rfsafety/images/data-sheets/en/W
PT_Datasheet_EN.pdf.

[14] Narda Safety Test Solutions GmbH, SRM3006, Selective radiation meter, operating manual, Narda, 2012.

[15] Law of the Republic of Serbia, "Regulation on the limits of exposure to non-ionizing radiation," no. 104/09.

[16] D. Kljajic and N. Djuric, "The adaptive boundary approach for exposure assessment in a broadband EMF monitoring," *Measurement*, vol. 93, pp. 515–523, Nov. 2016.

Dragan R. Kljajić was born on April 29, 1987, in Novi Sad, the Republic of Serbia. He received a Ph.D. in Electrical and Computer Engineering, at Faculty of Technical Sciences in Novi Sad, at Department of Power, Electronic and Telecommunication Engineering. He works as an Associate Professor at the same Department. His scientific area is theoretical electrotechnics, while his research interests are in the field of theoretical electrical engineering, theoretical and applied electromagnetics and microelectronics. He is the author or co-author of more than 70 scientific papers, published in proceedings of international conferences and high impact factor journals. He is a member of IEEE society.

Nikola M. Djuric was born in Novi Sad, Serbia, in 1973. He received M.Sc. and Ph.D. degrees in Telecommunication and Signal Processing from the Faculty of Technical Sciences, University of Novi Sad, in 2003 and 2009, respectively. From 1997 to 2010 he was a Teaching Assistant; from 2010 to 2015 Assistant Professor; from 2015 to 2020 Associate Professor; while since 2020 he has been a Full Professor at FTN-UNS. He is the author or co-author of more than 100 journal and conference articles. His research interests include computational and applied electromagnetics, with environmental EMF measurement and monitoring for EMF compliance testing, estimation, and simulation of EMF whole-body exposure. He is a member of IEEE society.

Karolina K. Kasas-Lazetic was born in Novi Sad, Serbia, in 1964. She received her Ph.D. degree in Electrical and Computer Engineering from the Faculty of Technical Sciences, University of Novi Sad. She has been with the same institution since the beginning of her teaching and scientific carrier. Currently, she is an Associate Professor at the Department of Power, Electronic and Telecommunication Engineering. Her main research interests are in the field of theoretical and applied electromagnetics, electromagnetic field analysis and measurement, as well as electromagnetic compatibility. She is the author and co-author of more than 100 scientific papers in refereed journals and international conferences. She is a member of IEEE society.

Miodrag M. Milutinov was born on August 28, 1976, in Zrenjanin, the Republic of Serbia. He received a Ph.D. in Electrical and Computer Engineering, at Faculty of Technical Sciences in Novi Sad, in the Department of Power, Electronic and Telecommunication Engineering in 2017. He works as an Associate Professor in the same Department. His scientific area is theoretical electrotechnics, while his research interests are calculation and measurements of electric and magnetic fields, electromagnetic compatibility, and human exposure to electromagnetic fields. He is the author or co-author of more than 80 scientific papers. He is a member of IEEE society.

Snezana M. Djuric is a Research Associate Professor at the BioSense Institute, University of Novi Sad. She received the M.Sc. and Ph.D. degrees in Electrical and Computer Engineering from the Faculty of Technical Sciences, University of Novi Sad. Her research interest is focused on sensors, wearable electronics, computational and applied electromagnetics, energy harvesting and energy storage.

Analysis and Simulations of Electrothermal Characteristics of Water-based Ultrawideband Absorber Using HIE-FVM Hybrid Method

WenBin Yan, Yi Wang, and QunSheng Cao

College of Electronic and Information Engineering, Nanjing University of Aeronautics and Astronautics
Nanjing, 21000, China
yanwebin4721@163.com, jflsjfls@nuaa.edu.cn, qunsheng@nuaa.edu.cn

Abstract – In this study, the dispersion characteristics, impedance features, and absorption conditions of water-based electromagnetic (EM) absorbers are investigated. A methodology for the rapid construction of a three-layer water-based absorber structure is proposed. Concurrently, a weakly conditionally stable Hybrid Implicit-Explicit Finite Difference Time Domain (HIE-FDTD) method is introduced to enhance the computational efficiency of thin layer structures. Furthermore, the EM computation integrates thermal effect calculations. A hybrid approach, combining the HIE-FDTD and Finite Volume Method (FVM), is employed to analyze temperature variations induced by EM wave incidence on the absorber.

Index Terms – Electrothermal coupling computation, FVM, HIE-FDTD, Water-based absorber.

I. INTRODUCTION

Water-based absorbers are a unique type of absorptive structure that utilizes the inherent properties of water to attenuate EM waves. Because of their distinctive nature, these absorbers showcase significant potential in applications such as stealth technology and EM susceptibility (EMS) shielding. Their primary advantages include tunability [1], multi-band and broadband absorption capabilities [2, 3], and flexibility [4]. However, this structure also faces some challenges. For instance, the physical properties of water are easily affected by temperature changes, which can lead to performance inconsistencies. Ensuring stable performance under various environmental conditions, such as temperature fluctuations, humidity changes, and atmospheric pressure variations, remains the primary concern.

The Finite-Difference Time-Domain (FDTD) method [5, 6] is a widely adopted numerical technique used to solve EM problems, such as electromagnetic-thermal coupling and dispersive media calculations [7, 8]. The Hybrid Implicit-Explicit Finite Difference Time Domain (HIE-FDTD) approach augments the conventional FDTD methodology by using both implicit and explicit schemes [9–11]. Its hybrid nature introduces a conditionally weak stability, permitting a more extensive time step size compared to the traditional explicit FDTD method, thereby accelerating computational speed in simulations. This method exhibits computational advantages particularly when analyzing thin layered structures.

With the growing attention to electrothermal coupling issues, the traditional practice of conducting EM simulations and thermal simulations independently is being re-evaluated . As the complexity of the problems being addressed increases, and the demand for solution accuracy intensifies, joint electrothermal solutions are emerging as a trend. Thermal effects, leading to material alterations, subsequently influence the EM response, which in turn affects the temperature distribution , forming a multi-physics computational loop. It is applied in multiple fields, such as electromagnetic-thermal analysis of absorbing structures [12], thermal-electric losses in circuits [13], material phase change at microwave frequencies [14], and electromagnetic-thermal calculations in dispersive media [15].

This paper initially investigates the fundamental principles of water-based absorbers and presents a broadband absorption structure based on absorption criteria, computed using the HIE-FDTD method. Subsequently, the temperature distribution and its impact on EM wave absorption performances are elucidated through electrothermal coupling calculations.

II. THEORETICAL ANALYSIS
A. HIE method and heat transfer calculation

In this section, we introduce the HIE-FDTD method and the associated update formulas for the calculation of EM fields. Many articles have already provided detailed derivation steps and proofs [10, 11]. This paper presents a simplified derivation process to demonstrate the characteristics of the method. This method is distinguished by its manipulation of the update time steps for magnetic and electric fields, which leads to implicit updates for specific field components, while preserving explicit updates for one component. Herein, we adopt the

notation $P = (i, j, k), P(i) - 1$ means $(i - 1, j, k)$. Then, the update equations for the HIE can be derived:

$$\frac{E_z^{n+1}(P) - E_z^n(P)}{\Delta t} = \frac{1}{2\varepsilon_z(P)\Delta x} \left(H_y^{n+1}(P) + H_y^{n+1}\right)$$

$$(P(i) - 1) - H_y^n(P) - H_y^n(P(i) - 1))$$

$$- \frac{1}{\varepsilon_z(P)\Delta y} \left(H_x^{n+1/2}(P) - H_x^{n+1/2}\right) \quad (1)$$

$$(P(j) - 1)) + \frac{\sigma_z^e(P)}{2\varepsilon_z(P)} \left(E_z^{n+1}(P)\right.$$

$$+ E_z^n(P)) + \frac{1}{2} \left(J_{zp}^{n+1}(P) + J_{zp}^n(P)\right),$$

$$\frac{H_y^{n+1}(P) - H_y^n(P)}{\Delta t} = \frac{1}{2\mu_y(P)\Delta x} \left(E_z^{n+1}(P(i) + 1)\right.$$

$$+ E_z^n(P(i) + 1) - E_z^{n+1}(P) - E_z^n(P)) \quad (2)$$

$$- \frac{1}{\mu_y(P)\Delta z} \left(E_x^{n+1/2}(P(k) + 1) - E_x^{n+1/2}(P)\right),$$

where Δx, Δy, and Δz denote the spatial discretization steps along the x, y, and z directions, respectively. ε_z is permittivity in the z direction, μ_z and μ_y are permeability in the x and y directions. This method places the time steps for both E_x and H_x at the $n + \frac{1}{2}$ position, while the remaining components are positioned at the n time step. It results in a lack of uniformity in the time step values for the E_z and H_y components but this discrepancy can be addressed by taking the average with an implicit solving step, which requires simultaneous resolution at the $n + 1$ time step. By substituting Eq. (2) into (1), a tridiagonal matrix is derived, which can be solved using the TDMA method as equation (3) and (4). $\{E_z^n, E_x^{n+1/2}, H_x^n, J_{zp}\}$ are the sum of EM values of available present step:

$$- C_1(P)C_2(P(i) - 1)E_z^{n+1}(P(i) - 1)$$

$$+ [1 + C_2(P)(C_1(P) + C_1(P(i) - 1))]E_z^{n+1}(P) \quad (3)$$

$$- C_1(P)C_2(P)E_z^{n+1}(P(i) + 1) = \{E_z^n, E_x^{n+1/2}, H_x^n, J_{zp}^n\},$$

where:

$$C_1(P) = \frac{\Delta t}{2\mu_y(P)\Delta y}, \quad (4)$$

$$C_2(P) = \frac{\Delta t}{(2\varepsilon_z(P) + \Delta t \sigma_z^e(P))\Delta x}.$$

The advantages of this method include the relaxation of stability constraints. It is highly efficient when using finely detailed spatial grid divisions in specific directions, such as in the calculation of thin-layer structures. Additionally, this method requires fewer tridiagonal matrix solutions, leading to an improvement in overall efficiency.

$$c\Delta t \leq \frac{1}{\sqrt{\left(\frac{1}{\Delta y^2} + \frac{1}{\Delta z^2}\right)}}. \quad (5)$$

As depicted in equation (5), c is the speed of EM wave propagation in free space and, compared to the conventional FDTD method, the stability condition of HIE-FDTD eliminates the need to consider the spatial step in the x-direction, allowing for a larger time step selection. Furthermore, when solving EM computational problems, we also consider the thermal effects generated in the material when EM waves incident on the target. Then, the simulation problem of a single EM phenomenon becomes a multi-physics solving problem. The thermal conduction equation is given as follow [15]:

$$\alpha \rho c_H \frac{\partial T}{\partial t} = \alpha k \frac{\partial^2 T}{\partial x^2} + \alpha k \frac{\partial^2 T}{\partial y^2} + \alpha k \frac{\partial^2 T}{\partial z^2} + \alpha S, \quad (6)$$

where, c_H represents specific heat capacity, ρ stands for density, k denotes thermal conductivity, S signifies an additional heat source, and α represents an acceleration factor. The acceleration factor increases the thermal property parameters, speeding up the heat conduction process and causing more temperature changes in shorter time steps. This method aims to correlate significantly different electromagnetic simulation times with thermal simulation times, enabling simultaneous computational programming. In the absence of acceleration factors, the Finite Volume Method (FVM) form of equation (6) is:

$$M_p T^{n+1}(P) = M_l T^{n+1}(P(i) - 1) + M_r T^{n+1}(P(i) + 1)$$

$$+ M_u T^{n+1}(P(j) - 1) + M_d T^{n+1}(P(j) + 1)$$

$$+ M_b T^{n+1}(P(k) - 1) + M_f T^{n+1}(P(k) + 1)$$

$$+ M_{p0} T^n(P) + S\Delta x \Delta y \Delta z$$

$$M_l = M_r = \frac{k\Delta y\Delta z}{\Delta x}, M_u = M_d = \frac{k\Delta x\Delta z}{\Delta y} \quad (7)$$

$$M_u = M_d = \frac{k\Delta x\Delta z}{\Delta y}, M_{p0} = \frac{\rho c_H \Delta x\Delta y\Delta z}{\Delta t}$$

$$M_p = M_l + M_r + M_u + M_d + M_b + M_f + M_{p0}.$$

Equation (7) presents the expression for the FVM method post-discretization. As observed from equation (7), the differential form of the FVM method bears a strong resemblance to the FDTD method, suggesting the feasibility of employing a unified grid partitioning scheme for analysis. An important aspect of integrating EM and thermal processes is to treat the resulting EM losses as new heat sources [16]. The EM field energy can be obtained through Poynting theorem as follows:

$$\frac{1}{2}\frac{\partial}{\partial t}(\mathbf{E} \cdot \mathbf{D} + \mathbf{H} \cdot \mathbf{B}) + \nabla \cdot (\mathbf{E} \times \mathbf{H}) = -\mathbf{E} \cdot \mathbf{J}$$

$$- \left(\frac{1}{2}\mathbf{E} \cdot \frac{\partial \mathbf{D}}{\partial t} - \frac{1}{2}\mathbf{D} \cdot \frac{\partial \mathbf{E}}{\partial t}\right) - \left(\frac{1}{2}\mathbf{H} \cdot \frac{\partial \mathbf{B}}{\partial t} - \frac{1}{2}\mathbf{B} \cdot \frac{\partial \mathbf{H}}{\partial t}\right),$$

$$(8a)$$

$$\mathbf{E} \cdot \mathbf{J_p} = \mathbf{E} \cdot \varepsilon_0 \Delta\varepsilon \frac{\partial \mathbf{E}}{\partial t} - \mathbf{E} \cdot \tau_0 \frac{\partial \mathbf{J_p}}{\partial t} \qquad (8b)$$

$$\frac{1}{2}\frac{\partial}{\partial t}\left(\varepsilon_0\varepsilon_S E^2 - 2\tau_0 \mathbf{E}\cdot\mathbf{J_p} + \frac{\tau_0^2}{\varepsilon_0\Delta\varepsilon}J_p^2 + \mathbf{H}\cdot\mathbf{B}\right), \qquad (8c)$$

$$+\nabla\cdot(\mathbf{E}\times\mathbf{H}) = -\mathbf{E}\cdot\mathbf{J} - \frac{\tau_0}{\varepsilon_0\Delta\varepsilon}J_p^2$$

$$S = P_{\text{loss}} = \mathbf{E}\cdot\mathbf{J} + \frac{\tau_0}{\varepsilon_0\Delta\varepsilon}J_p^2.$$

From equation (8), it is noted that the energy loss in the EM field is given by $\mathbf{E}\cdot\mathbf{J}$. In addition, based on the characteristics of Debye dielectric, its energy loss can be derived [16]. The sum of these two losses constitutes the heat source term in equation (8c), thereby conducting EM thermal multi-physics computations.

B. Absorption rate computation of water-based absorber

For reflective EM absorbers, the absorption function can be studied by investigating whether the impedance generated by the combination of multi-layer materials or structures meets the absorption criteria. The same research approach can also be applied to the study of water-based absorbers. Figure 1 is shown the schematic diagram of the absorber structure, l_1, l_2, and l_3 are the thickness of three media layers. Here, l_1 and l_3 are conventional dielectric materials, and l_2 is the water layer. Z_1, Z_2, and Z_3 are the corresponding impedance values. According to the transmission line theory, the input impedance Z_{in} of each layer can be calculated using the following formulas:

$$Z_{in1} = Z_1 \tanh\left[(\alpha_1 + j\beta_1)\ell_1\right]$$

$$Z_{in2} = Z_2 \frac{Z_{in1} + Z_2\tanh\left[(\alpha_2+j\beta_2)\ell_2\right]}{Z_2 + Z_{in1}\tanh\left[(\alpha_2+j\beta_2)\ell_2\right]} \qquad (9)$$

$$Z_{in3} = Z_3 \frac{Z_{in2} + Z_2\tanh\left[(\alpha_3+j\beta_3)\ell_3\right]}{Z_2 + Z_{in2}\tanh\left[(\alpha_3+j\beta_3)\ell_3\right]}.$$

Water is a typical dispersive medium that conforms to the Debye model. When water is used in absorbers($Z_2 = Z_{water}$), the initial step is to study its impedance characteristics. Based on the equation (9), it can be observed that the key equation governing the characteristics of water is significant. Therefore, it is singled out as Z_{tmp} for further study.

$$Z_{tmp} = Z_{\text{water}} \tanh\left[(\alpha_w + j\beta_w)\ell_2\right]$$

$$= Z_{\text{water}} \frac{\tanh(\alpha_w\ell_2) + j\tan(\beta_w\ell_2)}{1 + j\tan(\beta_w\ell_2)\tanh(\alpha_w\ell_2)} \qquad (10)$$

$$Z_{\text{water}} \frac{(\tanh(\alpha_w\ell_2)\to 1) + j\tan(\beta_w\ell_2)}{1 + j\tan(\beta_w\ell_2)(\tanh(\alpha_w\ell_2)\to 1)} \approx Z_{\text{water}}. \qquad (11)$$

The α_w is the attenuation factor, β_w is the propagation factor, l_2 is the thickness and Z_{water} is the impedance of water. It can be observed that when the water layer is sufficiently thick, the impedance of
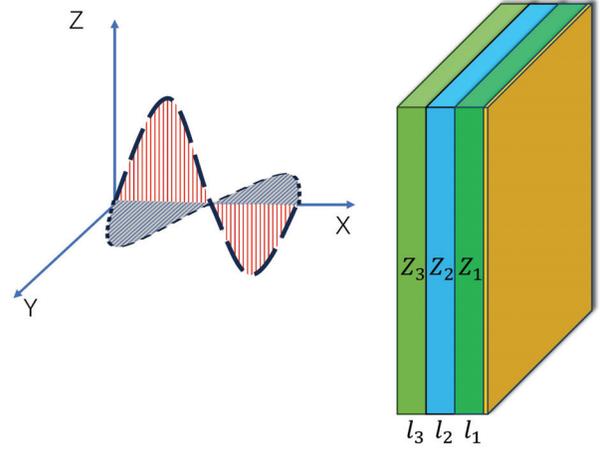
Fig. 1. Schematic diagram of the absorber structure.

water for high-frequency EM waves remains constant, as described in equation (11) and Fig. 2 (a). This occurs because losses in water impede the propagation of high-
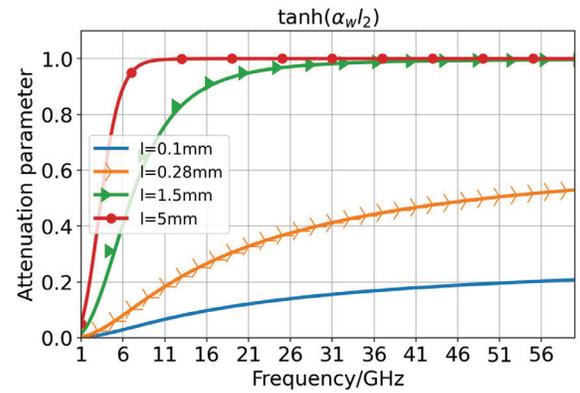
(a)
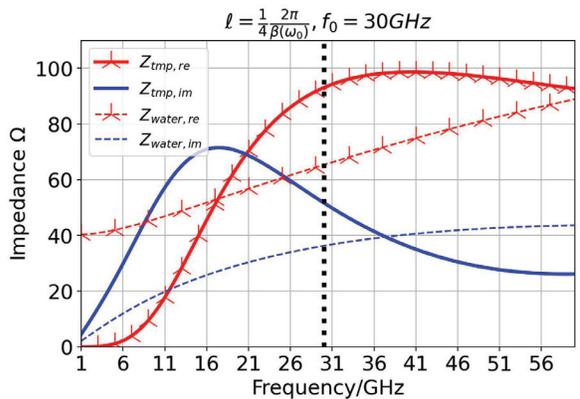
(b)

Fig. 2. Curves of transmission characteristics of water layer varied as a function of frequency: (a) variations in attenuation factors and (b) changes in impedances.

frequency EM waves, a phenomenon known as the skin effect.

Secondly, due to the dispersive nature of water, its impedance characteristics are different from those of ordinary dielectrics. The resonance characteristics of ordinary dielectrics can be easily adjusted by varying the thickness to change the resonance points. However, it is unrealistic to arbitrarily change the thickness of water in an absorber. As illustrated in Fig. 2 (b), despite the thickness corresponding to a quarter wavelength at 30 GHz, it does not reach its maximum value at this frequency. Considering a three layers absorber structure, the impedance expression for this structure is given as follows:

$$Z_A = Z_{F4B} \frac{2Z_c Z_{l1} + \left(Z_c^2 + Z_{l1}^2\right) Z_{lw}}{Z_c \left(1 + Z_{l1}^2\right) + \left(1 + Z_c^2\right) Z_{lw}} \quad (12)$$

$$Z_c = Z_{\text{water}}/Z_{F4B}$$
$$Z_{l1} = \tanh\left[(\alpha_1 + j\beta_1)\ell_1\right]$$
$$Z_{lw} = \tanh\left[(\alpha_w + j\beta_w)\ell_w\right],$$

where, l_w stands for the thickness of the water layer in the middle layer. As shown in Fig. 1, a water-based absorber is a sandwich structure with a water layer placed between two layers having equal thickness of F4B materials. Extensive research has been conducted on the resonance characteristics of conventional materials, primarily controlling the resonant maxima and minima by adjusting the thickness to $\lambda/2$ and $\lambda/4$.

$$\tanh\left[(\alpha_1 + j\beta_1)\ell_1\right] = \frac{\tanh\alpha_1\ell_1 + j\tan\beta_1\ell_1}{1 + j\tan\beta_1\ell_1\tanh\alpha_1\ell_1}$$
$$\approx \begin{cases} \alpha_1\ell_1, \ell_1 = \frac{1}{2}\frac{2\pi}{\beta_1} \\ \frac{1}{\alpha_1\ell_1}, \ell_1 = \frac{1}{4}\frac{2\pi}{\beta_1} \end{cases}, \quad (13)$$

$$Z_A = \begin{cases} Z_{F4B}\frac{2Z_c\alpha_1\ell_1 + \left(Z_c^2 + (\alpha_1\ell_1)^2\right)Z_{lw}}{Z_c\left(1 + (\alpha_1\ell_1)^2\right) + \left(1 + Z_c^2\right)\alpha_1\ell_1 Z_{lw}}, \ell_1 = \frac{1}{2}\frac{2\pi}{\beta_1} \\ Z_{F4B}\frac{2Z_c\alpha_1\ell_1 + \left(Z_c^2(\alpha_1\ell_1)^2 + 1\right)Z_{lw}}{Z_c\left(1 + (\alpha_1\ell_1)^2\right) + \left(1 + Z_c^2\right)\alpha_1\ell_1 Z_{lw}}, \ell_1 = \frac{1}{4}\frac{2\pi}{\beta_1} \end{cases}. \quad (14)$$

It can be easily observed that the value of α_1 is significantly smaller than the real or imaginary parts of Z_c, approaching zero. Therefore, this equation can be approximated as:

$$Z_A = \begin{cases} Z_{\text{water}} Z_{lw}, \ell_1 = \frac{1}{2}\frac{2\pi}{\beta_1} \\ \frac{Z_{F4B}^2}{Z_{\text{water}}} Z_{lw}, \ell_1 = \frac{1}{4}\frac{2\pi}{\beta_1} \end{cases}. \quad (15)$$

Equation (15) illustrates that when $l_1 = \lambda/2$, the impedance of the sandwich structure absorber is only related to the impedance of water. When $l_1 = \lambda/4$, the impedance is determined by the impedance of F4B and water. In both cases, the impedance of the absorber at the corresponding frequency point is directly controlled by the thickness of the water layer. Therefore, subsequent research only needs to consider the thickness variation of the water layer.

In the case of absorbers with metal backplanes, achieving a perfect absorption condition with a reflection coefficient of zero is often challenging in practical applications. Therefore, in the simulations and measurement of absorbers, it is usually specified the absorption rate should exceed -10 dB, corresponding to a reflection coefficient less than 0.316.

$$\Gamma = \left|\frac{Z_{\text{in}} - Z_0}{Z_{\text{in}} + Z_0}\right| = \left|\frac{R + jX - Z_0}{R + jX + Z_0}\right| \leq 0.316$$
$$Z_0 = 120\pi \quad (16)$$
$$(R - 460.643)^2 + X^2 \leq 264.695^2.$$

Equation (16) demonstrates that the absorption condition fundamentally entails the real and imaginary parts of impedance satisfying the equation of a circle. When R and X fall within the impedance circle, Z_{in} will meet the specified absorption requirements. Furthermore, the conditions of R and X can be extended to other frequencies. As long as the values of R and X at a specific frequency point satisfy this condition, absorption can be achieved at that frequency point. Figure 3 illustrates a schematic diagram of the absorption condition circle based on equation (16). For the sake of research convenience, the absorption circle in Fig. 3 is projected onto the R and X axes, and the frequency range is expanded to cover a broader spectrum.
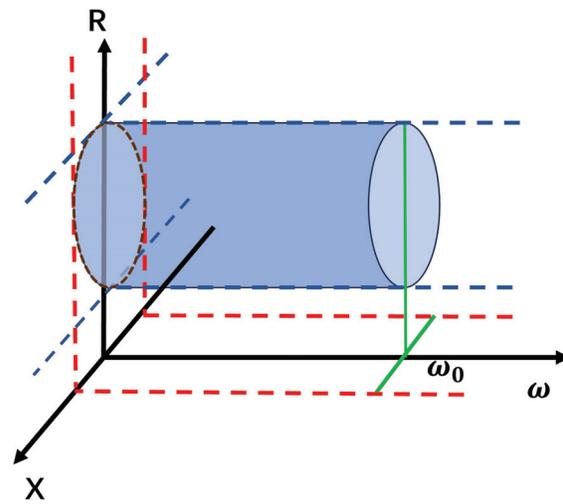
Fig. 3. Schematic diagram of the absorption condition circle.

Based on the above discussion, the following steps can be taken to design an absorber with a frequency up to 42 GHz. Firstly, the value of l_1 given in equaion (15) can be rapidly determined. Furthermore, the properties of water dictate that the thickness l_w of the water layer in the sandwich structure should not exceed 1.5 mm,

effectively constraining the range of l_w values. Subsequently, it becomes very convenient to assess absorption by calculating the impedance values at a single point and substituting it into the absorption condition circles. As shown in Fig. 4, the impedance real part $R_{(max,l1)}$ exceeds the range of absorption condition at 42 GHz, so the absorber will not absorb at this frequency. It is found that the absorption condition is only met between 11 and 15 GHz, indicating that water-based absorber only exhibits absorption within this range. Note that between frequencies 27 to 31 GHz, it appears to meet the absorption conditions because the blue and red areas are used as direct projections of the circles. However, in positions near the boundaries of these two regions, the absorption conditions are not actually satisfied. Figure 4 (b) depicts the relevant absorption rate, which is quite consistent with the conclusions, with only a narrow absorption band.

Using this approach, it is easy to design an absorber that meets the absorption bandwidth of 42 GHz in a 20°C environment. Additionally, it can be reasonably inferred that the impedance of the three-layer water-based absorber is continuous. Therefore, as shown in

(a)

(b)
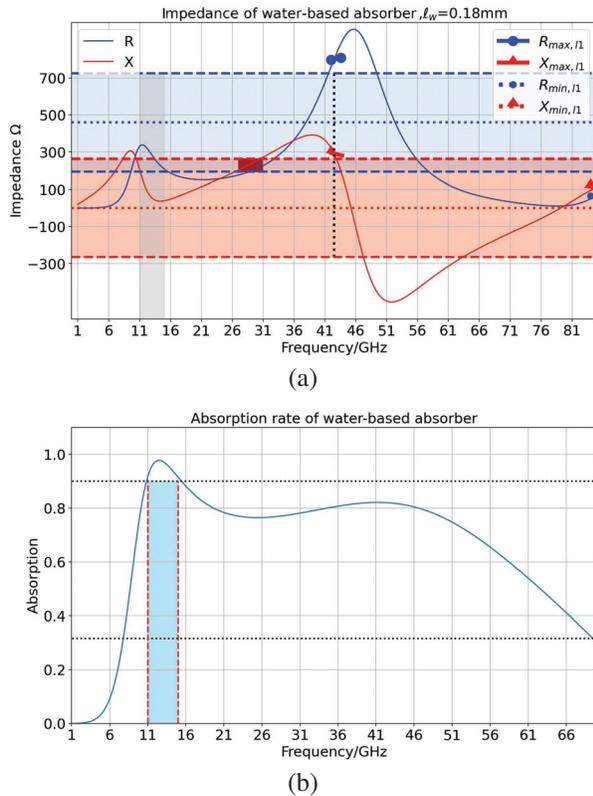
Fig. 4. Absorption characteristic of a water-based absorber varied with frequency: (a) impedance values of absorber and (b) absorption rate with narrow bandwidth.

Fig. 5, by adjusting the thickness of the water layer, it is possible to make the impedance conditions around 42 GHz also satisfy the absorption criteria, thus achieving broadband absorption effectiveness. Calculations performed using HIE, FDTD, and other methods show a high degree of consistency between the absorption rate and analytical values.

(a)

(b)
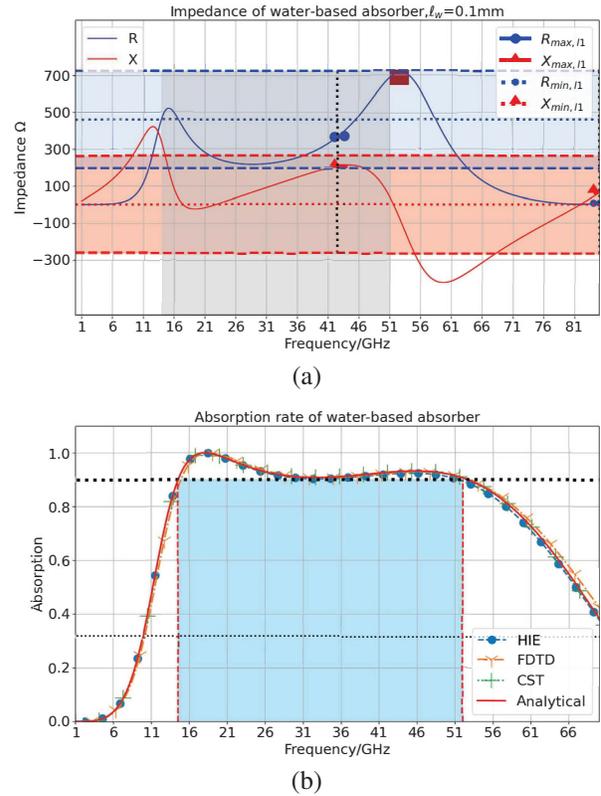
Fig. 5. Wideband water-based absorber: (a) impedance values of absorber and (b) wideband absorption rate.

On a computer equipped with an AMD Ryzen 3900X CPU and 32 GB of RAM, a complete FDTD method example takes 144.2 seconds, while HIE-FDTD only consumes 77.3 seconds. This demonstrates that the introduction of the HIE method can significantly accelerate computational speed, thereby saving computational resources.

III. ELECTROTHERMAL COUPLING RESULTS AND DISCUSSION

In the discussions above, it is assumed that an ambient temperature is 20°C. In reality, the process that generates absorptive effects inevitably involves energy conversion, espectically the conversion between EM energy and thermal energy. Temperature variations caused by thermal energy play a crucial role in certain materials that exhibit temperature-dependent properties.

Therefore, research on the EM-thermal coupling of absorbers holds practical significance.

A. The impact of temperature on water

The properties of water are temperature-dependent and the effect of temperature on water is as follows [4]:

$$\varepsilon(\omega) = \varepsilon_\infty(T) + \frac{\varepsilon_s(T) - \varepsilon_\infty(T)}{1 + i\omega\tau(T)}, \quad (17)$$

$$\varepsilon_s(T) = a_1 - b_1 T + c_1 T^2 - d_1 T^3,$$

$$\varepsilon_\infty(T) = \varepsilon_s(T) - a_2 exp(-b_2 T),$$

$$\tau(T) = c_2 exp(T_2/(T + T_1)),$$

where, $a_1 = 87.9$, $b_1 = 0.404 K^{-1}$, $c_1 = 9.59 \times 10^{-4} K^{-2}$, $d_1 = 1.33 \times 10^{-6} K^{-3}$, $a_2 = 80.7$, $b_2 = 4.42 \times 10^{-3} K^{-1}$, and $a_2 = 80.7$, $b_2 = 4.42 \times 10^{-3} K^{-1}$. T is temperature in °C. According to equation (17), as the temperature varies, the changes in water are primarily reflected in the permittivity. Building upon this, the variations in water impedance characteristics with temperature are provided.

As observed from Fig. 6, an increase in water temperature leads to a decrease in the real and imaginary parts of water impedance within the range up to 80 GHz.
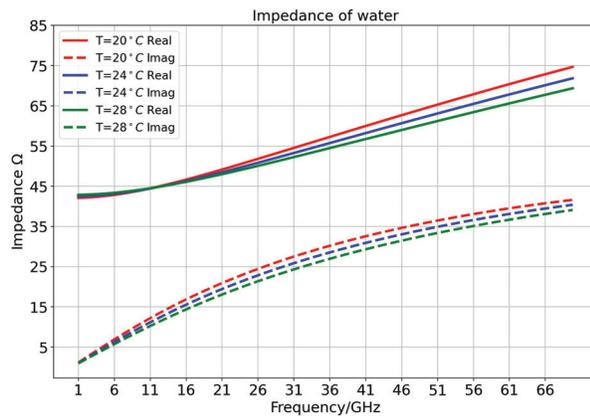
Fig. 6. Impedance variation of water with temperature.

B. The impact of temperature on absorber

The fundamental approach in designing typical absorbers is to utilize resonance points where energy is directly deposited into resistive components or structures, leading to the dissipation of EM energy and the generation of heat. This process of energy conversion is equally applicable to water-based absorber.

As temperature increases, material properties also change, as discussed in Section 3.1. This alteration can affect the absorption performance, and the changes in absorption performance, in turn, influence temperature variations. This electrical-thermal coupling process is rather complex.

Based on equations (3) and (7), let us combine of the HIE-FDTD and FVM methods to provide the temperature variation and absorption performance changes of water-based absorbers under higher radiation power (10 kV).

The computation process is as follows: first, use the HIE method to obtain the electric field and polarization current distribution, then calculate the heat source. Based on this heat source, the temperature distribution can be calculated, and then the electrical properties of the absorber material can be updated using the new temperature distribution.

As seen from Fig. 7 (a), it is evident that in an ambient temperature of 20°C, the water layer is the region with the fastest temperature rise during the EM wave radiation process. This is consistent with the energy conversion principle in absorbers, indicating that the EM energy in water-based absorbers is primarily dissipated within the water layer. To facilitate the observation of temperature changes with time, two points in the Fig. 7 (a) serve as temperature observation points at different positions, and an additional observation point is set in the middle of the water layer.

(a)

(b)

(c)
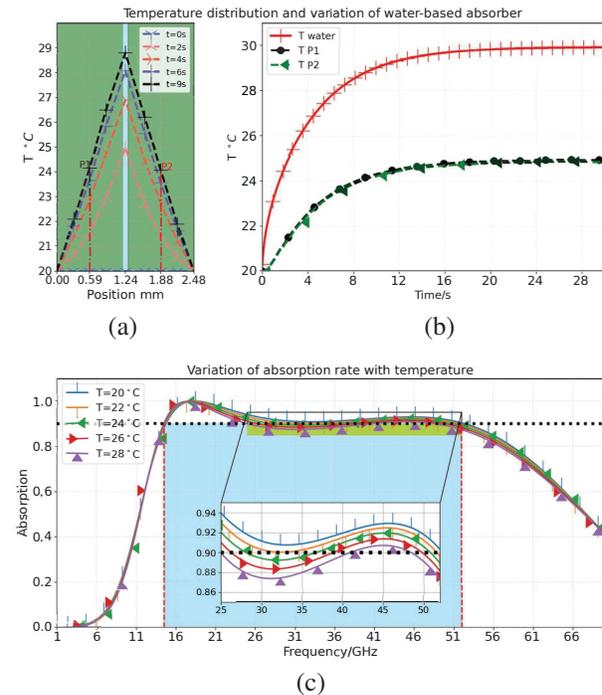
Fig. 7. Absorption rate and temperature variations of broadband water-based absorber: (a) temperature distribution with position, (b) temperature variations with time, and (c) variations in absorption rate with temperature.

Figure 7 (b) illustrates that continuous radiation of EM waves causes the temperature of the water layer in

the absorber structure to be higher than that of the F4B layer of the medium, and the temperature rises faster. When the water temperature rises to 29 °C, the overall temperature of the absorber reaches a steady state, indicating that the structure reaches thermal equilibrium at ambient temperature environment.

Figure 7 (c) depicts the variation in absorption rate of the EM-thermal processes. It can be observed that compared to an ambient temperature of 20°C, the absorption rate deteriorates with an increase of temperature. Particularly, when it approaches steady state, the absorption rate in the frequency range of 25 to 40 GHz no longer meets the requirement of greater than 0.9.

In addition, the conclusions can be obtained from the perspective of impedance from equation (15) and Figs. 5 (a) and 6. As the temperature rises, the impedance of water decreases, causing an increase in the maximum value in equation (15). Figure 5 (a) shows that the maximum value of the imaginary part is already close to the edge of the absorption condition. With further increase, it can be foreseen that the absorption condition will no longer be met.

IV. CONCLUSION

In this study, we introduced the HIE-FDTD method for EM simulations, which offers advantages in terms of computational efficiency. We also considered the impact of temperature on water and absorbers, shedding light on the EM-thermal coupling process. Through our analysis, absorber performance is affected by temperature, with higher temperatures leading to decreased absorption rates. This complex interplay between EM properties and temperature variations underscores the need for careful consideration in absorber design. Our research also demonstrated the feasibility of obtaining water-based absorbers that meet absorption criteria at specific frequencies, with practical implications for applications requiring broadband absorption. By adjusting the thickness of water layer, we can achieve effective broadband absorption. The HIE method has improved computational efficiency, making it a useful tool for future research and design efforts.

REFERENCES

[1] Y. Zhang, H. Dong, N. Mou, H. Li, X. Yao, and L. Zhang, "Tunable and transparent broadband metamaterial absorber with water-based substrate for optical window applications," *Nanoscale*, vol. 13, no. 16, pp. 7831–7837, 2021.

[2] H. Xiong and F. Yang, "Ultra-broadband and tunable saline water-based absorber in microwave regime," *Optics Express*, vol. 28, no. 4, pp. 5306–5316, 2020.

[3] Z. Wu, X. Chen, Z. Zhang, L. Heng, S. Wang, and Y. Zou, "Design and optimization of a flexible water-based microwave absorbing metamaterial," *Applied Physics Express*, vol. 12, no. 5, p. 057003, 2019.

[4] W. Zhu, I. D. Rukhlenko, F. Xiao, C. He, J. Geng, X. Liang, M. Premaratne, and R. Jin, "Multiband coherent perfect absorption in a water-based metasurface," *Optics Express*, vol. 25, no. 14, pp. 15737–15745, 2017.

[5] A. Taflove and S. C. Hagness, *Computational Electrodynamics: The Finite-Difference Time-Domain Method,* 3rd ed. London: Artech House, 2005.

[6] A. Z. Elsherbeni and V. Demir, *The Finite-Difference Time-Domain Method for Electromagnetics with MATLAB Simulations,* 2nd ed. Raleigh, NC, 2015.

[7] N. J. Ryan, B. Chambers, and D. Stone, "FDTD modeling of heatsink RF characteristics for EMC mitigation," *IEEE Transactions on Electromagnetic Compatibility*, vol. 44, no. 3, pp. 458–465, 2002.

[8] M. A. Alsunaidi and A. A. Al-Jabr, "A general ADE-FDTD algorithm for the simulation of dispersive structures," *IEEE Photonics Technology Letters*, vol. 21, no. 12, pp. 817–819, 2009.

[9] J. Chen and J. Wang, "A three-dimensional semi-implicit FDTD scheme for calculation of shielding effectiveness of enclosure with thin slots," *IEEE Transactions on Electromagnetic Compatibility*, vol. 49, no. 2, pp. 354–360, 2007.

[10] J. Wang, B. Zhou, L. Shi, C. Gao, and B. Chen, "A novel 3-D HIE-FDTD method with one-step leapfrog scheme," *IEEE Transactions on Microwave Theory and Techniques*, vol. 62, no. 6, pp. 1275–1283, 2014.

[11] K. Niu, Z. Huang, X. Ren, M. Li, B. Wu, and X. Wu, "An optimized 3-D HIE-FDTD method with reduced numerical dispersion," *IEEE Transactions on Antennas and Propagation*, vol. 66, pp. 6435–6440, Nov. 2018.

[12] W. Yan, Q. Cao, and Y. Wang, "Analysis of electromagnetic/thermal coupling of debye media using HIE-FDTD method," *Journal of Electromagnetic Waves and Applications*, vol. 37, no. 10-12, pp. 939–949, 2023.

[13] S. Wunsche, C. Clauß, P. Schwarz, and F. Winkler, "Electro-thermal circuit simulation using simulator coupling," *IEEE Transactions on Very Large Scale Integration (VLSI) Systems*, vol. 5, no. 3, pp. 277–282, 1997.

[14] S. Watanabe, M. Karakawa, and O. Hashimoto, "Computer simulation of temperature distribution of frozen material heated in a microwave oven," *IEEE Transactions on Microwave Theory and Techniques*, vol. 58, no. 5, pp. 1196–1204, 2010.

[15] F. Torres and B. Jecko, "Complete FDTD analysis of microwave heating processes in frequency-dependent and temperature-dependent media," *IEEE Transactions on Microwave Theory and Techniques*, vol. 45, no. 1, pp. 108–117, 1997.

[16] K.-M. Huang and Y.-H. Liao, "Transient power loss density of electromagnetic pulse in debye media," *IEEE Transactions on Microwave Theory and Techniques*, vol. 63, no. 1, pp. 135–140, 2014.

Yi Wang Associate professor, the School of Electronic and Information Engineering at Nanjing University of Aeronautics and Astronautics, specializes in computational electromagnetics, frequency-selective surface design, and the development of metamaterials.

WenBin Yan Ph.D. student, the School of Electronic and Information Engineering at Nanjing University of Aeronautics and Astronautics, focuses on computational electromagnetics and the Finite-Difference Time-Domain (FDTD) method.

QunSheng Cao Professor, the School of Electronic and Information Engineering at Nanjing University of Aeronautics and Astronautics, specializes in computational electromagnetics, the Multi-Resolution Time-Domain (MRTD) method, high-speed signal integrity, electromagnetic stealth metamaterials, and the design of antenna radomes.

Improving Kriging Surrogate Model for EMC Uncertainty Analysis Using LSSVR

Shenghang Huo[1], Yujia Song[2], Qing Liu[1], and Jinjun Bai[1]

[1]College of Marine Electrical Engineering
Dalian Maritime University, Dalian 116026, China
hg1120231340@dlmu.edu.cn, liuqing@dlmu.edu.cn, baijinjun@dlmu.edu.cn

[2]School of Electrical Engineering
Dalian University of Technology, Dalian 116000, China
songyujia@dlut.edu.cn

Abstract – As the in-depth study of uncertainty analysis in electromagnetic compatibility (EMC) progresses, the surrogate model-based uncertainty analysis method has increasingly become a popular research topic. The Kriging model is one of the classical surrogate models and plays an important role in EMC uncertainty analysis. However, an in-depth study of the Kriging sampling strategy is missing in the existing research on uncertainty analysis. The traditional sampling strategy employs Latin hypercube sampling (LHS) to select all sampling points at once, which makes the computational efficiency and accuracy of the surrogate model uncontrollable. This paper proposes a strategy that applies least squares support vector machine regression (LSSVR) to assist Kriging in sampling, significantly improving the efficiency and accuracy of the Kriging surrogate model.

Index Terms – Electromagnetic compatibility (EMC), Kriging, least squares support vector machine regression (LSSVR), surrogate model, uncertainty analysis method.

I. INTRODUCTION

In recent years, uncertainty analysis has emerged as a popular research topic in electromagnetic compatibility (EMC). By treating the input parameters in numerical simulations as uncertain parameters (e.g. random variables), the reliability and practicality of EMC simulation models can be significantly enhanced. Typically, uncertainty in simulation inputs arises from various factors, including geometric positional uncertainty due to motion or vibration, dimensional uncertainty due to manufacturing tolerances, and cognitive uncertainty due to researcher cognitive deficiencies.

The Monte Carlo method (MCM) is widely recognized as the most accurate method for uncertainty analysis [1]. It describes the randomness of the simulation inputs by exhaustively enumerating the sampling points. Because MCM considers all possible scenarios, it aligns well with the researcher's understanding of uncertainty. Therefore, MCM is suitable for use as a standard in theoretical studies to validate the accuracy of other uncertainty analysis methods. While MCM offers the advantages of high computational accuracy and ease of implementation, its poor convergence leads to significantly low computational efficiency, rendering it less competitive in practical engineering applications [2].

In 2013, a research team at Politecnico di Torino in Italy introduced the generalized polynomial chaos (GPC) theory to EMC simulation and proposed the stochastic Galerkin method (SGM) [3]. Another numerical analysis method based on GPC theory is the stochastic collocation method (SCM) [4]. Both methods are computationally accurate and efficient. SGM is an embedded uncertainty analysis method, while SCM is a non-embedded uncertainty analysis method. With the continuous adoption of various new finite element simulation techniques in computer science, EMC design increasingly relies on commercial electromagnetic simulation software. This trend has made non-embedded simulation modes a primary focus of uncertainty analysis research in the EMC field. Consequently, the applicability of SCM exceeds that of SGM. However, SCM suffers from the serious problem of the dimensional curse of dimensionality [5] and is not applicable when dealing with a large number of random variables. The Method of Moments (MoM) [6] and the Stochastic Reduced Order Models (SROM) [7] are superior non-embedded uncertainty analysis methods for addressing the dimensional curse of dimensionality problem. However, MoM and SROM are suitable for EMC simulation solvers with good linearity. When the solver exhibits high nonlinearity, the complexity of uncertainty analysis results increases significantly, posing a risk of failure for both MoM and SROM.

Since 2020, uncertainty analysis methods based on surrogate models have been gradually proposed [8]. The principle is to treat the surrogate model as a black box and train it using deterministic simulation results repeatedly. Subsequently, a large number of samples of input randomness are taken to obtain the final results. Uncertainty analysis methods based on surrogate models can be considered as highly effective non-embedded uncertainty analysis methods. Among these, the Kriging model is a typical surrogate model used for uncertainty analysis [9,10]. It is suitable for solvers with high non-linearity and does not encounter the issue of the dimensional curse of dimensionality. The traditional Kriging model employs a static Latin hypercube sampling (LHS) to select sampling points all at once [11], lacking the ability to actively adjust the sampling points according to specific characteristics of different situations. To enhance the accuracy and computational efficiency of the Kriging model in EMC simulation uncertainty analysis, this paper proposes an active sampling strategy that uses least squares support vector machine regression (LSSVR) to assist Kriging sampling.

The structure of this paper is as follows. Two traditional methods of uncertainty analysis, MCM and Kriging, are presented in section II. In section III, LSSVR is introduced and applied to improve the Kriging model. The improved uncertainty analysis method is applied to the parallel cable crosstalk example in section IV. Section V summarizes this paper.

II. TRADITIONAL METHODS OF UNCERTAINTY ANALYSIS

In uncertainty analysis, the random variable model is typically used to describe the uncertainty of random events:

$$\zeta = \left\{ \zeta_1, \zeta_2, ..., \zeta_j, ..., \zeta_N \right\}, \qquad (1)$$

where ζ_j is a random variable, ζ is a vector of random variables, and N is the number of random variables.

A. Monte Carlo method

MCM is grounded in the weak law of large numbers, which uses exhaustive sampling points $S_1 = [X_1, X_2, \cdots, X_n]$ to characterize a random variable ζ, encompassing all possible cases. Where the number of sampling points is assumed to be n, and each sampling point X_i consists of an N-dimensional vector:

$$X_i = \{X_i(1), X_i(2), ..., X_i(j), ..., X_i(N)\}, \qquad (2)$$

where $X_i(j)$ are all determined constant values that correspond to ζ_j in equation (1).

Deterministic EMC simulation is performed at each sampling point X_i:

$$Y_i = \text{EMC}[X_i], \qquad (3)$$

where EMC [ ] represents the single deterministic EMC simulation process and Y_i is the EMC simulation result.

$Y = [Y_1, Y_2, \cdots, Y_n]$ is the set of EMC simulation results, i.e., MCM-based simulation results.

The simulation results are analyzed statistically to derive uncertainty analysis results such as expectation, standard deviation, worst-case estimates, and probability density curves. Algorithm 1 shows the process of writing the code for the uncertainty analysis method based on MCM. The uncertainty analysis results of MCM are used as a reference standard in this paper.

Algorithm 1 MCM
1:   Exhaustive sampling points S_1 (n)
2:   for (do i=1:n)
3:   EMC simulation $Y_i = \text{EMC}[X_i]$
4:   end for
5:   EMC simulation result set $Y = [Y_1, Y_2, \cdots, Y_n]$
6:   Results of uncertainty analysis

B. Traditional Kriging model

Surrogate models significantly enhance the computational efficiency of EMC uncertainty analysis. Among these methods, the Kriging model, originating from geostatistics, is a prominent example. This section outlines the traditional Kriging-based uncertainty analysis method.

The traditional Kriging model uses LHS to select all sampling points $S_2 = [x_1, x_2, \cdots, x_L]$ simultaneously, with the number of sampling points denoted as L, which is significantly smaller than n. x_i is also an N-dimensional constant value vector data. Deterministic EMC simulations are performed at each sampling point x_i:

$$y_i = \text{EMC}[x_i]. \qquad (4)$$

The training set $\{x_i, y_i\}_{i=1}^{L}$ is obtained, which is used to train the surrogate model. The Kriging model is an interpolation model that computes the interpolation result as a linear combination of the known sample response values:

$$M_{Kriging} = \sum_{i=1}^{L} w_i y_i, \qquad (5)$$

where $w = [w_1, w_2 \cdots w_L]^T$ represents the weighting coefficient, and the response value at any point in the design space can be obtained by specifying the value of the weighting coefficient w. The detailed procedure for computing the weighting factor w is provided in [12]. The process of writing the code for the uncertainty analysis method based on traditional Kriging is shown in Algorithm 2.

Algorithm 2 Traditional Kriging

1:	Exhaustive sampling points S_1 (n)
2:	Sampling points S_2 (L) in LHS screening S_1
3:	for (do i=1:L)
4:	EMC simulation $y_i = $ EMC $[x_i]$
5:	end for
6:	Training set $\{x_i, y_i\}_{i=1}^{L}$
7:	Construction of $M_{Kriging}$
8:	Bring S_1 into $M_{Kriging}$
9:	Results of uncertainty analysis

The Kriging-based uncertainty analysis method requires only deterministic EMC simulation for L samples, which is obviously much more computationally efficient than MCM.

The sampling strategy of the traditional Kriging model is to select sample points at one time by using LHS, which aims to make the sample points evenly distributed and cover the whole sampling space. However, it uses random sampling for sampling, which is a passive sampling method. It lacks the initiative to accurately select sample points that make the surrogate model more accurate. It also wastes a lot of computational resources when a single simulation takes a long time.

III. IMPROVED KRIGING BASED ON LSSVR

LSSVR is a widely used surrogate model in EMC uncertainty analysis, offering fast training speed, good generalization performance, and a strong ability to fit nonlinear functions [13]. This section presents the application of LSSVR to assist Kriging in selecting sampling points, introducing a highly proactive sequential sampling strategy that significantly enhances the accuracy and efficiency of the Kriging-based uncertainty analysis method. This combined approach is referred to as Kriging-LSSVR.

Figure 1 illustrates the structure of LSSVR, which maps the input space to a high-dimensional feature space through a nonlinear mapping $\phi(\bullet)$. The optimal linear function is then identified in this feature space.
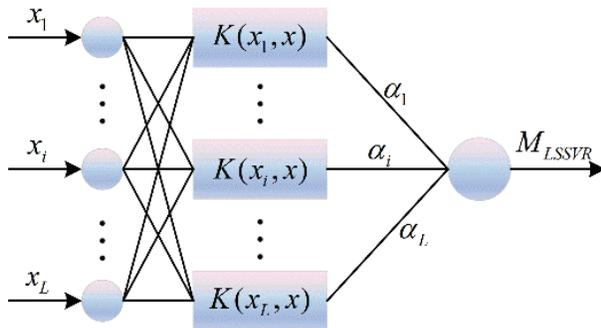
Fig. 1. Structure of the LSSVR.

The dimension of the high-dimensional feature space may be infinite, and the specific expression of the nonlinear mapping $\phi(\bullet)$ is usually unknown. Thus, the kernel function technique in equation (6) is used to simplify the computation significantly by replacing the direct computation of the nonlinear mapping with the inner product of the nonlinear mapping:

$$K(x_i, x_j) = \phi(x_i) \bullet \phi(x_j), \quad (6)$$

where $K(x_i, x_j)$ is the kernel function.

According to [13], LSSVR based on the Gaussian kernel function $K(x_i, x_j) = \exp(- \parallel x_i - x_j \parallel^2 / \rho^2)$ performs best in uncertainty analysis. Therefore, the Gaussian kernel function is chosen in this paper.

In this paper, LSSVR also selects sample points using LHS, and Kriging-LSSVR requires the same initial sample space for both Kriging and LSSVR. So LSSVR is trained with the training set $\{x_i, y_i\}_{i=1}^{L}$ obtained in the previous section to obtain the LSSVR model of equation (7) [14]:

$$M_{LSSVR} = \mu^T \phi(x) + b = \sum_{i=1}^{L} \alpha_i K(x_i, x) + b, \quad (7)$$

where $\mu = \sum_{i=1}^{L} \alpha_i \phi(x_i)$, α_i are scalar coefficients, and b is the bias term.

The flowchart for applying LSSVR to improve Kriging for uncertainty analysis is shown in Fig. 2. The code writing process is described in Algorithm 3. First, the initial sample space $S_0 = [x_1, x_2, \cdots, x_q]$ is obtained by LHS, and it is worth noting that q is very small, even less than one-fourth of L mentioned in the previous section. The deterministic EMC simulation described in equation (3) is performed on the initial sample space S_0 to obtain the deterministic simulation result y_i, which then produces the training set $\{x_i, y_i\}_{i=1}^{q}$. Then, the Kriging model $M_{Kriging}$ and the LSSVR model M_{LSSVR} are constructed based on the training set. $Y_{Kriging}$ is the response value estimated by $M_{Kriging}$ on the exhaustive sample space S_1 and is a vector of length n. Y_{LSSVR} is the response value estimated by M_{LSSVR}.

Statistics are performed on $Y_{Kriging}$ and Y_{LSSVR} to obtain the probability density curves. These curves are then transformed into cumulative distribution function (CDF) curves, and the K-S distance D between the CDF curves of Kriging and LSSVR is calculated. The K-S distance is the test statistic of the Kolmogorov-Smirnov test [15]. The statistic D is determined by the maximum vertical deviation between the two curves of the CDF of the data set:

$$D = \max\left(|CDF_1(x) - CDF_2(x)|\right), \quad (8)$$

where $CDF_1(x)$ is the proportion of values in the Kriging dataset that are less than or equal to x, and $CDF_2(x)$ is the proportion of values in the LSSVR dataset that are less than or equal to x. The larger the D, the greater the difference between the two CDF curves.
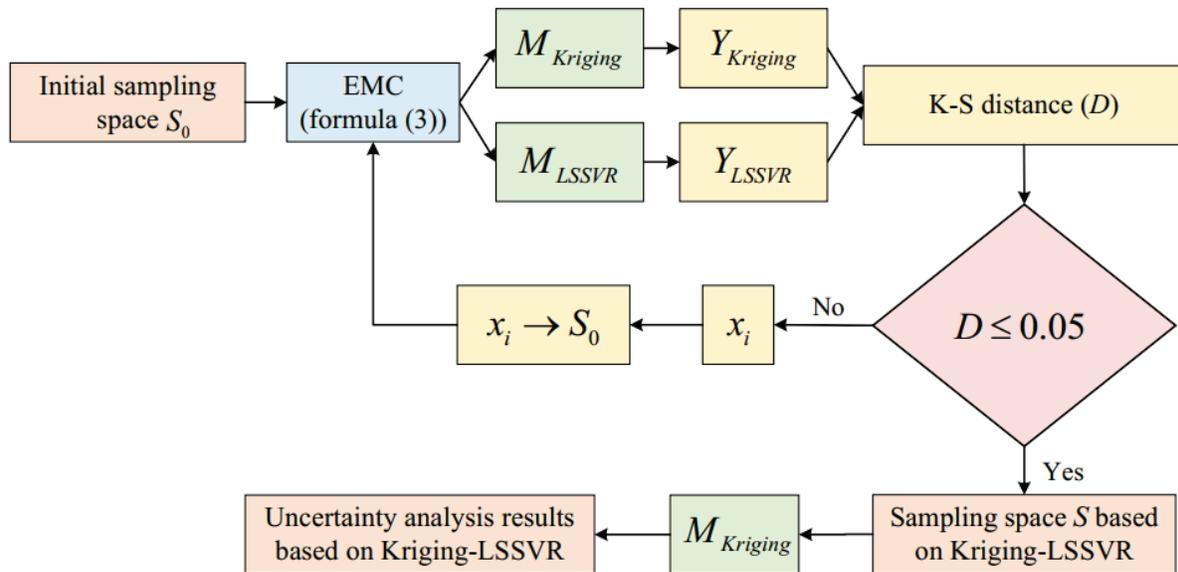
Fig. 2. Flowchart of Kriging-LSSVR.

In this paper, the K-S distance D is used as a criterion to select sampling points actively. If the K-S distance exceeds 0.05, the difference between the CDF curves is considered large, indicating that the current sample space does not meet the accuracy requirements of the Kriging-LSSVR model. Find the sample point x_i corresponding to the value with the largest difference between $Y_{Kriging}$ and Y_{LSSVR}, and add it to the initial sample space S_0. The purpose of this sequential sampling strategy is to identify the point with the greatest difference between the two surrogate models, achieve uniform coverage of the sampling points in the sample space with maximum efficiency, and thereby enhance the accuracy and efficiency of the uncertainty analysis. As the sample space S_0 expands, the K-S distance D decreases. When D is less than or equal to 0.05, the final sample space S is output. The EMC simulation result of sample space S is the training set. The final Kriging model $M_{Kriging}$ is constructed based on the training set. Finally, the response value $Y_{Kriging}$ is statistically analyzed to obtain the uncertainty analysis results based on Kriging-LSSVR, such as expectation, standard deviation, worst-case estimate, and probability density curve.

Algorithm 3 Kriging-LSSVR

1:      Exhaustive sampling points S_1 (n)
2:      LHS selects the initial sample space S_0 (q)
3:      for (do $i=1$:q)
4:      EMC simulation $y_i = $ EMC $[x_i]$
5:      end for
6:      Initial training set $\{x_i, y_i\}_{i=1}^{q}$
7:      Construction of $M_{Kriging}$ and M_{LSSVR}

8:      Bring S_1 into $M_{Kriging}$ and M_{LSSVR}
9:      Statistical $Y_{Kriging}$ and Y_{LSSVR}
10:    Generate PDF curves
11:    PDF $\Rightarrow$ CDF
12:    Calculate the K-S distance D
13:    while $D > 0.05$ do
14:    Find x_i and add it to S_0
15:    $y_i = $ EMC $[x_i]$
16:    Construction of $M_{Kriging}$ and M_{LSSVR}
17:    Bring S_1 into $M_{Kriging}$ and M_{LSSVR}
18:    Statistical $Y_{Kriging}$ and Y_{LSSVR}
19:    Generate PDF curves
20:    PDF $\Rightarrow$ CDF
21:    Calculate the K-S distance D
22:    end while
23:    Output the final sample space S
24:    Determining the final Kriging model $M_{Kriging}$
25:    Bring S_1 into $M_{Kriging}$
26:    Results of uncertainty analysis

IV. EXAMPLE OF APPLICATION

The Kriging-LSSVR method proposed in section III is applied to the parallel cable crosstalk example shown in Fig. 3 to verify its advantages over conventional Kriging. In practical engineering, uncertainties in cables include geometric positional uncertainties due to motion or vibration, and dimensional uncertainties due to manufacturing tolerances. Predicting crosstalk between cables considering these uncertainties is a typical EMC problem. Parallel cables are the most fundamental example of this, as discussed in [1, 16].
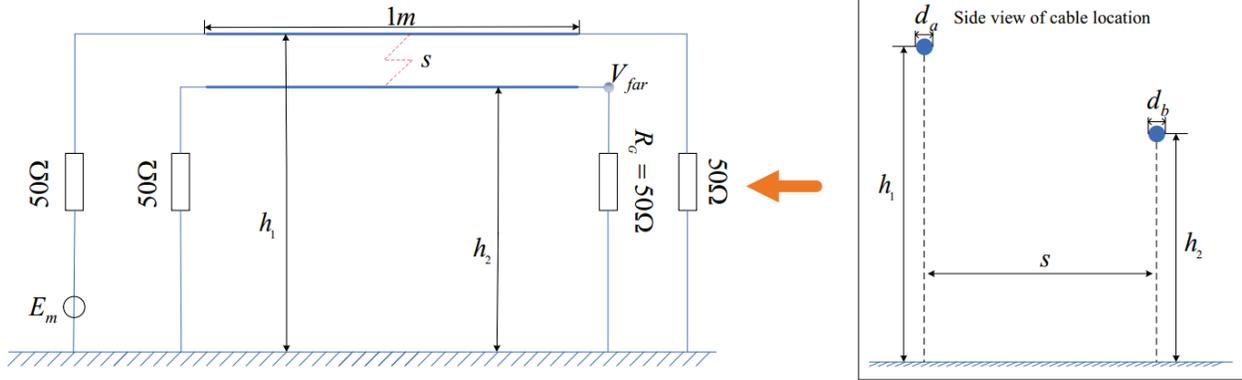
Fig. 3. Parallel cable crosstalk example schematic.

Two cables are parallel to each other and both have a length of 1 m. The horizontal distance between them is s. One of them serves as the receptor wire and is grounded to a 50 Ω load at each end. The other wire, the generator wire, needs to be connected not only to a 50 Ω load, but also to an excitation source E_m with an amplitude of 1 V. The height of the generator wire is h_1 and the diameter is d_a. The height of the receptor wire is h_2 and the diameter is d_b.

A. The proposed method is applied to the example with two random variables

In classical uncertainty analysis based on parallel cable crosstalk example, h_1 and h_2 are considered as two uncertain factors [1]. Here, they are assumed to follow a uniform distribution, and the results of applying random variable modeling are shown below.

$$\begin{cases} h_1 = 0.045 + 0.005 \times \zeta_1 \ [\text{m}] \\ h_2 = 0.035 + 0.005 \times \zeta_2 \ [\text{m}] \end{cases}, \quad (9)$$

where ζ_1 and ζ_2 are uniformly distributed random variables in the interval [-1,1].

The partial parameters of the two cables are as follows: $s = 0.05$ m, $d_a = 0.7$ mm, $d_b = 0.7$ mm.

The MCM is applied to perform 10,000 deterministic simulations at exhaustive sampling points, and the results of its uncertainty analysis are used as standard data. The initial sample space S_0 of Kriging-LSSVR has five sampling points, i.e., $q = 5$. The number of sampling points in the final sample space S obtained by the sequential sampling strategy is 26. In order to compare the performance of traditional Kriging and the Kriging-LSSVR proposed in this paper more objectively, the number of sampling points chosen at one time for the traditional Kriging application of LHS is also 26, i.e. $L = 26$. Deterministic simulation is performed on the sampling points to obtain the training set, which is used to construct the surrogate model. Subsequently, the uncertainty analysis results are obtained. Figures 4 and 5 show the probability
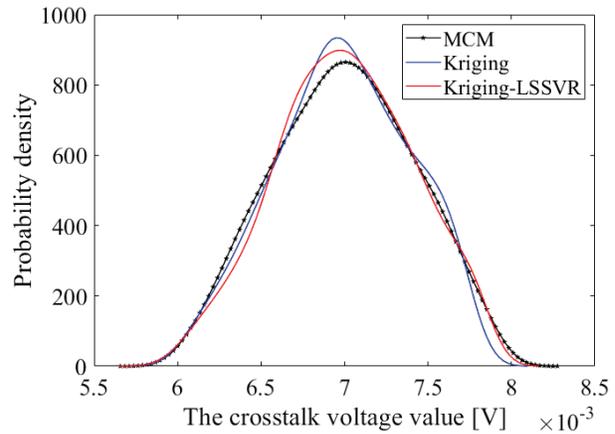
Fig. 4. Probability density of crosstalk voltage values at 2 MHz.
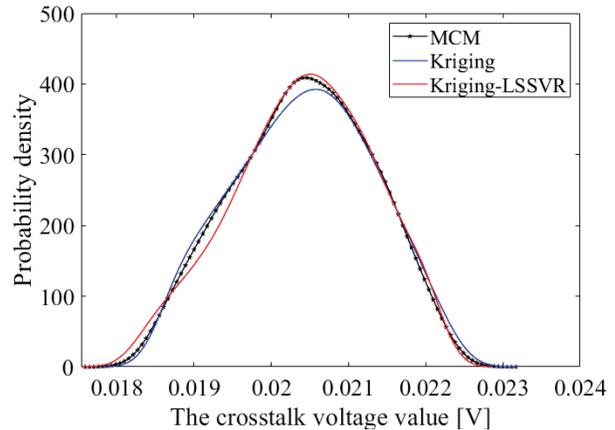
Fig. 5. Probability density of crosstalk voltage values at 50 MHz.

density curves for MCM, Kriging and Kriging-LSSVR at frequencies of 2 MHz and 50 MHz, respectively.

Table 1: Results of MEAM evaluation

Method	2 MHz	50 MHz
Kriging	0.9573	0.9792
Kriging-LSSVR	0.9724	0.9866

As can be seen from the figure, the Kriging-LSSVR seems to be more accurate than Kriging, but it is not obvious. Therefore, this paper applies the mean equivalent area method (MEAM) proposed in [17] for further validation. The evaluation results of MEAM are shown in Table 1. The closer the MEAM value is to 1, the higher the accuracy of the tested method. As seen in Table 1, the accuracy of Kriging-LSSVR is higher than Kriging. However, since Kriging is already very accurate, this means the improvement in the accuracy of Kriging-LSSVR is not obvious. In order to further validate the performance of Kriging-LSSVR, the number of random variables in the parallel cable crosstalk example is expanded in this paper.

B. The proposed method is applied to the example with multiple random variables

In the parallel cable crosstalk example, in addition to the heights h_1 and h_2 of the two cables, the cable diameter and the horizontal distance between the two cables also impact the simulation results. Consider these five parameters as uniform random variables, as shown in Table 2.

Table 2: Uncertainty parameters for parallel cables

Uniform Random Variables	Unit	U [min, max]
Height of generator wire h_1	m	U [0.04, 0.05]
Height of receptor wire h_2	m	U [0.03, 0.04]
Diameter of generator wire d_a	mm	U [0.6, 0.8]
Diameter of receptor wire d_b	mm	U [0.6, 0.8]
Distance between two wires s	m	U [0.04, 0.06]

MCM is applied for 10,000 simulations to obtain the standard data. Due to the increase in the number of random variables, the number of sampling points must be increased to ensure the accuracy of the surrogate model. Assume that the initial sample space S_0 of Kriging-LSSVR has 20 sampling points, i.e. $q = 20$. The number of sampling points in the final sample space obtained by the sequential sampling strategy is 97. The number of sampling points chosen once for the traditional Kriging application of Latin hypercube sampling is also 97, i.e. $L = 97$.

Figures 6 and 7 show the probability density curves at frequencies of 2 MHz and 50 MHz, respectively, and Table 3 shows the evaluation results of MEAM. As can be seen from Table 3, the accuracy of Kriging-LSSVR
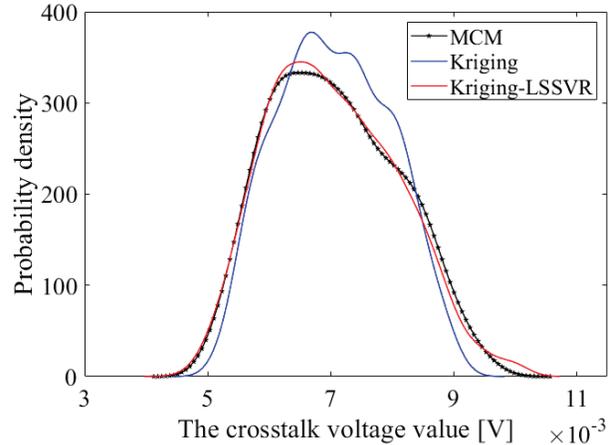
Fig. 6. Probability density of crosstalk voltage values at 2 MHz.
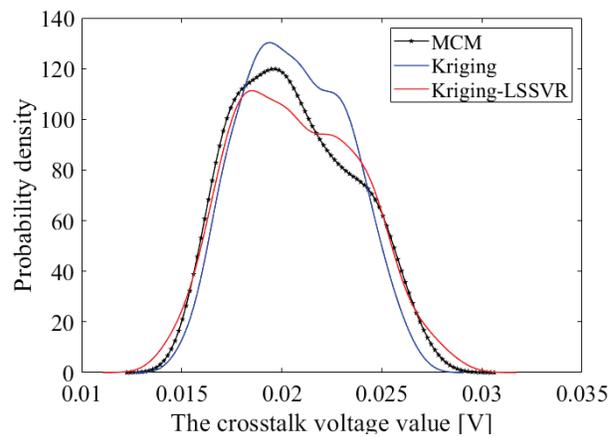
Fig. 7. Probability density of crosstalk voltage values at 50 MHz.

at 2 MHz is much higher than Kriging. The accuracy of Kriging-LSSVR at 50 MHz is also higher than Kriging, but not as much as at 2 MHz.

Table 3: Results of MEAM evaluation

Method	2 MHz	50 MHz
Kriging	0.8678	0.8813
Kriging-LSSVR	0.9873	0.9485

To further investigate the performance of Kriging-LSSVR, the frequency range is extended to 1-100 MHz. As shown in Figs. 8 and 9, the expectation and standard deviation information, rather than the probability density function information, are presented. The global difference metric (GDM) values between the results to be measured and the MCM are calculated using FSV, as shown in Table 4. FSV has been successfully applied to
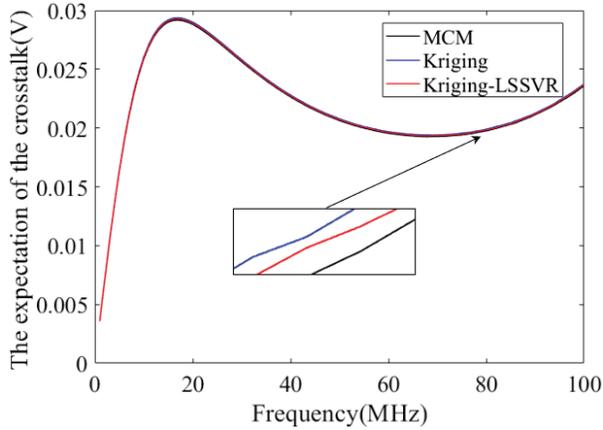
Fig. 8. Far-end crosstalk voltage expectation for frequency range 1 MHz to 100 MHz.
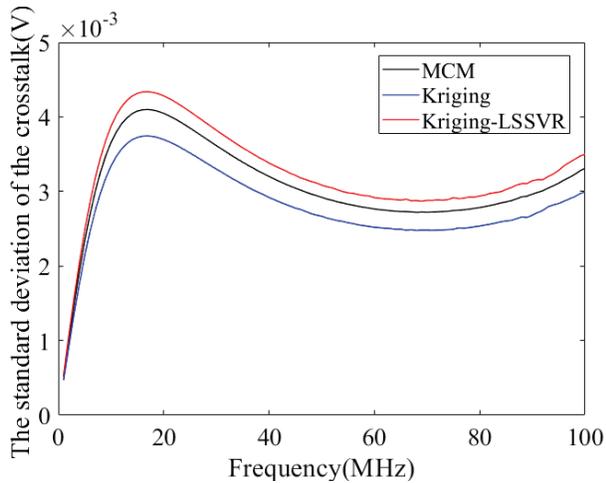
Fig. 9. Standard deviation of far-end crosstalk voltage in the frequency range 1 MHz to 100 MHz.

the credibility assessment of uncertainty in EMC simulation results [1].

According to Table 4, the evaluation results of the expectation value of the simulation results for both surrogate models are "Excellent". The standard deviation of Kriging is evaluated as "Very Good", while the standard deviation of Kriging-LSSVR is rated as "Excellent". The standard deviation evaluation result of Kriging-LSSVR is one level higher than that of Kriging, further proving that Kriging-LSSVR has higher accuracy than Kriging.

Table 4: FSV value results

	Kriging	Kriging-LSSVR
Expectation	0.0097	0.0051
Standard deviation	0.1369	0.0155

In terms of computational efficiency, it takes 28.9 seconds to perform one crosstalk computation. MCM performs a total of 10,000 simulations, taking 80 hours. Kriging and Kriging-LSSVR require only 97 computations, taking 46.7 minutes. The model prediction time of the surrogate model is negligible in comparison. The simulation time for each specific method is shown in Table 5. The model prediction time t_{modle} for Kriging-LSSVR is slightly longer than that of Kriging and is negligible compared to the total time t_{cost}. If the time for a single simulation is measured in hours, then MCM does not work. The efficiency of the surrogate model is demonstrated.

Table 5: Comparison of simulation time

Method	$t_{\text{crosstalk}}$	t_{modle}	t_{cost}
MCM	80 h	/	80 h
Kriging	46.7 min	8.3 s	46.8 min
Kriging-LSSVR	46.7 min	6.7 min	53.4 min

V. CONCLUSION

In this paper, LSSVR is applied to enhance the Kriging model, combining the strengths of both surrogate models to develop a more accurate and efficient EMC uncertainty analysis method, namely Kriging-LSSVR. This method enhances the proactivity of the sampling process, significantly improving the efficiency of uncertainty analysis. At high levels of simulation complexity, Kriging-LSSVR demonstrates notable advantages in accuracy and efficiency. In the parallel cable crosstalk example with multiple random variables, Kriging-LSSVR demonstrates one level higher accuracy compared to conventional Kriging. The method proposed in this paper can be applied to large-scale complex electromagnetic simulations in the future to ensure the feasibility and accuracy of large-scale simulations.

REFERENCES

[1] J. Bai, K. Guo, J. Sun, and N. Wang, "Application of the multi-element grid in EMC uncertainty simulation," *Applied Computational Electromagnetics Society Journal*, vol. 37, no. 4, pp. 428-434, Apr. 2022.

[2] R. Trinchero, M. Larbi, H. M. Torun, F. G. Canavero, and M. Swaminathan, "Machine learning and uncertainty quantification for surrogate models of integrated devices with a large number of

parameters," *IEEE Access*, vol. 7, pp. 4056-4066, Dec. 2019.

[3] A. Biondi, D. Vande Ginste, D. De Zutter, P. Manfredi, and F. G. Canavero, "Variability analysis of interconnects terminated by general nonlinear loads," *IEEE Trans. Compon. Packag. Manufact. Technol.*, vol. 3, no. 7, pp. 1244-1251, July 2013.

[4] J. Shen, H. Yang, and J. Chen, "Analysis of electrical property variations for composite medium using a stochastic collocation method," *IEEE Trans. Electromagn. Compat.*, vol. 54, no. 2, pp. 272-279, Apr. 2012.

[5] J. Bai, G. Zhang, A. P. Duffy, and L. Wang, "Dimension-reduced sparse grid strategy for a stochastic collocation method in EMC software," *IEEE Trans. Electromagn. Compat.*, vol. 60, no. 1, pp. 218-224, Feb. 2018.

[6] J. Bai, B. Hu, H. Cao, and J. Zhou, "Uncertainty analysis method for EMC simulation based on the complex number method of moments," *PIER Letters*, vol. 121, pp. 7-12, 2024.

[7] Z. Fei, Y. Huang, J. Zhou, and Q. Xu, "Uncertainty quantification of crosstalk using stochastic reduced order models," *IEEE Trans. Electromagn. Compat.*, vol. 59, no. 1, pp. 228-239, Feb. 2017.

[8] Z. Ren, J. Ma, Y. Qi, D. Zhang, and C.-S. Koh, "Managing uncertainties of permanent magnet synchronous machine by adaptive Kriging assisted weight index Monte Carlo simulation method," *IEEE Trans. Energy Convers.*, vol. 35, no. 4, pp. 2162-2169, Dec. 2020.

[9] P. Besnier, F. Delaporte, and T. Houret, "Extreme values and risk analysis: EMC design approach through metamodeling," *IEEE Electromagn. Compat. Mag.*, vol. 10, no. 4, pp. 80-93, 2021.

[10] T. Houret, P. Besnier, S. Vauchamp, and P. Pouliguen, "Controlled stratification based on Kriging surrogate model: An algorithm for determining extreme quantiles in electromagnetic compatibility risk analysis," *IEEE Access*, vol. 8, pp. 3837-3847, 2020.

[11] H. Li, B. Zhu, and J. Chen, "Optimal design of photonic band-gap structure based on Kriging surrogate model," *PIER M*, vol. 52, pp. 1-8, 2016.

[12] S. Kasdorf, J. J. Harmon, and B. M. Notaroš, "Kriging methodology for uncertainty quantification in computational electromagnetics," *IEEE Open J. Antennas Propag.*, vol. 5, no. 2, pp. 474-486, Apr. 2024.

[13] M. Sedaghat, R. Trinchero, Z. H. Firouzeh, and F. G. Canavero, "Compressed machine learning-based inverse model for design optimization of microwave components," *IEEE Transactions on Microwave Theory and Techniques*, vol. 70, no. 7, pp. 3415-3427, July 2022.

[14] S. Kushwaha, N. Soleimani, F. Treviso, R. Kumar, R. Trinchero, F. G. Canavero, S. Roy, and R. Sharma, "Comparative analysis of prior knowledge-based machine learning metamodels for modeling hybrid copper-graphene on-chip interconnects," *IEEE Trans. Electromagn. Compat.*, vol. 64, no. 6, pp. 2249-2260, Dec. 2022.

[15] F. J. Massey, "The Kolmogorov-Smirnov test for goodness of fit," *Journal of the American Statistical Association*, vol. 46, no. 253, pp. 68-78, Mar. 1951.

[16] J. Bai, Y. Wan, M. Li, G. Zhang, and X. He, "Reduction of random variables in EMC uncertainty simulation model," *Applied Computational Electromagnetics Society Journal*, vol. 37, no. 9, pp. 941-947, Sep. 2022.

[17] J. Bai, J. Sun, and N. Wang, "Convergence determination of EMC uncertainty simulation based on the improved mean equivalent area method," *Applied Computational Electromagnetics Society Journal*, vol. 36, no. 11, pp. 1446-1452, Nov. 2021.

Shenghang Huo received the B.Eng. degree in electrical engineering and automation from Dalian Maritime University in 2023. He is currently a graduate student in electrical engineering at Dalian Maritime University, where his research interests include machine learning and uncertainty analysis methods in EMC simulation.

Yujia Song received a Ph.D. in the School of Energy and Power Engineering at Dalian University of Technology in 2024. Her main research interests are integrated energy system design, novel power system modeling for offshore wind power, and computational electromagnetics simulation.

Qing Liu received the B.Eng. degree in electrical engineering and automation from Hubei University of Technology in 2023. He is currently a graduate student in electrical engineering at Dalian Maritime University, where his research interests include microgrid optimal dispatch, computational electromagnetics simulation for offshore wind power.

Jinjun Bai received the B.Eng. degree in electrical engineering and automation in 2013, and Ph.D. degree in electrical engineering in 2019 from the Harbin Institute of Technology, Harbin, China. He is now a lecturer at Dalian Maritime University. His research interests include uncertainty analysis methods in EMC simulation, multi-physics field simulation method.

Correlations of Salivary and Blood Glucose Level Detection using Flexible Sensor Technique

Yusnita Rahayu[1], Fildza Arifa[1], Mudrik Alaydrus[2], Anhar[1], Teguh Praludi[3], Huriatul Masdar[4], and Syah Alam[5]

[1]Department of Electrical Engineering
Faculty of Engineering, Universitas Riau, Pekanbaru 28290, Indonesia
yusnita.rahayu@lecturer.unri.ac.id, fildza@graduate.utm.my, anhar@lecturer.unri.ac.id

[2]Department of Electrical Engineering
Faculty of Engineering, Universitas Mercu Buana, Jakarta 11650, Indonesia
mudrikalaydrus@mercubuana.ac.id

[3]National Research and Innovation Agency
Indonesia
teguhpraludi@gmail.com

[4]Medical Faculty
Universitas Riau, Pekanbaru 28133, Indonesia
huriatul.masdar@gmail.com

[5]Department of Electrical Engineering
Universitas Trisakti, Jakarta Barat 11440, Indonesia
syah.alam@trisakti.ac.id

Abstract – Indonesia had a total of 19.47 million individuals diagnosed with diabetes in 2021, the fifth position globally, as reported by the International Diabetes Federation (IDF). Diabetes requires periodic medical examinations, yet many individuals are hesitant to utilize invasive medical devices. The ring slot circular resonator (RSCR) inspired this sensor's design. Non-invasive glucose measurement was done with flexible 2.45 GHz sensors. The reflection coefficient (S11) simulation result is -20.76 dB at 2.458 GHz and 894.8 MHz bandwidth. Saliva samples obtained from 20 individuals were subjected to 20 separate tests. Before collecting saliva samples, the volunteers' blood sugar levels were assessed. Research indicates that the appropriate frequency range for average blood sugar levels (less than 125 mg/dl) is 1.55 GHz to 2.16 GHz, while diabetes patients with blood glucose levels (BGL) above 125 mg/dl had frequencies above 2.3 GHz. Test results show a positive correlation between glucose level and testing frequency. In addition to blood samples, saliva samples can serve as alternate specimens for assessing an individual's BGL.

Index Terms – Blood glucose, flexible sensor, non-invasive, ring slot circular resonator, salivary.

I. INTRODUCTION

Elevated blood sugar (glucose) leads to diabetes. The International Diabetes Federation (IDF) estimates that one in 10 people globally suffers from diabetes. The IDF estimate has grown by 16%, or 74 million people, since 2019. The projected populations are 643 million in 2030 and 784 million in 2045. A total of 19.47 million Indonesians is expected to have diabetes in 2021, according to IDF forecasts [1]. Diabetes is an increase in blood sugar due to decreased insulin secretion by pancreatic beta cells and/or impaired insulin function [2].

Diabetics need to monitor and control their blood glucose levels (BGL) to keep their levels within normal ranges. To monitor blood sugar levels, a finger prick is used to extract blood, which is then placed on a blood strip. Some diabetics fear blood, so they avoid regular checkups [3]. This work was driven by the desire to eliminate the use of invasive blood sugar testing. Thus, the requirement for a non-invasive blood sugar monitor arises.

The diagnostic criteria for diabetes mellitus, as outlined in the guidelines, involve the measurement of fluctuating venous plasma glucose [4]. The diagnostic criteria for diabetes include the following thresholds: a

plasma glucose value of $\geq$200 mg/dl ($\geq$11.1 mmol/l) on an occasional basis, a fasting plasma glucose level of $\geq$126 mg/dl (7.0 mmol/l) after a fasting period of 8-12 hours, and a 2-hour value in venous plasma during an oral glucose tolerance test (OGTT) of $\geq$200 mg/dl ($\geq$11.1 mmol/l).

According to scientific literature, fasting plasma glucose concentrations below 6 mmol/L (100 mg/dL) are considered within the normal range. Fasting plasma glucose concentrations ranging from 6.1 to 6.9 mmol/L (100-125 mg/dL) indicate impaired fasting glucose. Furthermore, fasting plasma glucose concentrations equal to or exceeding 7.0 mmol/L (126 mg/dL) are diagnostic criteria for diabetes [5].

RF transmission, breath analysis, fluorescence, interstitial fluid chemistry, and ocular spectroscopy are the most widely used non-invasive techniques [6]. A saliva nano-biosensor with a polyvinylidene fluoride (PVDF) membrane was used by Zhang et al. to monitor glucose non-invasively [7]. In 2019, Wang et al. also investigated antennas using commercial beverages and sweat samples on polyethylene terephthalate (PET) substrates [8]. A six-element dipole arm antenna was constructed by Bakkali et al. [9] to monitor glucose. Deshmukh and Chorage created microstrip antenna configurations as microwave sensors in 2020, including spiral, narrowband, and ultrawideband antennas. They quantified return loss by observing the antenna test frequency response for a specific BGL [10]. A 50 mg/dl glucose solution was used by Firdausi et al. to build a proximity couple-based microstrip antenna that operates at 50-60 GHz [11].

This study involved conducting extensive research on saliva testing with volunteers to ascertain its viability as an alternate sample for detecting an individual's blood sugar levels. The disparity in sugar levels in saliva between those with diabetes and those without diabetes is the reason behind this. The sensor is composed of a circular resonator with a ring slot, which is printed on a flexible PET substrate. It operates within the frequency range 2.4-2.48 GHz, with the center of the ring slot as the sensing hotspot. This could be a promising solution to detect a person's saliva sugar levels that correlate with blood sugar levels with high accuracy.

II. MATERIALS AND METHODS
A. Flexible sensor design

This research involves the construction of a flexible sensor that utilizes a PET substrate and a Coplanar Waveguide (CPW) feed mechanism. The PET substrate has a relative dielectric constant of 3, a dielectric loss tangent of 0.001, and a thickness of 0.13 mm [12]. The conductive film on the PET substrate uses silver nano ink. The PET substrate is chosen due to its ease of pro-

cessing in various forms, such as molding and cutting. This facilitates the manufacturing of sensors according to the desired design and expected quantity. PET has a relatively stable dielectric constant at various frequencies and temperatures [13, 14]. The dielectric stability of PET contributes to the long-term performance of the sensor by minimizing the impact of temperature changes. This stability improves the sensitivity of the glucose sensor. Additionally, PET provides effective electrical isolation, reducing interference between the sensor elements and the surrounding structure. Table 1 presents the dimensions of the sensor that has been proposed. Figure 1 illustrates the geometry of the sensor with the measurement scenario.

Table 1: Dimensions of sensor design

Dimension	Parameters (mm)
L (Substrate length)	35
W (Substrate width)	40
h (Substrate thickness)	0.135
WF (Feedline width)	5.8
LF (Feedline length)	12
WG (Ground width)	2.3
LG (Ground length)	16.9
R1	20
R2	17
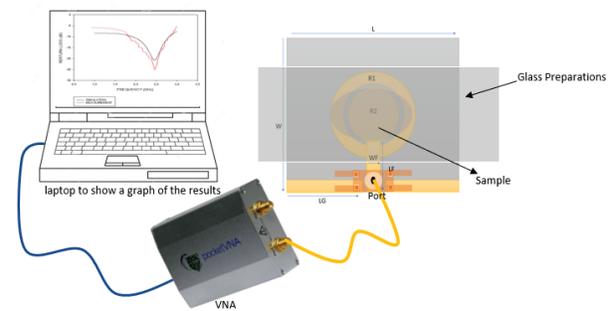
Fig. 1. RSCR sensor and measurement scenario.

This sensor operates at a frequency of 2.45 GHz, in accordance with the Industrial Science and Medical (ISM) Band standard. It adheres to health standards and is specifically designed to detect glucose using non-invasive techniques.

The error value for measuring the sensor's frequency is calculated using equation (1) as follows:

$$Error = \left| \frac{f_{simulated} - f_{measured}}{f_{simulated}} \right| x100\%. \qquad (1)$$

B. Research methods

This study involved 20 participants who had different blood sugar levels. The blood sugar levels were

initially assessed using an intrusive medical tool called an easy-touch glucometer, which involved pricking the volunteer's finger with a specialized needle to obtain a blood sample. The levels were categorized as low, normal, or high. A total of 20 tests were carried out on each volunteer using saliva samples for non-invasive sensor testing. To ensure accurate measurements, volunteers were instructed to fast for 8 hours before testing. After fasting for at least 8 hours, subjects were tested before eating for more reliable findings. This study was conducted in accordance with the principles of the Declaration of Helsinki, and all patients provided verbal informed consent prior to enrollment.

As in [15] the correlation between saliva glucose and blood glucose was found to be relatively high and stable before breakfast. In general, unstimulated parotid salivary glucose before breakfast presents an ideal saliva collection method to replace blood glucose used to detect

(a)

(b)

Fig. 2. (a) Sensor measurement process for detecting glucose levels with saliva samples using a vector network analyzer and (b) process of injecting saliva sample on flexible sensor.

diabetes mellitus, providing a reference for the prediction of diabetes mellitus. This study uses invasive medical devices to analyze saliva and blood test results.

Similar to previous research analysis, frequency was used to enable blood sugar sensor feasibility, with a particular focus on examining variations in testing frequency. Figure 2 shows the measurement procedure of the saliva glucose sensor. The testing technique utilizes needleless injection equipment, glass slides, sensors, a pocket Vector Network Analyzer (VNA), and a laptop.

The initial stage of examination involves placing an individual saliva specimen and positioning it close to the sensor on the slide. This is achieved by employing a needle-free injection of 1 mg/dl with a uniform sample volume for every measurement, positioning the sample directly on the object glass, which is situated above the sensor. In this work, the author employed a sensor equipped with a disposable glass preparation to ensure the safety of volunteers from potential biomolecular effects present in the saliva of participants. The glass preparation was used only once by each volunteer and subsequently discarded. After connecting the SMA connector and pocket VNA, the measurement signal can be directly checked on the laptop. The impact of saliva on a sensor with a PET substrate is mainly visible from the frequency shift caused by the spillage of saliva on the sensor.

III. RESULTS AND DISCUSSION
A. Sensor performance on saliva samples

Figure 3 shows the S-parameter of the flexible sensor, both measured and simulated. The CPW feeding line is connected to the sensor using a SMA connector. The simulation yielded an S11 value of -20.76 dB at a frequency of 2.458 GHz, with a bandwidth of 894.8 MHz, as shown by the black curve in Fig. 3. By contrast, the prototype sensor's measurement yielded a red curve with an S11 value of -25.14 dB at a frequency of 2.462 GHz and 1200 MHz bandwidth. The measurements were conducted solely on the sensor, without any samples being used.

According to the results of the conducted comparisons, there are discrepancies between the simulation results and the sensor measurements, which result in variations in the working frequency, S11, and bandwidth of the sensors. The frequency shift may result from a large reflection when measuring the sensors and loss from the connector port and the measuring apparatus. The error value for both results is 0.16% as calculated using equation (1).

To analyze and measure the electric field (E-field) of the proposed resonator, we conducted an E-field simulation at the resonant frequency of 2.45 GHz. This simulation was done for the circular resonator both before
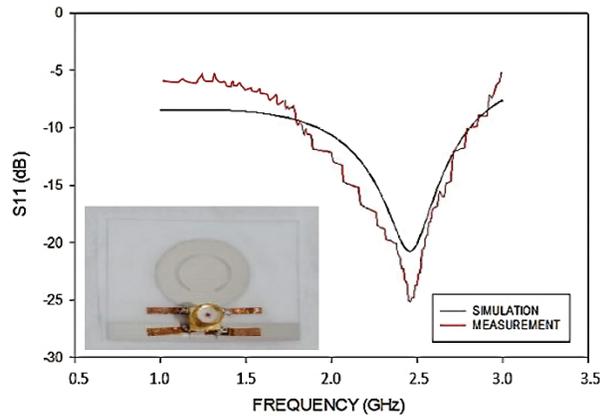
Fig. 3. Measured and simulated S-parameters of the proposed flexible sensor.

Fig. 4. (a) E-field of the circular resonator and (b) E-field of the circular resonator with a ring slot added.

and after the ring slot was added. Figure 4 (a) presents the E-field of the circular resonator without a ring slot added. Figure 4 (b) shows the circular resonator with a ring slot added. The results clearly demonstrate that the ring slot yields the highest E-field intensity in the central area. However, the E-field of a circular resonator without a ring slot is located near the edge of the patch. Consequently, the region with the strongest E-field, which includes the ring slot, can serve as a precise location for detecting hotspots and placing the saliva sample. It should be noted that saliva placement on the hot spot area greatly affected the frequency shift, sensitivity, and performance of the sensor. The maximum E-field was observed at 13 kV/m.

Table 2 lists the experimental results using saliva samples from 20 volunteers. Studies have shown that the frequency range for blood sugar levels below 125 mg/dl is between 1.5 GHz and 2.16 GHz. Diabetic frequency occurs when blood sugar levels exceed 125 mg/dl and goes beyond 2.3 GHz. This demonstrates that the frequency of high blood sugar levels rises.

Fluctuations in BGLs can alter the permittivity of saliva, which is a bodily sample similar to blood. Consequently, the sensor exhibits high sensitivity to changes in permittivity. This is supported by Turgul's research [16], which demonstrates that the frequency shift is more pronounced when liquid samples containing high concentrations of glucose are used. In addition, Jha's research [17] demonstrated that higher concentrations of glucose led to an increase in frequency. Specifically, samples with 20% glucose levels had a frequency of 2.97 GHz, whereas samples with 30% glucose levels had a frequency of 3 GHz. This demonstrates that frequency moves towards higher values when the glucose level in a sample is high. This aligns with the research findings we acquired, as illustrated in Fig. 5.
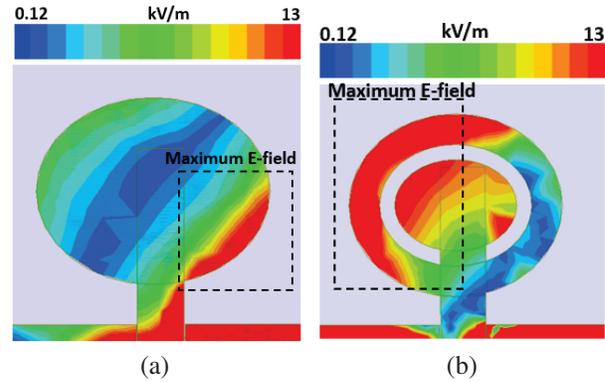
Table 2: Experiments using saliva samples on the RSCR sensor

No.	BGL (mg/dl)	Frequency (GHz)	S11 (dB)	Bandwidth (MHz)
1	74	1.5588	-19.98	84.05
2	78	1.6801	-27.35	111.6
3	82	1.8316	-22.39	75.4
4	83	1.8582	-25.42	65.1
5	87	1.9274	-19.82	64.9
6	88	1.9338	-20.00	83.75
7	89	1.9903	-19.56	66.1
8	90	2.0209	-26.14	73.8
9	91	2.0314	-19.71	54
10	92	2.0812	-36.33	82.6
11	102	2.1109	-26.54	68.8
12	105	2.1505	-25.99	80.85
13	112	2.1615	-24.62	87.7
14	145	2.3387	-21.46	51.55
15	200	2.6022	-18.01	52.65
16	202	2.6071	-19.45	52
17	202	2.6075	-19.34	87.8
18	215	2.6196	-28.03	50.7
19	216	2.6318	-27.66	53.2
20	230	2.7596	-20.57	52.95

Figure 5 illustrates the relationship between sampling conducted using saliva and blood. Both samples underwent testing using the proposed RSCR sensor. The graph clearly demonstrates that both samples exhibit identical characteristics. The frequency of occurrence rises in direct correlation with the elevation of sugar levels. Furthermore, we conducted experiments utilizing various quantities of saliva through a needle without injection, as detailed in Table 3.

Table 3 presents the findings of experiments conducted on saliva samples with varying sample volumes.
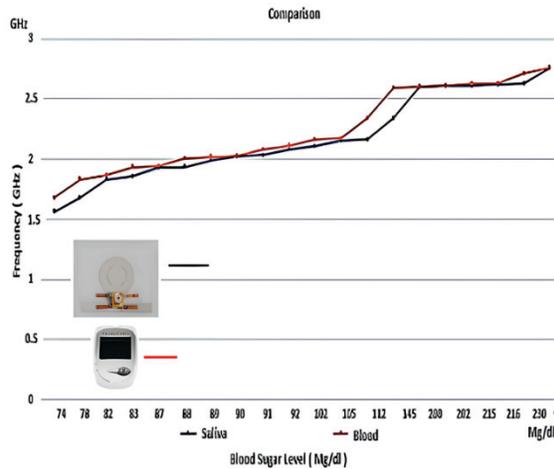
Fig. 5. Saliva and blood samples correlation graph.

Table 3: Saliva experiments using different volumes of saliva

No	mg/dl	0.1 cc/ml	0.2 cc/ml	0.3 cc/ml	0.4 cc/ml
1	80	1.722 GHz	1.716 GHz	1.752 GHz	1.754 GHz
2	83	1.862 GHz	1.878 GHz	1.869 GHz	1.859 GHz
3	216	2.719 GHz	2.7732 GHz	2.7349 GHz	2.756 GHz

The experiments examined three different glucose levels: 80 mg/dl, 83 mg/dl, and 216 mg/dl. The results indicate that there was no notable variation in frequency when sample volumes ranged from 0.1 cc/ml to 0.4 cc/ml for these glucose levels. These findings show that a large volume of a sample does not have a significant influence.

Furthermore, as stated in [18], diabetics exhibited significantly elevated amounts of glucose in their saliva compared to the control group. A significant positive correlation was found between salivary glucose level (SGL) and BGL in diabetics as well as controls. SGL is directly influenced by glycemia and thus can be used to monitor BGL in diabetics. No positive correlation was found between SGL and HbA1c, nor was any correlation found between SGL, age, sex, and duration of disease.

Through the findings obtained, saliva can be used as a routine potential diagnostic tool in assessing diabetes mellitus. It is a simple and noninvasive technique for screening and monitoring this disease. Repeated painful finger pricks, the hazard of getting infections, complications in hemophiliac patients, and various other disadvantages that involve the blood tests currently used for diagnosis and monitoring of this widely prevalent diabetes mellitus disease, can be replaced by noninvasive tests involving saliva, which is also cost-effective. Therefore, this research focuses on saliva samples.

B. Comparison of past research results

In this paper, we introduce a flexible RSCR as a sensor for salivary glucose testing. The proposed sensor has a sensing hot spot at the center, allowing it to detect and respond to any sample placed on top of the sensing area, resulting in a significant frequency change. Table 4 shows a comparison between the proposed work and the existing sensors. Table 4 presents the novelty of the proposed sensor by the introduction of the flexible RSCR. Another novelty, the RSCR has independent characteristics, it is suitable for detecting glucose levels in saliva. Moreover, this study also presents the correlation between BGL and saliva by involving 20 volunteers with 20 times separated tests. Additionally, the study involved trials utilizing varying volumes of saliva. Based on the measurements, the frequency of saliva secretion increased in direct correlation with the rise in glucose levels.

Previously, sweat and skin samples have been utilized by researchers. In [19], the skin was subjected to frequencies ranging from 0.5 to 4 GHz. Similarly, [20] utilized PET material in conjunction with sweat samples for their research. The antenna was positioned on the skin by the researcher to unveil a frequency shift that exhibited a positive correlation with the concentration of glucose. This study utilized a skin adhesion method for data collection, but it did not include a comparison of the obtained results with established industry-standard instruments. Consequently, the correctness of the findings remains undetermined.

Authors [21] discovered that the frequency was 2.14 GHz at 10% glucose levels, 2.18 GHz at 30% ethanol, 2.24 GHz at 50%, 2.3 GHz at 70%, and 2.37 GHz at 90%. Therefore, a sample with a higher glucose concentration generates a larger frequency even with varied substrates. According to [17], the frequency of water was 2.89 GHz, 20% of glucose samples had a frequency of 2.97 GHz, 25% had a frequency of 2.99 GHz, and 30% had a frequency of 3 GHz. Two percent glucose in ethanol samples produced frequencies at S11 of 165 MHz, 170 MHz, 180 MHz, 190 MHz, 200 MHz, 220 MHz, 230 MHz, and 240 MHz, and 80% ethanol produced 240 MHz in the study [2]. This demonstrates that as liquid glucose levels rise, so does the test frequency. According to [17], the frequency was 3.52 GHz at 0 mg/dl and 3.55 GHz at 2000 mg/dl of glucose. This attests to the frequency increase in glucose levels. Table 4 provides a summary.

Table 4: Comparison of the results of previous studies

Ref	Model	Resonance Frequency (GHz)	Material Under Test	Sample Under Test	Measured Parameter
[7]	NA	NA	Flexible	Saliva	NA
[8]	NA	NA	Flexible	Sweat and sugary drinks	NA
[19]	NA	$0.5 - 4$	Flexible	Skin	S11
[20]	NA	> 1	Flexible	Sweat	S11
[21]	Multiple Complementary Split-Ring Resonator	2.45	Solid	Liquids	S21
[17]	NA	1-18	Solid	Glucose liquid	S21
[22]	Planar U-Shaped Resonator	$0.1664 - 0.2875$	Solid	Ethanol	S11
[16]	NA	$0.3 - 15$	Solid	Liquids	S11
[23]	NA	2.45	Flexible	Saliva	S11
[24]	NA	60	Solid	Glucose liquid sample	S21
[25]	NA	$0.3 - 67$	Solid	Glucose solution and blood samples	S21
[26]	NA	7.5	Flexible	Glucose solution	S21
[27]	Cylindrical Biosensor	2.4	Flexible	Finger	S11
[28]	Microstrip Ring Resonator	0.0855	Solid	Constration of glucose	S11
This Work	Ring Slot Circular Resonator	2.45	Flexible	Saliva	S11

IV. CONCLUSION

In this paper, we have successfully developed a flexible ring slot circular resonator for salivary glucose detection. The proposed sensor operates at 2.45 GHz for unloaded frequency and shifts to 1.55 GHz for loaded frequency. In addition, the proposed device has independent characteristics with the center sensing area, so that it can be used for biological liquid sample measurements such as saliva and blood. From these measurements, the frequency range for blood sugar levels below 125 mg/dl is from 1.5 GHz to 2.16 GHz. Diabetic frequency arises when blood sugar levels surpass 125 mg/dl and exceed 2.3 GHz. The error of 0.16% was obtained for the S11 simulation and measurement results. This sensor can be recommended as an alternative solution for BGL detection. The findings indicate that the quantification of 20 saliva samples was successfully accomplished. In addition, throughout the testing process utilizing blood samples, the findings were mostly similar to those obtained from saliva samples. Furthermore, there was a noticeable shift towards higher frequencies when the blood sugar levels of the volunteers were elevated.

ACKNOWLEDGMENT

REFERENCES

[1] IDF Diabetes Atlas 2021, *IDF Atlas 10th Edition* [Online]. Available: https://diabetesatlas.org/atlas/tenth-edition.

[2] R. N. Fatimah, "Diabetes Mellitus type 2," *J. Majority*, vol. 4, no. 5, pp. 93-101, 2015.

[3] L. Tang, S. J. Chang, C. J. Chen, and L. T. Liu, "Non-invasive blood glucose monitoring technology: A review," *Sensors*, vol. 20, no. 23, p. 6925, 2020.

[4] A. Petersmann, D. Müller-Wieland, U. A. Müller, R. Landgraf, M. Nauck, G. Freckmann, and, E. Schleicher, "Definition, classification, and diagnosis of diabetes mellitus," *Experimental and Clinical Endocrinology & Diabetes*, vol. 127, no. S 01, pp. S1-S7, 2019.

[5] V. Mohan, R. Deepa, and M. Rema, "Correlation between fasting plasma glucose and two-hour plasma glucose during oral glucose tolerance test in South Indians," *Metabolism*, vol. 49, no. 4, pp. 455-457, 2000.

[6] S. J. Kim, S. J. Choi, J. S. Jang, H. J. Cho, and I. D. Kim, "Innovative nanosensor for disease diag-

nosis," *Acc. Chem. Res*, vol. 50, no. 1, pp. 1587-1596, 2017.

[7] W. Zhang, Y. Du, and M. L. Wang, "Non-invasive glucose monitoring using saliva nano-biosensor," *Sensing and Bio-Sensing Research*, vol. 4, pp. 23-29, 2015.

[8] Y. Wang, X. Wang, W. Lu, Q. Yuan, Y. Zheng, and B. Yao, "A thin film polyethylene terephthalate (PET) electrochemical sensor for the detection of glucose in sweat," *Talanta*, vol. 198, pp. 86-92, 2019.

[9] A. Bakkali, C. Buisson, L. Mounien, J. Landrier, V. Tishkova, and P. Sabouroux, "First microwave tomography approach towards a truly non-invasive, pain-free, and wearable blood glucose monitoring device," *Progress in Electromagnetics Research M*, vol. 102, pp. 193-206, 2021.

[10] V. V. Deshmukh and S. S. Chorage, "Microstrip antennas are used for the non-invasive determination of blood glucose levels," in *2020 4th International Conference on Intelligent Computing and Control Systems (ICICCS),* pp. 720-725, May 2020.

[11] A. Firdausi, G. P. Hakim, F. A. Kurniawan, D. Septiyana, and M. Alaydrus, "Development of a microstrip antenna for glucose detection at millimeter waves," in *2019 IEEE Conference on Antenna Measurements & Applications (CAMA)*, pp. 181-183, Oct. 2019.

[12] T. Carlson and L. E. Asp, "Structural carbon fibre composite/PET capacitors-effects of dielectric separator thickness," *Composites Part B: Engineering*, vol. 49, pp. 16-21, 2013.

[13] S. Chisca, I. Sava, V. E. Musteata, and M. Bruma, "Dielectric and conduction properties of polyimide films," in *CAS 2011 Proceedings (2011 International Semiconductor Conference)*, vol. 2, pp. 253-256, Oct. 2011.

[14] H. Li, Y. Zhou, Y. Liu, L. Li, Y. Liu, and Q. Wang, "Dielectric polymers for high-temperature capacitive energy storage," *Chemical Society Reviews*, vol. 50, no. 11, pp. 6369-6400, 2021.

[15] Y. Cui, H. Zhang, J. Zhu, Z. Liao, S. Wang, and W. Liu, "Correlations of salivary and blood glucose levels among six saliva collection methods," *International Journal of Environmental Research and Public Health*, vol. 19, no. 7, p. 4122, 2022.

[16] V. Turgul and I. Kale, "Permittivity extraction of glucose solutions through artificial neural networks and non-invasive microwave glucose sensing," *Sensors and Actuators A: Physical*, vol. 277, pp. 65-72, 2018.

[17] A. K. Jha, Z. Akhter, N. Tiwari, K. M. Shafi, H. Samant, M. J. Akhtar, and M. Cifra, "Broadband wireless sensing system for non-invasive testing of biological samples," *IEEE Journal on Emerging and Selected Topics in Circuits and Systems*, vol. 8, no. 2, pp. 251-259, 2018.

[18] L. S. Vagish Kumar, "Salivary glucose levels and its correlation with serum glucose and glycemic status in diabetic patients," *Cukurova Med. J.*, vol. 39, pp. 7-18, 2014.

[19] J. Hanna, Y. Tawk, S. Azar, A. H. Ramadan, B. Dia, E. Shamieh, and A. A. Eid, "Wearable flexible body-matched electromagnetic sensors for personalized non-invasive glucose monitoring," *Scientific Reports*, vol. 12, no. 1, p. 14885, 2022.

[20] Q. Xue, Z. Li, Q. Wang, W. Pan, Y. Chang, and X. Duan, "Nanostrip flexible microwave enzymatic biosensor for non-invasive epidermal glucose sensing," *Nanoscale Horizons*, vol. 5, no. 6, pp. 934-943, 2020.

[21] A. Javed, A. Arif, M. Zubair, M. Q. Mehmood, and K. Riaz, "A low-cost multiple complementary split-ring resonator-based microwave sensor for contactless dielectric characterization of liquids," *IEEE Sensors Journal*, vol. 20, no. 19, pp. 11326-11334, 2020.

[22] M. Karami, P. Rezaei, S. Kiani, and R. A. Sadeghzadeh, "Modified planar sensor for measuring the dielectric constant of liquid materials," *Electronics Letters*, vol. 53, no. 19, pp. 1300-1302, 2017.

[23] Y. Rahayu, F. Arifa, D. A. Kholik, H. Masdar, and T. Praludi, "Design flexible microstrip antenna for non-invasive blood glucose detection," in *2022 International Conference on Radar, Antenna, Microwave, Electronics, and Telecommunications (ICRAMET)*, pp. 179-182, Dec. 2022.

[24] S. Saha, H. Cano-Garcia, I. Sotiriou, O. Lipscombe, I. Gouzouasis, M. Koutsoupidou, and E. Kallos, "A glucose sensing system based on transmission measurements at millimeter waves using microstrip patch antennas," *Scientific Reports*, vol. 7, no. 1, p. 6855, 2017.

[25] A. E. Omer, S. Safavi-Naeini, R. Hughson, and G. Shaker, "Blood glucose level monitoring using an FMCW millimeter-wave radar sensor," *Remote Sensing*, vol. 12, no. 3, p. 385, 2020.

[26] T. Chretiennot, D. Dubuc, and K. Grenier, "Microwave-based microfluidic sensor for non-destructive and quantitative glucose monitoring in aqueous solution," *Sensors*, vol. 16, no. 10, p. 1733, 2016.

[27] Y. Rahayu, W. N. Nugraha, T. Praludi, M. Alaydrus, and H. Masdar, "Experimental based blood glucose monitoring with a non-invasive cylindrical biosensor," *Progress in Electromagnetics Research M*, p. 115, 2023.

[28] F. Jiang, S. Li, Y. Yu, Q. S. Cheng, and S. Koziel, "Sensitivity optimization of antenna for non-invasive blood glucose monitoring," in *2017 International Applied Computational Electromagnetics Society Symposium (ACES)*, pp. 1-2, Aug. 2017.

Yusnita Rahayu was born in Pekanbaru, Indonesia. She received a B.Eng. degree in Electrical Engineering from the Department of Electrical Engineering, National Institute of Science and Technology Jakarta 1999. She received her M.Eng. and Ph.D. degrees from Universiti Teknologi Malaysia in 2004 and 2009, respectively. She is currently a Senior Lecturer in the Department of Electrical Engineering at Universitas Riau and a Senior Member of IEEE. Her research interests include antennas and propagation, microwave and millimeter wave components, sensors, and wireless communication.

Fildza Arifa is a Master of Philosophy student in the Faculty of Electrical Engineering at Universiti Teknologi Malaysia. She earned a B.Eng. degree from the Universitas Riau in 2023. She is very interested in studying the field of antennas and propagation. She was a presenter at the international conference on radars, antennas, microwaves, electronics, and telecommunications (ICRAMET) with the research title "Design Flexible Microstrip Antenna for Non-Invasive Blood Glucose Detection" on 7 December 2022 besides publishing a paper with the title "A WDM Scheme to Analyze the Performance of Rof Systems by Giving Various Bits Rates" in the *Journal of Informatics and Telecommunication Engineering*, July 2023.

Mudrik Alaydrus was born in Jakarta, Indonesia. He received the Dipl.-Ing. and Dr.-Ing. degrees in Electrical Engineering from Universitaet Hannover and Universitaet Wuppertal in 1997 and 2001, respectively. Since 2003, he has worked at Universitas Mercu Buana, Jakarta. Dr. Alaydrus is a Senior Member of IEEE and a member of Verein der Deutschen Elektroingenieure (VDE).

His current research includes microwave and millimeter wave components, wireless power transfers, wireless sensor networks, interaction between electromagnetics and materials, and mathematical modeling in signal processing.

Anhar has been a lecturer at the University of Riau since 2002. He took his Ph.D. at Brunel University London, UK, and finished in 2019. Currently, he is a senior lecturer and has been teaching many subjects such as data communication, traffic engineering, wireless sensor networks, electrical measurement, and signals and systems. In terms of research, he has been supervising many students and publishing many articles related to the performance analysis of sensor networks. He is also interested in investigating the performance of medium access control (MAC) and routing protocols in sensor networks, the Internet of Things (IoT), and Wi-Fi.

Teguh Praludi has been a researcher at the telecommunications research center of the National Research and Innovation Agency since 2003. He completed his master's program at Bandung Institute of Technology in 2013, study program of Radar. He currently researches telecommunications, especially radio frequency modules such as filters and antennas. He is currently a member of the Indonesian Engineers Association (PPI). Various research results have been published in journals and conference proceedings.

Huriatul Masdar was born in Limapuluh Kota, West Sumatra, Indonesia, in 1979. She received her S.Ked. and Dr. degrees from the Faculty of Medicine, Universitas Andalas, in 2004, and her M.Sc. degree in biomedical sciences from Vrije Universiteit, Amsterdam, in 2009. She is currently a senior lecturer and researcher at the Faculty of Medicine, Universitas Riau (UR). In addition, she conducts various research projects through national grants. Her research interests included histology and immunology. She has published five articles and attended four national and international symposia.

Syah Alam was born in Jakarta, Indonesia. He received a Bachelor Education of Engineering (S.Pd.) degree in electrical engineering from Universitas Pendidikan Indonesia (UPI) and an M.Eng. (M.T.) degree in telecommunication engineering from the Graduate Program of Electrical Engineering, Universitas Trisakti, in 2010 and 2012, respectively. In 2018, he joined the Department of Electrical Engineering Universitas Trisakti as a researcher and lecturer. From 2021, he is pursuing his Ph.D. at Universiti Teknikal Melaka Malaysia (UTeM) in the field of electronic engineering (RF and microwave). His research interests include microstrip antennae and microwave sensors for various applications.

Study on Esophageal Tumor Detection Based on the MTV Algorithm in Electrical Impedance Imaging

Peng Ran[1], Wei Liu[1], Minchuan Li[1], Yingbing Lai[1], Zhuizhui Jiao[2], and Ying Zhong [1]

[1]School of Bioinformatics

Chongqing University of Posts and Telecommunications, Chongqing 400065, China LLLVVV1145@163.com,
1145059948@qq.com, s210501009@stu.cqupt.edu.cn, s220501008@stu.cqupt.edu.cn,
s230501018@stu.cqupt.edu.cn

[2]School of Automation
Chongqing University of Posts and Telecommunications, Chongqing 400065, China
s220302003@stu.cqupt.edu.cn

Abstract – This paper presents a method for detecting and locating esophageal tumors using electrical impedance tomography (EIT) based on the modified total variation (MTV) regularization algorithm, utilizing a four-layer electrode array balloon detection structure. The optimal structure of the electrode array was obtained using the uniform design (UD) method. By integrating esophageal tissue structure information, physical models containing tumors at different locations were constructed. Using the adjacent excitation mode, the study compared average voltage, voltage dynamic range, and boundary voltage changes of electrode pairs within one-quarter of a cycle to analyze esophageal tumor characteristics. By comparing the correlation coefficients, relative errors, and imaging times of three reconstruction algorithms, the MTV algorithm, which best matches the morphological characteristics of the esophagus, was selected for image reconstruction. The calculated tumor height showed an error (ΔH) within 1 mm, indicating that EIT can provide vital information on the position, size, and electrical properties of esophageal tumors, demonstrating significant potential for clinical application in esophageal examinations.

Index Terms – Electrical impedance imaging, esophageal tumor, finite element inverse problem.

I. INTRODUCTION

Gastrointestinal tumors are a category of high-risk cancers, accounting for five of the top ten most common cancer types globally, with esophageal cancer particularly notable for its high incidence and mortality rates [1–2]. Esophageal tumors, malignant growths originating from the epithelial tissue of the esophagus, have the best treatment outcomes when detected early, hence timely detection can improve patient survival rates [3].

Traditional diagnostic methods for esophageal cancer have several limitations. For example, esophageal biopsies can cause bleeding and other complications, and CT scans are relatively expensive and involve radiation exposure. Because of the significant electrical property differences between tumor tissues and normal tissues [4], non-invasive and safe electrical impedance tomography (EIT) can reconstruct the electrical property distribution of the esophagus, obtain anatomical information, and facilitate the detection of esophageal conditions, further reflecting the positional information of pathological tissues.

EIT originated in archaeological geophysics and is characterized by functional imaging. Being non-destructive and non-invasive, it is gaining extensive application in medical diagnostics. After decades of research and innovation, EIT's clinical utility has been confirmed in monitoring lung function [5–6] and breast cancer [7], and it has shown potential in detecting seizure zones [8], strokes [9], and cerebral edema during dehydration treatment [10]. In recent years, many research teams have started using EIT for studies on the gastrointestinal tract, primarily focusing on the stomach. Research from the Chinese Academy of Medical Sciences has shown that EIT can non-invasively detect and assess gastric motility functions [11], and scholars at home and abroad have expanded its application to studies on gastric transport, gastric emptying [12–13], and the relationship between gastric fluid pH and conductivity [14–15]. Medical diagnostics based on EIT mainly involve external monitoring devices placed outside the monitored area. Recently, intraluminal impedance tomography has also been developed. For instance, evaluating the efficacy of localized prostate cancer ablation using a multi-electrode urethral impedance probe [16], and a needle-based impedance imaging system for tissue classification [17].

However, research on esophageal wall impedance imaging is still in its early stages. In this study, utilizing the structural information and prior knowledge of the conductivity of esophageal tissues and tumors, and employing a detection balloon device with a four-layer electrode array at varying depths, we analyze esophageal tissue functions and determine the location of esophageal tumors through model design, finite element calculations, and reconstruction algorithms.

II. THEORETICAL METHOD

A. Model establishment

Based on the optimal structure discussed later in this paper, the model was constructed and algorithm analysis was performed using the balloon detection device shown in Fig. 1 (a). The detection balloon contains four arrays of sensing electrodes, spaced 20 mm apart, with each array consisting of six uniformly arranged elec-

(a)

(b)
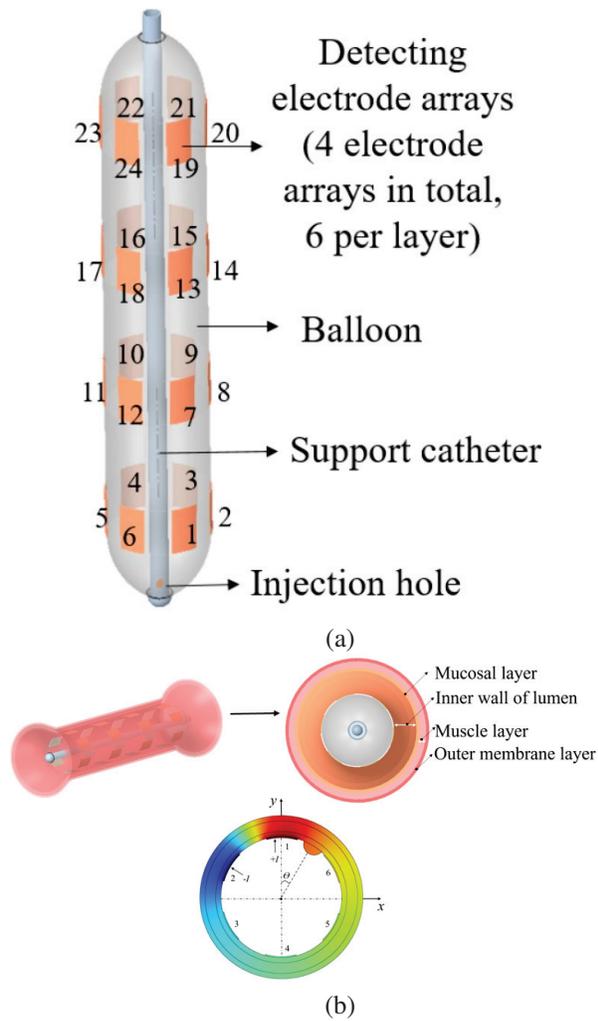
Fig. 1. (a) Detection balloon and (b) esophageal model structure.

trodes. Data collection for the electric field is achieved by slowly infusing the sealed balloon, allowing the surface electrodes of the balloon to make sufficient contact with the inner wall of the esophagus.

The human esophagus is approximately 25-30 cm in length, varying with individual chest lengths, has a wall thickness of 3-4 mm and a diameter of about 2 cm, and contains three narrow sections. By integrating esophageal tissue structure information, a three-dimensional EIT electric field model of a healthy esophagus and esophageal tumors was established using COMSOL to solve the forward problem. In studying the impact of the placement of a balloon within the esophagus on its morphological structure, the modeling considered two typical forms: Type 1 containing narrow sections and Type 2 without narrow sections. Healthy esophageal tissue is divided from the inside out into three layers: the mucosal layer, muscle layer, and outer layer, with respective thicknesses of 1 mm, 2 mm, and 1 mm. A two-dimensional cross-sectional structure of esophageal tissue is shown in Fig. 2 (b). The electrode-covered length of the esophagus is 10 cm, with tumors located at 5 cm ($h5$) and 8 cm ($h8$) positions in both Type 1 and Type 2, resulting in a model of the esophagus with a radius of 2, as shown in Fig. 2.
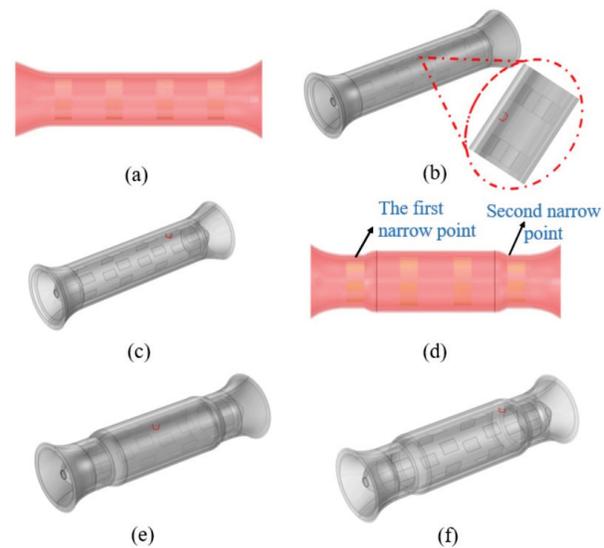
Fig. 2. Three-dimensional simulation model of the esophagus: (a) Type 1 including narrow areas, (b) model 1 $h5$, (c) model 2 $h8$, (d) Type 2 excluding narrow areas, (e) model 3 $h5$, and (f) model 4 $h8$.

B. UD optimization theory

The electrode array was optimized using a uniform design (UD) method based on finite element simulation. UD was introduced by Fang and Wang [18] in 1980, utilizing number theory to uniformly distribute sampling

points in space. This method enhances optimization efficiency, making it widely applicable in experiments. The general steps for multivariate optimization are as follows:

(1) Identify the variables and their search ranges, and set an appropriate number of levels for each variable.

(2) Select an appropriate UD table. Typically, a UD table is denoted as $U_n(q^m)$, where n represents the number of experimental runs, m represents the number of variables, and each variable has q levels [19].

(3) Determine the variable combinations based on the UD table and conduct the experiments.

(4) Analyze the experimental results to identify the "optimal" variable combination that corresponds to the maximization/minimization of the objective function.

(5) Based on the optimal variable combination, narrow down the search range for the next round of experiments. Repeat this process until the objective function stabilizes, at which point the final variable combination is obtained.

In this experiment, the standard deviation of current density is used to evaluate the uniformity of current distribution within the body. By comparing the standard deviations under different electrode array configurations, the configuration that yields the most uniform current distribution can be selected. The mathematical expression for the electrode array optimization objective function is:

$$\sigma_J = \sqrt{\frac{1}{N}\sum_{i=1}^{N}(J_i - \overline{J})^2},\qquad(1)$$

where J_i is the current density value at the i-th sampling point, $\overline{J}$ is the mean current density, and N is the total number of sampling points.

C. Solving the forward problem

The solution to electrical impedance imaging is derived through Maxwell's equations, which formulate a mathematical model for the electromagnetic field problem. Here, the forward problem involves knowing the conductivity distribution within a region and the boundary drive signals, and solving for the voltage distribution both inside and at the boundaries, essentially solving the boundary value problem of the electromagnetic field. The excitation current generates a specific electromagnetic field in the target area and, using electromagnetic field theory, an EIT mathematical model is constructed. The potential distribution function φ within the field and the conductivity distribution function σ satisfy the Laplace equation:

$$\nabla \bullet [\sigma(x,y)\nabla\phi(x,y)] = 0, (x,y) \in \Omega.\qquad(2)$$

The boundary conditions are:

$$\phi(x,y) = f(x,y), (x,y) \in \partial\Omega,\qquad(3)$$

$$\sigma(x,y)\frac{\partial\phi(x,y)}{\partial n} = j(x,y), (x,y) \in \partial\Omega.\qquad(4)$$

In equations (3) and (4), $\partial\Omega$ represents the boundary of the field domain, f represents the known boundary potential, j represents the current density flowing into the field domain Ω, and n represents the outward unit normal vector of the field domain.

In the simulated esophageal model, the electrical conductivity parameters are set as follows: mucosal conductivity is 1.02 S/m, muscle conductivity is 1.16 S/m, outer layer conductivity is 0.82 S/m, and electrode conductivity is 5.96×10^7 S/m. Tumor staging is an important means to evaluate the development of cancer, based on factors such as tumor size and depth of invasion. T1a denotes an early-stage tumor, while T2a represents an intermediate stage of cancer with a larger tumor size. To simulate different stages of tumor tissue, the esophageal lesion sizes and conductivities are set according to Table 1 in references [20–22].

Table 1: Tumor parameters of the esophagus

Parameter	T1a	T2a
Radius (mm)	2	3
Conductivity (S/m)	2.98~3.21	3.65~4.28

This study used 10 kHz, 5 mA alternating current for excitation. The adjacent excitation mode was employed, where current was injected between two adjacent electrode pairs, and the differential voltage was measured across other adjacent electrode pairs. This process was repeated with different electrode pairs until all pairs were used for excitation, resulting in a total of 504 boundary voltage data points used for EIT image reconstruction.

D. Image reconstruction

The inverse problem of EIT involves determining the distribution or changes in bioelectric resistivity given known voltage distributions and boundary information. A simulation was conducted using COMSOL and MATLAB, and a mesh was generated in EIDORS. The voltage data obtained from the forward simulation was used to reconstruct the esophageal EIT images using three algorithms: Laplace prior Gauss-Newton method, Tikhonov regularization, and conjugate gradient.

The Laplace prior Gauss-Newton method is performed within a Bayesian inference framework to estimate the posterior distribution of model parameters. The objective function is expressed as:

$$S(\theta) = \sum_{i=1}^{N}(y_i - f(x_i;\theta))^2 + \lambda\sum_{j=1}^{M}|\theta_j|.\qquad(5)$$

In this context, λ is the regularization factor controlling the strength of the regularization term and $|\theta_j|$

represents the L1 norm, which encourages sparsity in the parameters θ_j.

The motivation behind regularization methods is to address the numerical instability caused by ill-posed problems. The Tikhonov regularization method introduces a penalty term with an L2 norm to constrain the solution, and its objective function can be expressed as:

$$E_{T\text{ik}}(g) = \frac{1}{2} \parallel Ag - b \parallel_2^2 + \lambda_{T\text{ik}} \parallel L(g - \bar{g}) \parallel^2 . \quad (6)$$

In equation (6), the first term is the fidelity term and the second term is the penalty term. $\lambda_{T\text{ik}}$ is the regularization factor, $\bar{g}$ is the estimated value obtained from prior information, and L is a specific differential operator.

Modified total variation (MTV) regularization defines the minimization objective function for three-dimensional EIT as:

$$E(\sigma, u) = \min_{\sigma, u} \left\{ \begin{array}{l} \frac{1}{2} \parallel V_{\text{measured}} - V_{\text{simulated}}(\sigma) \parallel_2^2 + \\ \lambda_1 \parallel \sigma - u \parallel_2^2 + \lambda_2 \parallel u \parallel_{\text{TV}} \end{array} \right\}. \quad (7)$$

In equation (7), V_{measured} represents the actual measured voltage data and $V_{\text{simulated}}(\sigma)$ represents the simulated voltage calculated based on the current conductivity distribution σ. λ_1 and λ_2 are regularization parameters that control the contribution weights of the smoothing term and the total variation term to the overall optimization problem.

This function is used with an alternating minimization method. When u is fixed in equation (8), σ is updated to minimize the difference with the measured voltage and the auxiliary variable. When σ is fixed in equation (9), u is updated to minimize the difference with σ and the total variation. By alternately fixing u and σ, the nonlinear conjugate gradient method and the split Bregman method are used to iteratively solve for σ and u. Convergence is checked by examining whether $\parallel \sigma^{(k+1)} - \sigma^{(k)} \parallel$ is less than a preset threshold or whether the maximum number of iterations has been reached:

$$\sigma^{(k+1)} = \arg\min_\sigma \left\{ \begin{array}{l} \frac{1}{2} \parallel V_{\text{measured}} - V_{\text{simulated}}(\sigma) \parallel_2^2 + \\ \lambda_1 \parallel \sigma - u^{(k)} \parallel_2^2 \end{array} \right\}, \quad (8)$$

$$u^{(k+1)} = \arg\min_u \left\{ \begin{array}{l} \lambda_1 \parallel \sigma^{(k+1)} - u \parallel_2^2 + \\ \lambda_2 \parallel u \parallel_{\text{TV}} \end{array} \right\}. \quad (9)$$

The image quality is quantitatively evaluated using the correlation coefficient (CC) and relative error (RE), and the accuracy of tumor localization is assessed using the height error (ΔH) method.

(1) Correlation coefficient

The correlation coefficient evaluates the correlation between the actual conductivity distribution and the reconstructed result, defined as:

$$CC = \frac{\sum\limits_{i=1}^{z} (\xi^* - \bar{\xi}) \cdot (\xi - \bar{\xi})}{\sum\limits_{i=1}^{z} (\xi^* - \bar{\xi}*)^2 \cdot \sum\limits_{i=1}^{z} (\xi - \bar{\xi})^2}. \quad (10)$$

(2) Image relative error

The image relative error evaluates the deviation between the reconstructed conductivity distribution and the actual conductivity distribution, assessing the deviation between the reconstructed image and the ideal image. It is defined as:

$$RE = \frac{\parallel \xi^* - \xi \parallel_2}{\parallel \xi \parallel_2}. \quad (11)$$

In this context, ξ represents the actual distribution of electrical conductivity within the field, $\bar{\xi}$ denotes the mean of ξ, ξ^* signifies the computed distribution of electrical conductivity, and $\bar{\xi}*$ stands for the mean of ξ^*. A smaller RE and a closer CC to 1 indicate a more accurate reconstruction of the image.

(3) Height error

Establishing a coordinate system with the electrode covering the esophageal section, with the center of the bottom cross-sectional circle as the coordinate origin, let the actual height of the tumor be H and the simulated calculated height be h. Then, the height error is defined as:

$$\Delta H = |H - h|. \quad (12)$$

A smaller height error, ΔH, reflects a better reconstruction of the imaging results.

III. EXPERIMENTAL RESULTS AND ANALYSIS

A. Optimization of electrode array

Table 2 lists the five parameters to be optimized along with their respective optimization ranges. Below are the criteria and explanations for selecting these parameters:

(1) The electrodes are attached to the surface of the balloon, with the width represented by the central angle. Furthermore, the product of the electrode unit width and the number of electrodes in a single layer must be less than 360°.

Table 2: Electrode array optimization parameters

Variable	Unit	Level
L Electrode length	mm	[5.2,14.8]
D Electrode width	deg	[20,32]
T Electrode thickness	mm	[1.2,2.4]
$S1$ Number of electrodes per layer		[3,15]
$S2$ Number of electrode layers		[1,13]

(2) The product of the electrode length and the number of electrode layers must be less than the length of the target region.

(3) If the number of electrodes results in a decimal value, then it should be rounded to the nearest integer.

Table 3 presents the UD for the first round of electrode array optimization. $U_n(13^5)$ UD was selected, with a deviation $D=0.0194$, indicating good uniformity that meets the design requirements of this study. The numbers in parentheses represent the sampling points of UD, and the actual optimization parameters can be calculated based on the corresponding sampling points. For example, the first sampling point combination in $U_n(13^5)$ is (11, 6, 10, 2, 3), which corresponds to the variable combination of optimization parameters $(L, D, T, S1, S2)$ as (13.2, 25, 2.1, 4, 3).

Table 3: UD table for the first round of electrode array parameter optimization

No.	L	D	T	S1	S2
1	13.2(11)	25(6)	2.1(10)	4(2)	3(3)
2	9.2(6)	27(8)	2.4(13)	8(6)	10(10)
3	8.4(5)	32(13)	1.4(3)	9(7)	2(2)
4	6(2)	26(7)	1.3(2)	13(11)	11(11)
5	14.8(13)	28(9)	1.5(4)	12(10)	5(5)
6	11.6(9)	24(5)	1.2(1)	7(5)	7(7)
7	14(12)	21(2)	2.3(12)	11(9)	1(1)
8	6.8(3)	22(3)	1.9(8)	10(8)	12(12)
9	7.6(4)	31(12)	1.6(5)	3(1)	9(9)
10	5.2(1)	29(10)	2(9)	6(4)	6(6)
11	10.8(8)	30(11)	1.7(6)	5(3)	13(13)
12	10(7)	20(1)	1.8(7)	15(13)	4(4)
13	12.4(10)	23(4)	2.2(11)	13(12)	8(8)

According to the UD update method, the optimization trajectory of the electrode array is shown in Fig. 3. As can be seen from Fig. 3, after three rounds of UDs, the objective function tends to stabilize and reaches its minimum value. The optimal parameters of the electrode array are shown in Table 4.

Table 4: Optimal electrode array structural parameters

L (mm)	D (deg)	T (mm)	S1	S2
10	30	1.9	6	4

B. Positive simulation results

Figure 4 presents the simulation results obtained using the finite element method under uniform excitation conditions, with Fig. 4 (c) showing the two-

Range of L/mm	5.2:0.8:14.8	7.6:0.4:12.4	8.8:0.2:11.2
Range of D/deg	20:1:32	25:0.5:31	28:0.25:31
Range of T/mm	1.2:0.1:2.4	1.5:0.05:2.1	1.5:0.05:2.1
Range of S1	3:1:15	3:0.5:9	3:0.5:9
Range of S2	1:1:13	1:0.5:7	1:0.5:7
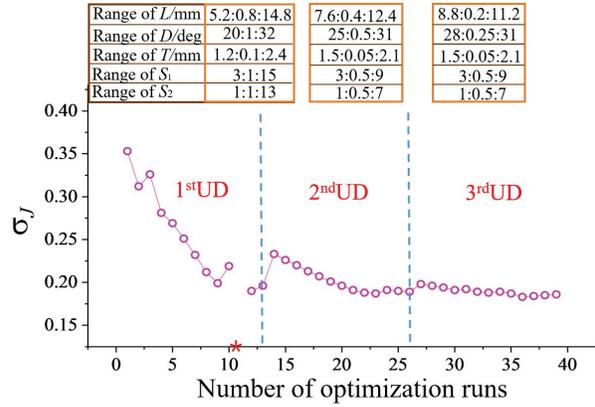
Note: The parameters for the 11th experiment were inconsistent and thus excluded.

Fig. 3. Trace plot of electrode array optimization.

dimensional cross-sectional electric potential distribution of esophageal tumors. There is a significant difference in the electric potential distribution between healthy esophagi and those with tumors, for the same esophageal morphology. Furthermore, when the tumor position is fixed, the electric potential distribution varies with different esophageal morphologies. Figure 5 shows the average voltage and voltage dynamic range results for six scenarios obtained by simulating the esophagus without tumors in two esophageal morphologies, and with tumors of radii 2 mm and 3 mm at positions 5 cm and 8 cm in the esophagus. The voltage dynamic range is
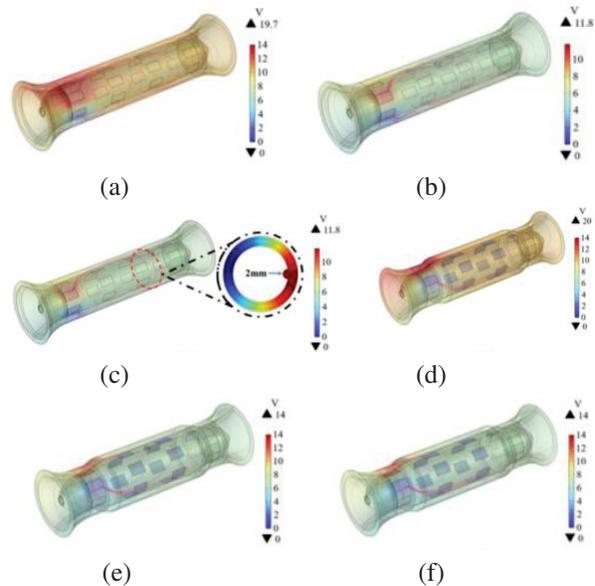
Fig. 4. Simulated distribution of esophageal potential: (a) Type 1 healthy esophagus, (b) model 1, (c) model 2, (d) Type 2 healthy esophagus, (e) model 3, and (f) model 4.
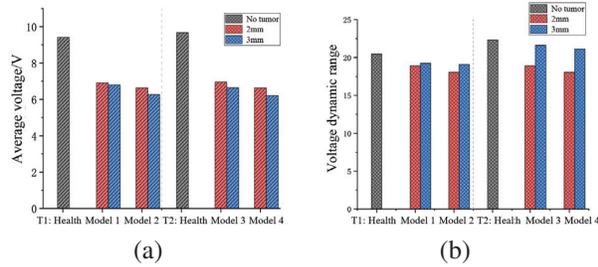
Fig. 5. (a) Average voltage and (b) voltage dynamic range of different models.

defined as:

$$V_{DR} = 20\log_{10}\left(\frac{V_{\max}}{V_{\min}}\right) dB. \tag{13}$$

In the formula, $V_{\max}$ and $V_{\min}$ represent the maximum and minimum voltage, respectively.

In the two types of models with tumor radii of 2 mm and 3 mm, the average voltage in the esophagus with tumors is lower than in the healthy esophagus, reflecting that the higher electrical conductivity of tumor tissue reduces the local potential. This result validates the application value of impedance imaging in distinguish-

ing between normal and pathological esophageal tissues. Meanwhile, the smaller voltage dynamic range indicates the high quality of the model reconstruction.

To investigate the effect of tumor position at different locations on boundary voltage, Fig. 1 (b) establishes a Cartesian coordinate system for the cross-section with the tumor located at 2 cm, recording the tumor position through angles. Figure 6 shows the variation in boundary voltage during one-fourth of the excitation signal cycle when electrodes 1 and 2 are the excitation electrode pair and the tumor is located at 30°, 90°, 150°, and -90°, with the other adjacent electrodes serving as measurement electrodes. To facilitate better comparison of the data in the figure, the measurement values of electrode pair 6-7 are symmetrical about y=0. When the tumor is at 30°, the adjacent electrodes are 1 and 6. It can be clearly seen from Fig. 6 (a) that the largest changes are observed in the measurement electrode pairs 5-6 and 6-7, which are adjacent to the tumor. Similarly, in Figs. 6 (b-d), it is found that the closer the electrodes are to the tumor area, the greater the changes in the relevant measurement electrode pairs. This result suggests that the trend of changes in measurement electrode pairs can be used to preliminarily locate the tumor position.
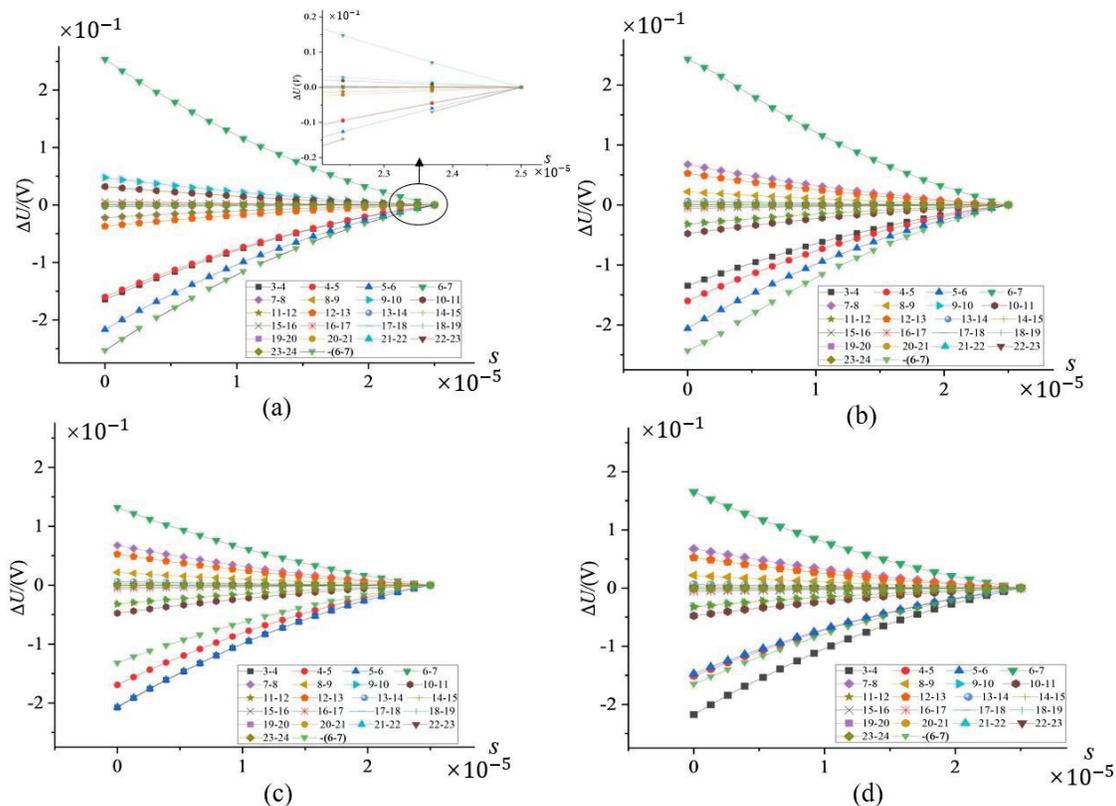
Fig. 6. Relationship between changes in boundary voltage and tumor location: (a) tumor located at 30°, (b) tumor located at 90°, (c) tumor located at 150°, and (d) tumor located at -90°.

C. Reconstructed image comparison

In this study, we employed the Laplace prior Gauss-Newton method, the Tikhonov regularization algorithm, and the MTV algorithm to reconstruct EIT images of the esophageal model. The imaging results were presented as two-dimensional slices with 0.01 mm intervals. Figures 7 (a-c) illustrate the conductivity distribution of the esophagus at 4 cm, 5 cm, 6 cm, 7 cm, and 8 cm. Due to the inherent smoothness of the Tikhonov regularization algorithm, the conductivity differences between esophageal tissue and tumors were significant and had clear boundaries, resulting in a blurred boundary between the target and background regions [23]. The application of the MTV algorithm ensured the contrast of the reconstructed images, with better edge preservation, effectively mitigating the excessive smoothing issue caused by the Tikhonov algorithm. Table 2 provides a quantitative analysis of the imaging results at different layers using the correlation coefficient and relative error. Additionally, the reconstruction times for the Laplace prior Gauss-Newton method, Tikhonov regularization algorithm, and MTV algorithm were 1.163 s, 1.124 s, and 0.654 s, respectively.

(a)

(b)

(c)
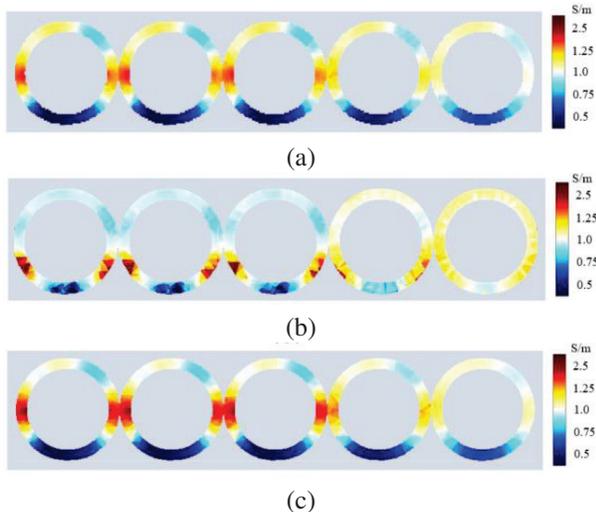
Fig. 7. Reconstruction images of different layers of the esophagus: (a) GN (Laplace prior), (b) Tikhonov regularization (TK), and (c) MTV.

The results in Table 5 show that the imaging correlation coefficient of the MTV algorithm ranges from 0.797 to 0.845, and it has the smallest relative error. The imaging quality using the Laplace prior Gauss-Newton method and Tikhonov regularization algorithm is reduced by an average of 24.02% and 16.96%, respectively. Therefore, due to its superior imaging quality and real-time performance, the MTV algorithm is particularly suitable for EIT in clinical esophageal detec-

Table 5: Evaluation of reconstructed images from different positions

Algorithm	Position	CC	RE
GN		0.706	0.268
TK	4 cm	0.814	0.232
MTV		0.845	0.196
GN		0.723	0.256
TK	5 cm	0.784	0.244
MTV		0.797	0.213
GN		0.687	0.236
TK	6 cm	0.765	0.241
MTV		0.811	0.217
GN		0.715	0.258
TK	7 cm	0.782	0.237
MTV		0.830	0.193
GN		0.692	0.247
TK	8 cm	0.812	0.239
MTV		0.823	0.201

tion scenarios that require handling large-scale high-dimensional data.

Using the MTV algorithm, the conductivity was set to 3.65 S/m, 3.94 S/m, and 4.28 S/m according to the conductivity range for a tumor radius of 3 mm as shown in Table 1. Voltage data were collected for each conductivity setting, and image reconstruction was performed using the conjugate gradient algorithm. Figure 8 shows that as the conductivity increases, the color of the esophageal lesion in the reconstructed image becomes darker, which corresponds to the actual situation.
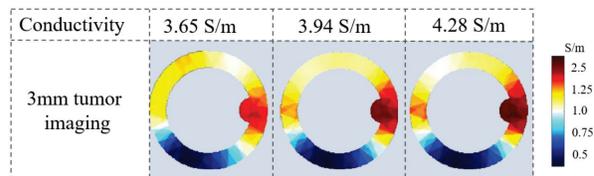
Fig. 8. Tumor reconstruction image slice.

D. Positioning analysis

Using the MTV algorithm for EIT, the 3D reconstructions of two different esophageal shapes with 2 mm tumors located at 5 cm and 8 cm are shown in Fig. 8. The tumor locations are indicated by black arrows in Figs. 8 (b-d). Table 6 presents the tumor layer height h after imaging and the results of evaluating the 3D reconstructed esophageal tumor positions using height error ΔH. Quantitative analysis shows that ΔH is within 1 mm, further demonstrating that the esophageal reconstruction images obtained using this impedance imaging algorithm are closer to the original model, making tumor localization more accurate. This also proves the feasibility of

(a)   (b)   (c)   (d)
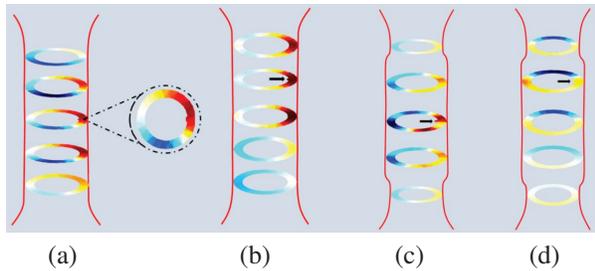
Fig. 9. Results of three-dimensional reconstruction of the esophagus based on simulation data: (a) model 1, (b) model 2, (c) model 3, and (d) model 4.

Table 6: Height error of tumors at different locations

Parameter	Model 1	Model 2	Model 3	Model 4
H (mm)	50.42	80.90	40.26	80.86
ΔH (mm)	0.42	0.90	0.74	0.68

using EIT for detecting esophageal tumors and its capability in localizing tumor regions.

IV. CONCLUSION

This study employed the UD method to optimize the electrode array and established EIT models for both healthy esophagus and esophagus with tumors at different locations. We discussed the boundary voltage changes of tumors at different positions on the same horizontal plane, noting that the measurement electrode pairs nearest to the tumor exhibited the most significant changes. This trend was used for the preliminary localization of the tumor. The Laplace prior Gauss-Newton method, the Tikhonov regularization algorithm, and the MTV algorithm were employed for image reconstruction of the esophageal model. The MTV algorithm achieved the highest imaging correlation coefficient and the smallest relative error, while requiring the least amount of time and providing the best imaging quality. MTV method was used to reconstruct the 3D structure of the esophagus, and tumor position evaluation through height error ΔH showed that all errors were within 1 mm. This demonstrates the capability of EIT in localizing tumors.

REFERENCES

[1] R. L. Siegel, K. D. Miller, H. E. Fuchs, and A. Jemal, "Cancer statistics, 2022," *CA: A Cancer Journal for Clinicians*, vol. 72, no. 1, pp. 7-33, Jan. 2022.

[2] H. Li, J. Yu, R. Zhang, X. Li, and W. Zheng, "Two-photon excitation fluorescence lifetime imaging microscopy: A promising diagnostic tool for digestive tract tumors," *Journal of Innovative Optical Health Sciences*, vol. 12, no. 5, art. 1930009, 2019.

[3] Z. Yu, X. Bai, R. Zhou, G. Ruan, M. Guo, W. Han, and H. Yang, "Differences in the incidence and mortality of digestive cancer between Global Cancer Observatory 2020 and Global Burden of Disease 2019," *International Journal of Cancer*, vol. 154, no. 4, pp. 615-625, 2024.

[4] Q. Huang, D. Lu, J. Han, H. Yu, W. Dong, K. Cai, and X. Yu, "Comparison of dielectric properties of normal human esophagus and esophageal cancer using an open-ended coaxial probe," *Journal of Southern Medical University*, vol. 41, no. 11, pp. 1741-1746, 2021.

[5] M. Xu, H. He, and Y. Long, "Lung perfusion assessment by bedside electrical impedance tomography in critically ill patients," *Frontiers in Physiology*, vol. 12, art. 748724, 2021.

[6] V. Tomicic and R. Cornejo, "Lung monitoring with electrical impedance tomography: Technical considerations and clinical applications," *Journal of Thoracic Disease*, vol. 11, no. 7, art. 3122, 2019.

[7] F. Xu, M. Li, J. Li, and H. Jiang, "Diagnostic accuracy and prognostic value of three-dimensional electrical impedance tomography imaging in patients with breast cancer," *Gland Surgery*, vol. 10, no. 9, pp. 2673-2680, 2021.

[8] A. Witkowska-Wrobel, K. Aristovich, M. Faulkner, J. Avery, and D. Holder, "Feasibility of imaging epileptic seizure onset with EIT and depth electrodes," *Neuroimage*, vol. 173, pp. 311-321, 2018.

[9] T. Dowrick, C. Blochet, and D. Holder, "In vivo bioimpedance changes during haemorrhagic and ischaemic stroke in rats: Towards 3D stroke imaging using electrical impedance tomography," *Physiological Measurement*, vol. 37, no. 6, pp. 765-784, 2016.

[10] B. Yang, B. Li, C. Xu, S. Hu, M. Dai, J. Xia, and F. Fu, "Comparison of electrical impedance tomography and intracranial pressure during dehydration treatment of cerebral edema," *Neuro Image: Clinical*, vol. 23, art. 101909, 2019.

[11] Z. Li and C. Ren, "Gastric motility measurement and evaluation of functional dyspepsia by a bio-impedance method," *Physiological Measurement*, vol. 29, no. 6, art. S373, 2008.

[12] M. R. Huerta-Franco, M. Vargas-Luna, J. B. Montes-Frausto, C. Flores-Hernández, and I. Morales-Mata, "Electrical bioimpedance and other techniques for gastric emptying and motility evaluation," *World Journal of Gastrointestinal Pathophysiology*, vol. 3, no. 1, pp. 10-18, 2012.

[13] R. Wicaksono, P. N. Darma, A. Inoue, H. Tsuji, and M. Takei, "Wearable sectorial electrical impedance

tomography and k-means clustering for measurement of gastric processes," *Measurement Science and Technology*, vol. 33, no. 9, art. 094002, 2022.

[14] W. R. Wicaksono, P. N. Darma, K. Sakai, D. Kawashima, and M. Takei, "Imaging of gastric acidity scale by integration of pH-conversion model (pH-CM) into 3D-gastro electrical impedance tomography (3D-g-EIT)," *Sensors and Actuators B: Chemical*, vol. 366, art. 131923, 2022.

[15] C. S. Chaw, E. Yazaki, and D. F. Evans, "The effect of pH change on the gastric emptying of liquids measured by electrical impedance tomography and pH-sensitive radiotelemetry capsule," *International Journal of Pharmaceutics*, vol. 227, no. 1-2, pp. 167-175, 2001.

[16] J. Liu, Ö. Atmaca, and P. P. Pott, "Needle-based electrical impedance imaging technology for Needle Navigation," *Bioengineering*, vol. 10, no. 5, art. 590, 2023.

[17] Z. Cheng, D. Dall'Alba, P. Fiorini, and T. R. Savarimuthu, "Robot-assisted electrical impedance scanning system for 2D electrical impedance tomography tissue inspection," in *Proc. 2021 43rd Annual International Conference of the IEEE Engineering in Medicine & Biology Society (EMBC)*, pp. 3729-3733, Nov. 2021.

[18] K. T. Fang and Y. Wang, *Number-Theoretic Methods in Statistics*. Boca Raton: CRC Press, 1993.

[19] K. T. Fang, D. K. Lin, P. Winker, and Y. Zhang, "Uniform design: Theory and application," *Technometrics*, vol. 42, no. 3, pp. 237-248, 2000.

[20] A. Zandi, A. Gilani, F. Abbasvandi, P. Katebi, S. R. Tafti, S. Assadi, and M. Abdolahad, "Carbon nanotube based dielectric spectroscopy of tumor secretion; electrochemical lipidomics for cancer diagnosis," *Biosensors and Bioelectronics*, vol. 142, art. 111566, 2019.

[21] D. G. Smith, S. R. Potter, B. R. Lee, H. W. Ko, W. R. Drummond, J. K. Telford, and A. W. Partin, "In vivo measurement of tumor conductiveness with the magnetic bioimpedance method," *IEEE Transactions on Biomedical Engineering*, vol. 47, no. 10, pp. 1403-1405, 2000.

[22] P. I. Wu, J. A. Sloan, S. Kuribayashi, and H. Gregersen, "Impedance in the evaluation of the esophagus," *Annals of the New York Academy of Sciences*, vol. 1481, no. 1, pp. 139-153, 2020.

[23] M. Vauhkonen, D. Vadász, P. A. Karjalainen, E. Somersalo, and J. P. Kaipio, "Tikhonov regularization and prior information in electrical impedance tomography," *IEEE Transactions on Medical Imaging*, vol. 17, no. 2, pp. 285-293, 1998.

Peng Ran was born in February 1981. Ph.D., associate professor, Chongqing Innovative Young Talents Training, Chongqing smart Medical system and core technology innovation team member, Chong-qing Medical Electronics and Information Technology Engineering Research Center team member. Since 2006, he has been engaged in cutting-edge research and development of new medical equipment and detection technology.

Wei Liu was born in February 1999. Currently pursuing a master's degree in Biomedical Engineering at the School of Bioinformatics, Chongqing University of Posts and Telecommunications. Her main research direction is the study of esophageal force electrical imaging models based on mechanical and impedance feature reconstruction.

Minchuan Li, born in September 1997, is currently a postgraduate student specializing in Biomedical Engineering at the School of Bioinformatics, Chongqing University of Posts and Telecommunications. His research is centered on advanced esophageal dynamic function detection methods, particularly focusing on piezoelectric impedance feature coupling.

Yingbing Lai was born in December 1998 and is a graduate student majoring in Biomedical Engineering at the School of Bioinformatics, Chongqing University of Posts and Telecommunications. His main research direction is the analysis of the coupling characteristics between esophageal bioelectrical impedance and mechanics.

Zhuizhui Jiao was born in February 1996. Currently a graduate student majoring in Instrument Science and Technology at the School of Automation, Chongqing University of Posts and Telecommunications. The research direction is the fluid structure coupling characteristics and dynamic functional detection methods of narrow liquid cavities.

Ying Zhong was born in October 1998. Currently studying at the School of Bioinformatics, Chongqing University of Posts and Telecommunications. Her research direction includes classification and evaluation methods for gastrointestinal diseases based on the coupling characteristics of biological impedance and biomechanics.

High Gain Circularly Polarized Patch Antenna for Communications Between Cutting Tools and the Control Unit of Mining Equipment

Collin T. Kringlen[1], Atef Z. Elsherbeni[1], and Jamal Rostami[2]

[1]Department of Electrical Engineering
Colorado School of Mines, Golden, CO, USA
collinkringlen@mines.edu, aelsherb@mines.edu

[2]Department of Mining Engineering
Colorado School of Mines, Golden, CO, USA
rostami@mines.edu

Abstract – A 2.44 GHz high gain circular polarized (CP) patch antenna is designed, fabricated and tested for operation while mounted on a rotating cutting drum of a mining or excavation machine. This design incorporates a radiating element that is elevated above the ground plane to increase the antenna gain. The design utilizes a single feed source and a square truncated corner patch to produce CP radiation. The gain of the final design reached 9 dBi with a sufficiently CP axial ratio and more than -25 dB cross-polarization isolation. This system enables the data communication between the rock cutting tools installed on the machine and the unit to enable the remote monitoring of tool conditions as well as identification of the formations being mined.

Index Terms – Circular polarization, high gain, mining and excavation equipment, patch antenna.

I. INTRODUCTION

The mining industry is considered to be inherently dangerous, where workers are constantly exposed to risks such as confined spaces, dust, falling debris and heavy machinery [1, 2]. In response to the working conditions at various mining operations, there has been a trend in the mining and heavy civil construction industries towards the automation of excavation equipment, primarily aimed at minimizing operator presence in hazardous environments. This project seeks to advance this mission by developing a sensing system for various excavation units such as continuous miner (CM) or similar machines equipped with a pick cutter drum. Figure 1 shows an example of this machine. The sensing system, called "Smart Pick" or "Smart Bit" will provide the necessary data to operate the machine as if operatives were in close proximity to the machine. These data include cutting forces on the pick cutters which allows for monitoring bit wear and identification of the forma-

tion being mined. This is based on the measurement of cutting forces on the picks and analysis of signals using AI and ML algorithm for feature extraction to enable the machine to perform the above noted goals. Cutting force is combined with additional information such as drum rotation speed, thrust, rate of penetration, and drum torque/power to allow for identifying the type of rock being excavated. These data also have the potential to increase operational efficiency through the analysis of equipment wear data. Bit sensors, which are customized capacitive or piezoelectric load sensors, are installed between the pick cutter and the bit block mounted on the cutting drum.

To transfer data from the rotating cutting drum to an onboard computer, control system or base remote station for analysis and real time monitoring of the working

Fig. 1. Picture of a continuous miner commonly used in mining of coal, trona, salt and soft rock types. Pick cutters are mounted on a drum to apply force and break the rock [14].

conditions, specialized antennas were developed to collect and transmit the data from the cutting tools to the control unit. The data transmission component should function in an environment that involves dust, presence of water or moisture in the air, impact by objects, and very high intensity vibration.

A block diagram of the system can be seen in Fig. 2. The yellow traces represent the signal output from each pick's sensor. These data are then aggregated and pre-processed on the drum (orange box), and then transmitted by the designed data transmission system through the circular polarized (CP) antenna. Given the possibility of impact and interferences, a protective system had to be installed to prevent damage to the antenna by the impact of other objects. The protective system has to be designed in such way not to interfere or impede data transmission. As such, a special box was designed to offer protection against impact to the antennas. The transmitting and receiving antennas are placed inside the shown protective green box/cover.
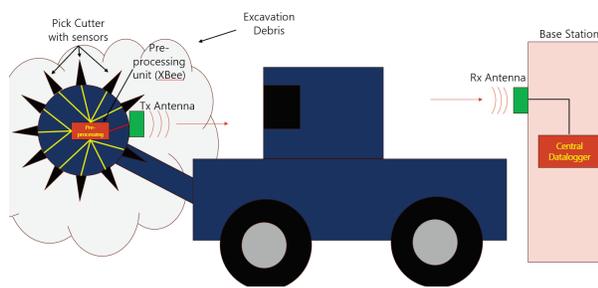
Fig. 2. Overall system configuration.

The antennas were required to have the following specifications for good communications: operation at 2.44 GHz, more than 6 dBi of gain, CP radiation and more than -25 dB isolation from the cross-polarized radiation. The unlicensed 2.44 GHz operation was chosen to be compatible with the rest of the communication hardware [3]. More than 6 dBi was selected to ensure a strong wireless link in the presence of debris, dust and water in the operational environment. This was determined through the Friis transmission equation. CP was necessary because the input data will be from the cutting tools on a rotating drum/cutterhead, thus putting the antennas at constantly changing orientations. Lastly, strong isolation of the cross polarized radiation is useful to reject any reflections produced in the underground environment [4].

Many different designs were reviewed to completely comprehend how a patch antenna might be optimized to this application [5–13]. Through this review, the elevation of the patch antenna above the ground plane stood

out as a common strategy to develop high gain patch antennas.

II. L-SHAPED PATCH ANTENNA DESIGN

The current antenna design was initially based on the typical design outlined in [15, 16]. However, this published antenna design utilized copper sheets without any substrate backing for rigid support. The substrate backed antenna in Fig. 3 creates a more physically robust design which is required for the current application, given the harsh environment the antenna will be experiencing and the need for amplification of the signal. The substrate utilized was FR4 with $\varepsilon_r = 4.4$ and electric conductivity $\sigma = 0.02$. Furthermore, the antenna incorporates a two-piece patch: the main radiating element and a triangle vertical patch acting as a feed. The main radiating element is oriented parallel to the ground plane and utilizes a square, with truncated corner patch shape to produce CP radiation. This patch is elevated above the ground plane, leaving an air gap. The air gap acts as a low loss substrate, which contributes to the high gain in the proposed design. The small triangle patch, which is perpendicular to the ground plane, is used to feed the radiating element. Figure 4 shows the connection between the two patch components along with the coaxial center pin joint. The coaxial center pin is fixed directly at the bottom point of the triangle. This triangle acts as an efficient feeding method and contributes to the gain by directing more energy in the broadside direction and reducing losses that occur on the sides of the antenna. Lastly, a large ground plane is utilized to direct more energy in the broadside direction and further increase the gain. Right-hand and left-hand circularly polarized (RHCP and LHCP) antennas were designed and fabricated based on this design methodology and configuration.
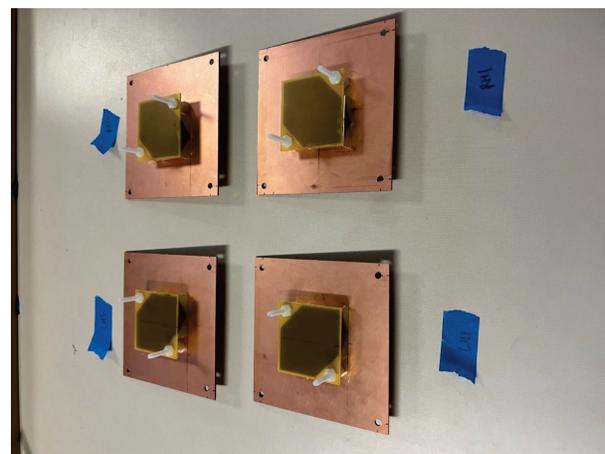
Fig. 3. Fabricated LHCP L-shaped patch antenna.
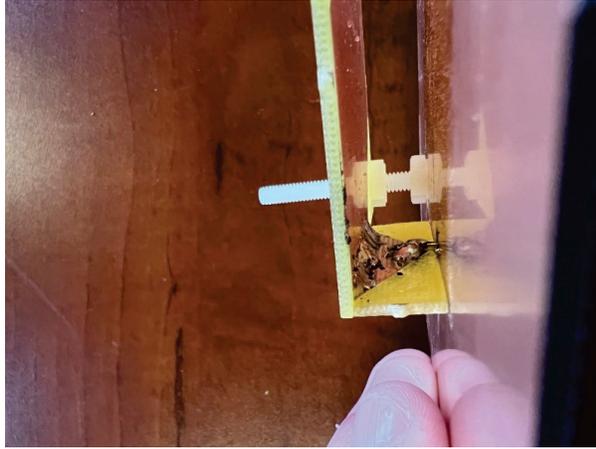
Fig. 4. Inside view of solder joint of L-shaped patch.

A. Protective antenna covers

Given the violent, dusty, wet, underground environment, the antenna must have some functional protection. Thus, protective antenna covers were designed and fabricated. The box can also be sealed from air circulation to prevent gases from entering the area around the antenna, a measure that would be critical in getting pertinent certifications for the use of this system in gassy environments such as underground coal mines. The antenna utilizes a vertical coaxial feed as shown in Fig. 5. This required a two-piece cover, with a top and bottom portion, to act as enclosure. Furthermore, a 90-degree connector had to be used on the coaxial connection to allow for the design of a flat cover for a flush mounting solution on the drum. This cover is shown in Fig. 6.
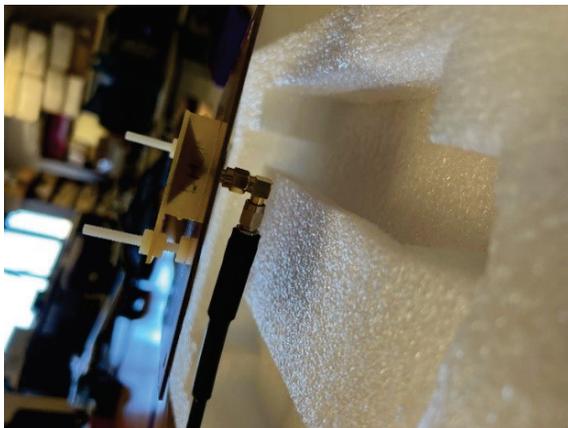
Fig. 5. L-shaped patch antenna coaxial feed.

B. Simulations

The simulations were conducted using the computational electromagnetic simulator (CEMS v5) which uti-
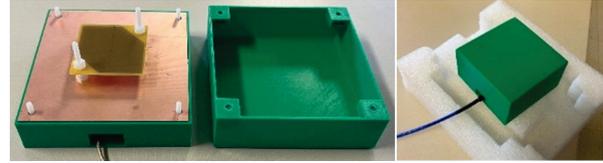
Fig. 6. L-shaped patch protective antenna cover.

lizes the finite difference time domain (FDTD) method [17, 18]. The RHCP and LHCP simulated models can be seen in Fig. 7. Figure 8 shows a dimensioned image of this design. The corresponding values for each dimension are shown in Table 1. These designs were optimized in the simulation tool for the requirements described in the introduction section. Various simulated results are shown in Figs. 9 to 13. Figure 9 shows input reflection of -20 dB at 2.44 GHz for the LHCP and RHCP simulations. Moving into the far field results, less than 1 dB AR is shown at broadside direction for both models in Figs. 10 and 11. Lastly, in Figs. 12 and 13, more than -25 dB cross-polarized isolation and 9 dB
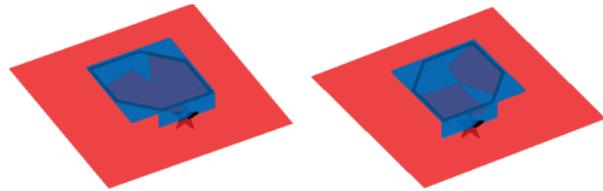
Fig. 7. L-shaped patch LHCP and RHCP simulated antennas.
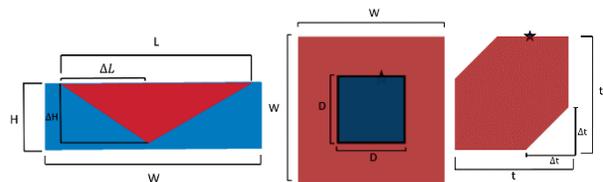
Fig. 8. L-shaped patch antenna with dimensions defined.

Table 1: L-shaped patch dimension values

Parameter	Dimension (mm)
W	120
D	54.5
T	51.5
Δt	19.25
H	11
ΔH	10
L	32.25
ΔL	14.5
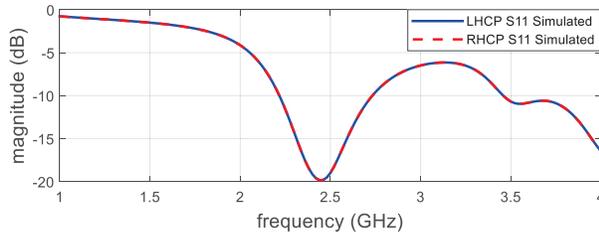
Fig. 9. L-shaped patch LHCP and RHCP simulated S_{11}.
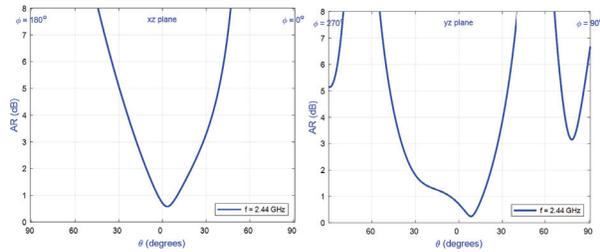
Fig. 10. L-shaped patch LHCP AR in xz (left) and yz (right) planes.
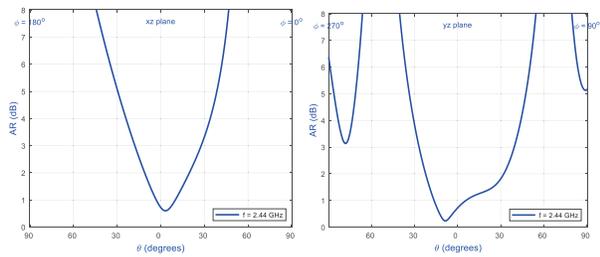
Fig. 11. L-shaped patch RHCP AR in xz (left) and yz (right) planes.
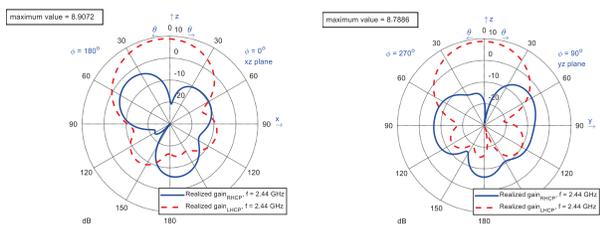
Fig. 12. LHCP simulated radiation patterns with realized gain in xz (left) and yz (right) planes.

Fig. 13. LHCP simulated radiation patterns with realized gain in xz (left) and yz (right) planes.

Fig. 14. RHCP+RHCP antenna simulation (co-pol) configuration.
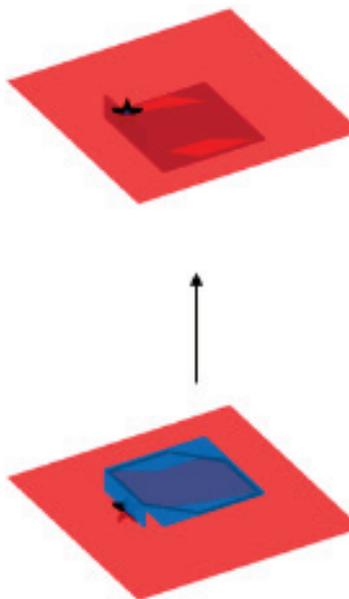
Fig. 15. RHCP+LHCP antenna simulation (cross-pol) configuration.

of gain are shown. Thus, the simulated model meets all requirements.

A separate set of simulations with two antennas were also conducted to collect simulated S_{21} data which will later be used to verify the antenna gain. The simulations were conducted with a co-pol antenna pair and a cross-pol antenna pair. Figures 14 and 15 show the simulation setups. The antennas are separated by 22 mm

from ground plane to ground plane. The corresponding S_{21} results are shown in Fig. 16. As expected, in a line-of-sight transmission set up, the co-pol antennas are most efficient with -9.8 dB S_{21} when compared to the cross-pol S_{21} of -30 dB. The cross-pol antenna pair would be used in an application where a reflection of the wave between transmit and receive occurs, such as radar systems. At that time the S_{21} would be in the order of -9.8 dB.
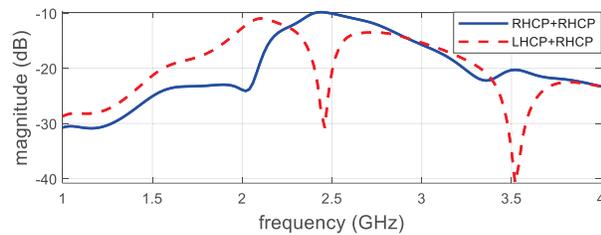
Fig. 16. RHCP+RHCP (co-pol) and RHCP+LHCP (cross-pol) simulated S_{21}.

C. Fabrication and testing

Two RHCP and two LHCP antennas were fabricated as seen in Figs. 17 and 18. For brevity, one of each polarization will be shown with its corresponding measured results. The holes on all four corners of the antenna ground planes are for the plastic mounting screws of the antenna covers. These antennas were then tested, and results were compared with the simulated data.

The antenna S_{11} was measured using a VNA where the covered and uncovered antennas are shown in Fig. 19. The data collected was then plotted with the simulated data to allow for a comprehensive comparison. These plots are shown in Figs. 20 and 21, where Fig. 20
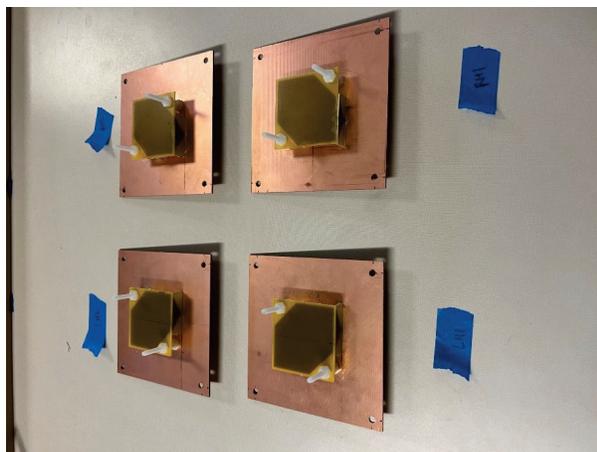
Fig. 17. Fabricated LHCP L-shaped patch antenna.
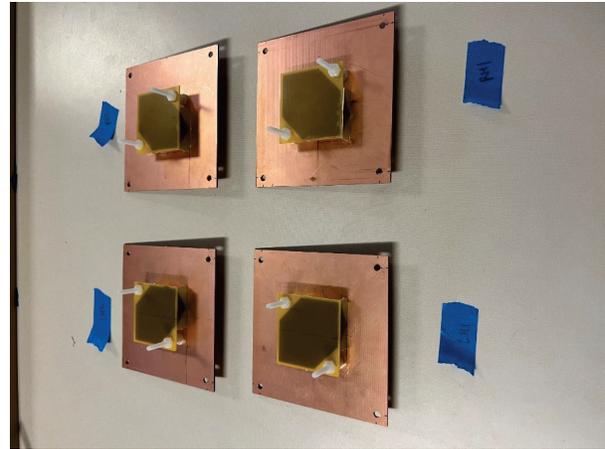
Fig. 18. Fabricated RHCP L-shaped patch antenna.
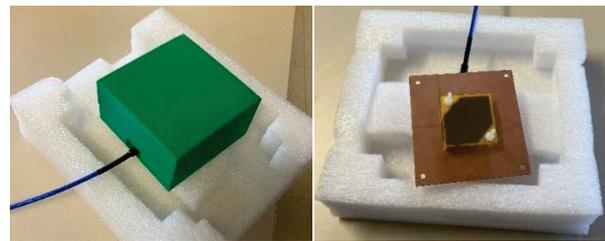
Fig. 19. Covered and uncovered S_{11} measurement set up.
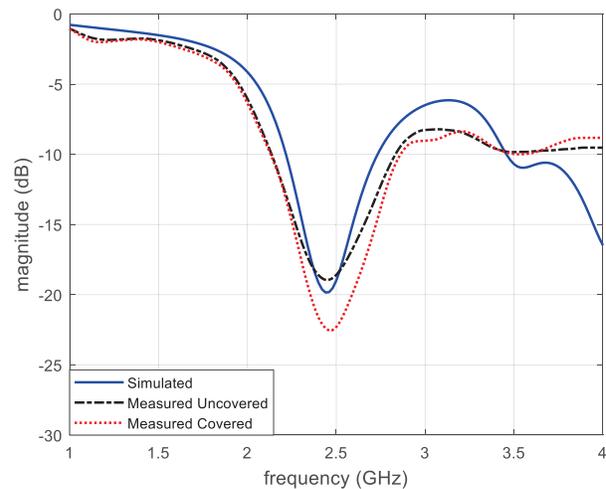
Fig. 20. L-shaped patch antenna LHCP S_{11}.

shows a LHCP antenna S_{11} and Fig. 21 shows a RHCP antenna S_{11}. Through these figures, a close correlation is seen between the three traces. The covered measurements appear to result in a better S_{11} when compared to the simulation and the uncovered measurement. Thus,
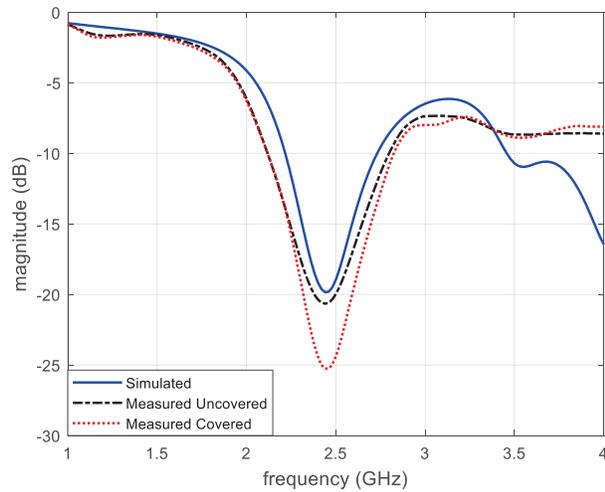
Fig. 21. L-shaped patch antenna RHCP S_{11}.

Fig. 23. Co-pol antenna S_{21} measurement.

the fabricated antennas preform as expected and the covers do not cause any negative effects on S_{11}.

The S_{21} measurement set up for two of the LHCP antennas when they are covered and uncovered is shown in Fig. 22. This setup is used to measure the S_{21} to verify the simulated realized gain values shown in Figs. 12 and 13. Providing the simulated and measured S_{21} values at 2.44 GHz are close, it can be assumed that the gain of the fabricated antennas is close to that of the simulated value. The antennas are separated by 22 mm from ground plane to ground plane. Like the simulation, this test was conducted with co-pol antenna combinations and cross-pol antenna combinations. The results are plotted in Figs. 23 and 24. The covered and uncovered measured data nearly matched the simulated data in the co- and cross-pol cases. The measured data has more loss in the S_{21} measurement due to cable losses. Furthermore, the covered and uncovered data are similar. Overall, the covered and uncovered measured data shows the realized gain of the fabricated antennas is likely close to the simulated realized gain of 9 dB. Lastly, the data also shows that the covers have no negative effects on the ability of the antennas to transmit data.

Fig. 24. Cross-pol antenna S_{21} measurement.

Finally, radiation patterns of the fabricated antennas were measured in the Electrical Engineering Department's anechoic chamber. The chamber is pictured in Fig. 25. The range utilizes a single ridge source horn as shown in Fig. 26. Thus, circular polarization measurements were not able to be taken in one sweep. As a workaround, the E_{θ} and $E_{\emptyset}$ components of each antenna were measured in the xz and yz planes. These are visualized in Figs. 27 and 28. The source horn ridges are simply aligned with whichever component is being measured and the antenna is swept from -90 to 90. These were then compared with the simulated E_{θ} and $E_{\emptyset}$ in both planes to confirm the fabricated antenna radiation patterns. These results are plotted in Figs. 29 and 30. Through close examination of the normalized data, it can be concluded that the simulation and measured

Fig. 22. Covered and uncovered S_{21} measurement set up.
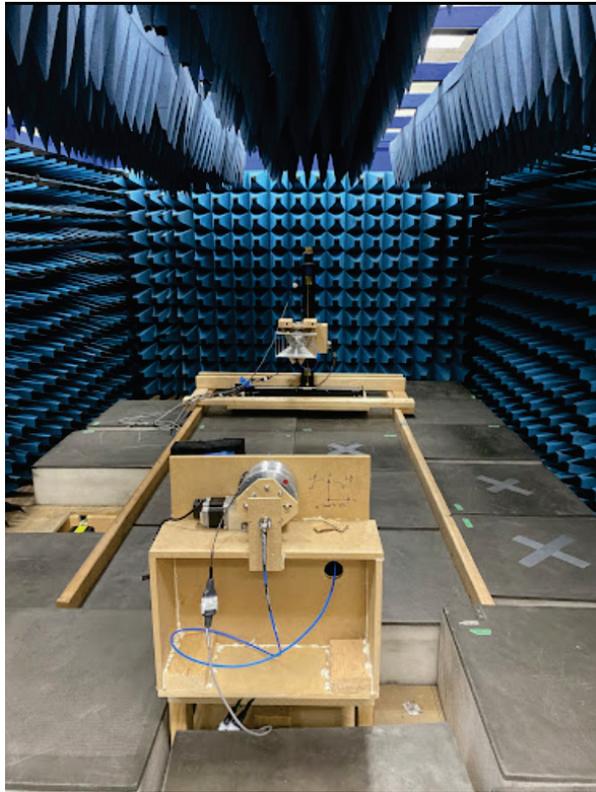
Fig. 25. Anechoic chamber.
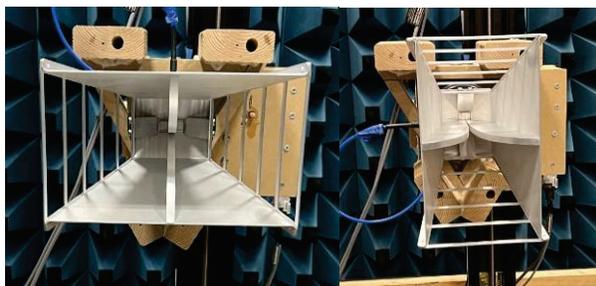
Fig. 26. Anechoic chamber source horn in vertical (left) and horizontal (right) orientations from the view of the AUT.
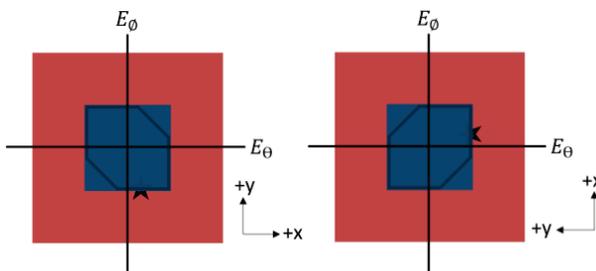
Fig. 27. L-shaped patch E_θ and $E_\emptyset$ components for the LHCP antenna xz (right) and yz (left) planes.
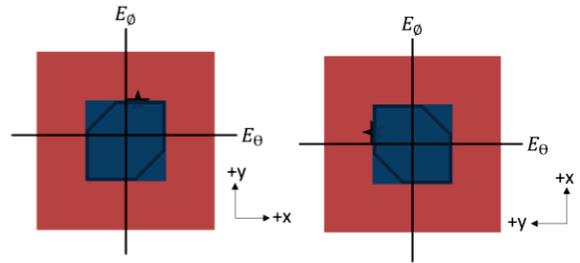
Fig. 28. L-shaped patch E_θ and $E_\emptyset$ components for the RHCP antenna xz (right) and yz (left) planes.
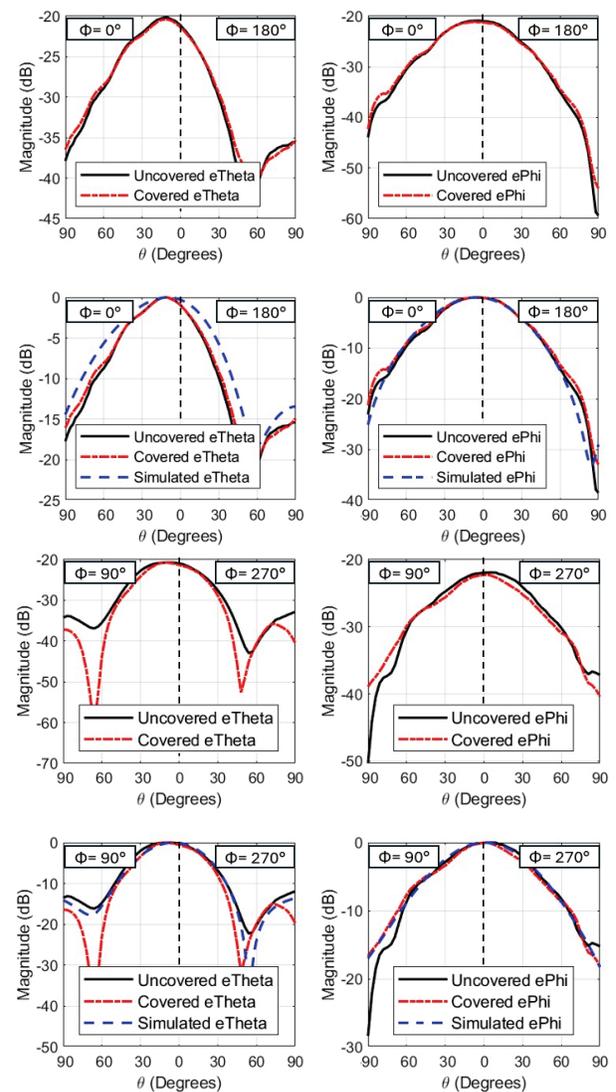
Fig. 29. L-shaped patch LHCP normalized E_θ and $E_\emptyset$ plot for the xy (top) and yz (bottom) plane.

results match very closely in both antennas for both planes. Thus, the radiation patterns and axial ratios of the fabricated antennas will be the same as the simulated
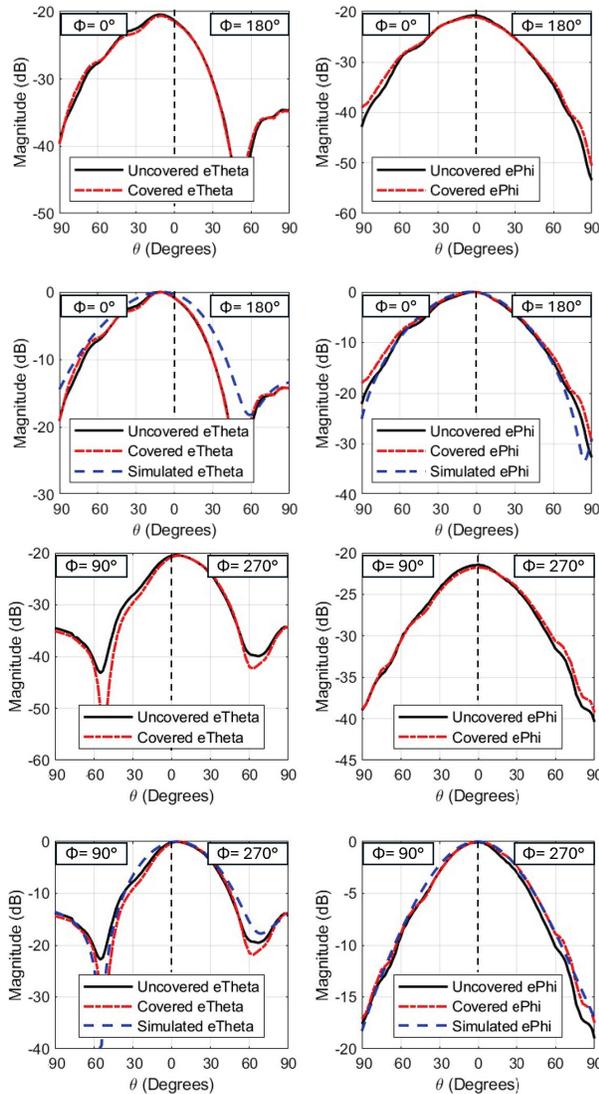
Fig. 30. L-shaped patch RHCP normalized E_θ and $E_\emptyset$ plot for the xy (top) and yz (bottom) plane.

models. Lastly, the results show the covers do not negatively affect the radiation patterns or axial ratio of the antennas.

III. CONCLUSION

The mining industry's transition to automation allows enhancement in safety and operational efficiency amidst its inherent hazards. This project contributes to this transition by developing a sensing system for a typical rock excavation machine equipped with a pick cutter drum. The project seeks to enable remote operation of the machine by providing crucial real time operational data for efficient control and maneuvering of the machine as well as data on wear condition of the cutting tools. Through the integration of capacitive or piezoelectric load sensors into the cutter drum's pick cutters and

the development of high-gain antennas for data transmission, this project addresses key challenges in the transition toward automation, especially in underground mining operations. The L-shaped patch antenna design was optimized through simulations, fabricated and validated through testing. Additionally, the protective antenna covers ensure functional protection without compromising antenna performance. Lastly, the L-shaped patch antenna fulfills the stringent requirements by utilizing various gain increasing design aspects. This project sets a benchmark for the integration of wireless data transmission and load sensing technologies in the mining industry.

REFERENCES

[1] National Safety Council, "Most dangerous industries," Injury Facts 2023 [Online]. Available: https://injuryfacts.nsc.org/work/industry-incidence-rates/most-dangerous-industries/

[2] J. R. Bartels, C. C. Jobes, J. P. DuCarme, and T. J. Lutz, "Evaluation of work positions used by continuous miner operators in underground coal mines," *Proceedings of the Human Factors and Ergonomics Society Annual Meeting*, vol. 53, no. 20, pp. 1622-1626, Oct. 2009.

[3] "Digi XBee 3 Zigbee 3 RF Module" [Online]. Available: https://www.digi.com/products/embedded-systems/digi-xbee/rf-modules/2-4-ghz-rf-modules/xbee3-zigbee-3

[4] "Circular Polarization" [Online]. Available: https://sciencedemonstrations.fas.harvard.edu/presentations/circular-polarization

[5] Y.-B. Tzeng, C.-W. Su, and C.-H. Lee, "Study of broadband CP patch antenna with its ground plane having an elevated portion," in *Asia-Pacific Microwave Conference Proceedings*, Mar. 2006.

[6] G. Yang, M. Ali, and R. Dougal, "A wideband circularly polarized microstrip patch antenna for 5-6 GHz wireless LAN applications," *Microwave and Optical Technology Letters*, vol. 45, no. 4, pp. 279-285, Apr. 2005.

[7] Z. Wang, S. Fang, S. Fu, and S. Jia, "Single-fed broadband circularly polarized stacked patch antenna with horizontally meandered strip for universal UHF RFID applications," *IEEE Transactions on Microwave Theory and Techniques*, vol. 59, no. 4, pp. 1066-1073, Apr. 2011.

[8] Y. Guo and D. C. H. Tan, "Wideband single-feed circularly polarized patch antenna with conical radiation pattern," *IEEE Antennas and Wireless Propagation Letters*, vol. 8, pp. 924-926, July 2009.

[9] Nasimuddin, K. P. Esselle, and A. K. Verma, "Wideband high-gain circularly polarized stacked microstrip antennas with an optimized C-type feed and a short horn," *IEEE Transactions on Antennas and Propagation*, vol. 56, no. 2, pp. 578-581, Feb. 2008.

[10] S. Shekhawat, P. Sekra, D. Bhatnagar, V. K. Saxena, and J. S. Saini, "Stacked arrangement of rectangular microstrip patches for circularly polarized broadband performance," *IEEE Antennas and Wireless Propagation Letters*, vol. 9, pp. 910-913, Sep. 2010.

[11] C. Chen, "A single-layer single-patch dual-polarized high-gain cross-shaped microstrip patch antenna," *IEEE Antennas and Wireless Propagation Letters*, vol. 22, no. 10, pp. 2417-2421, Oct. 2023.

[12] Nasimuddin, K. P. Esselle, and A. K. Verma, "Wideband circularly polarized stacked microstrip antennas," *IEEE Antennas and Wireless Propagation Letters*, vol. 6, pp. 21-24, July 2007.

[13] S. L. S. Yang, K. F. Lee, and A. A. Kishk, "Design and study of wideband single feed circularly polarized microstrip antennas," *Progress in Electromagnetics Research*, vol. PIER, no. 80, pp. 45-61, Nov. 2008.

[14] "Joy12CM12," Komatsu [Online]. Available: https://mining.komatsu/en-in/product-details/joy-12cm12

[15] F. S. Chang, K. L. Wong, and T.-W. Chiou, "Low-cost broadband circularly polarized patch antenna," *IEEE Transactions on Antennas and Propagation*, vol. 51, no. 10, pp. 3006-3009, Oct. 2003.

[16] C.-W. Su, F.-S. Chang, and K.-L. Wong, "Broadband circularly polarized inverted-L patch antenna," *Microwave and Optical Technology Letters*, vol. 38, no. 2, pp. 134-136, May 2003.

[17] A. Z. Elsherbeni, "FDTD Course Notes," Department of Electrical Engineering, The University of Mississippi, MS, Spring 2001.

[18] V. Demir and A. Z. Elsherbeni, "Computational Electromagnetic Simulator," Software Package version 5, veysdemir@gmail.com, Apr. 2024.

Collin T. Kringlen obtained his M.S. degree from the Electrical Engineering Department, Colorado School of Mines in 2024. He is currently working with Lockheed Martin, in Colorado. His research interest includes computational electromagnetics, antenna design and phased array systems.

Atef Z. Elsherbeni received his Ph.D. degree in Electrical Engineering from Manitoba University, Winnipeg, Manitoba, Canada, in 1987. He started his engineering career as a part time Software and System Design Engineer from March 1980 to December 1982 at the Automated Data System Center, Cairo, Egypt. From January to August 1987, he was a Post-Doctoral Fellow at Manitoba University. Dr. Elsherbeni joined the faculty at the University of Mississippi in August 1987 as an Assistant Professor of Electrical Engineering and progressed to the full professor and the Associate Dean of the College of Engineering for Research and Graduate Programs. He then joined the Electrical Engineering and Computer Science (EECS) Department at Colorado School of Mines in August 2013. Dr. Elsherbeni is an IEEE Life Fellow and ACES Fellow. He is the Editor-in-Chief for *Applied Computational Electromagnetics Society (ACES) Journal*, and a past Associate Editor to the *Radio Science* journal. He was the Chair of the Engineering and Physics Division of the Mississippi Academy of Science, the Chair of the Educational Activity Committee for IEEE Region 3 Section, and the past President of ACES Society. He recently received the 2023 IEEE APS Harington-Mittra Award for his contribution to computational electromagnetics with hardware acceleration.

Jamal Rostami is the Haddon/Alacer Gold Endowed Chair, the Director of Earth Mechanics Institute (EMI), and Professor at Mining Engineering at Colorado School of Mines.

A Tunable Broadband Absorber Based on Active Frequency Selective Surface

Bingmei Zhang[1], Xianglin Kong[1], Ruofeng Xu[1], Lei Zhao[1], Hang Song[2], Shengjun Zhang[2], and Jiaqi Liu[2]

[1]School of Information and Control Engineering
China University of Mining and Technology, Xuzhou 221116, China
bmzhangmax@163.com, xlkong@cumt.edu.cn, xuruofeng@cumt.edu.cn, leizhao@cumt.edu.cn

[2]Test Physics & Numerical Mathematical,
National Key Laboratory of Science and Technology, Beijing, China
songhang0412@163.com, zhangsj98@sina.com, ljq006@vip.sina.com

Abstract – In this paper, a tunable metamaterial absorber (MMA) based on active frequency selective surface (FSS) is proposed, which can dynamically tune three absorption bands. The equivalent circuit model (ECM) was used to design the MMA and elucidate its mechanism of switchable absorption. By changing the state of the PIN diode in the lossy layer and FSS layer, the absorption frequency can be tuned continuously. The tuning of the three absorption bands from S- to C-band is achieved. The numerical simulation results show that the described MMA can achieve a bandwidth of 6.2 GHz and can dynamically tune between 1.86-2.70 GHz, 2.42-5.29 GHz, and 4.16-8.10 GHz. The reflectivity is lower than -10 dB, and the fractional bandwidth reaches 125.3%. In addition, the MMA's prototype was produced and measured. The measurement results are generally consistent with the simulation results.

Index Terms – Frequency selective surface, microwave absorber, pin diode, tunable absorber.

I. INTRODUCTION

Metamaterial absorber (MMA) is a new type of artificial electromagnetic structure [1, 2] which converts the energy of incident electromagnetic waves into other energy to achieve perfect absorption. MMA is used in a variety of applications, such as stealth systems [3], electromagnetic interference [4], and reducing radar cross section (RCS) [5, 6]. In recent years, there has been much research based on MMA. Landy firstly proposed a perfect MMA [7]. Although the advantages in thickness and absorption rate are obvious, the bandwidth still needs to be expanded. As a result, the researchers began to study methods to achieve broadband absorption and obtained fruitful results [8–10]. An ultra-wideband MMA based on the cascade of multilayer resistive films has been reported, achieving an absorption rate of over 98% between 4.9-22.6 GHz and stable performance at oblique incidence [11]. However, due to the complexity of the electromagnetic environment, the absorber with fixed frequency bands has certain limitations. Tennant and Chambers utilized dipoles loaded with PIN diodes instead of resistance films to tune the reflectivity covering the spectrum from 9 GHz to 13 GHz, providing a new idea for absorption performance [12].

A tunable MMA based on four split semi-circle resonators was proposed in [13], which tunable bandwidth covered 3.8-6.8 GHz. To enhance the controllable range, an MMA based on four-axis symmetry was introduced, which can attain a tunable bandwidth of 1.6-8.0 GHz [14]. Although the tunable bandwidth increased, the absorption rate was less than 90%. Then, an active MMA based on a circular open-loop band splice strategy was demonstrated, ensuring perfect absorption of each resonant peak and achieving bandwidth reconfigurability from 2.9 GHz to 8.12 GHz [15]. However, the complex feed network was difficult to apply. To solve this problem, a MMA based on the parasitic capacitance of the PIN diode has been designed [16]. Even though it had a great advantage in adjustable bandwidth, it was limited by the unpredictable parasitic capacitance of PIN diodes and could not be applied in practice. Therefore, designing a broadband tunable MMA is technically very challenging.

This paper designs a bandwidth-reconfigurable MMA. The absorber consists of a lossy layer and a switchable frequency selective surface (FSS) layer. The loss layer is equipped with PIN diodes, which are responsible for adjusting the impedance of the absorber to change the absorption frequency. The switchable FSS layer is loaded with PIN diodes, which control the transmission and reflection states. The absorber can achieve the continuously varying reflection coefficient below -

10dB in the band of 1.86-8.10 GHz, and the thickness is only 11.5 mm.

II. DESIGN AND ANALYSIS
A. Structure of the absorber

The unit structure is shown in Fig. 1. The lossy layer is designed with two opposite irregular hexagons in which a PIN diode NXP BAP 70-03 [17] is inserted into the gap. The switchable FSS layer consists of four 90° crossed slotted metal strips in an array arrangement, where a PIN diode SMP1340-079LF [18] is inserted at the split of each cross-metal strip. There is also a metal ground at the bottom of the MMA. The metallic portion of the lossy layer and switchable FSS layer are composed of copper and printed in periodic arrangement on the Rogers 5880 with thickness of d_1 and d_2 (relative permittivity of 2.2, dielectric loss of 0.0009), respectively. Each layer is separated by a polymethacrylimide (PMI) foam with thickness of h_1 and h_2. The period of the unit cell is p. The parameters are (mm): $d_1 =d_2 =0.254$, $h_1 =h_2=5.5$, $p=19.5$, $b=2.7$, $a=1.5$, $t=1.5$, $w=0.5$, $v=18$, $s=3.2$, $m=2.4$, $g=1.2$.
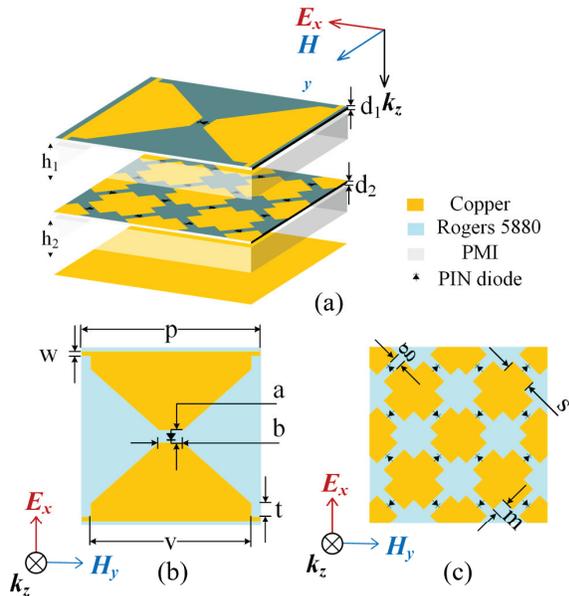
Fig. 1. Structure of the design: (a) the primary structure of the proposed MMA, (b) the primary structure of the lossy layer, and (c) the primary structure of the switchable FSS layer.

CST Microwave Studio was adopted to simulate the electromagnetic response of MMA. The reflection coefficient was obtained by simulation as shown in Fig. 2. Three different states cover the frequency band of 1.86-8.10 GHz. The lossy layer is equivalent to two dipoles with a quarter-wavelength. Depending on the resistance

and current characteristics of the PIN diodes, their resistance can be controlled by the forward current of the external bias voltage. The resistance shown is the equivalent resistance of the active device of the lossy layer at different currents. The on-state and off-state of the PIN diode in the switchable FSS layer are denoted by ON and OFF, respectively. The PIN diodes loaded on the switchable FSS layer are treated as radio frequency (RF) switches, which are equivalent to small resistors and inductors in the on-state. However, they are equivalent to large resistors and capacitors in the off-state. The simulation results show that the reflection coefficient of the MMA is changed by adjusting the equivalent resistance of the lossy layer and the state of the switchable FSS layer. When the PIN diodes of the switchable FSS layer are in the off-state, the equivalent resistance of the lossy layer is 75 Ω, and the reflection coefficient is lower than -10 dB in the frequency band of 1.86-2.77 GHz. Simultaneously, the equivalent resistance of the lossy layer is adjusted to 175 Ω, and the reflection coefficient is less than -10dB in the frequency band from 2.43 GHz to 5.20 GHz. In order to produce absorption effects in the frequency band of 4.14-8.10 GHz, the PIN diodes of the switching FSS layer are in the on-state, and the equivalent resistance of the lossy layer is 200Ω.
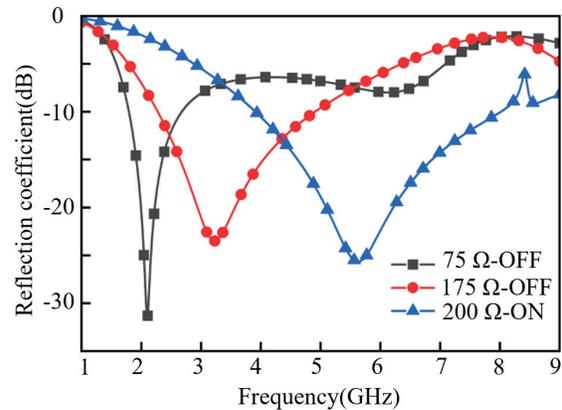
Fig. 2. Reflection coefficient of the MMA calculated from CST for normal incidence.

When the PIN diode is in the on-state, the switchable FSS layer presents a reflective plane. Based on the metal shielding characteristics, incident electromagnetic waves cannot penetrate this layer, and the effective thickness of the MMA is h_1. When the PIN diodes are in the off-state, the incoming electromagnetic wave passes the switchable FSS layer to reach the metal ground, and the effective thickness of the MMA is h_1+h_2. Therefore, the effective thickness of MMA can be changed by adjusting the state of the PIN diodes on the switchable FSS layer, which enables switching between different
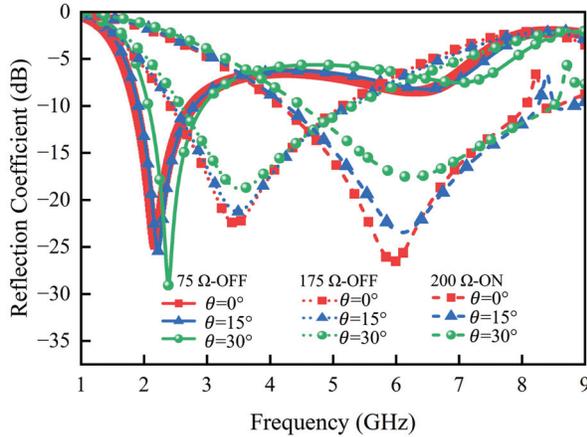
Fig. 3. Simulated reflectivity at different oblique incidence θ.

frequency bands. Under oblique incidence θ, the reflection coefficient of the MMA is shown in Fig. 3. MMA has little effect on performance between 0 and 30°.

B. Equivalent circuit of the absorber

Figure 4 shows the equivalent circuit model (ECM) of this MMA. The ECM of MMA consists of two parts, including the lossy layer circuit and the switchable FSS layer circuit. The equivalent circuit structure of the lossy FSS layer includes C_1, C_2, C_3, L_1, L_2, and R. C_1 is the capacitance effect generated by the gap between the units in the lossy layer. The gap capacitance between the hypotenuse sides of the hexagonal in the lossy layer is regarded as C_2. C_3 is the gap capacitance in the middle gap of the lossy layer. L_1 and L_2 both represent the equivalent inductance of the hexagonal to the lossy
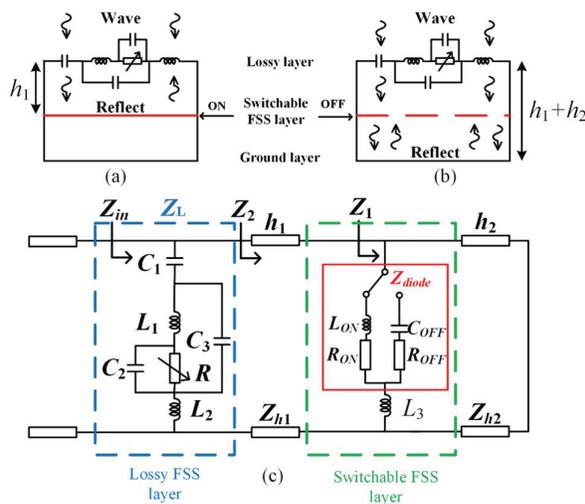
Fig. 4. ECM of the proposed wideband reconfigurable MMA.

layer. The equivalent circuit of the switchable FSS layer includes L_3 and Z_{diode}. L_3 is the equivalent inductance of the metal strip on the switchable FSS layer. Z_{diode} has two states, including the on-state and the off-state. The substrate is equivalent to lossy transmission line models, where the substrate thickness is represented by h_1 and h_2, and their characteristic impedances are represented by Z_{h1} and Z_{h2}, respectively. In this paper, the absorption rate is improved by reducing the reflectivity. When the input impedance Z_{in} of the MMA matches the free space impedance Z_0, the reflectivity of the MMA is diminished.

The input impedance of the overall MMA is:

$$Z_{in} = Z_L || Z_2, \tag{1}$$

$$Z_L = \left(R||\frac{1}{j\omega C_2} + j\omega L_1\right)||\frac{1}{j\omega C_3} + \frac{1}{j\omega C_1} + j\omega L_2, \tag{2}$$

$$Z_2 = Z_{h1}\frac{Z_1 + jZ_{h1}\tan\beta_1 h_1}{Z_{h1} + jZ_1\tan\beta_1 h_1}, \tag{3}$$

$$Z_1 = (Z_{diode} + j\omega L_3)||jZ_{h2}\tan(\beta_2 h_2), \tag{4}$$

$$Z_{diode} = \begin{cases} R_{ON} + j\omega L_{ON} & \text{on - state} \\ R_{OFF} + \frac{1}{j\omega C_{OFF}} & \text{off - state} \end{cases}, \tag{5}$$

where Z_L represents the impedance of the loss FSS later, and β_1 and β_2 are the phase constants of the substrate (Z_{h1}) and the substrate (Z_{h2}).

The reflection coefficient of this MMA is expressed as:

$$\Gamma = -20\log\frac{Z_{in} - Z_0}{Z_{in} + Z_0}. \tag{6}$$

When the resistance is very small, it is equivalent to the PIN diode in the on-state. The PIN diode of the switching FSS layer is in the on-state, causing the gaps in the structure to connect. This layer acts as an ideal reflector, and the equivalent thickness of the MMA is shortened to h_1. At this point, if the equivalent resistance of the PIN diode in the lossy layer is adjusted to 200 Ω, this MMA produces a wide absorption band at high frequency. The PIN diode is in the off-state when the equivalent resistance is large. When the switchable FSS layer's PIN diodes are turned off, this layer is regarded as a transparent window. The thickness of the MMA increases and the absorption peak is generated in the medium frequency band. In addition, when the equivalent resistance of the lossy layer's PIN diodes was tuned to 75 Ω, the absorption band moved to a lower frequency. Therefore, the absorption frequency band variation of the absorber is affected by the combined action of the PIN diode in the lossy layer and the switchable FSS layer.

Comparison between the simulation results of ECM and the simulation results of CST can well verify the correctness of the equivalent circuit model. As shown in Fig. 5, the curve of the two results coincides well.
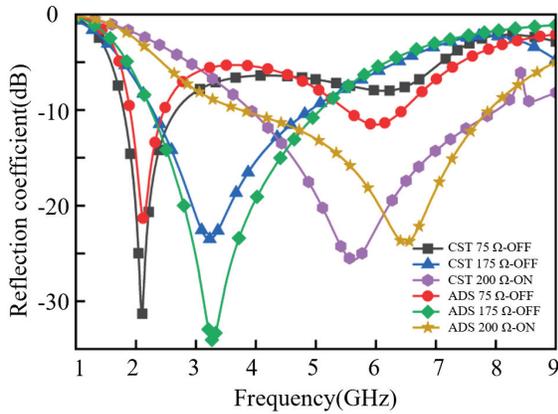
Fig. 5. Reflection coefficient of MMA from CST and ECM.

C. Analysis of absorption mechanism

Figures 6 (a) and (b) show the vector current density and electric field distribution of resonant points at 2.1 GHz and 3.47 GHz, at which point all PIN diodes in the switchable FSS layer can be in the off-state. Figure 6 (c) shows the vector current density and electric field distribution at the resonance point of 6.0 GHz when the PIN diodes in the switchable FSS layer are in the on-state.

At different resonance points, the PIN diode of the lossy layer exhibits induced current and correspondingly generates a strong electric field. This indicates that the energy of the incident wave is dissipated by the equivalent resistance of the PIN diode in the lossy layer. At 2.1 GHz and 3.47 GHz, the electric field is distributed on the conductive metal of the lossy layer and the switchable FSS layer. The current is distributed across the conductive metal of the lossy layer. The difference equivalent resistance of the PIN diode in the lossy layer changes the input impedance of the MMA and thus affects the res-

onant frequency of the MMA. At 6.0 GHz, the electric field is distributed over the lossy layer conducting the metal, while the current flows between the lossy layer and the switchable layer. The existence of the FSS layer is equivalent to a switching ground plane, which realizes the thickness change of the MMA.
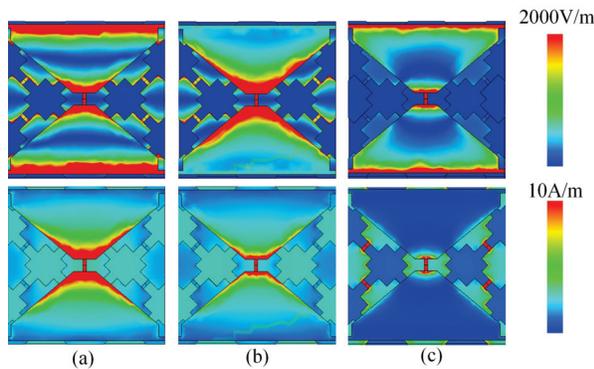
III. EXPERIMENTAL VERIFICATION

The DC bias feed network of the MMA is shown in Fig. 7. The lossy layer's feed network arrangement is shown in Fig. 7 (a), which has paths that allow DC flow. Figure 7 (b) shows a switchable FSS layer feed network arrangement. The switchable FSS layer separately sets multiple dedicated bias lines and connects the anode and the cathode of the PIN diode to different bias lines without affecting the absorption effect of the structure. In addition, the main reason for introducing RF chokes is to eliminate the effect of the feed network on MMA. Based on the analysis of the above simulated results, a 13×13 absorber sample was fabricated using printed circuit board (PCB) technology. The overall size of the sample is 277.5 mm×257.5 mm.

To affirm the proposed MMA, the reflection coefficient is measured by the free space method in the direct measurement method in the microwave darkroom. The measurement environment and the sample to be tested are shown in Fig. 8. Two wideband horn antennas (LB-10125-SF) working in 1-12.5 GHz [19], one for transmitting and one for receiving, are connected to the vector network analyzer via coaxial cable. During measurement, the DC voltage sources provide different bias voltages for the lossy layer and the switchable FSS layer PIN diodes. The resistance value of each PIN diode under different bias voltages is predicted by measuring the forward current value of the channel. To prevent the absorber to be measured from being damaged by excessive voltage, a resistor can be inserted into the circuit for voltage division. Figure 9 shows comparisons between simulation results and measure results. In general, the absorber has frequency reconfiguration characteristics.

Fig. 6. Vector current density distribution and electric field distribution of MMA: (a) f = 2.1 GHz, (b) f = 3.47 GHz, and (c) f = 6.0 GHz.
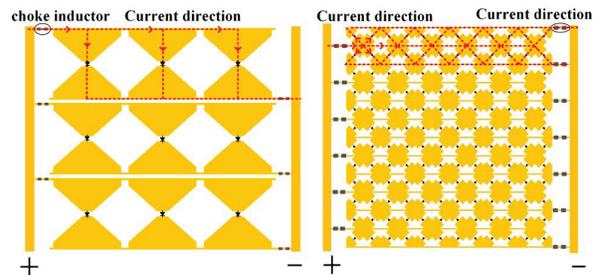
Fig. 7. MMA's vector current density and electric field origin of resonance: (a) feed network of the lossy layer and (b) feed network of the switchable layer.
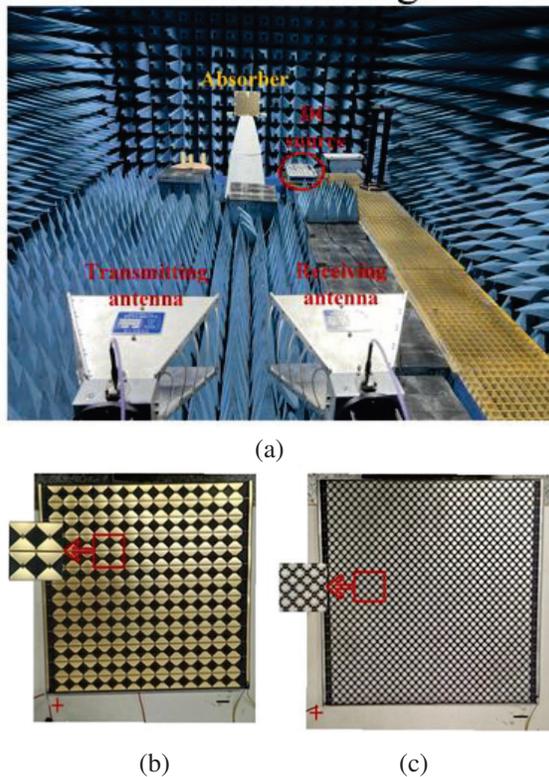
Fig. 8. (a) Measurement environment of the proposed MMA, (b) the lossy layer, and (c) the switchable FSS layer.
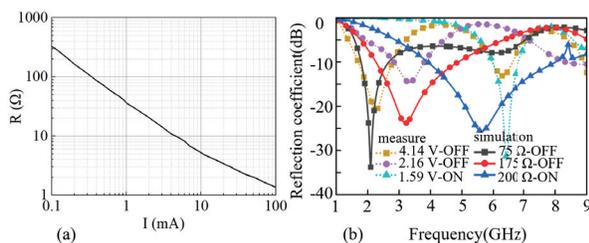
Fig. 9. (a) Relationship between on-state current and resistance and (b) comparison between simulation results and measured results.

The simulation results are in agreement with the measured results.

IV. CONCLUSION

This paper proposes a wideband reconfigurable MMA for electromagnetic shielding in different bands (S, C). The MMA structure comprises a lossy layer and a switchable FSS layer. The absorption band tuning can be achieved by reasonably adjusting the PIN diode state of each layer. Under normal incident conditions, the absorber can achieve a bandwidth of 6.2 GHz and is dynamically tuned between 1.86-2.70 GHz, 2.42-5.29 GHz, and 4.16-8.10 GHz. The thickness of the MMA is only 11.5 mm, with a fractional bandwidth of 125.3%. Additionally, this design holds promising applications in electromagnetic cloaking and shielding.

REFERENCES

[1] S. Narayan, J. Sreeja, V. V. Surya, B. Sangeetha, and R. U. Nair, "Radar absorbing structures using frequency selective surfaces: Trends and perspectives," *Journal of Electronic Materials*, vol. 49, no. 3, pp. 1728-1741, Jan. 2020.

[2] H. Lv, Z. Yang, H. Pan, and R. Wu, "Electromagnetic absorption materials: Current progress and new frontiers," *Progress in Materials Science*, vol. 127, p. 100946, June 2022.

[3] J. Wen, Q. Ren, R. Peng, and Q. Zhao, "Ultrabroadband saline-based metamaterial absorber with near theoretical absorption bandwidth limit," *IEEE Antennas and Wireless Propagation Letters*, vol. 21, no. 7, pp. 1388-1392, July 2022.

[4] M. A. Shukoor and S. Dey, "Novel dual-mode polarization insensitive wide angular stable circular ring based Deca-band absorber for RCS and EMI shielding applications," *IEEE Transactions on Electromagnetic Compatibility*, vol. 64, no. 5, pp. 1337-1345, Oct. 2022.

[5] S. Dey and S. Dey, "Conformal multifunction FSS with enhanced capacitance loading for high angle stable stopband filtering and microwave absorption," *IEEE Transactions on Electromagnetic Compatibility*, vol. 64, no. 2, pp. 315-326, Apr. 2022.

[6] A. Dhumal, M. Bisht, A. Bhardwaj, M. Saikia, S. Malik, and K. Srivastava, "Screen printed polarization independent microwave absorber for wideband RCS reduction," *IEEE Transactions on Electromagnetic Compatibility*, vol. 65, no. 1, pp. 96-103, Feb. 2023.

[7] N. I. Landy, S. Sajuyigbe, J. J. Mock, D. R. Smith, and W. J. Padilla, "Perfect metamaterial absorber," *Physical Review Letters*, vol. 100, no. 20, May 2008.

[8] X. Kong, S. Zhang, X. Pang, Y. Fu, L. Zhao, and Z. Shen, "Fast design of ultra-wideband absorbers based on equivalent circuit model," *IEEE Antennas and Wireless Propagation Letters*, pp. 1-5, 2024.

[9] P. Chen, X. Kong, J. Han, W. Wang, K. Han, H. Ma, L. Zhao, and X. Shen, "Wide-angle ultra-broadband metamaterial absorber with polarization-insensitive characteristics," *Chinese Physics Letters*, vol. 38, no. 2, p. 027801, Feb. 2021.

[10] X. Kong, L. Zhao, F. Wang, S. Zhang, Y. Fu, X. Pang, X. Liu, and X. Shen, "A fast design method for ultra broadband absorbers using RC equivalent circuit model," in *2022 International Applied Computational Electromagnetics Society Symposium (ACES-China)*, Dec. 2022.

[11] C. Liang, X. Kong, F. Wang, R. Xu, Y. Fu, X. Pang, S. Zhang, X. Shen, and L. Zhao, "A broadband perfect metamaterial absorber with angle-insensitive characteristics," *Journal of Electromagnetic Waves and Applications*, vol. 37, no. 3, pp. 401-410, Feb. 2022.

[12] A. Tennant and B. Chambers, "Adaptive radar absorbing structure with PIN diode controlled active frequency selective surface," *Smart Materials and Structures*, vol. 13, no. 1, pp. 122-125, Dec. 2003.

[13] S. An, H. Xu, Y. Zhang, S. Wu, J. Jiang, Y. He, and L. Miao, "Design of a polarization-insensitive wideband tunable metamaterial absorber based on split semi-circle ring resonators," *Journal of Applied Physics*, vol. 122, no. 2, July 2017.

[14] H. Wang, P. Kong, W. Chen, W. Bao, X. Yu, L. Miao, and J. Jiang, "Broadband tunability of polarization-insensitive absorber based on frequency selective surface," *Scientific Reports*, vol. 6, no. 1, Mar. 2016.

[15] T. Wu, W. Li, S. Chen, and J. Guan, "Wideband frequency tunable metamaterial absorber by splicing multiple tuning ranges," *Results in Physics*, vol. 20, p. 103753, Jan. 2021.

[16] Z. A. P. Jibran and K. R. Jha, "Design of active tunable wide frequency covering absorber," in *2021 International Conference on Intelligent Technologies (CONIT)*, June 2021.

[17] NXP Semiconductors, "BAP70-03 Silicon PIN Diode Rev. 6 – 7 March 2014," https://www.nxp.com/docs/en/data-sheet/BAP70-03.pdf

[18] Skyworks Solutions Inc, "SMP1340 Series: Fast Switching-Speed, Low-Capacitance, Plastic-Packaged PIN Diodes," https://www.mouser.cn/datasheet/2/472/SMP1340_Series_200051U-3050131.pdf

[19] Ainfoinc, "LB-10125-SF LB Specification Brochure," https://www.ainfoinc.cn/tianxian-chanpin/laba-tianxian/kuandai-laba-tianxian/lb-10125-sf-kuandai-labatianxian-1-12-5-ghz-zengyi-11db-sma-zuo

Xianglin Kong (Member, IEEE) is currently pursuing the Ph.D. degree with the China University of Mining and Technology, Xuzhou, China. His research interests include the design of RF/microwaves antennas and metasurface.

Ruofeng Xu received the B.S. (2004) degree from Suzhou University in electronics and science and technology, and the M.S. (2006) and Ph.D. (2010) degrees in electronic engineering from the University of Kent, UK. He joined the China University of Mining and Technology, Xuzhou, China, in 2011. His main interests include microwave technology and applications.

Lei Zhao (Senior Member, IEEE, Fellow, ACES), received the B.S. degree in mathematics from Jiangsu Normal University, China, in 1997, and the M.S. degree in computational mathematics and the Ph.D. degree in electromagnetic fields and microwave technology from Southeast University, Nanjing, China, in 2004 and 2007, respectively.

He joined the China University of Mining and Technology, Xuzhou, China, in 2019, where he is currently a full Professor. From August 2007 to August 2009, he worked with the department of electronic engineering, The Chinese University of Hong Kong, as a research associate. From February 2011 to April 2011, he worked with the department of electrical and computer engineering, National University of Singapore, as a research fellow. From September 2016 to September 2017, he worked with the department of electrical and computer engineering, University of Illinois at Urbana-Champaign, Champaign, IL, USA, as a visiting scholar. He has authored or coauthored more than 120 refereed journal and conference papers. His current research interests include spoof surface plasmon polaritons theory and its applications, RF/microwave antenna

and filter design, computational electromagnetics, and electromagnetic radiation to human's body.

Dr. Zhao serves as an Associate Editor for *IEEE Access*, an Associate Editor-in-Chief for *Applied Computational Electromagnetics Society (ACES) Journal* and a reviewer for multiple journals and conferences including the *IEEE Trans. on Microwave Theory and Techniques, IEEE Trans. Antennas and Propagation, IEEE Antennas and Wireless Propagation Letters, ACES Journal,* and other primary electromagnetics and microwave related journals.

Hang Song is a doctoral candidate at the National Key Laboratory of Experimental Physics and Computational Mathematics. He obtained his master's degree from Beihang University. His research interests focus on target feature control technology, and he possesses specialized knowledge in the design of low-scattering characteristic metamaterials.

Shengjun Zhang received the B.Sc. degree from China University of Geosciences (Wuhan), Wuhan, China, in 1995, M.Sc. degree from China University of Geosciences (Beijing), Beijing, China, in 1998, and Ph.D. degree in Optics from Beijing University of Technology, Beijing, China, in 2001. After that, he joined National Key Laboratory of Science & Technology on Test Physics & Numerical Mathematics. He is currently the full professor of China Academy of Launch Vehicles Technology, and adjunct professor of Xi'Dian University. He is a member of space security committee of International Astronautics Federation (IAF). His research interests include electromagnetic signature simulation and control approaches, effects of cold plasma on electromagnetic waves, FSS, tuning of scattering by active array, and space security.

Jiaqi Liu was born in Yueyang, China, in 1963. He received the Ph.D. degree in circuit and systems from Beihang University, Beijing, China, in 2007. He currently serves as the Vice Director and leading Research Fellow with the National Key Laboratory of Science and Technology on Test Physics and Numerical Mathematics. His research area is signal processing and target recognition.

Design of DC to 40 GHz GaAs-based MMIC Attenuators by Utilizing Full-chip Numerical Analyses

Mehmet Emin Bayrak, Harun Tekin, and Huseyin Serif Savci

Department of Electrical and Electronics Engineering
Istanbul Medipol University, Istanbul, 34810, Turkey
hsavci@medipol.edu.tr

Abstract – In this study, a numerical analysis-based design methodology of monolithic microwave integrated circuit (MMIC) attenuators on a GaAs-based microwave integrated passive device (IPD) technology is presented. The designs have 0 dB, 3 dB, 4 dB, 6 dB, 10 dB, 12 dB, 20 dB, and 30 dB attenuation from DC to 40 GHz. The attenuators are designed for a maximum RF power of 26 dBm and a maximum die area of 0.25 mm^2. The circuits are physically compact but electrically large. The finite element method and Method of Moments (MoM)-based analyses are used. The MoM-based solutions show close correlations with the measurements. The measured return losses are better than 20 dB, and insertion loss variation is less than 0.5 dB across the entire band. This paper explains the detailed design steps and numerical electromagnetic setup to achieve first-pass success.

Index Terms – Finite element method, GaAs integrated passive device, Method of Moments, monolithic microwave integrated circuit, wideband attenuator.

I. INTRODUCTION

In recent years, millimeter wave radios entered our daily lives as integrated with several different types of consumer equipment, from 5G cellular handsets to automotive radars. These radios utilize many die products, packaged chips, or modules in their architectures. The type of architecture varies depending on the application. While high-volume products use all integrated solutions on a single die, mostly on complementary metal oxide semiconductor (CMOS) technology, the others favor combining bare dies from different technologies for several different reasons, such as design flexibility, performance, and lower development costs. The advancement of packaging technology resulted in reduced associated costs and rises in yield. Therefore, many applications utilize system-in-package (SiP) solutions where dies developed on cost-effective semiconductor processes are put together. This, coupled with the high overhead cost of the modern semiconductor process, made the system architects revisit every portion of the system for proper

technology considerations. The integrated passive device (IPD) process is one of the cost-efficient solutions for passive microwave networks. The IPD can be developed on different bases such as high-resistance silicon wafers, GaAs wafers [1–7], layered ceramic substrates in either low-temperature co-fired ceramic (LTCC) [8] or high-temperature co-fired ceramic (HTCC) form [9], and several recent ones such as graphene [10, 11]. Although they essentially serve the same purpose, their electrical specs vary. The silicon and GaAs-based IPD processes are widely used for SiP solutions. Even though silicon has several times higher thermal conductivity than GaAs with less risk of local overheating under high power, the GaAs devices are more resilient to radiation exposure owing to the high proton absorption coefficient. In addition, the GaAs process allows higher voltage ratings than silicon, such as 8V, 28V, and 50V, by utilizing epitaxial layers with proper electrical properties, enabling them to be compatible with GaN power processes. GaAs IPD technologies have been used for the design of various microwave circuits.

Modern wireless communication systems, from beamformers to RF front-ends, utilize many control products, such as attenuators, switches, and phase shifters in the signal chain. They are used for conditioning the signal's amplitude, phase, and direction through the multi-throw switches. Among all the control products, attenuators are used ubiquitously, after almost every other component in a cascaded system, for the proper amplitude adjustments of the signals. Three types of attenuators are used in RF systems; fixed, voltage-variable, and digital-step.

Fixed-value attenuators, which are also called PADs, are passive devices that provide a flat attenuation value across the specified frequency range. The fixed attenuators are classified as narrow-band (tuned), broadband, or high-power. Voltage-variable attenuators use analog DC control voltages for the attenuation level adjustment in a continuous manner [18], whereas digital step attenuators use serial or parallel control bits for discrete attenuation adjustment. Step attenuators are cascaded

blocks of switchable fixed attenuators that utilize single-pole single-throw (SPST) switches to be switched in or bypassed using digital bits [16], [17]. The on-resistance and off-capacitance of these SPST switches should be considered in the design of the attenuator. These attenuators have binary-weighted attenuation values and usually take values such as 0.25, 0.5, 1, 2, 4, 8, and 16 dB [19]. The switch structures in digital attenuators can be realized using PIN diodes, MESFET, MOSFET, and pHEMT devices [20].

The building blocks of all the attenuators are resistors. However, several different topologies can be constructed with these resistors. The three significant topologies of attenuators are Tee, Pi, and Bridged-Tee topologies, as seen in Fig. 1. Although all topologies can essentially be used to obtain the desired attenuation levels, some topologies are preferred over others depending on the number and value of the resistors as well as the system requirements.
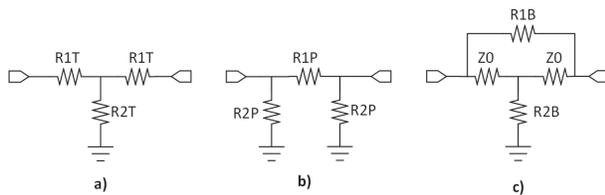
Fig. 1. Attenuator topologies: (a) Tee, (b) PI, and (c) Bridged-Tee.

The value of series and shunt resistors are calculated by solving the voltages and currents using Kirchoff's voltage and current laws. The attenuators are symmetrical and reciprocal devices allowing identical component values around the mid-symmetry line. The resistance values can be extracted using the characteristic impedance and attenuation value in dB [23], [24]. Equations (1) and (2) show the calculation of the series resistor values, R1T, and the shunt resistor value, R2T, in Tee topology. Equations (3) and (4) show the calculation of the series resistor values, R1P, and the shunt resistor value, R2P, in PI topology. Equations (5) and (6) show the calculation of the series resistor values, R1B and the shunt resistor value, R2B in Bridged-Tee topology.

$$R1T = Z0 * \left(\frac{K-1}{K+1} \right), \tag{1}$$

$$R2T = Z0 * \left(\frac{2*K}{K^2 - 1} \right), \tag{2}$$

$$R1P = Z0 * \left(\frac{K+1}{K-1} \right), \tag{3}$$

$$R2P = Z0 * \left(\frac{K^2 - 1}{2*K} \right), \tag{4}$$

$$R1B = Z0 * (K-1), \tag{5}$$

$$R2B = Z0 * \left(\frac{1}{K-1} \right), \tag{6}$$

$$K = 10^{\left(\frac{ATTdB}{20} \right)}. \tag{7}$$

These formulas are for ideal resistors without taking real resistor models and the connecting metals into account. However, resistors have parasitic capacitors and inductors dependent on their sizes, which are dictated by the resistance values and the level of current they must handle. The formulas can be updated by replacing each ideal resistor with a complex model of a real resistor. However, solving analytical equations will be error-prone as electromagnetic couplings between the structures would also affect the solutions. As an optimum solution, we analyzed the topologies to find the one with the smallest-sized resistors. The resistance values change with the attenuation levels. The IPD process used in this study has only one resistor type: thin film resistor (TFR), which has a sheet resistance of 50 Ω per square. Considering the attenuator family would include attenuation levels from as low as 2 dB to as high as 30 dB, it would be ideal to have the lower value of resistors and not change too much with attenuation levels. It would be a prime concern to have all the designs fitting the same die area and maintaining a broadband response without introducing too much capacitance. Figure 2 shows the resistor values versus attenuation levels for the three attenuator topologies. In general, the solid lines are for the series resistance, and the dashed lines represent the shunt resistance. The blue curves are for PI-type attenuators, the red curves are for Tee-type attenuators, and the black curves are for Bridged-Tee-type attenuators. It is seen from the plots that the red curves in Fig. 2, which are for the
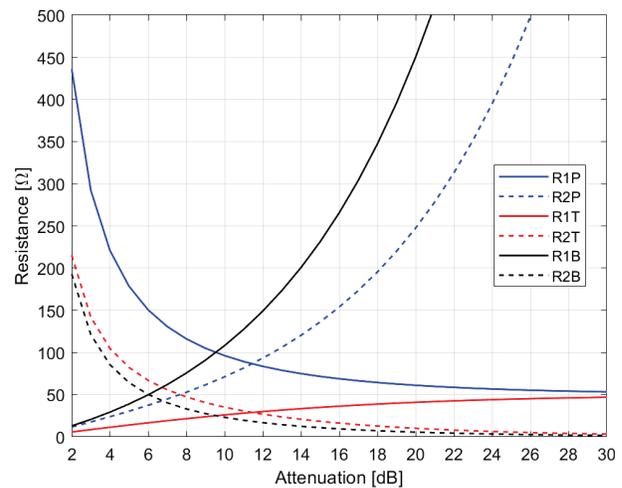
Fig. 2. Resistance versus attenuation curves: blue: PI, red: Tee, black: Bridged-Tee.

Tee-type attenuator, have lower resistance values and present the least variance over the attenuation levels. In PI topology, the value of the shunt resistor becomes as high as 790 Ω, and in Bridged-Tee topology, the value of the series resistor is as high as 1530 Ω. It is concluded that the Tee topology or its distributed derivative should be adopted for this study.

II. DESIGN METHODOLOGY

The attenuator family is designed using a 28V GaAs-based IPD process. The process contains three active metal layers, two capacitor options with different capacitance densities, and voltage durability. The GaAs substrate has a dielectric constant of 12.88 and roughly 0.0004 tangent loss. The die thickness is around 100 um. A half-wavelength, 50 Ω line is 70 mum wide and around 1.3 mm long at 40 GHz.

The process has only a 50 Ω per square TFR, which is co-planar with the first metal layer. The process has two metal-insulator-metal capacitors and backvia.

All the attenuators designed in this family have broadband response between DC to 40 GHz frequency range. The circuits' die size is as small as possible to have 0.470 mm × 0.430 mm and 0.430 mm × 0.570 mm, almost the minimum valid die size in this process. The attenuators can withstand up to 26 dBm of continuous RF signal power as the power levels beyond that cause excessive joule heating on the metal traces. Also, the size of resistors is adjusted to withstand up to 140°C temperature values, which complies with a maximum power level of 26 dBm.

Most of today's monolithic microwave integrated circuit (MMIC) attenuators have performance requirements such as high power handling, compact area size, and broadband operation. These requirements are contradictory. The broadband nature of the design favors small resistor sizes to reduce the associated parasitic capacitance, whereas the high input power requirements dictate larger resistors. A high-power broadband attenuator with a flat response requires a distributed design with a detailed device model and its parasitic compensation over the frequency range.

The Tee-type attenuator has two 150 μm pitch Ground-Signal-Ground pads, at least two backvias for ground connection, and a minimum of three resistors. A complex equivalent circuit model for the TFR resistor and its value-limited simplified model are given in Fig. 3, where Rcore models the resistor value, Cpar models the parallel capacitor between metal connections, Csub and Rsub models shunt substrate parasitic, Lcont, and Rcont model the parasitic of metal1 to TFR connection. Although the complex model reflects a physics-based generic model for a broad range of resistance values, the simplified model also holds its validity for the
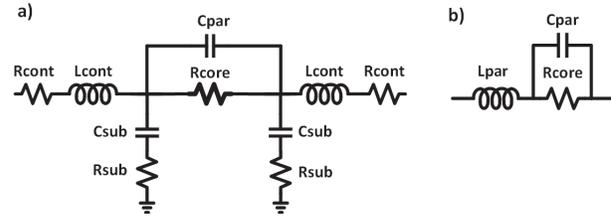
Fig. 3. Equivalent circuit of the TFR: (a) complex and (b) simplified.

range of values used in this study. The Ground-Signal-Ground pad also has a significant effect on the circuit performance with its capacitive behavior due to the large bonding plate. The backvia has an inductive behavior with roughly 0.4nH per mm.

The attenuator design starts with calculating the resistor values based on the topology and sizing it according to the required power. After the resistances are sized to cope with the rated current, their equivalent model is constructed. To compensate for the capacitive parasitic elements of the resistor and capacitance coming from the pads, low-impedance transmission lines between series resistors and high-impedance transmission lines between resistors and pads are used. The line's rated current handling ability in those sections limits the minimum width of high-impedance lines. Sizing the width of metals below the minimum value specified in the design manual causes different failure mechanisms for different types of currents. It is electromigration failure for direct-current, whereas a joule heating failure is triggered for the RF currents. The reactive parts will be matched through these transmission lines to obtain a broadband attenuator response [21], [22]. The transmission lines are designed mainly with top metal due to their low sheet resistance, less parasitic capacitance, and higher power handling. Matching the circuits by tuning the characteristic impedance and electrical length of transmission lines is done using the equivalent schematic models. Ultra-wide-band design techniques through simplified real frequency techniques or parametric representation of Brune functions can be utilized for the desired performance [25], [26]. The desired performance should be achieved by constructing the layout within the designated area. Fitting the transmission lines, resistances, bond pads, and ground vias within such a tight area causes lots of electric and magnetic inter-couplings. Furthermore, the chip ring also causes unwanted feed, which should also be considered and embedded in the final response. The size of the die is more than a quarter wavelength at the frequency of interest, making the designs electrically large. Therefore a successful design can only be achieved with full-die electromagnetic simulations.

The broadband operation of the designs from DC to Ka-band dictates solving the complex electromagnetic interactions within the die. Keysight ADS software is used to find full-chip electromagnetic solutions utilizing FEM (Finite-Element-Method) and MoM (Method-of-Moments) numerical methods. Although commercial software guides the user to set up the simulations, the parameters such as mesh frequency, mesh density, how to mesh the vias, how to mesh the transmission line edges, method of matrix solving (direct, iterative), delta error level, order of basis function should be tailored for each structure as these would directly affect the accuracy, the convergence and the duration of analyses. The optimum settings are structure-dependent and require a good insight into the method itself [28]. For MoM simulations, an adaptive frequency plan is selected between 1 MHz and 40 GHz with a maximum of 50 points. The mesh is generated based on the highest frequency of simulation, 40 GHz. The mesh density is adjusted to have 50 cells per wavelength. The computation is done by enabling the edge mesh and transmission line mesh options, which help to improve the accuracy. The matrix is solved using the iterative dense method where the post-solvers are enabled. For FEM simulations, the same adaptive frequency plan is used. The mesh refinement is done based on the maximum frequency. The edge and vertex meshing are adjusted with 0.2 and 0.06 multiples of the estimated conductor width, respectively. As the computation stop criterion, the delta error is chosen as 0.02, along with the minimum and maximum number of adaptive passes of 2 and 15, respectively. The iterative matrix-solving method with 2nd order basis functions is used.

Besides the planar solutions, to observe the package, wire-bond, and die interactions, the dies are attached to 50 Ω launcher through the bond wires. The wire bond effects are captured by using the 3D full-wave electromagnetic simulations of various wire and ribbon transitions based on the FEM. Keysight EmPro software is used for the 3D simulations. Wire bonding was performed with 25 μm diameter, Au-based wires, whereas 250 μm × 25 μm, Au-based connections are used for ribbon bonding. Among different profiles, spline shape and JEDEC5 profile with five-defined coplanar points are used. It is verified that bond-wire length is more critical to obtaining better insertion loss than having better impedance matching [27]. The setup details and parameters of both planar and 3D numerical methods are presented throughout the paper, and the solutions are compared with the measurement results to give the reader a good insight into the setup dependency and accuracy of the solution of interest. It is shown that without correctly setting up a full-die electromagnetic numerical analysis, it is nearly impossible to achieve a first-pass success MMIC design at millimeter wave frequencies.

In the EM simulations configured with the MoM, the solution is obtained for 50 adaptive frequency points swept between DC and 40 GHz. The mesh frequency is set to 40 GHz with a mesh density of 40 cells per wavelength. The edge mesh and transmission line mesh are used for increased accuracy. The matrix is solved using the iterative dense method. The port solver is also enabled. The circular shapes in Through-Wafer-Via (TWV) are simplified with an arc resolution of 45 degrees.

A. 0 dB (THRU) design

Although considered a part of the attenuator family, THRU design is a substitute for attenuators in the system wherever no attenuation is needed. The primary target spec of the THRU design is to provide a broad matching and minimum insertion loss in the DC-40 GHz band. This circuit has the same die size and pad locations as other attenuators. The return loss value will be better than 27 dB.

Figure 4 provides an equivalent design schematic for the THRU circuit. The circuit has a single transmission line designed as a symmetrical structure. The maximum value of the line impedance is limited by the minimum metal width that can handle the current for the 26 dBm power requirement. The 0 dB attenuator layout is seen in Fig. 10 (a).
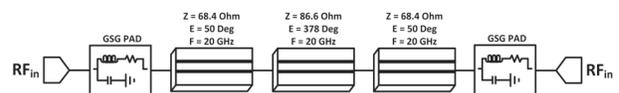
Fig. 4. Schematic of 0 dB attenuator circuit model.

B. 3 dB attenuator design

Figure 5 gives the schematic model design of the 3 dB attenuator. The attenuator complies with the maximum RF power of 26 dBm. Since a 3 dB attenuator dissipates half of that power, the transmission lines and the resistors are sized wide enough to handle as high as 90 mA rms current. It has a flat response from DC to 40GHz with less than 0.6 dB variation. The resistor values are calculated as R1T=8.6 Ω and R2T=141.9 Ω according to equations (1) and (2) which corresponds to 0.17 square and 2.84 square of TFR resistors. The 3 dB attenuator layout is seen in Fig. 10 (c). The design has 0.26 mm^2 area.

C. 2 dB, 4 dB, and 6 dB attenuator designs

The 2 dB, 4 dB, and 6 dB attenuators use the same distributed topology as shown in Fig. 6. All the designs have a flat response from DC to 40 GHz with less than 10% variation. The circuit is well-matched with a return loss value of better than 17 dB.
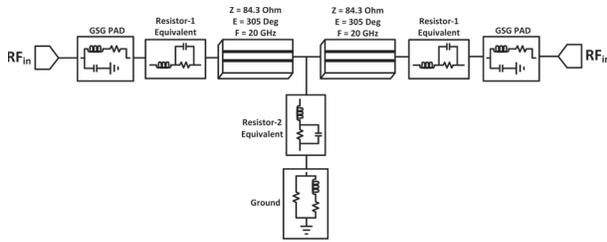
Fig. 5. Schematic of 3 dB attenuator circuit model.
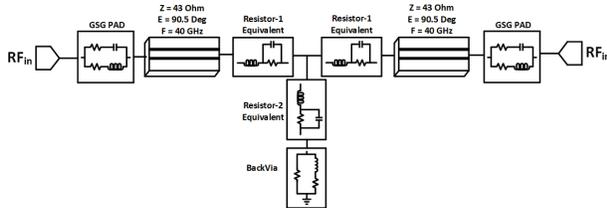
Fig. 6. Schematic of 6 dB attenuator circuit model.

The circuit is designed as a fully symmetrical distributed Tee-type architecture. The resistor values are calculated according to equations (1) and (2) as seen in Fig. 1. The 2 dB attenuator has the series resistor R1T of 5.7 Ω and the shunt resistor R2T of 215.2 Ω. The 4 dB attenuator has the series, R1T of 11.3 Ω, and the shunt resistor, R2T of 104.8 Ω. The 6 dB attenuator has the series resistor, R1T, of 16.6 Ω, and the shunt resistor, R2T, of 66.9 Ω where the series resistors correspond to 0.66 squares, and the shunt resistors correspond to 1.34 squares of TFR resistors. The 2 dB attenuator layout is seen in Fig. 10 (b). The 4 dB attenuator layout is seen in Fig. 10 (d), and the 6 dB attenuator layout is seen in Fig. 10 (e).

D. 10 dB and 12 dB attenuator designs

The 10 dB and 12 dB attenuators were designed with a tight variation of ±0.7 dB across the entire 40 GHz bandwidth using the same distributed topology. The flat insertion loss and good broadband matching performance are achieved by placing the resistors adjacent to each other and using low-impedance transmission lines for pad connections. The equivalent schematic is shown in Fig. 7. The shunt resistor splints into two parallel ones to achieve a broader response.

The resistor values are calculated as R1t=26.0 Ω and R2t=35.1 Ω for the 10 dB attenuator and R1t=29.9 Ω and R2t=26.8 Ω for the 12 dB attenuator according to equations (1) and (2). The series resistors correspond to 0.52 square, and the shunt resistors correspond to 0.7 square TFR resistors for the 10 dB attenuator. The 10 dB and 12 dB attenuator layouts are seen in Fig. 10 (f) and Fig. 10 (g), respectively.
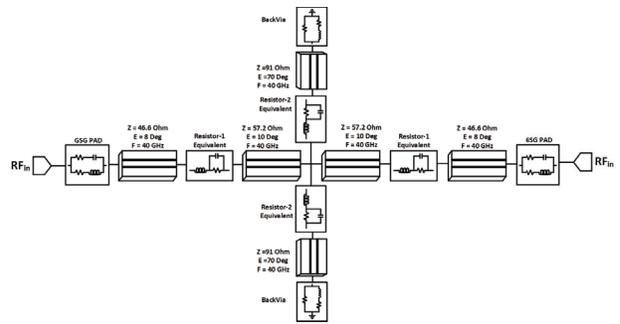
Fig. 7. Schematic of 10 dB attenuator circuit model.

E. 20 dB and 30 dB attenuator designs

Both 20 dB and 30 dB attenuators were designed with a flatness target of ±1.6 dB throughout the frequency range. These designs are slightly larger than previous ones. The return losses are better than 20 dB. The shunt resistor in Tee-topology is distributed as two parallel resistors making it a cross-topology. The equivalent schematic for the 20 dB attenuator is shown in Fig. 9. The series and shunt resistors are 40.9 Ω and 10 Ω for the 20 dB attenuator. The EM simulation view of the 20 dB attenuator is given in Fig. 8. The 30 dB attenuator is realized as a cascade of two identical distributed
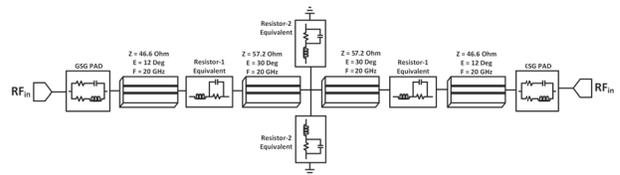
Fig. 8. Schematic of 20 dB attenuator circuit model.
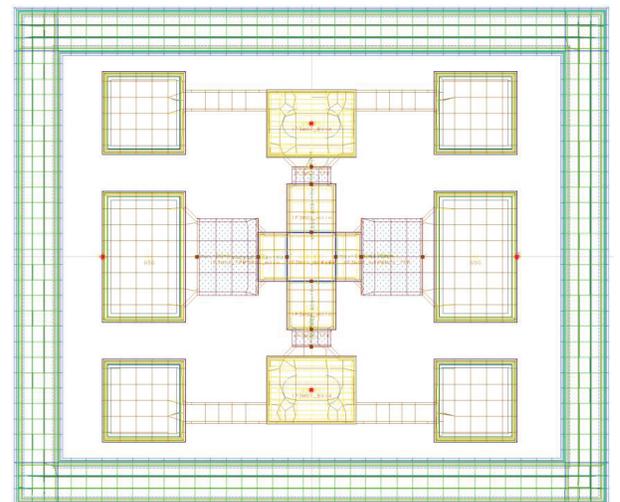
Fig. 9. MoM-based EM view of 20 dB attenuator with meshes.

cross topologies similar to the 20 dB one, where each one has 15 dB attenuation. The series resistors are 34.9 Ω, and each parallel shunt resistor is 36.8 Ω for the 15 dB attenuator. The 30 dB attenuator has four series and four shunt resistors. The 20 dB and 30 dB attenuator layouts are seen in Fig. 10 (h) and Fig. 10 (i), respectively.
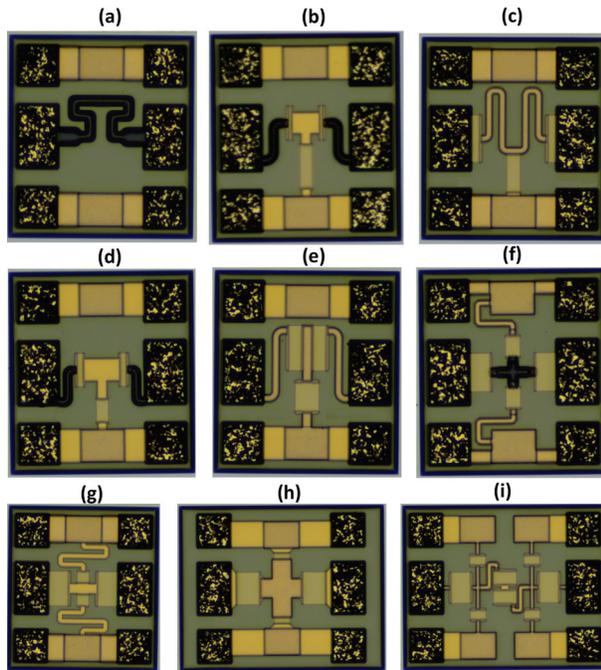
Fig. 10. Die micrographs of (a) 0 dB, (b) 2 dB, (c) 3 dB, (d) 4 dB, (e) 6 dB, (f) 10 dB, (g) 12 dB, (h) 20 dB, and (i) 30 dB attenuators.

F. Die micrographs

The designed circuits were manufactured on a 6-inch 28V GaAs IPD process. The wafer has 112 reticles sized 10 mm × 10 mm, including the process control monitors on the corners. The floor planning of the reticle is arranged to avoid sub-cuts and to yield the maximum number of dies. The photos of the selected circuits are shown in Fig. 10. The wafer is diced and placed on an expanded grip ring where the singulated dies remain in their original locations on the wafer. This allows a location-conscious measurement for determining the process spread across the wafer.

In Fig. 11, the FormFactor MPS150 probe station is used for measuring the singulated dies on various locations of the wafer. The pad metallization in the GaAs process is Au, which requires softer probe tips to avoid scratching and ensure better electrical contact. For this particular measurement, a pair of 150 μm pitched Ground-Signal-Ground RF probes (Model 40A-GSG-150-P) with beryllium-copper tips are used. The measurements are taken using the Rohde & Schwarz ZVA67
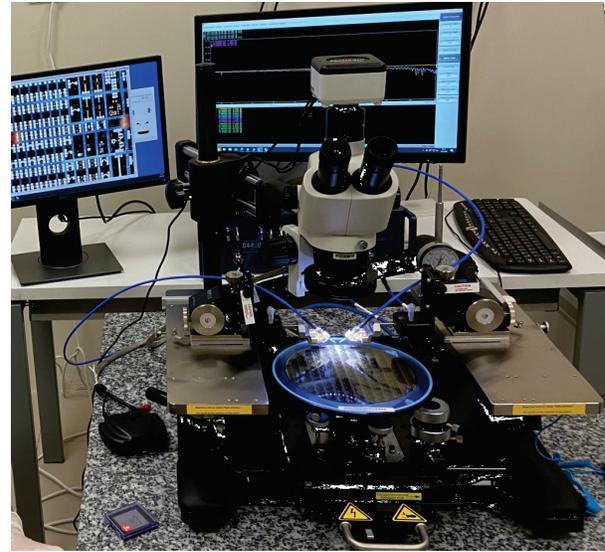
Fig. 11. Probe station for die level measurement.

Vector Network Analyzer, calibrated at the probe tips using the ISS 101-190 calibration substrate between DC and 40 GHz. The small signal measurements reported here are taken at room temperature, 25°C.

G. 0 dB attenuator (THRU) results

Figure 12 has simulation and measurement results for the 0 dB attenuator, namely the THRU circuit. The measurement agrees with the simulation well for both insertion and return loss performance.
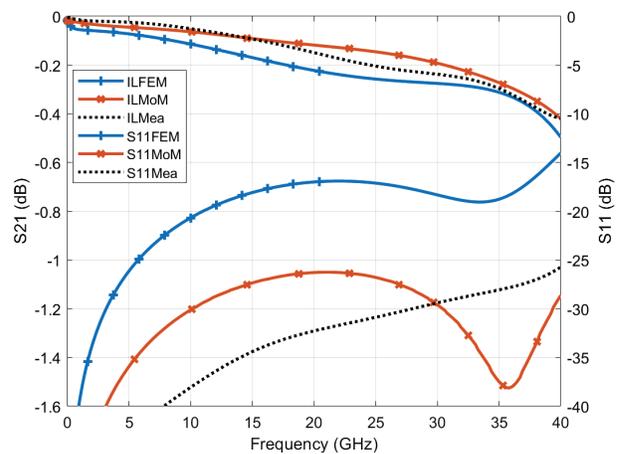
Fig. 12. Sim vs Mea for 0 dB attenuator: (left) s21 in dB and (right) s11 in dB.

H. 3 dB attenuator result

Figure 13 shows the simulated and measured insertion loss and input reflection coefficient of the 3 dB attenuator. It is seen from the insertion loss plot that a 0.4 dB

maximum variation is present. The measurement results were in good agreement with the full-chip electromagnetic simulations. The FEM simulations and the measurement results of the input reflection coefficient in dB for all designs are better than 22 dB.
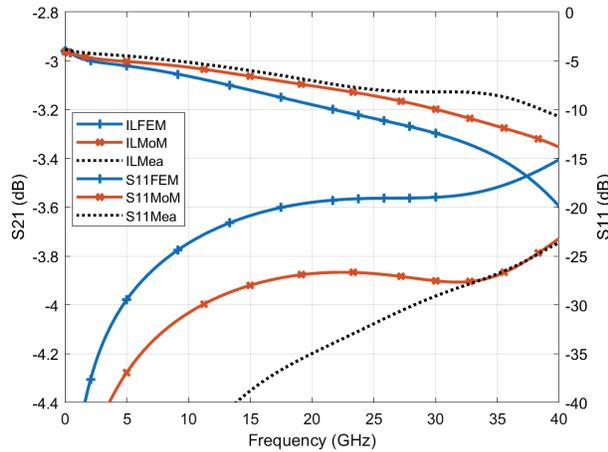
Fig. 13. Sim vs Mea for 3 dB attenuator: (left) s21 in dB and (right) s11 in dB.

I. 4 dB and 6 dB attenuator results

Figure 14 has simulation and measurement results for the 4 dB attenuator. The 6 dB attenuator results are shown in Fig. 15. The simulated and measured insertion loss shows only a 0.6 dB variation across the frequency range.

The FEM simulations and the measurement results of the input reflection coefficient for all designs are better than 20 dB. The design's distributed nature helped achieve such a wider frequency response.
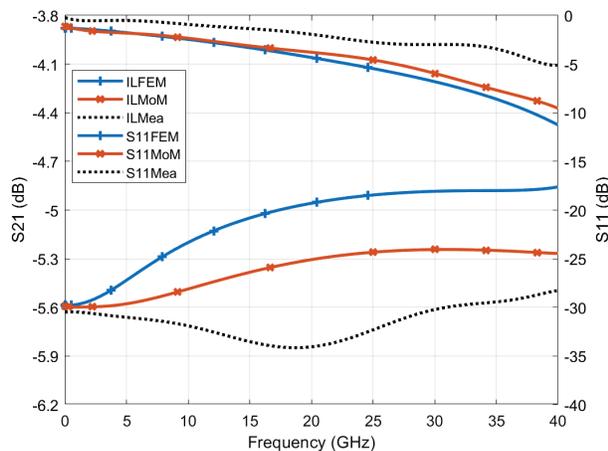
Fig. 14. Sim vs Mea for 4 dB attenuator: (left) s21 in dB and (right) s11 in dB
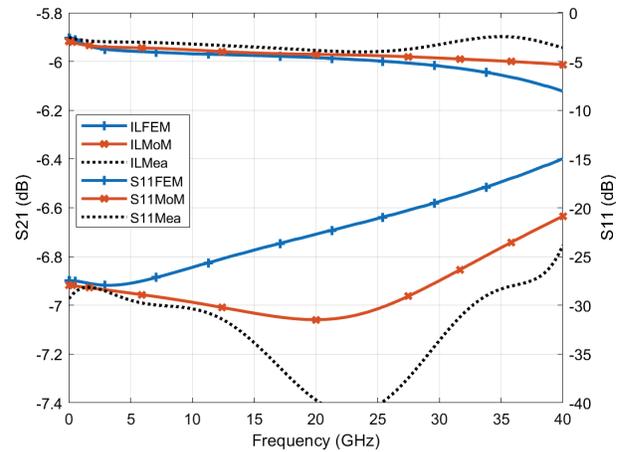
Fig. 15. Sim vs Mea for 6 dB attenuator: (left) s21 in dB and (right) s11 in dB.

J. 10 dB and 12 dB attenuator results

The simulated and measured performance plot of the 10 dB attenuator is shown in Fig. 16. The circuit has an ultra-flat broadband response with less than 0.25 dB variation from DC to 40 GHz, owning to its distributed design. The reflection coefficient is better than 22 dB. Insertion loss and return losses exceed the design targets and agree with the simulated performance.
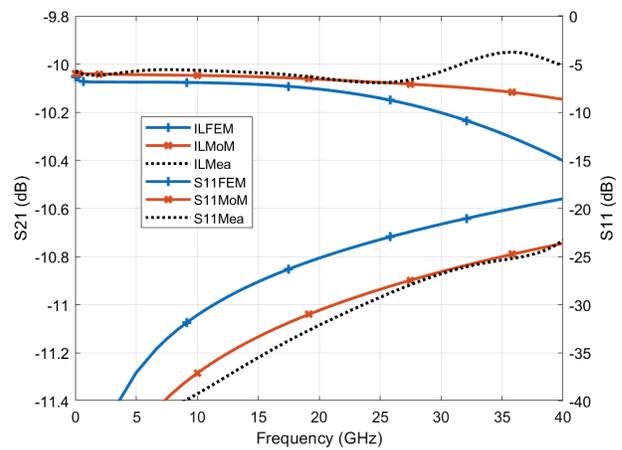
Fig. 16. Sim vs Mea for 10 dB attenuator: (left) s21 in dB and (right) s11 in dB

Figure 17 has simulation and measurement results for the 12 dB attenuator.

K. 20 dB and 30 dB attenuator results

Figure 18 shows the simulated and measured results of the 20 dB attenuator with only a 0.48 dB variation across the band. The reflection coefficient is better than 23 dB for both measurement and FEM simulation. Figure 19 has simulation and measurement results
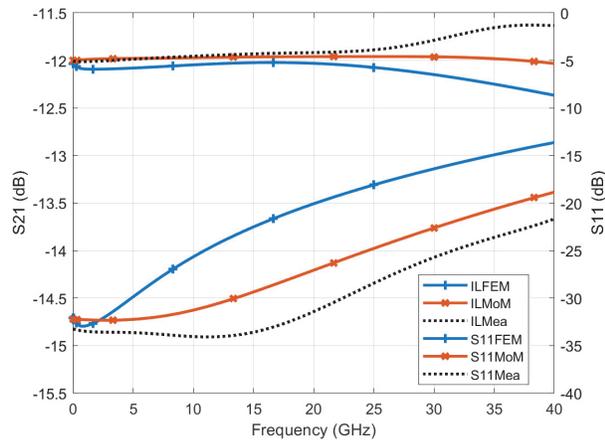
Fig. 17. Sim vs Mea for 12 dB attenuator: (left) s21 in dB and (right) s11 in dB
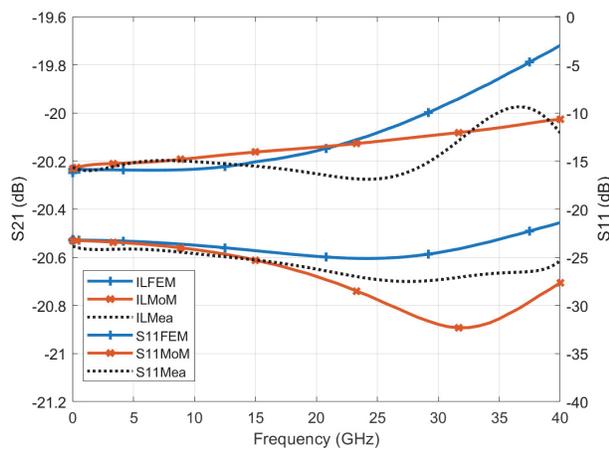
Fig. 18. Sim vs Mea for 20 dB attenuator: (left) s21 in dB and (right) s11 in dB
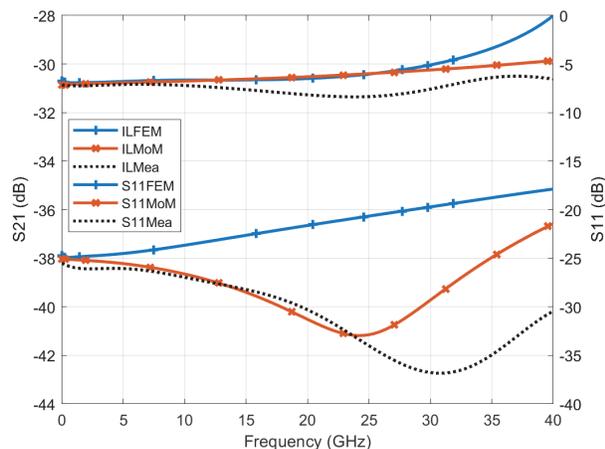
Fig. 19. Sim vs Mea for 30 dB attenuator: (left) s21 in dB and (right) s11 in dB.

for the 30 dB attenuator. Both designs have an ultra-flat response and highly matched behavior across the band.

A comparison of this study and other published ones is demonstrated in Table 1. This study produced the most compact fixed attenuators to the best of the authors' knowledge.

Table 1: Comparison of published fixed attenuators

Ref	Atten (dB)	Freq (GHz)	RL (dB)	Area (mm^2)	Process
[29]	3 /6	DC-40	23	1	GaAs
[29]	20	DC-40	24	2	GaAs
[30]	5	DC-50	16	0.49	Si
[31]	20	DC-20	27	0.45	Si
[32]	3 /6	DC-18	18	4	ThnFlm
[11]	3 /6	5-40	15	0.35	Graphn
Ours	0 - 12	DC-40	19	0.2	GaAs
Ours	20 / 30	DC-40	24	0.27	GaAs

III. CONCLUSION

A family of Ka-band MMIC attenuator dies with different attenuation levels has been designed in GaAs-based IPD process using numerical analyses such as finite element method and Method of Moments. A classical attenuator topology is modified as a highly distributed network to fit in an ultra-compact area and to achieve the desired performance from DC to 40 GHz with the aid of a commercially available electromagnetic solver. The wafer-level s-parameter measurements are done at the probe station. The comparison of the different numerical solutions with the measurement data is also reported in the paper. The differences between the two solutions are due to the EM setup. The Method of Moments solution uses a finer mesh size and takes the edge and via effects into consideration; however, the finite element method is set up for faster simulation by trading the solution accuracy. The measurement results show a good agreement with the simulations and prove the viability of the design methodology.

REFERENCES

[1] J.-W. Jung, K.-K. Nae, J.-H. Bae, E.-J. Lee, H.-R. Oh, Y.-R. Seong, and J. Park, "Compact size directional coupler for mobile RFID reader," in *2007 IEEE/MTT-S International Microwave Symposium*, Honolulu, HI, pp. 987-989, 2007.

[2] S. Li, L. Ma, L. Wang, B. Wu, Y. Cheng, X. Lei, F. Liu, and G. J. Cheng, "An ultrawideband GaAs

MMIC microstrip directional coupler with high directivity and very flat coupling," *IEEE Transactions on Microwave Theory and Techniques*, vol. 70, no. 4, pp. 2271-2279, Apr. 2022.

[3] S. Hu and G. Qian, "Design of a miniature X-band broadband unequal power divider MMIC using bridged-T coils," in *2021 International Applied Computational Electromagnetics Society (ACES-China) Symposium*, Chengdu, China, pp. 1-2, 2021.

[4] Y. Chen, X. Yan, H. Wu, and L. Sun, "The design and miniaturization of 6-15 GHz lumped-element Wilkinson power divider based on GaAs IPD technology," in *2018 IEEE Asia Pacific Conference on Circuits and Systems (APCCAS)*, Chengdu, China, pp. 207-210, 2018.

[5] K.-Y. Chen, B.-X. Fang, and H.-H. Yeh, "IPD broadband balun design for GSM applications," in *2010 IEEE Electrical Design of Advanced Package & Systems Symposium*, Singapore, pp. 1-4, 2010.

[6] Y. Lu, L. Shen, J. Wang, and Y. Shen, "The design of miniaturized broadband power divider utilizing GaAs-based IPD process and equivalent circuit model," *Chinese Institute of Electronics Journal of Semiconductors*, vol. 38, no. 8, Aug. 2017.

[7] E. S. Kim, Y. Li, Z. Yao, and N. Y. Kim, "A compact Wilkinson power divider with high performance by GaAs-based optimized IPD process," *International Journal of Engineering and Technical Research*, vol. 2, no. 10, Oct. 2014.

[8] X. Mi, T. Takahashi, and S. Ueda, "Integrated passives on LTCC for achieving chip-sized-modules," in *2008 38th European Microwave Conference*, Amsterdam, Netherlands, pp. 607-610, 2008.

[9] Y. Y. Zhu, Y.-J. Yang, and J.-X. Chen, "High performance bandpass filter using HTCC stepped-impedance resonators," *IET Microwaves, Antennas & Propagation*, vol. 12, no. 1, pp. 56-62, Jan. 2018.

[10] P. Kuzhir, A. Paddubskaya, N. Valynets, K. Batrakov, T. Kaplas, P. Lamberti, R. Kotilkova, and P. Lambin, "Main principles of passive devices based on graphene and carbon films in microwave—THz frequency range," *Journal of Nanophotonics*, vol. 11, no. 3, p. 032504, July 2017.

[11] K. Byun, Y. Ju Park, J.-H. Ahn, and B.-W. Min, "Flexible graphene-based microwave attenuators," *Nanotechnology*, vol. 26 no. 5, p. 055201, Feb. 2015.

[12] K.-H. Lee, E.-S. Kim, J.-G. Liang, and N.-Y. Kim, "Design and realization of a compact high-frequency band-pass filter with low insertion loss based on a combination of a circular-shaped spiral inductor, spiral capacitor and interdigital capacitor," *Electronics*, vol. 7, no. 9, p. 195, Sep. 2018.

[13] G. Shen, W. Che, W. Feng, Y. Shi, and Y. Shen, "Low insertion-loss MMIC bandpass filter using lumped-distributed parameters for 5G millimeter-wave application," *IEEE Transactions on Components, Packaging and Manufacturing Technology*, vol. 11, no. 1, pp. 98-108, Jan. 2021.

[14] C.-Y. Hsiao, Y.-C. Huang, and T.-L. Wu, "An ultra-compact common-mode bandstop filter with modified-T circuits in Integrated Passive Device (IPD) process," *IEEE Transactions on Microwave Theory and Techniques*, vol. 63, no. 11, pp. 3624-3631, Nov. 2015.

[15] K. W. Wong, R. R. Mansour, and G. Weale, "Reconfigurable bandstop and bandpass filters with wideband balun using IPD Technology for frequency agile applications," *IEEE Transactions on Components, Packaging and Manufacturing Technology*, vol. 7, no. 4, pp. 610-620, Apr. 2017.

[16] B. Lefebvre, A. Bessemoulin, H. Amara, R. Sevin, and P. Quentin, "High dynamic range, triple gate-based compact DC-40 GHz variable attenuator MMIC for Ka-band variable gain amplifier ICs," in *25th Annual Technical Digest 2003. IEEE Gallium Arsenide Integrated Circuit (GaAs IC) Symposium*, San Diego, CA, pp. 135-138, 2003.

[17] B. Khabbaz, A. Pospishil, E. R. Schineller, H. P. Singh, and J. Jorgenson, "DC-20 GHz MMIC multi-bit digital attenuators with on-chip TTL control," in *GaAs IC Symposium Technical Digest*, Monterey, CA, pp. 239-242, 1991.

[18] R. Teja N. P. Verma, A. Kumar, and A. N. Bhattacharya, "A broadband high linearity voltage variable attenuator MMIC," in *2015 6th International Conference on Computers and Devices for Communication (CODEC)*, Kolkata, India, pp. 1-4, 2015.

[19] D. Hao, W. Zhang, X. Liu, and Y. Liu, "A wideband 6-bit digital attenuator in a GaAs pHEMT MMIC," *Electronics*, vol. 11, no. 14, p. 2166, July 2022.

[20] R. Gupta, L. Holdeman, H. Carlson, J. Potukuchi, K. Hogan, and K. Pande, "Manufacturing technology and yield studies for MMIC 5-bit digital attenuators and phase-shifters," in *12th Annual Symposium on Gallium Arsenide Integrated Circuit (GaAs IC)*, New Orleans, LA, pp. 305-308, 1990.

[21] G. Lizama, T. Andrade, and R. Benton, "1-6 GHz GaAs MMIC linear attenuator with integral drivers," in *Microwave and Millimeter-Wave Monolithic Circuits*, Dallas, TX, pp. 105-107, 1987.

[22] H. Kondoh, "DC-50 GHz MMIC variable attenuator with a 30 dB dynamic range," in *IEEE MTT-S International Microwave Symposium Digest*, New York, NY, pp. 499-502, 1988.

[23] Y. Tajima, T. Tsukii, R. Mozzi, E. Tong, L. Hanes, and B. Wrona, "GaAs monolithic wideband (2-18 GHz) variable attenuators," in *MTT-S International Microwave Symposium Digest*, Dallas, TX, pp. 479-481, 1982.

[24] B. Maoz, "A novel, linear voltage variable MMIC attenuator," *IEEE Transactions on Microwave Theory and Techniques*, vol. 38, no. 11, pp. 1675–1683, Nov. 1990.

[25] A. Aksen, E. G. Çimen, and B. S. Yarman, "A numerical real frequency broadband matching technique based on parametric representation of scattering parameters," in *IEEE APCCAS'98, Asia Pacific Conference on Circuits and Systems*, Chiangmai, Thailand, pp. 351-354, 1998.

[26] B. S. Yarman and A. Fettweis, "Computer-aided double matching via parametric representation of Brune functions," *IEEE Transactions on Circuits and Systems*, vol. 37, no. 2, pp. 212-222, Feb. 1990.

[27] J. Lim, D. Kwon, J.-S. Rieh, S.-W. Kim, and S. W. Hwang, "RF characterization and modeling of various wire bond transitions," *IEEE Transactions on Advanced Packaging*, vol. 28, no. 4, pp. 772-778, Nov. 2005.

[28] A. Sadigh, K. Kottapalli, and P. Petre, "EM simulation of packaged MMIC and microstrip antennas using 'Microwave Explorer'," *ACES Journal*, vol. 10, no. 3, pp. 146–152, Mar. 1995.

[29] A. S. Zagorodny, N. N. Voronin, I. V. Yunusov, G. G. Goshin, A. V. Fateev, and A. Y. Popkov, "Microwave microstrip attenuators for GaAs monolithic integrated circuits," in *International Conference and Seminar of Young Specialists on Micro/ Nanotechnologies and Electron Devices*, Altai, Russia, pp. 67-71, 2012.

[30] L. Dong, Y. Huang and X. Chen, "Novel silicon-based attenuator chip," in *IEEE 4th International Conference on Electronics and Communication Engineering (ICECE)*, Xi'an, China, pp. 324-329, 2021.

[31] Q. Zhong, X. Liang, and Z. Liu, "Design of single thin film resistor network as 20dB attenuator for DC-20GHz application," in *16th International Conference on Electronic Packaging Technology (ICEPT)*, Changsha, China, pp. 297-300, 2015.

[32] H. J. Finlay, L. G. T. Hopkins, and J. M. Ozamiz, "Design and applications of precision microstrip multioctave attenuators and loads," in *6th European Microwave Conference*, Rome, Italy, pp. 692-696, 1976.

Mehmet Emin Bayrak received his B.S. degrees in both Biomedical Engineering and Electrical & Electronics Engineering as double major in 2019 and 2020, respectively. He graduated with M.S. degree from Electrical Electronics Engineering and Cyber Systems program at Istanbul Medipol University in 2022. His master's thesis was on passive MMIC devices. Since 2021, he has been working at TUBITAK, BILGEM as a Researcher. His research interests are III-V-based active and passive MMIC design.

Harun Tekin was born in Istanbul, Turkey, in 1997. He received his B.S. in Electrical & Electronics Engineering from Istanbul Medipol University, Istanbul, Turkey, in 2020. He is currently pursuing an M.S. student in the Electrical Electronics Engineering and Cyber Systems program at Istanbul Medipol University. Since 2022, he has been working as an RF Hardware Design Engineer at NETA Communications. His research topics are the design of passive MMIC, antennas, receiver, and transmitter systems.

Huseyin Serif Savci received the B.S. in Electronics & Communication Engineering from Yildiz Technical University, Istanbul, Turkey in 2001 and the M.S. and Ph.D. degrees in Electrical Engineering from Syracuse University, Syracuse, NY, USA, in 2005 and 2008, respectively. From 2008 to 2013, he was with Skyworks Solutions Inc., Cedar Rapids, IA, USA, as a Senior RFIC Design Engineer. Between 2013 and 2020, he worked as a Principal Design Engineer for Hittite Microwave Corporation, Chelmsford, Massachusetts, and Analog Devices Inc., Istanbul, Turkey. Over the years, he designed and released many RFIC and MMIC products on CMOS, SiGe, SOI, GaN, and GaAs technologies. He is currently an Associate Professor in the Department of Electrical and Electronics Engineering at Istanbul Medipol University, Istanbul, Turkey. He leads the RFMicroSense Research Group, which focuses on the design and modeling of RF and Microwave Integrated Circuits, devices, systems, and antennas. He is also an Associate Editor for the Applied Computational Electromagnetics Society.